Biomedical Applications of Free Solution Molecular Interaction Studies

By

Michael Nolan Kammer

Dissertation

Submitted to the Faculty of the

Graduate School of Vanderbilt University

For the degree of

DOCTOR OF PHILOSOPHY

in

Biomedical Engineering

December 15, 2018

Nashville, Tennessee

Approved

Frederick R. Haselton, Ph.D.

Darryl J. Bornhop, Ph.D.

Pierre P. Massion, M.D.

Brett C. Byram, Ph.D.

Todd D. Giorgio, Ph.D.

Copyright © 2018 by Michael Nolan Kammer
All Rights Reserved

Acknowledgements

This work was supported in part by the Centers for Disease Control and Prevention (CDC), the National Science Foundation (NSF Grant No. CHE-1610964, CHE-084878, and CHE-1307899), the National Institutes of Health (NIH Grant No. 1R41HD088138-01), The National Cancer Institute (NCI Grant No. UO1-CA186145) and the Vanderbilt Institute of Chemical Biology.

Table of Contents

List of Figures

List of Tables

Introduction

The work presented in this dissertation is based upon a simple but astonishing observation:

Free-solution interferometric measurements report changes in molecular conformation and hydration upon binding.

This observation is not particularly new, but historically it has not been well understood and its importance has been understated.

Chapter 1: Origin and prediction of free-solution interaction studies performed label-free (adapted here from Proceedings of the National Academy of Sciences, Volume 113) provides a historical background to the current state of optical methods for measuring molecular interactions and lays out the current theory of refractive index (RI) detection of free solution interactions. However, the current theory, which stems from surface immobilized RI techniques such as surface plasmon resonance, is incorrectly applied to free-solution measurements. In fact, the current prevailing theory conflicts with decades of free solution experiments, and in this work, we discuss discrepancies from numerous optical techniques performed in laboratories around the world over the past 50 years. Then, we posit a new theory: *changes in molecular conformation and hydration are the source of free solution refractive index signals*. I developed a heuristic model built on structural data from the Protein Databank that uses bound and unbound molecular structures to calculate the change in RI based upon changes in structure conformation. The chapter concludes with a rather simple method that accurately predicts both the magnitude and direction of free-solution RI signals. Additionally, this work provides detailed instructions on how to perform free solution assays (FSA) using a backscattering interferometer (BSI).

Interferometers are extremely sensitive optical sensors, which has been both a blessing and a curse. Interferometers have been employed to measure the distance to stars and even recently a 2.5-mile underground interferometer was used to measure gravitational waves, a phenomenon predicted by Albert Einstein more than 50 years ago. On the other hand, interferometers' high sensitivity to changes in RI, regardless of source, means high sensitivity to bulk property changes,

such as temperature and pressure, has limited their use in biosensing applications. The temperature sensitivity of RI sensors has been a particularly difficult barrier to overcome, making it necessary to actively control the system temperature and ultimately limiting the resolution of ΔRI sensitivity. The laboratory of Darryl Bornhop, Ph.D. has worked to mitigate this limitation by performing interferometric measurements in a glass chip with a microfluidic channel to serve as the optics. Because the glass chip is in intimate contact with an aluminum block that is temperature controlled by a Peltier and the surface area-to-volume ratio is high, the Bornhop Interferometer enabled RI sensing at high sensitivity in quite small volumes (100's of picoliters). The chip-based method employed to obtain these important results has enabled a wide array of RI biosensing applications to be demonstrated by the Bornhop lab, their collaborators, and even independent researchers. Yet, true translation and wide dissemination of the observations noted in Chapter 1 will require an easy to use, robust interferometer. In **Chapter 2: A Highly Compensated Interferometer for Biochemical Analysis**, adapted here from ACS: Sensors Volume 3, I demonstrate the first steps toward such a device. The compensated interferometer (CI) consists of a diode laser with an elongated beam and a CCD camera. The elongated beam allows the illumination of a 12.8 mm section of a microfluidic channel, producing a set of elongated interference fringes that allows a test sample and reference solution to be interrogated simultaneously. The practical implication of this unique optical configuration is that one beam illuminates a single object resulting in two nearly identical interferometers. The result of this optical approach is a significant reduction in environmental noise through common mode noise rejection, thereby enabling high sensitivity RI measurements without the need for external temperature control. Thus, the CI can be used to perform molecular interaction assays on a significantly simplified instrument, without the need for a high-resolution temperature controller, greatly reducing the cost, size, and power consumption of the device, while providing an *increase* in signal/noise. **Chapter 3: Longitudinal Pixel Averaging for Improved Compensation in Backscattering Interferometry**, adapted here from Optics Letters Volume 43, provides a quantitative demonstration of the necessary operating principles for CI, defining the channel interrogation properties needed to achieve true compensation between the two RI sensing regions.

Translation of this technology to the broader biomedical research community or to the clinical setting will necessitate higher throughput and a streamlined data analysis approach. To address the issue of throughput, I interfaced the CI with an automated microfluidic droplet

generator to facilitate hands-free, rapid sample introduction via a droplet train. This operation is detailed in **Chapter 4: Compensated Interferometric Reader Signal Extraction and Analysis.**

With an assay methodology and reader technology in hand I turned to addressing several biomedical applications for FSA-CIR. The first I will describe is found in **Chapter 5: Rapid assay development and quantification of two chemical nerve agents in serum,** which demonstrates that quantitative tests aimed at diagnosing exposure to organophosphorus nerve agents using aptamer probes can be developed rapidly and with excellent sensitivity. This work builds upon the work presented in my master's thesis [1] where the BSI method was applied to the quantification of aptamer-small molecule binding. Here, aptamer probes and our unique interaction sensing approach described in **Chapter 1** enabled the development of low cost, highly sensitive assays without the derivatization or immobilization steps that retard assay development for other techniques.

I describe in **Chapter 6: Quantitation of Opioids and the Prospect of Improved Diagnosis of Neonatal Abstinence Syndrome** the development of high sensitivity quantitative assays for three opioid targets and their primary metabolites in urine using the FSA-CIR approach. With a simple mix-and-read assay, I achieved sub-10 picograms per milliliter detection limits, and accurately quantified spiked test "unknowns" across a 3-decade span of concentrations. This assay development effort is accompanied by a pharmacokinetic analysis that demonstrates the added utility of the improved sensitivity and time-to-result provided by the FSA-CIR method over the current gold-standard technique in diagnosing neonatal abstinence syndrome and in analgesic dosing of neonates with opiates for pain management. This pharmacokinetic analysis shows that even in the most extreme circumstances, by the time symptoms of neonatal withdrawal symptoms are manifest (48-72 hours after birth) the levels of opioids in neonatal urine have decreased below the detection limit of mass spectrometry (MS) methods. Compared to MS methods, the lower projected cost, easier use, and FSA-CIR's improved detection limits are predicted to allow confirmation of opioids in neonatal urine samples well past the typical onset of symptoms, which could enable confirmatory testing in low resource, near patient settings.

In **Chapter 7: Preclinical Evaluation of a Free Solution Assay for the Quantification of a Candidate Lung Cancer Biomarker CYFRA 21-1** I describe my efforts to begin clinical translation of FSA-CIR. In this biomedical application, and perhaps the most exciting result presented here, I use

FSA-CIR to address the lack of an accurate diagnostic biomarker for lung cancer. FSA-CIR provided a 40-fold lower limit of quantitation (LOQ) for the cytokeratin candidate lung cancer biomarker CYFRA 21.1 when compared to the current gold-standard assay technique Electrochemiluminescence. We hypothesized that by lowering the LOQ of the biomarker it is possible to increase the discriminatory power of the biomarker (e.g. expand the separation between cases and controls)**. Chapter 7**: presents the initial results of this project, which show that the improved LOQ of FSA-CIR did provide greatly enhanced discrimination of cases vs controls in a 225-patient cohort of patients presenting indeterminate pulmonary nodules (IPNs).

Translation of this platform technology will require an automated approach to data analysis. **Chapter 8: CIR Analysis Tools** presents a first step towards the goal of automated analysis. I developed a data analysis algorithm and encoded it into an easy to use LabVIEW program that enables a user to turn the raw CI data output (phase shift over time) into usable data in a spreadsheet format. Description of the algorithm and a preliminary validation is presented in **Chapter 8**, while a step-by-step tutorial for analyzing data using this program presented in **Appendix C**, and additional troubleshooting information in **Appendix D.**

This collection of work demonstrates that I have made advancements in the underlying theory of free solution molecular interactions, engineered a nearly-mature compensated interferometric reader, and applied it to several important biomedical problems.

References

1. Kammer, M. N. Characterization of aptamer-small molecule interactions with backscattering interferometry. Masters Thesis, Vanderbilt University, Nashville, 2016.

Part I: Theory

Chapter 1: Origin and prediction of free-solution interaction studies performed label-free

As published in Proceedings of the National Academy of Sciences volume 113

Contemporary assays enabling single molecule detection [2-3] have accelerated the sequencing of the human genome [4] and facilitated imaging with extraordinary resolution without labels [5]. To most closely approximate the natural state, an interaction assay methodology would interrogate the processes (reaction, molecular interaction, protein folding event, etc.) without perturbation. Label-free chemical and biochemical investigations [6-7] transduce the desired signal without an exogenous label (fluorescent, radioactive, or otherwise) representing an essential step toward this goal. Many label-free methods require one of the interacting species to be either tethered or immobilized to the sensor surface, introducing a potential perturbation to the natural state of the species [8-9]. However, back-scattering interferometry (BSI) is a free-solution label-free technique with the added benefit of sensitivity that rivals fluorescence [10]. There are other techniques performed in free solution, such as mass spectrometry (MS) [11-12] and nuclear magnetic resonance (NMR) [13-14] and the widely used isothermal titration calorimetry (ITC) [15-16]. As with NMR, ITC has many advantages, but exhibits modest sensitivity and often requires large sample quantities. Another increasingly popular free-solution approach is micro-scale thermophoresis (MST). Yet for MST to operate label-free, one of the binding partners must have a significant absorption/fluorescence cross-section [17-18]. BSI represents an attractive alternative to these methods because of its high sensitivity, small sample volume requirement, optical simplicity and broad applicability [19-22]. Whereas ITC and MST are well known, the fundamental mechanistic basis for the signal observed in BSI is less well understood.

Herein we attempt to address the fundamental basis for the signal observed in label-free, free-solution interaction studies performed with an interferometer. We present a hypothesis for the mechanism of signal generation in free-solution assays (assumed to be label-free from this point forward) and pose a preliminary model for interaction studies. Our model is a work in

progress and as such has limitations. Here it is our intent to stimulate additional investigations and to address two questions:

1) *How can interactions be measured label-free and in free-solution, in the absence of absorbance, a significant mass change, or a thermal signature?*

2) What intrinsic property allows unprecedented sensitivities (picomolar to femtomolar) in complex milieu, when neither of the individual binding partners is detectable at those levels?

In addressing these questions, we show that *free-solution* methods properly performed by interferometry have a unique, enabling signal transduction mechanism and that the signal magnitude correlates with changes in quantifiable intrinsic properties. We also demonstrate that the **Free**-**S**olution **R**esponse **F**unction (from hereon, FreeSRF) can be quantified and within defined parameters can be predictive.

Results presented establish that the relative measurements performed in free-solution allow the solution refractive index (RI) to provide a reproducible, robust, and quantifiable readout of chemical reaction progression (interaction), *principally due to conformation and hydration changes upon binding*. We illustrate that the changes leading to a FreeSRF cannot be considered simply as mass weighted dη/dC responses, even though the interferometer exhibits a dη/dC response for a single analyte (salt, sugar, protein, antibody, or DHA strand) [23]. We describe how to properly employ BSI and configure the free-solution assay to ensure quantitation of binding affinities for a wide range of species: (e.g. ion binding a protein [10], a sugar binding a lectin [9], hydrogen bonds forming in non-aqueous media [24], small molecules to membrane-proteins embedded in cell-derived vesicles [19], merozoite proteins to intact human erythrocytes [22], and protein folding [25]). Finally, we show how to estimate the magnitude of free-solution signal using protein database-derived information.

Background

Nearly two decades ago the Bornhop lab published observations indicating that their unique interferometer could be used to measure protein folding [25]. The importance of these preliminary studies was not more fully realized until 2007, when our group showed that binding events, such as ion-protein, protein-protein, and small molecule-protein interactions, could be

measured using a RI technique in free-solution and without labels [10]. Numerous examples have validated that free-solution measurements by interferometry can be used to quantity interactions of widely different affinities μM – pM) and on interacting pairs with significant mass differences (>10,000 fold) [19-21]. While we, and others, have postulated the origin of the free-solution signal, no explicit explanation for the physical phenomenon has emerged. Here we capitalize upon the pioneering observations by Sota and others including Pitner and Koch [26-29], using techniques typically thought to be insensitive to *bulk* RI changes [26] that couple energy into an immobilized sensor surface layer, which suggest that a theory based purely on dη/dC considerations does not adequately describe the response for optical methods performed in free-solution. The background necessary to support this supposition is provided *vide infra* and in **Appendix A**.

A wide range of surface techniques have dη/dC signal dependence, where the performance is bounded by the relative change in mass-concentration at the *surface* (**Equations A.1 – A.3**). These observations have led to a reasonable but mistaken assumption that signal transduction in free-solution is the same as deflection, refraction, or wavelength shift, techniques where performance is bounded by the relative change in volume at the *surface* (mass or concentration). The dη/dC formalism was established in 1988 in one of the first papers describing surface plasmon resonance (SPR) [30]. Other descriptions on how to relate these changes to adsorbed films appeared thereafter [31-33]. In one of these reports, researchers showed the SPR response was linear with surface concentration of protein (ng/mm^2) for adsorbed species, and introduced the refractive index increment (RII), which was defined as dη/dC in ml/g [33]. They illustrated that the RI of the surface layer was the sum of the concentration weighted RII (**Eq A.1**). Using a Matthews report [34] indicating the fractional solvent content of a globular protein crystals ranges from 30-78%, they then estimate the probed surface thickness to range from 60 and 200nm. Yet, the closely packed protein crystal representation omitted values for solvent content and specific volume.

Yee and co-workers [31] recast the Lorenz-Lorenz equation (**Eq A.2**), further establishing the paradigm by showing that $\eta_{protein}$ = 1.57 RIU for the *water-free* (unreacted) protein was close to that of crystalline proteins of 1.60 RIU as confirmed by Schuck [35]. Importantly these values are greater than those estimated for "adsorbed protein films" using ellipsometric approaches assuming a single optical thickness, since the film volume does indeed include a great deal of water

[31, 36-37]. Yee et. al. referred to that part of the film that "are made of protein material itself, *not water*." They also noted, "we believe this approach, which *neglects the intermixed solvent* in the adlayer, is more direct and general for quantitative analysis of adsorbate coverages for proteins and adsorbates in general" [31]. A report by Marsh also suggests that hydration/conformation are important predictors of binding-induced structural changes [38].

In 2000, Davis and Wilson reported on an approach to determine the RII of small molecules for correction of SPR data [39]. They too employed the formalism of a concentration weighted RII (**Eq A.3**) and predicted the maximum (BIACORE) SPR instrument response for binding of a single ligand (**Eq 1.1**).

$$(RU_{pred})_{max} = RU_M * (MW_L/MW_M) * (d\eta/dC)_L / (d\eta/dC)_M \qquad \textbf{Eq. 1.1}$$

where $(RU_{pred})_{max}$ is the predicted maximum instrument response in resonance units for binding at a single site, RU_M is the experimental amount of macromolecule immobilized on the chip in resonance units, MW_L is the molecular weight of the ligand, MW_M is the molecular weight of the immobilized macromolecule, $(d\eta/dC)_L / (d\eta/dC)_M$ is the RII of the macromolecule. The relative mass was also shown to be an important parameter in predicting the maximal signal in flow injection gradient SPR systems [40].

The model described above and in **Appendix A** used to define the response for RI (bio)-sensing methods, does not take into account the possibility that the signal may be impacted by conformation and hydration changes upon chemical or biochemical transformation (binding, folding, shedding or gaining waters of hydration). Sota and co-workers were the first to question this supposition by reporting the detection of conformational changes in an immobilized protein using an SPR biosensor [26]. They observed that the SPR signal of the tethered protein and the molar ellipticity of dihydrofolate reductase *in solution* responded similarly to pH changes. Combined with tethered protein sensor surface measurements in the pH range of 0.12 – 7.80, they postulated that their observations were "consistent with the interpretation that changes in the SPR signal reflect conformational changes occurring during acid denaturation" [26].

Numerous others have questioned the paradigm of RI sensing exhibiting simply a mass weighted response. In 2000, Boussaad, Pean, and Tao employed multi-wavelength SPR to show that altering the reduction potential of a solution caused a change in the conformation of cytochrome *C* and a corresponding change in signal [41]. Salamon et al. reported the use of an SPR-related technique, coupled plasmon-waveguide resonance spectroscopy (CPWR), to study

ligand-induced conformational changes in a G-protein coupled receptor embedded in a lipid bilayer [42]. Gestwicki and coworkers exploited the observation that the SPR response is not strictly dictated by the RII to enhance small molecule detection [28]. In this work and a subsequent patent [43] they demonstrated that ligand-induced conformational changes can be used to report small molecule binding to immobilized maltose-binding protein and tissue transglutaminase by SPR, without the need for a high molecular weight (MW) competitor. For ligands binding to a receptor, they showed: a) there is a net *negative* ΔRI with a decrease in hydrodynamic radius; and b) when the interaction increases hydrodynamic radius, a net positive ΔRI results. Using response reversibility and similarities between reported and SPR-determined equilibrium dissociation constants, they confirmed that these signals could not be attributed to the addition of analyte molecular mass to the surface as would be predicted by **Eq. A.1-3** and **1.1**. They showed, with a high level of confidence, the observations were a consequence of specific receptor-ligand interactions.

The details of the Gestwicki, et. al. experiments are important here. X-ray crystal structures show that Maltose binding to Maltose Binding Protein (MBP) induces a conformational change. The hinge-twist structure change between the two domains of MBP causes a net decrease in hydrodynamic radius [28]. As predicted for a negative net change in hydrodynamic radius, the event produced a negative ΔRI. Also consistent with their hypothesis was the observation that a positive ΔRI resulted when calcium binds to tissue transglutaminase (tTG), which is allosterically regulated by Ca^{2+}. The positive ΔRI of roughly +1000 resonance units (RU) reported for Ca^{2+} binding to tTG, from a change in hydrodynamic radius resulting from a ca. 15° rotation, was much greater than the expected +28 RU from mass alone. Thus, the conformationally active form of tTG increased the SPR signal intensity by 36-fold upon calcium binding. Unlike calcium, maltose is of sufficient molecular mass (360 Da) to be detected directly by SPR. Yet, when maltose binds to MBP, a net *negative change* in RI is recorded in the SPR sensorgram, apparently because the binding event-induced conformational change overwhelms the positive response due to accumulation of mass from maltose (MBP-maltose interaction gave a net 5-30 RU signal).

After a period of silence, several SPR papers appeared on the topic of conformation-dependent sensing despite many considering the reports to be simply anomalous behavior [44-48], attributed to: 1) buffer mismatch, 2) volume exclusion due to ligand density differences [44-46], 3) non-specific matrix interaction [47], and 4) non-specific reference interactions [48]. Regardless,

a recent paper reported that the RI sensing figures of merit were dependent on shape and the size of the Au nanoparticles [49] with sensitivities generally increasing as the nanoparticles became elongated and their apexes become sharper. When nanobipyramids' aspect ratio was increased from 1.5 to 4.7 signal increased from 1.7 to 4.5. Then in 2010, SPR was employed to quantify *E. coli* DHA ligase using a hairpin DHA to probe self-structure change during the ligation process [50]. Clearly no change in MW was necessary to provide signal for this assay.

Because of the significant difference in the mass of the binding pair, ion - protein interactions are an important class of interactions to consider. Christopeit, Gossas, and Danielson [51] showed that SPR detects these interactions, provided that a large conformational change is induced upon binding. Here a Ca^{2+}-induced conformational change of C-reactive protein (CRP) made the protein more compact, decreasing the hydrodynamic radius, leading to an "unexpectedly" negative ΔRI change.

Recently the Koch group contributed two studies [29, 52] further bolstering the argument that free-solution signals correlate to binding-induced conformational changes. In 2010, they reported that SPR sensorgram amplitudes for saturated Ca^{2+}-binding of protein-coated surfaces greatly exceeded the theoretical values [52], concluding the SPR signal was a consequence of the concerted Ca^{2+}-binding induced protein conformational change in the vicinity of the protein–dielectric, rather than being due to a mere mass effect. Using NMR structures of Ca^{2+}-free (apo) and Ca^{2+}-bound myristoylated recoverin (mRec), reported as average structures, they illustrated Ca^{2+}-free recoverin has a tense (T), compact conformation in which the myristoyl group is sequestered in a hydrophobic pocket (**Figure A.1A**). Yet, in the Ca^{2+}-loaded form it undergoes a transition to a released (R), more extended conformation, where the myristoyl is solvent-exposed (**Figure A.1B**). The Ca^{2+}-induced transition is characterized by both an increase in the radius of gyration (R_{gyr}) and total solvent accessible surface area (SASA). They postulated that the solvation shell of the R conformation differs significantly from that of the T conformation, which affects the surrounding water structure and the overall change in RI signal measured. Recently, this group also showed a correlation between SPR, dynamic light scattering (DLS), and size-exclusion chromatography [29], confirming that conformational changes under conditions of molecular crowding yield fingerprint profiles reflecting different hydrodynamic properties for each Ca^{2+}-sensor protein under changing Ca^{2+} conditions. These properties were extremely sensitive to even

small alterations of structure/conformation induced by point mutations. The Bornhop group has made similar observations in free-solution for binding of folate to histone demethylase, LSD1 [53].

The work reported by the Koch the group indicates that the site-specific homogeneous immobilization of the proteins enhances the intensity of the phenomenon, but the RI changes induced by concerted Ca^{2+}-binding/conformational transitions are essentially isotropic. Using DLS, circular dichroism (CD), and ellipsometry as confirmatory and complementary methods, they concluded, "conformational changes can be detected even via the p-polarized resonance excited by the commercial SPR systems (Biacore, GE)…likely to be a direct result of the heterogeneous orientation … a different case (than) the anisotropic immobilization of membrane receptors in lipid bilayers that require both s- and p-polarizations to be fully characterized as in plasmon waveguide resonance spectroscopy (PWRS) [54]" [52]. Thus, Koch predicts that conformational changes are less likely to be observed in the absence of both polarizations with highly organized systems.

Like PWRA, dual polarization interferometry (DPI) [55], employs both s- and p-polarizations of light. DPI is based on the observation that a laser illuminated waveguide stack produces an interference fringe pattern that undergoes a phase change when an immobilized layer on the top stack changes. By introducing alternating polarization states [transverse electric (TE) and transverse magnetic (TM)], at right angles to each other into the stack, the difference in response allows two independent surface measurements. Using classical optical theory, these two outputs give a measure of thickness and density for the (protein) layer. Comparison of the TM and TE output has enabled shape, orientation, binding, and molecular conformation changes to be studied [56].

Overall, the collective literature described above are consistent with our hypothesis that systems with significant conformation and hydration changes, *do not* conform to the theory that predicts RI changes are equal the sum of the mass weighted RI values (**Eq. A.1-3** and **1.1**). Too much evidence exists, from a diverse set of chemical/biochemical processes, for these observations to be anomalous or spurious in origin. Particularly since the signal was observed in the presence of a large background arising from a mass adsorbed at the surface. Hence, configuring an assay to reduce or eliminate competing RI signals should result in a measurement that reports conformation/hydration changes. In 2007, Bornhop's group tested this hypothesis, showing that under the proper conditions a sensitive RI sensor can transduce solution-phase binding events [10].

Since this original report, BSI has been used widely [19-22, 24-25, 57], and benchmarked extensively, with comparisons to ITC, SPR and other established assay platforms.

Results and Discussion

A unique aspect of our free-solution methodology is that often the sensitivity of the assay *far exceeds* that for detecting the individual participating species. In other words, the *ligand* alone has no quantifiable dη/dC response under the conditions of the assay, but when *comparing* the bound sample to the receptor/target (reference) there is robust and reproducible signal (**Fig. A.2-3**). This observation has raised the two important questions: 1) How it is physically possible to perform these label-free studies in free-solution? 2) What is the signal source? Here we aim to definitively answer these questions, putting forth an explanation and a preliminary model for the free-solution signal and detailed transduction procedures by interferometry.

Conformation and Hydration Changes are the Origin of Free-Solution Signals

To quantify interactions in free-solution the experiment must be designed in a manner that places the chemical and optical focus on changes in conformation, hydrodynamic volume, hydration state, and to a lesser extent, the electronic state. Proper handling of index-matched sample and reference enable chemical focusing, while correct instrument alignment and operation maximize signal transduction by the interferometer. Our methodology should also apply to systems where there is no mass change, as in protein folding or where the difference in mass for the binding pair is large. We describe here how, the *relative mass* of the binding partners plays a minor role in determining the **Free**-**S**olution **R**esponse **F**unction (FreeSRF).

Many years ago, Bornhop's group demonstrated protein folding on very small sample quantities with an early generation capillary interferometer, showing that a readout for ubiquitin folding could be obtained [25]. In retrospect, we now realize the importance of this observation, which illustrated that in the absence of any mass change, we could employ an RI sensor to follow conformation changes in free-solution. Recent efforts to construct an assay for respiratory syncytial virus (RSV) provides additional evidence for our hypothesis that free-solution assays are reporting changes in conformation and hydration [57]. Bornhop's group found that the BSI sensitivity was not only related to the number of unpaired nucleotides, but also to the *structure* of the targeted regions of the RNA sequence. For example, locked nucleic acid (LNA) probes showed a 4-fold sensitivity improvement compared to DHA probes of the same sequence. To explain this

non-dη/dC behavior, Bornhop's group investigated how the free-solution signal was impacted by changes in the duplex structure. Using titration and incubation of DHA:DHA duplexes with trifluoroethanol (TFE), an established method for converting the duplex structure [58-59], they induced the transition from the B-form to A-form (**Figure A.4**). They then monitored these structural transformations with circular dichroism (CD) and ellipticity at 270nm showing that the BSI free-solution readout reports structural transformations in the DHA duplex. Other experiments performed by us and others [60] involving positional DHA mismatch binding experiments further validate our hypothesis, showing free-solution signal enhancement emanates from induced alterations to the helical geometry of the nucleic acid hybrid and *not a dη/dC* change.

The Interferometer

The technology used to perform free-solution studies represents a unique interferometry configuration [10]. The optical train depicted in **Fig. 1.1** is quite simple for a highly sensitive, small volume interferometer, consisting of a coherent source, an object (channel in a chip or capillary) and a transducer. Probing the object with an unfocused He-Ne beam at nearly 90° (± 7° to allow fringes to be viewed), results in a high-contrast interference fringe pattern in the back-scattered direction. Depending on configuration, tracking the position of the fringes enables RI changes to be quantified in the range from 10^{-4} - 10^{-9} [61-62], within picoliter – nanoliter probe volumes. A long effective path length results from multiple reflections at the fluid-channel interface and leads to the unprecedented sensitivity in constrained volumes [63]. We, and others, still use capillaries, yet the most common interferometer configuration is based on a microfluidic chip containing a nearly semicircular isotropically etched channel that is 100 µm deep and 210 µm wide. Based on empirical observations, we have found that fringe selection is best accomplished by filling the channel with the analysis solution (buffer, serum, etc.) and counting approximately 5 fringes from the centroid, then windowing or selecting 5-7 fringes in this region that exhibit a nearly single spatial frequency (see also: Alignment and Fringe Selection in **Appendix A**). While the fringes closest to the centroid appear to exhibit a greater shift [64], a binding signal has yet to elude us in the region described above. With proper alignment, the fringe contrast ratio approaches 99% and this metric, combined with response to a change in RI (detection limits with glycerol solutions) serves to consistently produce the desired outcome. Good thermal stabilization and environmental isolation is also necessary and allows the device to produce a detection limit of ΔRI

$< 5 \times 10^{-7}$. Typically, the sample/chip is probed with both planes of polarization as a result of coupling a linearly polarized laser into a non-polarization maintaining single mode fiber coupler.

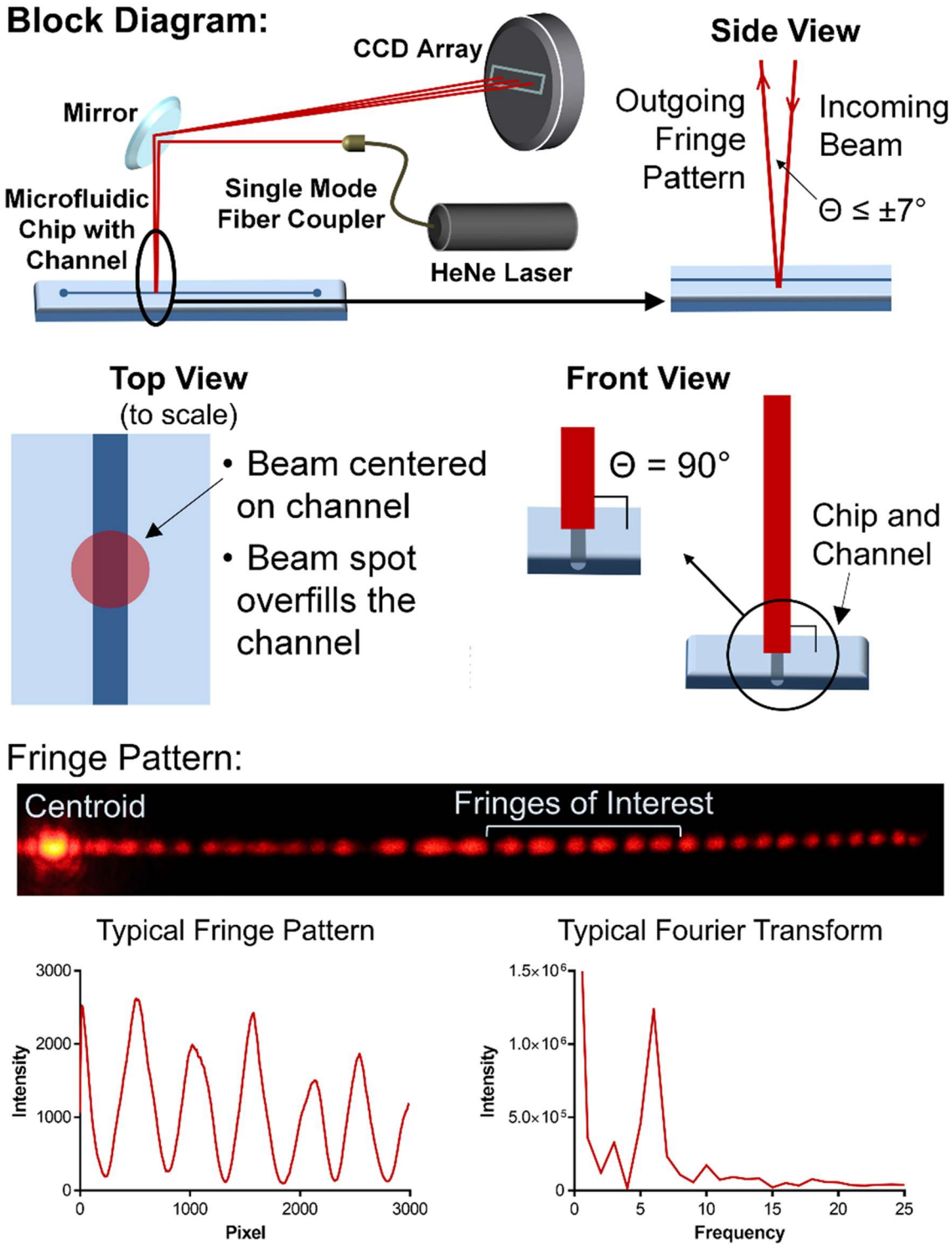

Fig. 1.1 BSI Block diagram showing orientation of the beam relative to the chip, a photograph of the fringe pattern, the line profile of the region of interest for a good fringe pattern and the FFT spectrum for that region of interest (ROI).

Misalignment will lead to slanted fringes and/or fringes with poor contrast. All of the configurations of BSI Bornhop's group and collaborators have investigated exhibit a classical dη/dC and dη/dT response expected of an RI detector.

It is likely that the multipass optical configuration of BSI *contributes* to success in performing free-solution and label-free measurements as does the ultra-small (constrained) volume of BSI, but it is unlikely these alone are *enabling* characteristics. While additional research is needed, we can state that there is a combination of factors that enable our free-solution measurements. These include: 1) the use of the proper assay methodology involving informed choice of reference and control and RI matching, 2) careful sample handling, 3) prudent instrument design with respect to temperature and pressure control, and 4) informed fringe selection as described *vide infra*.

If the conformation/hydration hypothesis described here has a physical basis, free-solution assays should be detectable by a device with comparable ΔRI sensitivity to those used in the SPR reports noted above. Detection limits vary for SPR, but consistently reach $\Delta RI = 10^{-6}$. In our hands the BSI detection limit is $\Delta RI = 10^{-6}$ or 10-fold below this level [20-21, 63]. Therefore, using proper methodology the signal to noise ratio (S/N) of our interferometer should enable molecular interactions to be measured. As shown in **Table A.1 and Figure A.2**; 1) the *actual* ΔRI measured by BSI for a binding event is well within the instrument detection limit and 2) as recently suggested [65] the predicted ΔRI using dη/dC considerations (**Equation A.13 – A.17**) would be *undetectable*.

The Signal is Not Calorimetric

Reactions and binding events can add or remove energy from a solution, changing the solution temperature, a property that has long been used to study interactions by calorimetry. Heat can also perturb the optical properties of a solution, in great part because of the relatively high dη/dT response exhibited by most fluids (1×10^{-4} °C for water). To rule out dη/dT perturbations as free-solution signals we have shown that the quantities of sample interrogated in the interferometer volume cannot generate a temperature change large enough to produce a detectable ΔRI signal [10] (**Appendix A**). Also the absence of signal decay by conduction to a heat sink in stop-flow kinetic binding studies further confirms that the heat of reaction is not the source of the free-solution signal [10]. Virtually all assays performed since 2008 have been run as end-point

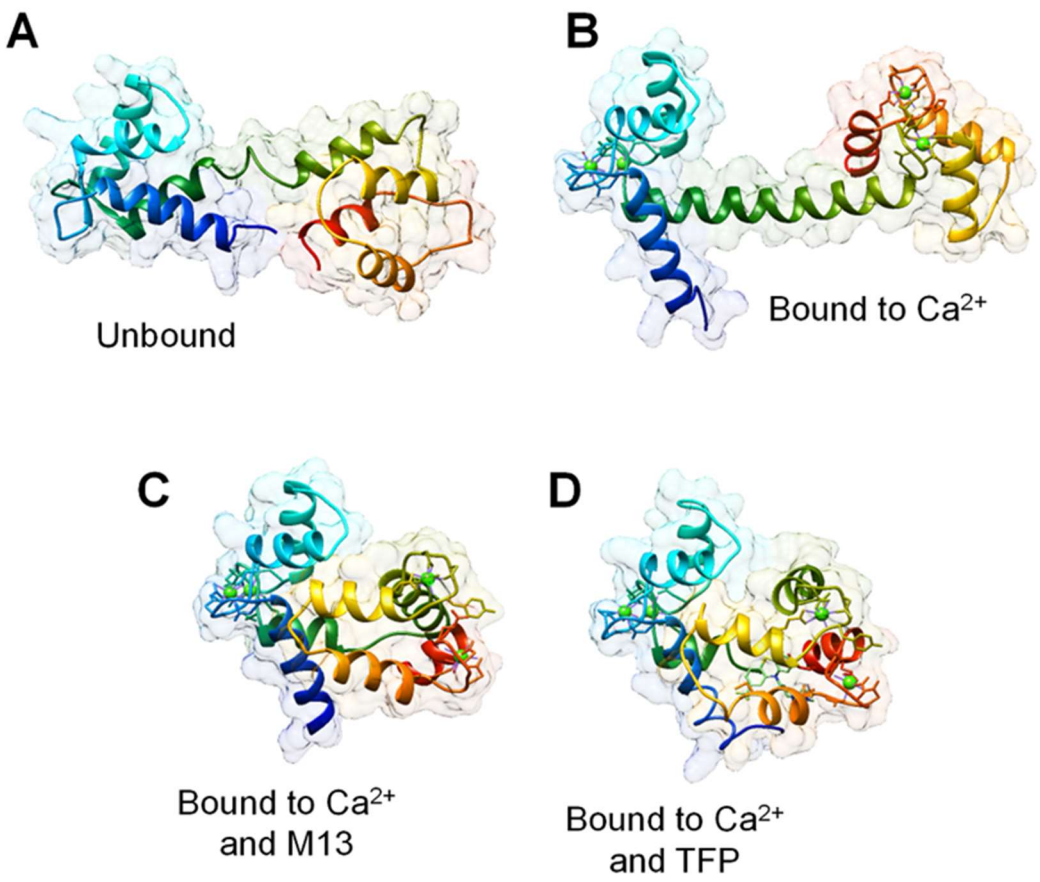

Fig. 1.2 Comparison of ribbon drawings for Calmodulin unbound and bound with various ligands **A)** unbound Calmodulin (PDB: 1CFD), **B)** Calmodulin bound to Calcium (PDB: 1OSA), **C)** Calmodulin bound to M13 (PDB: 1CDL), and **D)** Calmodulin bound to TFP (PDB: 1CTR).

determinations, with samples prepared, mixed, allowed to equilibrate (sometimes for hours), and then read by the interferometer. The end-point scenario excludes reaction-based calorimetric contributions to the signal.

The Free-Solution RI Signal for Interactions/Reactions

Consider the reaction between the two species A and B. As a chemist, it is tempting to write the equation for this reaction as: $\boldsymbol{A} + \boldsymbol{B} \rightarrow \boldsymbol{A\text{-}B}$, but this disregards the complexity of the interaction. When A and B *react* they undergo electronic transitions, lose or gain hydration, and experience significant changes in the atomic geometry. So, the *product* is just that, an entirely new species allowing the reaction to written as: $\boldsymbol{A} + \boldsymbol{B} \rightarrow \boldsymbol{C}$. If this is the case, then the product

formed from *the interaction of* A and B must have a unique and different dielectric constant or molecular dipole moment. The new species therefore responds differently to the probing electromagnetic radiation, in a manner analogous to the pH-change induced 'structural' transformations in a dye molecule that lead to a significant change in absorption (color). For example, even the subtle change produced by ionizing phenol to phenolate results in quantifiably different absorbance spectra.

To aid in visualizing the free-solution transduction phenomena, we use the structural diversity found in calmodulin (CaM) **Fig. 1.2**. Binding of Ca^{2+} to CaM (**Fig. 1.2A)** leads to a significant conformation and hydration change [66], resulting in a new complex, Ca^{2+}-CaM (**Fig. 1.2B**) which has a considerable and quantifiably different electromagnetic cross-section (dielectric constant). Then, if the Ca^{2+}-CaM complex reacts with the M13 protein kinase (**Fig. 1.2C**) the subsequent complex is unique and has a quantifiably different RI due to induced structural and hydration changes [67]. Binding the small-molecule inhibitor, TFP, induces changes in atomic arrangement and hydration that leads to yet another unique chemical entity (**Fig. 1.2D**) [68]. These graphical representations, generated from X-ray structures found in the Protein Data Bank (RSCB/PDB), for bound and unbound species pictorially illustrates that the potential magnitude of free-solution signal can be large (ca. $> 10^{-4}$ RIU) under the proper conditions. Calculations of ΔRI (**Table A.1, Figure A.2-3**) further illustrate this point.

While FreeSRF is *not* proportional to the sum of the mass-weighted change in RI for the reactants (**Appendix A, Eq A.13 – A.17, and Figure A.2 – A.3**), this property does not preclude non-reacting or non-interacting analytes from exhibiting an RI response. Only the proper preparation of the sample and reference, typically from the *same matrix*, enables the extraction of the free-solution signal by canceling out (often) very large bulk RI background signals. In other words, the determination is not made by comparing samples with huge RI differences, but nearly identical ΔRI values. For example, we don't compare $\eta_1 = 1.33131$ to $\eta_2 = 1.39131$, but samples with RI values of 1.391312 and 1.391318 ($\Delta RI = 6 \times 10^{-6}$). The use of *relative measurements* ensure that the interaction is the predominant signal. Further, to minimize the influence of non-specific binding at the surface we establish a base-line with the receptor present in the buffer or matrix under investigation and then to the best of our ability using rinse solutions, reestablish this level before introduction of every new concentration for the assay.

The Free-Solution Response Function and an Expression Predicting Performance

Our first attempt to formulate a model for label-free, free-solution assays was heuristic and based on the assumption that binding-induced change in hydrodynamic radius dominated the signal for CaM interactions. Preliminary calculations utilized the Protein Data Bank (RCSD/PDB) structural information to estimate the radius of gyration (R_{gyr}) and solvent accessible surface area (SASA) of the bound and unbound species (ΔR_{gyr} and ΔSASA). A simple multivariable linear equation was obtained that relates the interferometry signal in phase, to change in R_{gyr} and SASA for the CaM system ($\Delta BSI = 1.0 + 2.6\times10^{-4}\ \Delta SASA + 0.054\ \Delta R_{gyr}$). **Fig. A.5A** shows the correlation between the predicted and experimental values for free-solution interaction studies of CaM binding Ca^{2+}, Ca^{2+}-CaM – TFP, Ca^{2+}-CaM – calcineurin, Ca^{2+}-CaM – M13 peptide. The surprisingly good correlation ($R^2 = 0.88$) between the actual and predicted signal magnitude for these binding events encouraged us to further our investigation.

Next, we expanded our formalism and applied it to a training set of binding pairs. Our expression mirrors Beer's Law in its simplest form, which equates the absorbance of a species to the experimental parameters of the determination (path length and concentration) and the intrinsic property of the species (molar absorptivity). Here, we propose defining the response for free-solution sensing to be expressed as:

$$\rho = \chi\beta C \qquad \textbf{Eq. 1.2}$$

where: ρ is the FreeSRF measured in radians, χ is the Molar Refractometry in RIU/moles/L, β is the instrument response function in radians/RIU, and C is the concentration in moles/L. This simple equation demonstrates that the fringe shift (in radians) quantified by an interferometer when measuring a folding, binding, or hybridization event in free-solution (no labels) is directly proportional to: a) the magnitude of structural change (predominantly conformation and hydration) of the sample; b) the $d\theta/d\eta$ sensitivity of the interferometer (which incorporates the optical path length); and c) the concentration of the analyte. Below, we show that ρ is not a function of the RII or the relative mass of the interacting species and that it can be estimated for a binding pair with reasonable confidence.

Important caveats: Free-solution assays are predicated on the assumption that the solution is interrogated and not the surface (see below). The equation for FreeSRF states that the signal magnitude, ρ, is proportional to the number *and type* of transformations (See for example [57]),

not just the number of bonds formed or broken. Measurement of ρ is obtained as a change in RI reported by a fringe shift or estimated from χ, the species concentration and instrument performance. As such, the most significant contributors to error in ρ are instrument drift, run-to-run reproducibility, and the uncertainty in χ.

In defining χ as the molar refractometry, we recognize that the structural changes observed are a consequence of processes (folding, interactions, chemical reactions, biochemical transformations, etc.) that lead to changes in the analyte intrinsic properties, such as the dielectric constant, the molecular dipole moment, or other third order parameters. This premise is supported by evidence from complementary techniques including CD, ellipsometry (**Fig. A.4**), ITC, DLS [29] and NMR. Accuracy in χ is dominated by the quality of the initial training set data and the correctness of the structure prediction method and data derived from it. Several combined resources can provide quality structural data: the PDB; 2) PYMOL/MOLMOL (molecular analysis and display programs) and 3) M-FOLD for DHA/RNA structure prediction and 4) Chimera for structural analysis.

Note that β appears in the equation to account for path length variations, interferometer sensitivity (S/N) differences from device-to-device, lab-to-lab, or even operator-to-operator. Currently $d\theta/d\eta$ is expressed as milliradians/RIU, but other sensible units that accurately express the instrument figures of merit can be used for β. In consideration of β, is should be recognized that signal extraction from an interferometric fringe shift is enabled by proper optical alignment, as well as careful selection and handling of references and controls. As a cautionary note, it is our observation that BSI fringes do not exhibit uniform behavior with respect to free-solution sensitivity (Appendix A). What we have found is that optimized optical alignment for fringes 6-13 (counted from the centroid) yields a single spatial frequency when using fast Fourier Transform (FFT) [61] (**Fig. 1.1**) that has always reported the free-solution signal.

The magnitude of FreeSRF scales with concentration, therefore the addition of more protein always increases ρ, but it must be recognized that C is the *product* concentration, the quantity of the new shape or complex. So, circumstances can be imagined where increasing the amount of *receptor* doesn't produce a directly proportional change in ρ. For K_D determinations, this can be dealt with by avoiding a scenario where a high product concentration is reached in the assay. At this juncture for K_D determinations, we perform FreeSRF most often with target concentrations near the assumed affinity or at $K_D/10$. Additionally, we are mindful that error in C

impacts FreeSRF, contributing uncertainty to the training set employed to define χ and then used to predict ρ for a new system.

As with Beer's Law, which exhibits non-linearity for three major reasons [69], we do expect refined versions of our theory to take on higher order terms that could affect ρ similarly. While nonlinearities may be identified, our preliminary observations conform well to the simple expression proposed. We do acknowledge that our model can be improved and support that it will benefit from further investigation.

Testing the Validity of FreeSRF

As with other models [38, 70-73], it was necessary to use a learning set to establish the appropriate relationships and weighting parameters for FreeSRF. In our case, we determined χ from ρ_{exp} for a training set of well-characterized binding systems (**Table 1.1**). Multiple users performed the assays on several different interferometers (of similar configuration) to insure confidence in the result and minimize operator or device biases.

For each of the training systems the reference-corrected phase shift (ρ_{exp} in milliradians) was experimentally quantified at known concentrations of ligand. These values were used to determine the FreeSRF values for the experimental conditions: $\rho_{expBmax}$, β_{exp}, and C_{Bmax}, which in turn facilitates the calculation of values for χ_{exp} for the training set at the final concentration of *product*:

$$\frac{\rho_{expBmax}}{\beta * C_{B_{max}}} = \chi_{exp} \qquad \textbf{Eq. 1.3}$$

Running a dη/dC calibration experiment allows β to be determined in radians/RIU for the specific *instrument* used in the binding assay. This experiment consists of measuring the phase shift as a function of glycerol concentration in mM (or another suitable analyte). From this linear relationship, we obtain the slope, expressed in radians/mM. For example, the response of BSI_4 (instrument #4 of 9) for a glycerol calibration curve was found to be 0.011 radians/mM, a typical value for our chip-based device. Then we express β in RIU per mM glycerol using a conversion factor from the CRC for dη/dC; in the case of glycerol this parameter is 1.04863×10^{-5} RIU/mM [74]. Thus, for BSI_4:

$$\beta = \frac{0.015\ \frac{\text{radians}}{\text{mM}}}{1.04863\times10^{-5}\ \frac{\text{RIU}}{\text{mM}}} = 1442.308\ \frac{\text{radians}}{\text{RIU}} \qquad \textbf{Eq. 1.4}$$

To obtain the desired values for χ_{Bmax} we must know the concentration of the *product*, [Complex], detected upon physical transformation. Several approaches can be used to find this value. Here we used an equilibrium solver written in Excel to determine the [Complex] at each concentration of ligand. The solver uses the mass balance equation, the receptor concentration, ligand concentration, and K_D to calculate product concentration (**Appendix A**). Then the maximal concentration of product is determined by plotting the product versus ligand concentrations and fitting the curve using a single-site binding isotherm. B_{max} is equal to the maximal concentration of product that is formed under the experimental conditions with high accuracy and has less bias than results produced at lower concentrations with a reduced S/N. To check the validity of using B_{max} for the [Complex] and our solver, we used the quadratic equation to solve the equilibrium mass balance equation for the concentration of the complex at each point on the saturation isotherm produced from the end-point binding assay. Results shown in **Table A.2** illustrate that using the solver for B_{max} produces comparable values to the more computationally intensive approach based on the quadratic expression.

With ρ_{exp}/C_{Bmax} and β in hand, we have the experimentally determined value χ_{exp} for each of the training set species and can turn to the task of determining χ. From our experience with CaM and observations by others (see above), the hypothesis that the free-solution signal has its origin in the physical transformations upon binding or folding emerges. Therefore χ should be principally proportional to reaction/binding-induced conformation and hydration changes. Thus, allowing us to propose the expression for χ to be:

$$\chi_{model} = A(\Delta SASA) + B(ave SASA) + C(\Delta R_{Gyr}) + D(ave R_{Gyr}) + E \qquad \textbf{Eq. 1.5}$$

where ΔSASA is the difference in solvent addressable surface area for bound complex and the unbound species in $Å^2$, the *ave*SASA is the sum of SASA values divided by the number of values (PDB structures), ΔR_{Gyr} is difference for the radius of gyration for the unbound species and that of the complex (bound species) in Å, *ave*R_{Gyr} is sum of radius of gyration values divided by the number of values (PDB structures), and A, B, C, D, and E are fitting coefficients. The inclusion of the average quantities for Rgyr and SASA was motivated by a report by Marsh and Tiechmann [38] where they demonstrate that that the absolute SASA value of a protein taken from a complex is an indicator for the amount of conformational change expected upon binding and is thus

expected to affect X_{model}. The absolute Rgyr value is required to normalize the effects of the absolute SASA value with protein size as described by Marsh in equation 2 [38].

It is noteworthy that the quality and accuracy of the data-base structures used to determine the hydrodynamic properties directly impacts our predicted outcome. Here we used the RSCB/PDB (**Table A.3**) to calculate of R_{gyr} and SASA with methods described below. In some cases, the PDB files were only available for corresponding ligand/receptor pairs in varying multiples of subunits (for example, unbound calmodulin was found as a monomer, but calmodulin bound to calcineurin was found as a homodimer). In cases where appropriate, these multimers were split into monomers using Chimera [75].

Numerous approaches exist to quantify R_{gyr} [76-78]. Here we employed a Chimera script obtained from (http://plato.cgl.ucsf.edu/trac/chimera/wiki/Scripts), enabling the calculation of R_{gyr} using the expression:

$$R_{gyr} = \sqrt{\frac{\sum_{k=1}^{N} m_k (r_k - r_{mean})^2}{\sum_{k}^{N} m_k}} \qquad \textbf{Eq. 1.6}$$

where *r* is the position and *m* is the mass of each atom in the molecule. Hydrogens were removed for this calculation for consistency across species, because the Chimera program automatically adds these when displaying a new PDB file. Non-interacting species, such as ions, solvents and accessory ligands were also removed prior to determining the R_{gyr}. The results for these calculations are compiled in **Table A.4**. The values obtained from Chimera correlated well with a self-written MATLAB© script using the same coordinates obtained from the PDB files.

Chimera was also used to aid in calculation of the SASA values. As recommended, solvent excluded molecular surfaces were created with the help of the MSMS package: http://mgltools.scripps.edu/packages/MSMS/. Typically, the SASA of only the main protein chain is used, with the surface area obtained using the "Surface" command in the MSMS program, which uses four different algorithms to determine surface area. Non-protein molecules were discarded (including solvents, ions, and ligand) prior to calculations, except when the ligand was also a protein undergoing its own 'significant' structural change. To calculate the solvent accessible surface area of the molecule, a "probe" (sphere of radius 1.4 Å) is "rolled" across the surface of the molecule. To begin, the first atom is selected, and the probe is placed at a distance of the radius of the atom, and then moved around the atom in the tangential direction until the probe comes into contact with the nearest neighbor atom. Then, the probe is moved along a path of equal radial

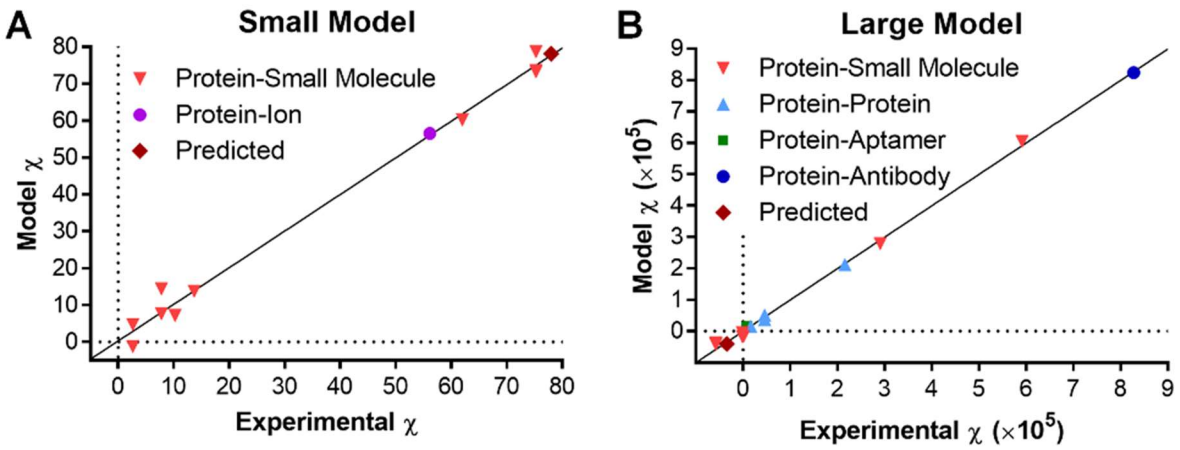

Fig. 1.3 Plots showing correlation of χ_{exp} and χ_{model} when the learning sets are split into small (**A**) and large (**B**) χ values.

distance between the two atoms until it encounters a third atom. This process is repeated to find the junctions between all atoms and their neighbors until the probe has been moved across the entire structure and the whole surface of the structure has been constructed. **Table A.4** presents the values for SASA for each of the learning set structures.

We now have ΔR_{gyr}, ΔSASA and their average values (from PDB structure) allowing us to determine the theoretical value for χ_{model} for each interaction. Using the experimentally determined value for χ_{exp}, obtained from $\rho_{exp}/C\beta$ and theoretical χ values for our entire training set, we determined the coefficients A, B, C, D, and E for Eq 5 (**Table A.5**) by performing a linear regression in MATLAB©. Using a wide range of χ values this simple model produced a "good" fit with a high correlation coefficient (**Fig. A.5B**), but with a modest Spearman correlation coefficient of ρ_s=0.853 (a nonparametric measure of statistical dependence between variables that indicates the relationship is not random and that the correlation between the variables can be described using a monotonic function). Yet, a relatively large residual error (20,249) (**Table A.5**) and percent difference between χ_{exp} and χ_{model} enhances the possibility of poor prediction accuracy, particularly for systems with a relatively small FreeSRF (ρ).

A better fit was found by separating the binding systems into two sets, 'large' and 'small' responders, based on the size of FreeSRF (ρ_{exp}). Since the interferometer reports the magnitude of structural changes (not the binding species MW), some proteins will populate both sets upon interaction with different ligands. For example, CaM can be found in both training sets. Using

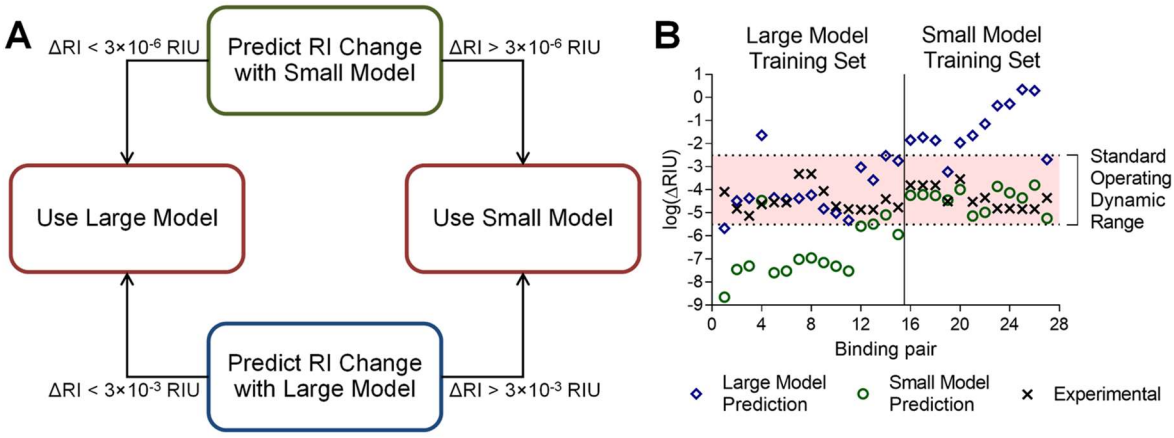

Fig. 1.4 A) Flow diagram for predicting the suitable model (small or large) for a binding pair. **B**) Results for predicting the model for the entire learning set.

the *signal-size* segregation approach produces the plots shown in **Fig. 1.3**. These plots clearly illustrate that the relation between the χ_{exp} versus χ_{model} predicted *a priori* produces two excellent results, with linear correlation coefficients of $R^2 = 0.991$ and 0.998 and p values of 2.76×10^{-6} and 3.13×10^{-12} for the small and large FreeSRF models, respectively. Further evaluation of the relationship yields Spearman Rank correlation coefficients of $\rho_s = 0.936$ and 0.979, respectively (**Table A.5**). It is important to note that our results don't necessarily split into *two best fit* models and we acknowledge that there are likely some scaling factors we haven't identified which could impact the quality of the fit. The model can really be split in any number of ways (2 subsets or 3, 4, 5 subsets) and provide similar results, yet a division into just large and small sets results in a relatively simple and easy-to-use model that produces a reasonably high-quality result. It is also possible that as the training set expands a group of intermediate species will emerge. To the best of knowledge, there's not really a way to ascribe a physical property to E, which is the *error term*, *disturbance term*, or *noise*. This variable captures all other factors which influence the dependent variable $\boldsymbol{y}_i$ other than the regressors $\boldsymbol{x}_i$ and is dissimilar for the large/small sets because of the significant difference in error between the two models.

It is noteworthy that the training set used has a significant level of diversity, including ion-protein, protein-protein, small molecule-protein, protein-aptamer, membrane protein targets analyzed as cell-derived vesicles, an antibody-antigen pair, and unaltered human erythrocytes [22]. Further, the highly correlated results were obtained over a period spanning more than three years,

Table 1.1 comparing χ_{model} to χ_{exp}

Large Model					Small Model				
Receptor	**Ligand**	**Experimental Chi (RIU/M)**	**Model Chi (RIU/M)**	**Percent Error**	**Receptor**	**Ligand**	**Experimental Chi (RIU/M)**	**Model Chi (RIU/M)**	**Percent Error**
IL-2 Antibody	Interleukin-2	827964	823965	0.5%	Calmodulin	TFP	75.2	73.6	2.2%
β2AR	Alprenolol	591423	604924	2.3%	Calmodulin	TFP	75.2	78.7	4.6%
β2AR	Isoproterenol	290953	278649	4.2%	Calmodulin	TFP	75.2	73.2	2.7%
Basigin	Rh5	215777	212174	1.7%	Carbonic Anhydrase II	Sulpiride	62.0	60.2	2.9%
Carbonic Anhydrase II	Acetazolamide	-57291	-42419	26.0%	Calmodulin	Calmodulin-Ca^{2+}	56.1	56.5	0.6%
Carbonic Anhydrase II	Acetazolamide	-57291	-37288	34.9%	HIV PR	Pepstatin 1F1N	13.7	13.7	0.5%
Calmodulin	Calcineurin	46087	37389	18.9%	HIV PR	Pepstatin 1F1	10.2	7.2	29.9%
Calmodulin	Calcineurin	46087	51594	11.9%	Con A	Mannose	7.8	14.4	85.4%
Calmodulin	M13	16458	15393	6.5%	Con A	Mannose	7.8	7.7	1.2%
Thrombin	Bock	9409	16261	72.8%	Con A	Glucose	2.6	-1.3	149.2%
Thrombin	Tasset	7109	12462	75.3%	Con A	Glucose	2.6	4.6	78.1%
Carbonic Anhydrase II	Benzene Sulfonamide	-1379	-16771	1116.4%	Recoverin	Ca^{2+}	78.0	78.1	0.1%
Carbonic Anhydrase II	Benzene Sulfonamide	-1379	-4607	234.2%					
Carbonic Anhydrase II	Sulfanilamide	782	-17018	2276.2%					
Carbonic Anhydrase II	Dansylamide	-34377	-40557	18.0%					

by numerous BSI operators and on six different BSI instruments. Overall, the model provides values for the Molar Refractometry, χ, which correlate well with those derived from the binding experiment (**Table 1.1**), suggesting it can be used to estimate the FreeSRF for systems where binding-induced conformation and hydration changes can be obtained with reasonable accuracy.

Predicting/Estimating FreeSRF

There are two levels of prediction applicable to FreeSRF: one is to determine whether the small or large model should be used, and the other is to estimate the free-solution signal for a molecular interaction not currently part of the training set. **Fig. 1.4A** illustrates the work flow used to estimate the applicability of using the small vs. large model. First, the structural information (PDB) and the large and small model-fitting parameters (A, B, C, D, and E) are used to calculate χ_{model}. Then, since most assays are run under these conditions, we estimate the final complex concentration by setting it equal to $K_D/10$ (**Table S1**). Upon performing these two calculations and using the FreeSFR relationship, either a non-sense or sensible answer for the predicted change

in ΔRI (e.g. detectable or not by BSI) emerges. Following the flow chart in **Fig.1.4A** and using a conservative estimate for the operating range for the interferometer (ca. ΔRI 3×10^{-3} to 3×10^{-6}) allows successful ranking of the binding pair with respect to large or small model. **Fig. 1.4B** illustrates that in most cases (23 of 27) or 85% of the time the prediction properly classifies the binding pair. An additional calculation (**Appendix A**) using the instrument response function β enables the determination of the actual ΔRI produced for a binding pair (**Table A.1**). Two important observations can be gleaned from this table. The first is that the experimentally measured value ρ correlates well with the predicted signal. Second, the table and **Fig. A.2 – A.3** illustrates that the magnitude of ΔRI for a binding event is relatively large.

Armed with the small vs. large selection method, we tested the capability of the model to estimate the free-solution signal for two molecular interaction pairs not used in the training set. These are Ca^{2+} – recoverin protein-ion interaction and the dansylamide – carbonic anhydrase (CAII) enzyme-inhibitor system. Using the PDB and **Eq 1.5** we first calculated χ_{model} for each of the two test systems. Based on ΔSASA, *ave*SASA, ΔR_{gyr}, *ave*R_{gyr}, we obtain χ_{model} of 78.1 RIU/M and -40,557 RIU/M for Ca^{2+} – recoverin and dansylamide – CAII respectively (**Table 1.1**).

To estimate FreeSRF (ρ_{pred}) we combine χ_{model} with β for the instrument to be employed and the values of *C* determined from the K_D using our solver and the concentrations to be used to generate a binding isotherm. We commonly use a receptor concentration of ~K_D/10 and a ligand concentration of 4-10-fold larger than K_D to reach saturation (B_{max}). For example, for Ca^{2+} – recoverin, use of the mass balance equation, a receptor concentration of 5.40×10^{-7} M, and a K_D = 0.27×10^{-6} M [79], allows the BSI equilibrium concentrations can be predicted (**Table A.2**). Substitution into the FreeSRF relationship, $\rho_{pred} = \chi_{model}\beta_{exp}C$, yields Eq 10:

$$\rho_c = 78.1 \frac{\text{RIU}}{\text{mM}} \times 1055663 \frac{\text{milliradians}}{\text{RIU}} \times C \text{ (M)} \qquad \text{Eq. 1.7}$$

which allows the ρ_c at each ligand concentration to be calculated. Plotting $\rho_{c\text{-model}}$ versus the ligand concentration gives the predicted free-solution binding assay (green curve **Fig. 1.5A**). The same procedure was performed for the dansylamide – CAII binding pair, producing values for *C* and the modeled FreeSRF ($\rho_{c\text{-model}}$) (**Table A.2**). Plotting these results gives the green binding curve displayed in **Fig. 1.5B**.

Independent of our prediction, we performed free-solution measurements with BSI to determine the K_D for both the recoverin and CAII systems. The saturation isotherm binding curves

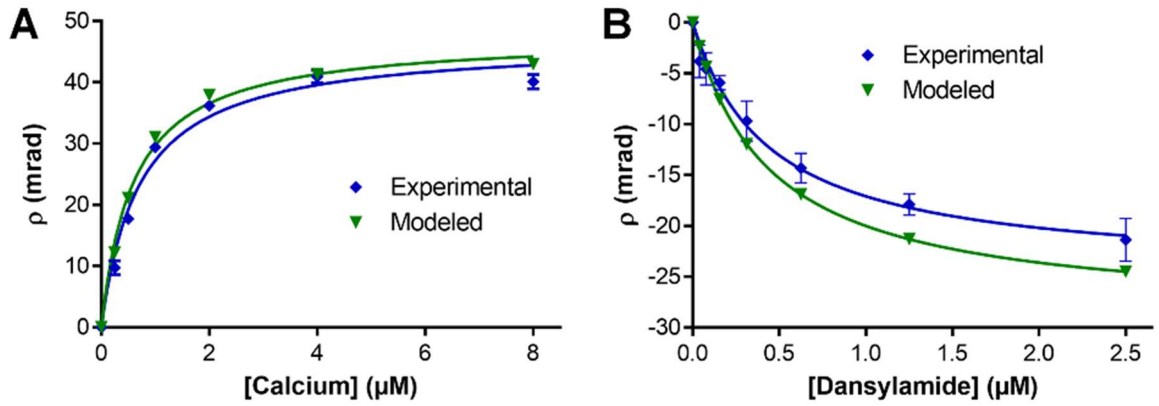

Fig. 1.5 Experimental (blue) and modeled (green) FreeSRF binding curves for A) Recoverin - Ca2+ and B) Carbonic Anhydrase II - Dansylamide.

for these experiments are presented as blue lines in **Fig. 1.5**. To further illustrate the correlation between measured and estimated FreeSRF, we plotted the χ_{exp} values on **Fig. 1.3** showing where they lie on the training-set line. The percent difference from χ_{model} was 0.13% for Ca^{2+}-Recoverin and 18.0% for dansylamide-CAII.

Overall there is a very good correlation between the empirical and theoretical results. The relative difference between the ρ_{exp} and ρ_{model} was found to be less than ~29%, except for one value for one dansylamide – CAII concentration reaching 37.8% (**Table A.2**). It is not surprising that the largest difference in ρ values occurs at the lowest concentrations on the binding curve, a region of lowest instrumental S/N, which typically reports the smallest phase change. As expected for the cluster of systems that have relatively small experimental FreeSRF signals (**Fig. 1.3**) and a larger difference in χ_{model}, will lead to a comparable error in the prediction. Yet, the ability to confidently estimate the signal for a binding event within a factor of 2, given only a K_D value and the structure, should enable rapid assay optimization, advancing the study of intermolecular interactions.

Also of note, our model accurately predicted a negative FreeSRF (ρ) value (relative to glycerol) for the CAII – system, which was subsequently reported in the binding curve by the interferometer. This phenomenon, having been ascribed to a reduction in hydrodynamic diameter, was also observed by SPR for numerous binding systems. Directionality of the signal is a poorly studied parameter at this stage for free-solution measurements, requiring considerably more

investigation to provide meaningful mechanistic insights. It is under intense investigation and does appear to inform about the binding mechanism as suggested by others [28, 43].

Even though the molecular shape and hydration changes predict the free-solution signal, it may be necessary to use additional parameters to more accurately describe the molecular dipole, dielectric constant or electronic structure. For example, systems that undergo oxidation/reduction may produce an electronic structure redistribution that would require use of a third-order term in the equation for χ. We opted for a linear model for simplicity and because it produces an excellent correlation. Yet, we do recognize that the dependence of RI from changes in structural and dynamical parameters could be more complex than the linear model we fit to, in part because the fitting was done with a somewhat limited number of experimental data points. Interestingly, Marsh et al [38] make a compelling argument that the absolute value of SASA correlates with the amplitude of conformational change, so ascribing the dependence of RI changes upon binding to alterations in SASA and Rgyr is quite reasonable. We acknowledge that with additional experimental data and a better understanding of the physical basis of these transformations, a more complex model could emerge that more accurately predicts changes in RI. Going forward we will be continually evaluating and adding systems to expand our training set, which should improve model performance. To enable broader use by the community we will be establishing a website to make our model available and for other investigators to contribute to the learning set.

The presentation of these results provides adequate evidence to address a recent assertion made by Soren, et.al. [65] that; "so far no explicit explanation into how binding could physically generate a BSI signal has been provided."

Experimental Parameters for Effective Free-Solution Measurements

Free-solution investigations are comparative analyses and it is only under the proper conditions that these *relative* RI signals become quantifiable. Therefore, we clearly define in **Appendix A** the experimental conditions needed to insure others can successfully perform free-solution assays.

Chapter 1 Conclusion

We have presented a hypothesis: "the signal origin for label-free, *free-solution* studies can be principally ascribed to alterations in structure upon reaction, interaction, or folding. These changes in conformation and hydration produce a quantifiable RI signal." Numerous examples

from the SPR literature describe unanticipated RI signals that could only be attributed to binding-induced changes of this type, findings that further support our supposition. An expression for the free-solution response function (FreeSRF) is proposed, $\rho = \chi\beta C$, which relates structural changes (χ) to the fringe shift ρ. A training set of a diverse set of binding systems was tested on multiple instruments over a several year period and used to derive the coefficients for χ derived from a linear relationship between the experimental and predicted value for FreeSRF (ρ). Using this relationship, we were able to predict, *a priori*, with reasonable accuracy the FreeSRF for two binding systems. To enable others to employ this approach and further refine the model, we have described in full detail the conditions and methodologies needed to perform free-solution assays. Using a carefully designed sample-reference assay that constrains background $d\eta/dC$ changes and working within the S/N of our interferometer, it is possible to study processes in the absence of a mass change as in protein folding or molecular interactions when the two interacting species are at undetectable starting concentrations.

Based on the strong correlation between FreeSRF and the structural changes detected by the system, our model and BSI enable the use ρ_{exp} to determine or predict χ. This capability could provide insights into mechanism of action, allow expedited medicinal chemistry activities, and potentially predict the impact on structure and/or affinity with environment. Additionally, quantitative free-solution assays can be rapidly optimized using our FreeSRF model.

While an excellent correlation between our theory and experiment has been obtained, we acknowledge more refinement of the model could be advantageous. As with Beer's Law, higher order terms may be required for some processes (particularly for electronic redistribution) to fully describe a label-free, free-solution experiment.

We predict that the availability of a user-friendly interferometric instrument could usher in a new era for label-free, free-solution chemical, biochemical and medical analyses.

References

2. Betzig, E.; Chichester, R. J., Single Molecules Observed by near-Field Scanning Optical Microscopy. *Science* **1993,** *262* (5138), 1422-1425.
3. Levene, M. J.; Korlach, J.; Turner, S. W.; Foquet, M.; Craighead, H. G., et al., Zero-mode waveguides for single-molecule analysis at high concentrations. *Science* **2003,** *299* (5607), 682-686.
4. Unsung Heroes. *Science* **2001,** *291* (5507), 1207.
5. Hell, S. W.; Wichmann, J., Breaking the Diffraction Resolution Limit by Stimulated-Emission - Stimulated-Emission-Depletion Fluorescence Microscopy. *Opt Lett* **1994,** *19* (11), 780-782.
6. Liedberg, B.; Nylander, C.; Lundstrom, I., Biosensing with Surface-Plasmon Resonance - How It All Started. *Biosens Bioelectron* **1995,** *10* (8), R1-R9.
7. Yu, Y.; Ramachandran, P. V.; Wang, M. C., Shedding new light on lipid functions with CARS and SRS microscopy. *Bba-Mol Cell Biol L* **2014,** *1841* (8), 1120-1129.
8. Moreira, B. G.; You, Y.; Behlke, M. A.; Owczarzy, R., Effects of fluorescent dyes, quenchers, and dangling ends on DNA duplex stability. *Biochem Bioph Res Co* **2005,** *327* (2), 473-484.
9. Olmsted, I. R.; Kussrow, A.; Bornhop, D. J., Comparison of Free-Solution and Surface-Immobilized Molecular Interactions Using a Single Platform. *Anal Chem* **2012,** *84* (24), 10817-10822.
10. Bornhop, D. J.; Latham, J. C.; Kussrow, A.; Markov, D. A.; Jones, R. D., et al., Free-solution, label-free molecular interactions studied by back-scattering interferometry. *Science* **2007,** *317* (5845), 1732-1736.
11. Cubrilovic, D.; Biela, A.; Sielaff, F.; Steinmetzer, T.; Klebe, G., et al., Quantifying Protein-Ligand Binding Constants Using Electrospray Ionization Mass Spectrometry: A Systematic Binding Affinity Study of a Series of Hydrophobically Modified Trypsin Inhibitors. *J Am Soc Mass Spectr* **2014,** *23* (10), 1768-1777.
12. Kaltashov, I. A.; Bobst, C. E.; Abzalimov, R. R.; Wang, G. B.; Baykal, B., et al., Advances and challenges in analytical characterization of biotechnology products: Mass spectrometry-based approaches to study properties and behavior of protein therapeutics. *Biotechnol Adv* **2012,** *30* (1), 210-222.
13. Hu, H. T.; Sheehan, J. H.; Chazin, W. J., The mode of action of centrin - Binding of Ca2+ and a peptide fragment of Kar1p to the C-terminal domain. *J Biol Chem* **2004,** *279* (49), 50895-50903.
14. Tzeng, S. R.; Kalodimos, C. G., Protein dynamics and allostery: an NMR view. *Curr Opin Struc Biol* **2011,** *21* (1), 62-67.
15. Ababou, A.; Ladbury, J. E., Survey of the year 2005: literature on applications of isothermal titration calorimetry. *Journal of Molecular Recognition* **2007,** *20* (1), 4-14.
16. Liang, Y., Applications of isothermal titration calorimetry in protein folding and molecular recognition. *J Iran Chem Soc* **2006,** *3* (3), 209-219.
17. Wienken, C. J.; Baaske, P.; Rothbauer, U.; Braun, D.; Duhr, S., Protein-binding assays in biological liquids using microscale thermophoresis. *Nat Commun* **2010,** *1*.
18. Zhang, W.; Duhr, S.; Baaske, P.; Laue, E., Microscale thermophoresis for the assessment of nuclear protein-binding affinities. *Methods Mol Biol* **2014,** *1094*, 269-276.
19. Baksh, M. M.; Kussrow, A. K.; Mileni, M.; Finn, M. G.; Bornhop, D. J., Label-free quantification of membrane-ligand interactions using backscattering interferometry. *Nat Biotechnol* **2011,** *29* (4), 357-360.

20. Kussrow, A.; Enders, C. S.; Bornhop, D. J., Interferometric Methods for Label-Free Molecular Interaction Studies. *Anal Chem* **2012,** *84* (2), 779-792.
21. Olmsted, I. R.; Hassanein, M.; Kussrow, A.; Hoeksema, M.; Li, M., et al., Toward Rapid, High-Sensitivity, Volume-Constrained Biomarker Quantification and Validation using Backscattering Interferometry. *Anal Chem* **2014,** *86* (15), 7566-7574.
22. Saetear, P.; Perrin, A. J.; Bartholdson, S. J.; Wanaguru, M.; Kussrow, A., et al., Quantification of Plasmodium-host protein interactions on intact, unmodified erythrocytes by back-scattering interferometry. *Malaria J* **2015,** *14*.
23. Wang, Z. L.; Swinney, K.; Bornhop, D. J., Attomole sensitivity for unlabeled proteins and polypeptides with on-chip capillary electrophoresis and universal detection by interferometric backscatter. *Electrophoresis* **2003,** *24* (5), 865-873.
24. Pesciotta, E. N.; Bornhop, D. J.; Flowers, R. A., Backscattering Interferometry: An Alternative Approach for the Study of Hydrogen Bonding Interactions in Organic Solvents. *Org Lett* **2011,** *13* (10), 2654-2657.
25. Houlne, M. P.; Hubbard, D. S.; Makhatadze, G. I.; Bornhop, D. J., Refractive Index-Based Calorimetric Studies of RNase T1 Unfolding in Small Volumes using Interferometric Backscatter. *Proceedings of the Society of Photo-Optical Instrumentation Engineers* **1996,** *2982*, 159-167.
26. Sota, H.; Hasegawa, Y.; Iwakura, M., Detection of conformational changes in an immobilized protein using surface plasmon resonance. *Analytical chemistry* **1998,** *70* (10), 2019-2024.
27. Craus, C.; Willand, N.; Villemagne, B.; Flipo, M.; Willery, E., et al., Unconventional surface plasmon resonance signals reveal quantitative inhibition of transcriptional repressor EthR by synthetic ligands. *Analytical biochemistry* **2014,** *452*, 54-66.
28. Gestwicki, J. E.; Hsieh, H. V.; Pitner, J. B., Using receptor conformational change to detect low molecular weight analytes by surface plasmon resonance. *Analytical chemistry* **2001,** *73* (23), 5732-5737.
29. Sulmann, S.; Dell'Orco, D.; Marino, V.; Behnen, P.; Koch, K. W., Conformational Changes in Calcium-Sensor Proteins under Molecular Crowding Conditions. *Chem-Eur J* **2014,** *20* (22), 6756-6762.
30. Daniels, P. B.; Deacon, J. K.; Eddowes, M. J.; Pedley, D. G., Surface-Plasmon Resonance Applied to Immunosensing. *Sensor Actuator* **1988,** *15* (1), 11-18.
31. Jung, L. S.; Campbell, C. T.; Chinowsky, T. M.; Mar, M. N.; Yee, S. S., Quantitative Interpretation of the Response of Surface Plasmon Resonance Sensors to Adsorbed Films. *Langmuir* **1998,** *14* (19), 5636-5648.
32. Sjolander, S.; Urbaniczky, C., Integrated Fluid Handling-System for Biomolecular Interaction Analysis. *Anal Chem* **1991,** *63* (20), 2338-2345.
33. Stenberg, E.; Persson, B.; Roos, H.; Urbaniczky, C., Quantitative-Determination of Surface Concentration of Protein with Surface-Plasmon Resonance Using Radiolabeled Proteins. *J Colloid Interf Sci* **1991,** *143* (2), 513-526.
34. Matthews, B. W., In *The Proteins III*, Academic Press: New York, 1977; pp 403-590.
35. Zhao, H.; Brown, P. H.; Schuck, P., On the Distribution of Protein Refractive Index Increments. *Biophys J* **2011,** *100* (9), 2309-2317.
36. Golander, C. G.; Kiss, E., Protein Adsorption on Functionalized and Esca-Characterized Polymer-Films Studied by Ellipsometry. *J Colloid Interf Sci* **1988,** *121* (1), 240-253.

37. Haussling, L.; Ringsdorf, H.; Schmitt, F. J.; Knoll, W., Biotin-Functionalized Self-Assembled Monolayers on Gold - Surface-Plasmon Optical Studies of Specific Recognition Reactions. *Langmuir* **1991,** *7* (9), 1837-1840.
38. Marsh, J. A.; Teichmann, S. A., Relative Solvent Accessible Surface Area Predicts Protein Conformational Changes upon Binding. *Structure* **2011,** *19* (6), 859-867.
39. Davis, T. M.; Wilson, W. D., Determination of the refractive index increments of small molecules for correction of surface plasmon resonance data. *Anal Biochem* **2000,** *284* (2), 348-353.
40. Tumolo, T.; Angnes, L.; Baptista, M. S., Determination of the refractive index increment (dn/dc) of molecule and macromolecule solutions by surface plasmon resonance. *Anal Biochem* **2004,** *333* (2), 273-279.
41. Boussaad, S.; Pean, J.; Tao, N. J., High-resolution multiwavelength surface plasmon resonance spectroscopy for probing conformational and electronic changes in redox proteins. *Anal Chem* **2000,** *72* (1), 222-226.
42. Salamon, Z.; Cowell, S.; Varga, E.; Yamamura, H. I.; Hruby, V. J., et al., Plasmon resonance studies of agonist/antagonist binding to the human delta-opioid receptor: New structural insights into receptor-ligand interactions. *Biophys J* **2000,** *79* (5), 2463-2474.
43. Hsieh, H. V.; Pitner, J. B.; Gestwicki, J. E. Detection of ligands by refractive surface methods. US 6,576,430 B1, June 10th, 2003.
44. Frostell-Karlsson, A.; Remaeus, A.; Roos, H.; Andersson, K.; Borg, P., et al., Biosensor analysis of the interaction between immobilized human serum albumin and drug compounds for prediction of human serum albumin binding levels. *J Med Chem* **2000,** *43* (10), 1986-1992.
45. Karlsson, R., Real-Time Competitive Kinetic-Analysis of Interactions between Low-Molecular-Weight Ligands in Solution and Surface-Immobilized Receptors. *Anal Biochem* **1994,** *221* (1), 142-151.
46. Karlsson, R.; Kullman-Magnusson, M.; Hamalainen, M. D.; Remaeus, A.; Andersson, K., et al., Biosensor analysis of drug-target interactions: Direct and competitive binding assays for investigation of interactions between thrombin and thrombin inhibitors. *Anal Biochem* **2000,** *278* (1), 1-13.
47. Metzger, J.; von Landenberg, P.; Kehrel, M.; Buhl, A.; Lackner, K. J., et al., Biosensor analysis of beta 2-glycoprotein I-reactive autoantibodies: Evidence for isotype-specific binding and differentiation of pathogenic from infection-induced antibodies. *Clin Chem* **2007,** *53* (6), 1137-1143.
48. Rich, R. L.; Myszka, D. G., Survey of the 2001 commercial optical biosensor literature. *Journal of Molecular Recognition* **2002,** *15* (6), 352-376.
49. Chen, H. J.; Kou, X. S.; Yang, Z.; Ni, W. H.; Wang, J. F., Shape- and size-dependent refractive index sensitivity of gold nanoparticles. *Langmuir* **2008,** *24* (10), 5233-5237.
50. Luan, Q. F.; Xue, Y.; Yao, X.; Lu, W., Hairpin DNA probe based surface plasmon resonance biosensor used for the activity assay of E. coli DNA ligase. *Analyst* **2010,** *135* (2), 414-418.
51. Christopeit, T.; Gossas, T.; Danielson, U. H., Characterization of Ca2+ and phosphocholine interactions with C-reactive protein using a surface plasmon resonance biosensor. *Anal Biochem* **2009,** *391* (1), 39-44.
52. Dell'Orco, D.; Muller, M.; Koch, K. W., Quantitative detection of conformational transitions in a calcium sensor protein by surface plasmon resonance. *Chem Commun* **2010,** *46* (39), 7316-7318.

53. Luka, Z.; Moss, F.; Loukachevitch, L. V.; Bornhop, D. J.; Wagner, C., Histone Demethylase LSD1 Is a Folate-Binding Protein. *Biochemistry-Us* **2011,** *50* (21), 4750-4756.
54. Hruby, V. J.; Tollin, G., Plasmon-waveguide resonance (PWR) spectroscopy for directly viewing rates of GPCR/G-protein interactions and quantifying affinities. *Current Opinions in Pharmacology* **2007,** *7*, 507-514.
55. Swann, M. J.; Peel, L. L.; Carrington, S.; Freeman, N. J., Dual-polarization interferometry: an analytical technique to measure changes in protein structure in real time, to determine the stoichiometry of binding events, and to differentiate between specific and nonspecific interactions. *Anal Biochem* **2004,** *329* (2), 190-198.
56. Cross, G. H.; Reeves, A. A.; Brand, S.; Popplewell, J. F.; Peel, L. L., et al., A new quantitative optical biosensor for protein characterisation. *Biosens Bioelectron* **2003,** *19* (4), 383-390.
57. Adams, N. M.; Olmsted, I. R.; Haselton, F. R.; Bornhop, D. J.; Wright, D. W., The effect of hybridization-induced secondary structure alterations on RNA detection using backscattering interferometry. *Nucleic Acids Res* **2013,** *41* (9), e103.
58. Ivanov, V. I.; Minchenk.Le; Minyat, E. E.; Frankkam.Md; Schyolki.Ak, Bbar to Abar Transition of DNA in Solution. *J Mol Biol* **1974,** *87* (4), 817-833.
59. Kypr, J.; Kejnovska, I.; Renciuk, D.; Vorlickova, M., Circular dichroism and conformational polymorphism of DNA. *Nucleic Acids Res* **2009,** *37* (6), 1713-1725.
60. Pesciotta, E. N.; Bornhop, D. J.; Flowers, R. A., Back-Scattering Interferometry: A Versatile Platform for the Study of Free-Solution versus Surface-Immobilized Hybridization. *Chemistry-an Asian Journal* **2011,** *6* (1), 70-73.
61. Markov, D.; Begari, D.; Bornhop, D. J., Breaking the 10(-7) barrier for RI measurements in nanoliter volumes. *Anal Chem* **2002,** *74* (20), 5438-5441.
62. Wang, Z. L.; Bornhop, D. J., Dual-capillary backscatter interferometry for high-sensitivity nanoliter-volume refractive index detection with density gradient compensation. *Analytical chemistry* **2005,** *77* (24), 7872-7877.
63. Swinney, K.; Markov, D.; Bornhop, D. J., Chip-scale universal detection based on backscatter interferometry. *Analytical chemistry* **2000,** *72* (13), 2690-2695.
64. Swinney, K.; Markov, D.; Bornhop, D. J., Ultrasmall volume refractive index detection using microinterferometry. *Rev Sci Instrum* **2000,** *71* (7), 2684-2692.
65. Jepsen, S. T.; Jorgensen, T. M.; Zong, W.; Trydal, T.; Kristensen, S. R., et al., Evaluation of back scatter interferometry, a method for detecting protein binding in solution. *The Analyst* **2015,** *140* (3), 895-901.
66. Project, E.; Friedman, R.; Nachliel, E.; Gutman, M., A molecular dynamics study of the effect of Ca2+ removal on calmodulin structure. *Biophys J* **2006,** *90* (11), 3842-3850.
67. Torok, K., Calmodulin conformational changes in the activation of protein kinases. *Biochem Soc T* **2002,** *30*, 55-61.
68. Vandonselaar, M.; Hickie, R. A.; Quail, J. W.; Delbaere, L. T., Trifluoperazine-induced conformational change in Ca(2+)-calmodulin. *Nat Struct Biol* **1994,** *1* (11), 795-801.
69. Skoog, D. A.; West, D. M.; Holler, F. J.; Crouch, S. R., *Fundamentals of Analytical Chemistry*. 9th ed.; Brooks/Cole: Belmont, CA, 2014.
70. Dickinson, T. A.; White, J.; Kauer, J. S.; Walt, D. R., A chemical-detecting system based on a cross-reactive optical sensor array. *Nature* **1996,** *382* (6593), 697-700.
71. Gharagheizi, F.; Ilani-Kashkouli, P.; Kamari, A.; Mohammadi, A. H.; Ramjugernath, D., Group Contribution Model for the Prediction of Refractive Indices of Organic Compounds. *J Chem Eng Data* **2014,** *59* (6), 1930-1943.

72. Katritzky, A. R.; Sild, S.; Karelson, M., Correlation and prediction of the refractive indices of polymers by QSPR. *J Chem Inf Comp Sci* **1998,** *38* (6), 1171-1176.
73. Koradi, R.; Billeter, M.; Wuthrich, K., MOLMOL: A program for display and analysis of macromolecular structures. *J Mol Graphics* **1996,** *14* (1), 51-55.
74. *CRC Handbook of Chemistry and Physics*. 77th ed.; Chemical Rubber Publishing Company: Boca Raton, 1996-1997.
75. Pettersen, E. F.; Goddard, T. D.; Huang, C. C.; Couch, G. S.; Greenblatt, D. M., et al., UCSF chimera - A visualization system for exploratory research and analysis. *Journal of computational chemistry* **2004,** *25* (13), 1605-1612.
76. Grosberg, A. Y.; Khokhlov, A. R., *Statistical Physics of Macromolecules*. American Institute of Physics: New York, 1994.
77. Fixman, M., Radius of Gyration of Polymer Chains. II. Segment Density and Excluded Volume Effects. *The Journal of Chemical Physics* **1962,** *36* (12), 3123-3129.
78. Sun, S. T.; Nishio, I.; Swislow, G.; Tanaka, T., The Coil-Globule Transition - Radius of Gyration of Polystyrene in Cyclohexane. *J Chem Phys* **1980,** *73* (12), 5971-5975.
79. Permyakov, S. E.; Cherskaya, A.; Senin, I. I.; Zargarov, A. A.; Shulga-Morskoy, S. V., et al., Effects of mutations in the calcium-binding sites of recoverin on its calcium affinity: evidence for successive filling of the calcium binding sites. *Protein Eng* **2000,** *13* (11), 783-790.

Part II: Instrumentation & Engineering

Chapter 2: A Highly Compensated Interferometer for Biochemical Analysis

As published in *ACS Sensors* volume 3, July 2018. Copyright 2018 American Chemical Society

Interaction assays have led to significant scientific discoveries in the biochemical, medical, and chemical disciplines. The basis of these inter- and intramolecular interactions includes London dispersion, hydrogen bonding, hydrophobic character, and electrostatics. In the past three decades, the sophistication and power of techniques to interrogate these processes has developed at an unprecedented rate. These methods range from Nuclear Magnetic Resonance (NMR) [80] and Mass Spectrometry (MS) [81-82] to calorimetric [83-84] and thermophoretic [85]. Among the most commonly used label-free interaction assay methods are the refractive index (RI) methods [86], including Biolayer Interferometry (BLI) [87] and Surface Plasmon Resonance (SPR) [88]. All these methods have advantages, but the free-solution methods calorimetery and NMR are limited by sensitivity. Many other label-free methods, including BLI and SPR, require analyte immobilization onto the sensor surface, increasing assay complexity [89] and impacting performance when working within complex matrices. Backscattering interferometry (BSI) offers an alternative to these methods, providing free-solution operation [10]. complex matrix compatibility [90]. no sensitivity to the relative mass of the participating species [91], and picogram/mL sensitivity [92].

Numerous other interferometric methods have been used to perform biosensing determinations. These include the Mach–Zehnder interferometer (MZI), the Young interferometer (YI), the Hartman interferometer (HI), and the dual polarization interferometer. For a more detailed discussion of these interferometric methods we direct the reader to two reviews on interferometry in biosensing [86, 93]. Not covered in these reviews are two methods, one is a variation of the porous Si surface sensing method [94] and the other is a hybrid approach using active and passive plasmonic interferometry [95].

The first method has been reported to measure bovine serum albumin (BSA) adsorption in the range from 150 pM to 15 μM [96] and the use of electrical double layer (EDL)-induced

accumulation of charged ions onto a negatively charged nanostructured surface of SiO_2 to give bulk measurements of ca. 10^{-7} RIU [97]. Here, a signal processing strategy based on subtracting before and after reflectance spectra provides an improvement over previous Si sensors. It is not clear just how the double layer system reported to provide bulk RI measurements might be used to perform solution-phase interaction studies. The second relatively new interferometric method uses fluorescence modulation of the interferometric signal allowing picoliter sample volumes to be interrogated [98]. This type of sensor can work with an incoherent source, providing detectable ΔRI changes estimated at 5×10^{-4} RIU in 1pL, but does require fluorescence modulation [98]. By comparison, BSI provides 10^{-6} - 10^{-7} RIU sensitivity in a 350 pL volume [91].

One limitation of most interferometers is that they exhibit a significant level of temperature sensitivity [99]. However, it has been reported that the MZI can be configured in a manner to limit temperature-induced drift [100]. Also, because temperature variations affect the RI and physical thickness inversely, instrumental thermostatting is less stringent in the HI than in other interferometric methods [101].

Here we report on a new interferometric design that addresses the thermal sensitivity problem, while allowing specific binding assays in free-solution using the Free-SRF-BSI methodology [91]. FreeSRF capitalizes on background elimination by RI-matching the sample and reference [102], yet up until now these assays required the use of sequential measurements in the same channel of a microfluidic chip. The accuracy of such determinations can be impacted by temperature fluctuations and source instabilities that lead to fluctuations in the measured RI. Thus, we have used a high-resolution temperature controller and a chip design to mitigate environmental perturbations of the laser beam in BSI.

The obvious improvement to the sequential measurement approach is a simultaneous sample-reference configuration. The laboratory of Dr. Bornhop has investigated two approaches to a simultaneous sample-reference BSI configuration: two adjacent capillaries [103] and two channels in a chip [104]. In the first case, we effectively demonstrated sensitivity in the nanoRIU regime [103], yet found the approach to be impractical due to alignment constraints and the necessity to encapsulate the capillaries. In the second case, we used a calcite beam splitter to produce two parallel, orthogonally polarized, equal intensity beams, which were used to illuminate two microfluidic channels etched into a micro-fluidic chip separated by 1 mm [104]. This approach allowed binding assays to be performed, yet alignment was extremely tedious. Upon

careful evaluation, we found the two-channel chip approach provided little environmental noise rejection, giving relatively low level of compensation. In theory, fabrication of microfluidic channels with channel diameter accuracy of ±5 nm should allow for compensation, yet, aligning the two discrete, adjacent interferometers proved problematic, requiring the use of a high-resolution temperature controller to compensate for room temperature variations. Now, we think it better to describe this optical train as a comparator, as opposed to a compensated interferometer.

Here we demonstrate an interferometric configuration with a high level of noise rejection, enabling operation in the *absence* of a temperature controller. The Compensated Backscattering Interferometer (CBSI), shown in **Fig. 2.1**, uses a single elongated laser to interrogate adjacent regions of the same microfluidic channel simultaneously. The result in essentially two identical interferometers, providing compensation of temperature variations and source instabilities, such as wavelength and intensity wander. Relative RI determinations are performed by spatially separating two solutions (a binding sample and reference sample) with air, oil, or a hole in the chip and then measuring the difference in spatial position of two discrete regions of an interference pattern (**Fig. 2.1**). Here we demonstrate that CBSI provides a noise floor of ca. 10^{-8} RIU without environmental control and in the presence of an 8°C external temperature excursion. We also show mix-and-read FreeSRF binding assays with CBSI allowing the quantification of protein-ion (Ca^{2+} - Recoverin) and protein-small molecule (Concanavalin A (ConA) - mannose) interactions in nanoliter volumes, label-free and in free solution in the absence of a temperature controller.

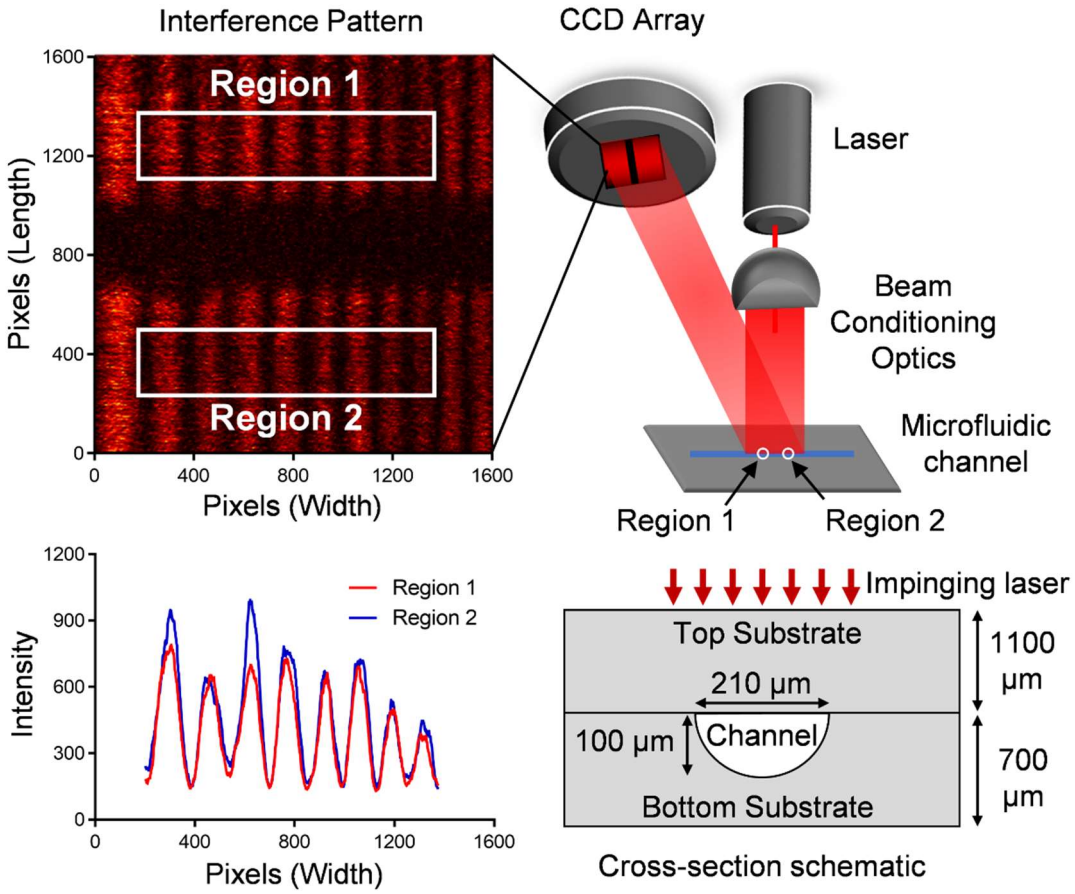

Fig. 2.1 Block diagram of the Compensated Backscattering Interferometer

Experimental

As shown in **Fig. 2.1**, a helium-neon (He-Ne) laser (wavelength 632 nm, Melles Griot, USA) illuminates a channel in a microfluidic chip. The glass chip was obtained from Micronit Microtechnologies (Netherlands), has an isotropically etched channel [105] that is nearly semi-circular with dimensions of (210 µm×100 µm radius) and served as both the sample container and the resonator for the interferometer. The chip, side-view shown in **Fig. 2.1**, has been described in detail elsewhere, with the modifications discussed below. Briefly, the He-Ne beam was shaped and conditioned by first passing it through a collimating lens (Oz Optics, Canada) giving a Gaussian beam diameter at $1/e^2$ of 0.8 mm. This beam was then stretched along one axis by a pair of anamorphic prism pairs, each with a 4-fold expansion (Thorlabs, New Jersey, USA). The prisms were arranged in series with identical orientation to produce a 16-fold expansion of the laser profile along one axis. The result was a beam that was about 12 mm in the long axis of the channel and

0.8 mm in the short axis. Interrogation of the channel by the elongated laser results in a series of interference "fringes" as shown in **Fig. 2.1**. The resulting fringe patterns were captured on a 2D CCD array (Basler, 12.8 mm×9.625 mm total detector size, 5.5 μm^2 pixels) that is placed 10 cm from the channel in the nearly 0° backscatter direction. The black shadow in the center of the fringe pattern is produced by a 1mm hole drilled through the center of the channel allowing the sample and reference regions to be separated.

Using an in-house LabVIEW^{TM} program, windows of the fringes from each detection zone measuring 200 pixels long×1200 pixels wide were selected for further analysis. The fringe selection method was similar to the one previously reported for BSI [106], consisting of choosing fringe windows with a nearly a single spatial frequency (**Fig. 2.1**). The fringe positional shifts from each of these two windows were quantified by a fast Fourier transform (FFT), allowing for tracking of the phase of the dominant frequency over time.

The sample introduction method used here takes advantage of the unique properties of microfluidic channels, capitalizing on the high surface tension of aqueous solutions and small dimensions of the channel [107]. The result is the ability to introduce samples unperturbed by a pressure source, using only capillary action to draw the droplets into chip. The hole drilled through the center microfluidic channel is large enough to serve as a passive "fluid stop," preventing the sample/reference solutions from jumping across the gap. The added benefit of this injection approach is that the sample/reference solutions are introduced at constant pressure. The hole also serves as the waste collection site. For clarity, an injection is pictorially demonstrated in **Fig. 2.2** using red and green dye. As shown, 1 μL is pipetted into the chip inlet at either end of the channel (**Fig. 2.2C**). Capillary action pulls the sample into the channel (**Fig. 2.2D**), and then stops once the sample reaches the hole drilled in the center of the channel (**Fig. 2.2E**).

Chip temperature was measured by thermistor embedded in an aluminum chip holder and controlled by a Peltier driven by a high-resolution temperature controller (Wavelength Electronics). Several precautions ensure optimum temperature regulation. The thermistor/thermal couple (Omega Engineering Inc., USA) and Peltier were selected of sufficient size and power and mounted in intimate contact with an aluminum block and cooling fins with a layer of thermal

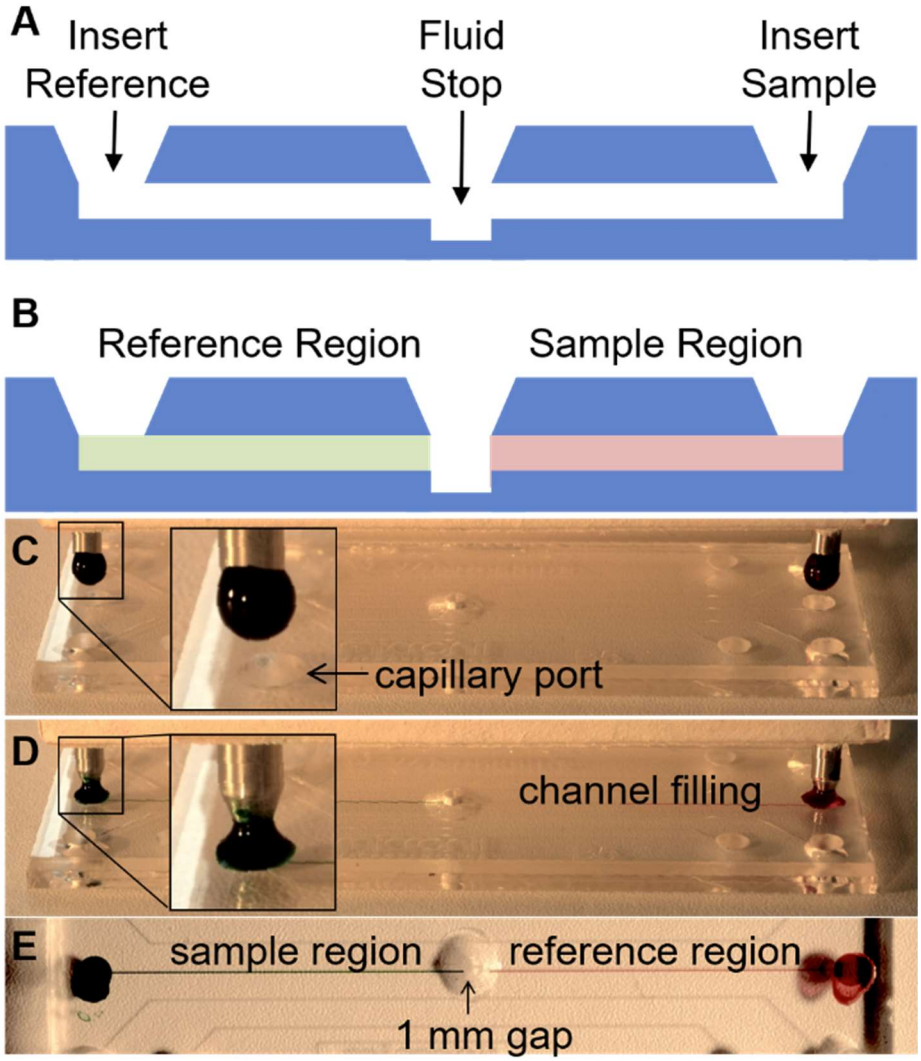

Fig. 2.2 CBSI sample introduction scheme. A side-view schematic of the microfluidic chip showing (A) the hole through the channel to function as a fluid stop and (B) the channel filled with both reference and sample.

grease. We used only thermistor/thermal couples specified for use with the Wavelength Electronics integral-differential controller. The controller was recently calibrated and was positioned in the laboratory so as to be as far as possible from sources of temperature variations, such as those induced by heating and A/C cooling vents.

Temperature compensation experiments were performed by injecting deionized (DI) water into both detection regions and measuring the phase difference between the two windows for five minutes to establish a baseline readout while the chip was held at a constant temperature of 25°C.

Then, the temperature of the entire chip was increased (by the Peltier) in increments of 0.5°C and the phase shifts were recorded for one minute. Following the one-minute measurement, temperature was increased again by 0.5°C. This procedure was repeated until measurements had been made from 25-27°C. The experiment was performed in triplicate. Glycerol 'compensation' determinations were performed by injecting the same concentration of glycerol (0, 0.5, 1, 3, and 5 mM in DI water) into both sides of the channel, and the phase shift were recorded for 30 seconds. Temperature was held constant at 25°C ± 0.001°C by the Peltier. After each measurement, the samples were removed by vacuum applied to the center hole, and the channel was rinsed with 100 µL of DI water and 100 µL Methanol. Concentrations were run from low to high and then the entire concentration range was repeated in triplicate. The glycerol 'calibration' experiment was performed using increasing concentrations of glycerol (0, 0.5, 1, 3, and 5 mM) in Phosphate Buffered Saline (PBS), introduced into the 'sample side' with PBS introduced into the 'reference side' of the chip. The measurement was performed by collecting 30 seconds of data for each sample-reference pair in absence of temperature control. The channels were rinsed with 100 µL PBS, 100 µL methanol, and 100 µL deionized water and then dried for 2 minutes before injection of the next sample. This procedure was performed in triplicate.

CBSI stability in the presence of large ambient temperature changes was tested by placing the entire optical train in a temperature-controlled chamber, inducing large temperature changes, and measuring the baseline noise. First, we established the baseline of the un-thermostatted CBSI at ambient temperature (22°C) inside the enclosure. Then, we heated the box by 4°C and measured the baseline noise for 5 minutes. This experiment was repeated by heating the chamber by an additional 4°C allowing for evaluation of compensation over an 8°C change in the environment.

Binding assays were performed in an endpoint format [91]. Concanavalin A (ConA) and Mannose samples were prepared in a buffer containing 50mM Sodium Acetate, 1 mM Ca^{2+}, and 1 mM Mn^{2+} in deionized water. Binding samples consisted of increasing concentrations of Mannose (0-800 µM) incubated with 2 µM ConA. Reference samples consisted of Mannose only. Samples were incubated at room temperature for 2 hours before measurement. Recoverin samples were prepared in modified Phosphate Buffered Saline (PBS) devoid of Ca^{2+} or Mg^{2+}. Binding samples consisted of increasing concentrations of Ca^{2+} (0-4 µM) in PBS incubated with 540 nM Recoverin (Novis Biologicals). Reference samples consisted of matched Ca^{2+} concentrations with no Recoverin present. Samples were incubated at room temperature for 1.5 hours with gentle

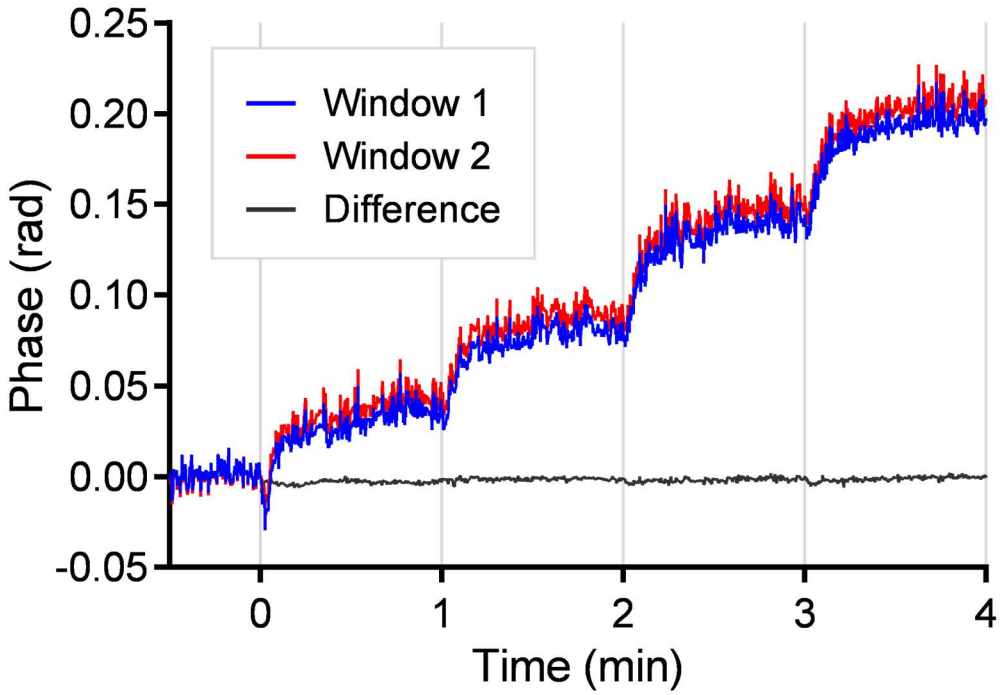

Fig. 2.3 CBSI phase output as a function of time for a temperature ramp of 2°C in 0.5°C steps, in 1-minute intervals. The reference/sample windows are plotted in red and blue, with the compensated (difference) signal plotted in black.

agitation. Sample-reference differential measurements were recorded over 15 seconds for each replicate measurement. Total analysis time from the end of incubation to finalized data analysis is 1 hour. To obtain dissociation constants (K_D), the data were fit to single-site saturation isotherms using Graphpad Prism (Graphpad Software, Inc.). Mannose, PBS, Ca^{2+}, and ConA were obtained from Sigma.

Results and Discussion

Interferometer Design. We hypothesized that by using an elongated beam to illuminate a microfluidic channel etched into a chip, a high contrast fringe pattern (**Fig. 2.1**) would allow for RI measurements in multiple locations along the channel simultaneously. Then, if chip and beam non-uniformities could be effectively averaged and two samples could be separated by a gap or hole, the optical train would form nearly identical interferometers. In short, comparing solutions in the *same* channel with the *same laser* should result in a significant level of noise reduction.

To test this theory, we first evaluated CBSI by measuring the instrument response to large temperature changes imparted to the chip with deionized water in both sides of the channel. After recording the phase difference between the two windows for 5 minutes to establish a baseline, the temperature of the chip was increased in increments of 0.5°C from 25 - 27°C (**Fig. 2.3**). The result of this temperature ramp experiment ($\Delta T = 2°C$) was a linear response in phase change for both of the two sensing regions (R^2=0.9995), with the slopes equal to 146.3 ± 1.15 and 146.4 ± 1.18 mrad/°C respectively. The difference in these phase values provides a level of compensation of 0.57 mrad/°C, or a maximum baseline excursion of ΔRI of 1.8×10^{-6} over the entire range. Using the value of $d\eta/dT$ for water of 1.06×10^{-4} RIU/°C (CRC Handbook of Chemistry and Physics) the total temperature induced perturbation corresponds to a $\Delta RI = 2.12\times10^{-4}$. Here the differential measurement provided a 122-fold reduction in RI sensitivity to environmental noise.

Next, we tested noise compensation for samples consisting of solutions of glycerol in PBS, at increasing concentrations, but using the same concentration in both the sample and reference region. This approach allowed us to evaluate compensation in more complex PBS matrix. Here, each glycerol concentration exhibited the expected RIU change in each window for the analyte (11.38 ± 0.09 mrad/mM in region 1 and 11.41 ± 0.13 mrad/mM in region 2) with R^2=0.9994. In the absence of any electronic filtering, the difference or compensated signal exhibited a baseline response of 1.6×10^{-7} RIU/mM.

Fig. 2.4A presents results from an experiment where we compared the S/N performance of CBSI to BSI [106]. Here, the standard deviation of the baseline for BSI and CBSI is plotted with both systems thermally stabilized (red and blue bars in **Fig. 2.4A**) and with CBSI operating *without temperature control* (green bar in **Fig. 2.4A**). The first two plots result from measuring the magnitude of the noise/drift over 5 minutes (1.6 µRIU and 1.4 µRIU) for BSI and CBSI respectively. Surprisingly, when turning off the Peltier for the CBSI instrument, the equilibrium baseline noise further decreased from 1.4 µRIU to 1.04 µRIU. This is a 27% reduction in baseline noise over the "temperature-stabilized" configuration illustrating the noise floor for CBSI is lower in the absence of active temperature control. A possible explanation for this observation is that the integral differential controller driving the Peltier cannot operate at a resolution high enough to contain the noise floor below 1×10^{-6} RIU (ca. 0.009ºC). As it cycles on and off based upon the measured temperature of the chip holder and the set point, minor temperature fluctuations will be induced by the Peltier causing the RI of the fluid to change.

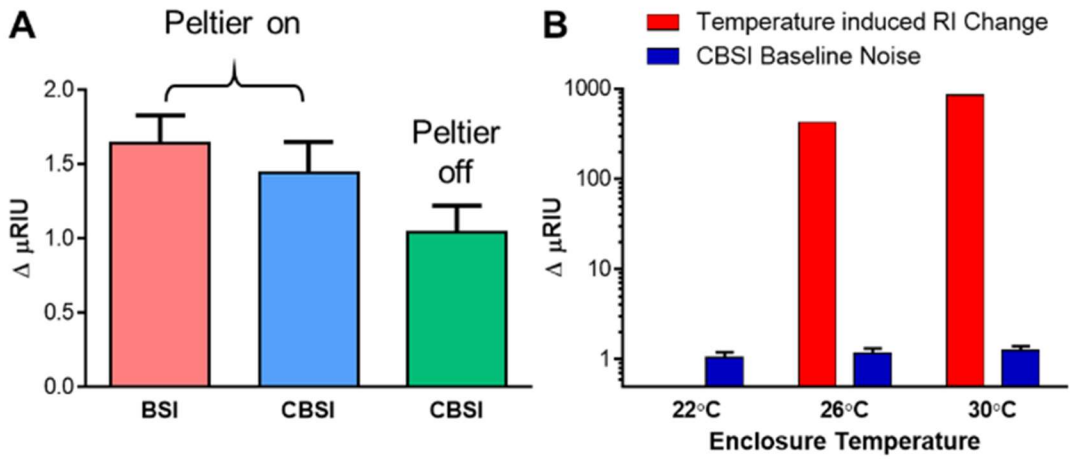

Fig. 2.4 (**A**) BSI and CBSI baseline noise with and in the absence of thermal stabilization. Error bars represent standard deviation of 3 measurements. (**B**) CBSI baseline noise and predicted ΔRI from a 4°C and 8°C ambient temperature change to the entire optical train. Error bars represent standard deviation of 3 measurements.

In the real world, environmental perturbations are never confined to the microfluidic chip, but rather will affect the entire optical train. Therefore, we tested CBSI stability in the presence of large ambient temperature changes by placing the entire optical train in a temperature-controlled chamber and inducing large temperature changes. First, we established the baseline of the un-thermostatted CBSI at ambient temperature (22°C) inside the enclosure (1.04 µRIU). Then we heated the box by 4°C and measured the baseline noise for 5 minutes. Using the dη/dT for water of 1.06×10^{-4} RIU/°C for a range of relevant temperatures (20-30°C), we calculated this 4°C change to correspond to a ΔRI of 424 µRIU (**Fig. 2.4B** first red bar). CBSI exhibited very little sensitivity to this large thermal perturbation, reporting an increase in baseline noise of 1.2×10^{-7} RIU or 0.12 µRIU (error bar on second blue bar). Here the overall noise level of CBSI was 1.16 µRIU. Upon further raising the temperature of the enclosure another 4°C, (final temperature 30°C, second red bar, note Y axis is a log scale), we measured an increase in drift (noise over 5 minutes) of just 0.08 µRIU. Interestingly the total 8°C temperature change, corresponding to a substantial perturbation of 8.5×10^{-4} RIU (848 µRIU) induced only a 2×10^{-7} RIU (0.20 µRIU) increase in drift noise. In other words, CBSI compensates for a 4280-fold temperature-induced change in RIU without any electronic filtering. This level of compensation should enable use in environments with widely changing temperatures, including benchtop and remote locations.

Further testing CBSI *without* temperature control, we performed glycerol calibration curves in PBS. Here five glycerol concentrations (0, 0.5, 1, 3, and 5 mM) were analyzed in triplicate, producing a robust response with a slope of 13.2 mrad/mM (1.25mRad/ μRIU) and R^2 of 0.9996 (**Fig. 2.5**). The LOD obtained without filtering or temperature control (measured as 3×baseline/slope) was found to be 7.0×10^{-7} RIU (0.11 mM glycerol) utilizing a baseline noise over 3 seconds of 0.39 μRIU. A more conservative value for performance, the LOQ (measured by 3×σ/slope) was calculated using the standard deviation of replicate injections (0.74 μRIU) and was found to be 1.8×10^{-6} RIU (1.8 μRIU or 0.17 mM glycerol). By applying a low pass filter (0.5 second time constant) to the data, the baseline noise was reduced to 2.8×10^{-8} RIU, resulting in an LOD of 6.7×10^{-8} RIU.

For comparison, we performed the same calibration experiment on a single channel BSI instrument with *no temperature* control. **Fig. 2.5** inset illustrates the significant ambient temperature sensitivity of the interferometer, showing that over the course of each 10-minute calibration trial, the signal drifted by roughly -2.1×10^{-5} RIU. Furthermore, the reproducibility of replicate injections reported an LOQ of 14.14 mM glycerol (148 μRIU), over 80-fold poorer than for CBSI.

BSI has been shown to provide high quality binding affinities and enable target quantitation at the level of several hundred molecules [90] when operating at level of ca. 10^{-6} RIU. Therefore, the LOQ provided by the CBSI of 1.8×10^{-6} RIU, in the absence of active thermal control, is well within performance criteria required to allow free-solution molecular interaction assays. Here we chose two binding systems to illustrate the use of CBSI for measuring bimolecular interactions. The first system was Concanavalin A (ConA), a protein-small molecule interaction system, chosen because of its physiological importance and well documented properties [108]. The second binding system was the well-studied studied ion - protein interaction, Ca^{2+} binding the neuronal calcium sensor (NCS) recoverin.

The study of carbohydrate−lectin interactions spans a multitude of disciplines, from virology and neuroscience to glycomics and immunology. Purified lectins can be used in biorecognition [109], such as blood typing, because various glycolipids and glycoproteins on an individual's red blood cells bind specifically to certain lectins. These principles of biorecognition can be applied to various diseases and have been used for *in-vitro* inhibition of HIV-1 [110]. Because of the size mismatch in the binding partners (100,000 Da for ConA and 180 Da for the

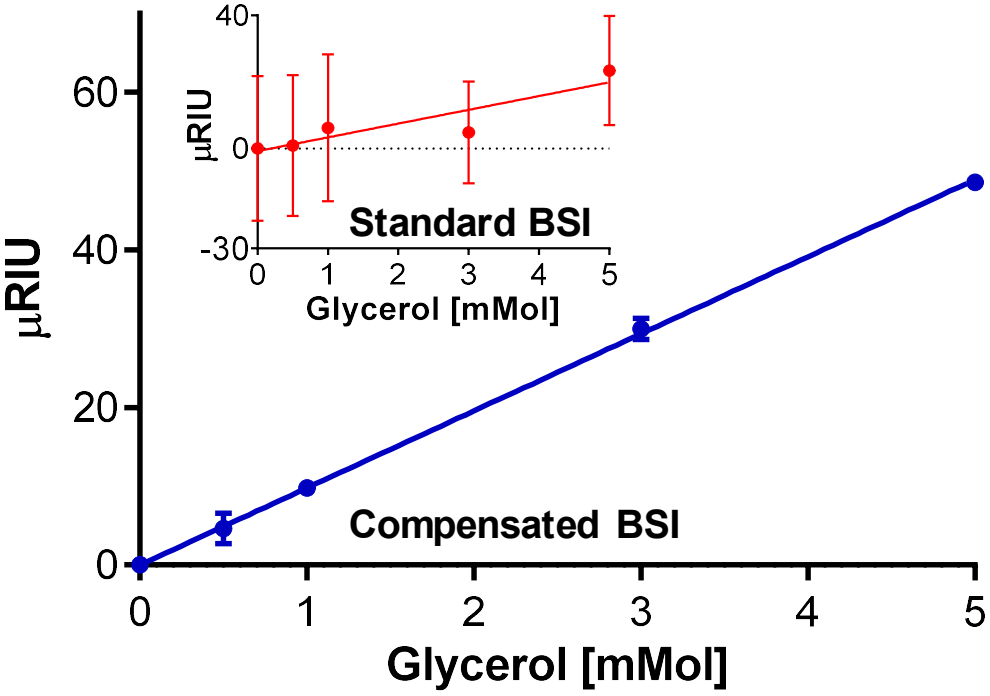

Fig. 2.5 Calibration curve consisting of glycerol in PBS performed with no temperature control, on CBSI. Error bars represent standard deviation of 3 trials. Inset: The same experiment performed on a standard single channel BSI in the absence of temperature control.

sugar) and the fact that carbohydrates do not usually contain functional groups that induce large changes in protein absorbance or fluorescence, quantitative determinations of binding affinities are often quite difficult to obtain. The installation of labels (fluorophores, spin labels, cross-linking agents) on the carbohydrate runs the risk of distorting the binding function that is being studied. Since CBSI is a label-free, free-solution measurement, we avoid these potential perturbations and/or limitation of labeled or tethered assays. **Fig. 2.6**A illustrates Concanavalin A – mannose binding assay performed on CBSI. In this experiment we obtained a K_D = 84 ± 17 µM, which compares favorably with both previous BSI results (96 ± 4 µM) [111] and calorimetry (265-470 µM) [108]. We attribute the slightly higher error in K_D for ConA-mannose binding to elements other than instrumental noise, such as age of protein, sample handling, incubation time/temperature, and temperature of measurement. Given the literature range for K_D determinations and typically published results, the measurement is well within acceptable experimental error. While the calorimetry results reported elsewhere were obtained in free

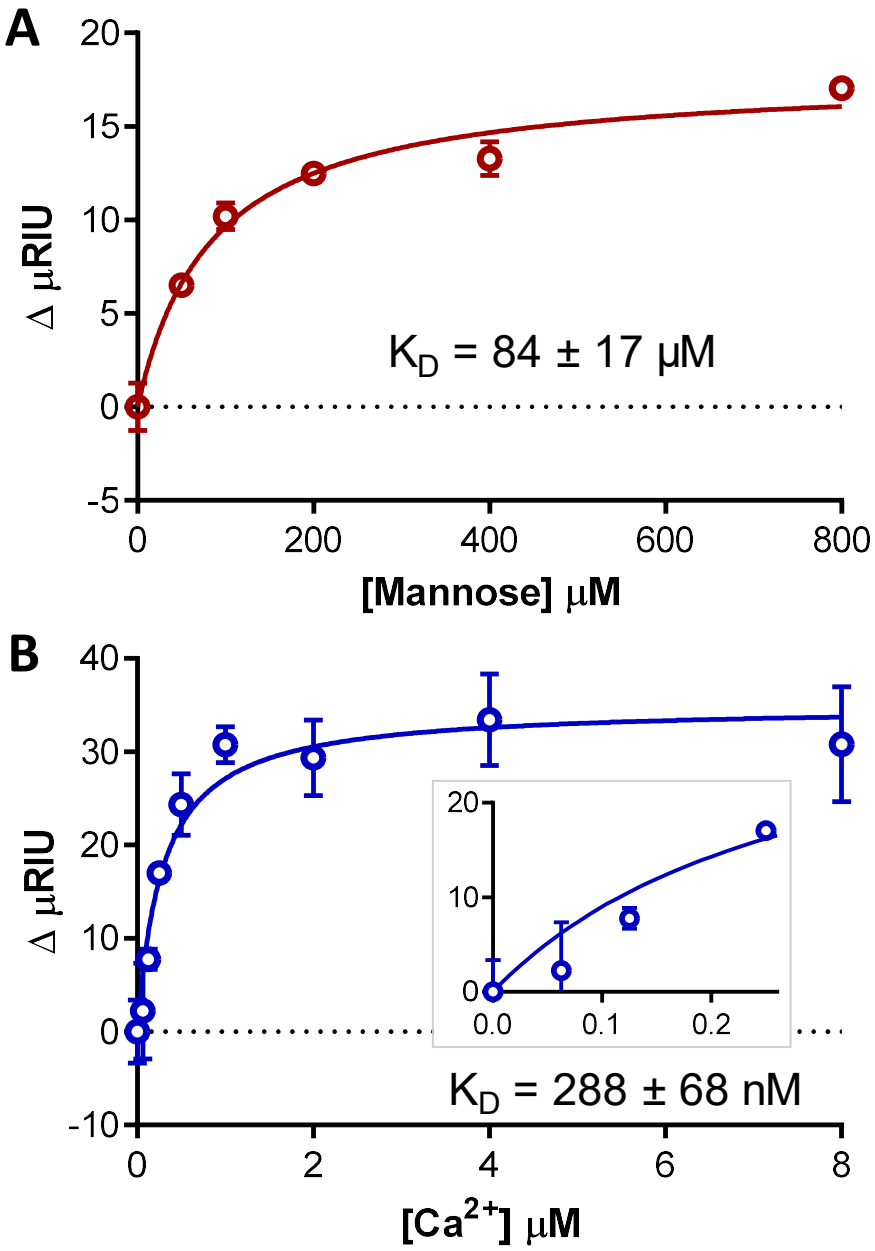

Fig. 2.6 Binding assays performed on CBSI with no temperature control. **A)** Saturation isotherm of the Concanavalin A/Mannose interaction. **B)** Saturation isotherm of recoverin binding Ca2+.

solution, the measurement required quite large volumes of sample at high concentration (1 mL of 100 μM to 1 mM carbohydrate and 2 mL of 10−100 μM lectin) increasing both cost and the potential for error due to aggregation.

Next, we measured the well characterized ion - protein interaction, Ca^{2+} binding recoverin. This binding pair has previously been studied by both interferometric methods in free solution [112] and by the surface immobilized format SPR [113]. Recoverin belongs to the family of NCS proteins and interacts with the N-terminal 25 amino acids of rhodopsin kinase (GRK1) thereby controlling phosphorylation of rhodopsin in a Ca^{2+}-dependent manner. It has been identified as an autoantigen in degenerative retinal diseases [114], and previous studies of Recoverin in context of other neuronal calcium binding proteins have advanced the understanding of calcium-dependent conformational changes [113],

The saturation isotherm measured for Ca^{2+}-recoverin interaction with CBSI is presented in **Fig. 2.6B**. Here the K_D value was found to be 288 ± 68nM. This value is quite similar to previous determinations of apparent binding constant by fluorescence (270 nM) [115] and 1.9 μM by SPR [113]. SPR applications need immobilization of one interaction partner, which can create heterogeneous surfaces and might account for the larger variations observed with this technique. We have observed and quantified this phenomenon with BSI by comparing surface and free solution measurements of binding affinity [111]. However, CBSI enabled the quantification of Ca^{2+}-recoverin binding in free-solution providing affinity constants that are not impacted by any modification, such as immobilization or tagging with a fluorophore.

For further perspective on the two binding events presented, the highest concentration used for Mannose was 800 μM and the lowest concentration of Ca^{2+} ~60 nM. These concentrations span about 4 decades (from nearly a micromolar to 10s of nanomolar), illustrating the range of performance possible with CBSI operating in the absence of any temperature stabilization. Assuming 100% binding would mean that 60 nM of Ca-Recoverin had been formed and quantified. Thus, within the CBSI probe volume of 25nL there is merely 1.5×10^{-15} moles or 1.5 femtomoles of Ca-Recoverin detected by CBSI.

Chapter 2 Conclusion

Here we demonstrated a compensated backscattering interferometer that is highly sensitive, has a nanoliter probe-volume, enables mix-and-read biochemical assays in free solution,

and can be operated without temperature control, even in the presence of large environmental perturbations. The utility of the device was shown by characterizing the binding affinity of the ConA/Mannose and the Recoverin/Ca^{2+} systems. These affinity measurements provided results that compared favorably with previous affinity measurements, but with much less sample required, no need for surface immobilization, and no modification of either binding partner with a fluorophore. Two major advantages of CBSI are the simplicity of the optical train (laser, object and detector/camera) and the ability to function without temperature control. These properties are anticipated to facilitate miniaturization, resulting in a low cost, highly stable, field deployable system that is assay agnostic.

10. Bornhop, D. J.; Latham, J. C.; Kussrow, A.; Markov, D. A.; Jones, R. D., et al., Free-solution, label-free molecular interactions studied by back-scattering interferometry. *Science* **2007,** *317* (5845), 1732-1736.
80. Nitsche, C.; Otting, G., NMR studies of ligand binding. *Curr Opin Struct Biol* **2017,** *48*, 16-22.
81. Ishii, K.; Noda, M.; Uchiyama, S., Mass spectrometric analysis of protein-ligand interactions. *Biophysics and physicobiology* **2016,** *13*, 87-95.
82. Cubrilovic, D.; Biela, A.; Sielaff, F.; Steinmetzer, T.; Klebe, G., et al., Quantifying Protein-Ligand Binding Constants using Electrospray Ionization Mass Spectrometry: A Systematic Binding Affinity Study of a Series of Hydrophobically Modified Trypsin Inhibitors. *J Am Soc Mass Spectr* **2012,** *23* (10), 1768-1777.
83. Ababou, A.; Ladbury, J. E., Survey of the year 2005: literature on applications of isothermal titration calorimetry. *Journal of molecular recognition : JMR* **2007,** *20* (1), 4-14.
84. Di Trani, J. M.; Moitessier, N.; Mittermaier, A. K., Measuring Rapid Time-Scale Reaction Kinetics Using Isothermal Titration Calorimetry. *Analytical chemistry* **2017,** *89* (13), 7022-7030.
85. Wienken, C. J.; Baaske, P.; Rothbauer, U.; Braun, D.; Duhr, S., Protein-binding assays in biological liquids using microscale thermophoresis. *Nat Commun* **2010,** *1*, 10.1038/ncomms1093.
86. Kussrow, A.; Enders, C. S.; Bornhop, D. J., Interferometric Methods for Label-Free Molecular Interaction Studies. *Analytical chemistry* **2012,** *84* (2), 779-792.
87. Ciesielski, G. L.; Hytonen, V. P.; Kaguni, L. S., Biolayer Interferometry: A Novel Method to Elucidate Protein-Protein and Protein-DNA Interactions in the Mitochondrial DNA Replisome. *Methods in molecular biology* **2016,** *1351*, 223-231.
88. Guerreiro, J. R. L.; Frederiksen, M.; Bochenkov, V. E.; De Freitas, V.; Sales, M. G. F., et al., Multifunctional Biosensor Based on Localized Surface Plasmon Resonance for Monitoring Small Molecule-Protein Interaction. *ACS nano* **2014,** *8* (8), 7958-7967.
89. Vashist, S. K.; Dixit, C. K.; MacCraith, B. D.; O'Kennedy, R., Effect of antibody immobilization strategies on the analytical performance of a surface plasmon resonance-based immunoassay. *The Analyst* **2011,** *136* (21), 4431-4436.
90. Wang, M.; Kussrow, A. K.; Ocana, M. F.; Chabot, J. R.; Lepsy, C. S., et al., Physiologically relevant binding affinity quantification of monoclonal antibody PF-00547659 to mucosal addressin cell adhesion molecule for in vitro in vivo correlation. *British journal of pharmacology* **2017,** *174* (1), 70-81.
91. Bornhop, D. J.; Kammer, M. N.; Kussrow, A.; Flowers, R. A., 2nd; Meiler, J., Origin and prediction of free-solution interaction studies performed label-free. *Proc Natl Acad Sci USA* **2016,** *113* (12), E1595-1604.
92. Olmsted, I. R.; Hassanein, M.; Kussrow, A.; Hoeksema, M.; Li, M., et al., Toward rapid, high-sensitivity, volume-constrained biomarker quantification and validation using backscattering interferometry. *Analytical chemistry* **2014,** *86* (15), 7566-7574.
93. Estevez, M. C.; Alvarez, M.; Lechuga, L. M., Integrated optical devices for lab-on-a-chip biosensing applications. *Laser Photonics Rev* **2012,** *6* (4), 463-487.
94. Lin, V. S.; Motesharei, K.; Dancil, K. P.; Sailor, M. J.; Ghadiri, M. R., A porous silicon-based optical interferometric biosensor. *Science* **1997,** *278* (5339), 840-843.

95. Feng, J.; Siu, V. S.; Roelke, A.; Mehta, V.; Rhieu, S. Y., et al., Nanoscale Plasmonic Interferometers for Multispectral, High-Throughput Biochemical Sensing. *Nano Lett* **2012,** *12* (2), 602-609.
96. Mariani, S.; Strambini, L. M.; Barillaro, G., Femtomole Detection of Proteins Using a Label-Free Nanostructured Porous Silicon Interferometer for Perspective Ultrasensitive Biosensing. *Analytical chemistry* **2016,** *88* (17), 8502-8509.
97. Mariani, S.; Strambini, L. M.; Barillaro, G., Electrical Double Layer-Induced Ion Surface Accumulation for Ultrasensitive Refractive Index Sensing with Nanostructured Porous Silicon Interferometers. *ACS sensors* **2018,** *3* (3), 595-605.
98. Li, D. F.; Feng, J.; Pacifici, D., Nanoscale optical interferometry with incoherent light. *Scientific reports* **2016,** *6*.
99. Born, M.; Wolf, E., *Principles of optics: electromagnetic theory of propagation, interference and diffraction of light*. 7th expanded ed.; Cambridge University Press: Cambridge ; New York, 1999; p xxxiii, 952 p.
100. Guha, B.; Gondarenko, A.; Lipson, M., Minimizing temperature sensitivity of silicon Mach-Zehnder interferometers. *Optics express* **2010,** *18* (3), 1879-1887.
101. Schneider, B. H.; Edwards, J. G.; Hartman, N. F., Hartman interferometer: versatile integrated optic sensor for label-free, real-time quantification of nucleic acids, proteins, and pathogens. *Clin Chem* **1997,** *43* (9), 1757-1763.
102. Baksh, M. M.; Kussrow, A. K.; Mileni, M.; Finn, M. G.; Bornhop, D. J., Label-free quantification of membrane-ligand interactions using backscattering interferometry. *Nature biotechnology* **2011,** *29* (4), 357-U173.
103. Wang, Z.; Bornhop, D. J., Dual-capillary backscatter interferometry for high-sensitivity nanoliter-volume refractive index detection with density gradient compensation. *Analytical chemistry* **2005,** *77* (24), 7872-7877.
104. Morcos, E. F.; Kussrow, A.; Enders, C.; Bornhop, D., Free-solution interaction assay of carbonic anhydrase to its inhibitors using back-scattering interferometry. *Electrophoresis* **2010,** *31* (22), 3691-3695.
105. Stjernstrom, M.; Roeraade, J., Method for fabrication of microfluidic systems in glass. *J Micromech Microeng* **1998,** *8* (1), 33-38.
106. Markov, D.; Begari, D.; Bornhop, D. J., Breaking the $10^{(-7)}$ barrier for RI measurements in nanoliter volumes. *Analytical chemistry* **2002,** *74* (20), 5438-5441.
107. Glière, A.; Delattre, C., Modeling and fabrication of capillary stop valves for planar microfluidic systems. *Sens Actuators, A* **2006,** *130-131*, 601-608.
108. Schwarz, F. P.; Puri, K. D.; Bhat, R. G.; Surolia, A., Thermodynamics of monosaccharide binding to concanavalin A, pea (Pisum sativum) lectin, and lentil (Lens culinaris) lectin. *The Journal of biological chemistry* **1993,** *268* (11), 7668-7677.
109. Sharon, N.; Lis, H., History of lectins: from hemagglutinins to biological recognition molecules. *Glycobiology* **2004,** *14* (11), 53R-62R.
110. Swanson, M. D.; Winter, H. C.; Goldstein, I. J.; Markovitz, D. M., A lectin isolated from bananas is a potent inhibitor of HIV replication. *The Journal of biological chemistry* **2010,** *285* (12), 8646-8655.
111. Olmsted, I. R.; Kussrow, A.; Bornhop, D. J., Comparison of Free-Solution and Surface-Immobilized Molecular Interactions Using a Single Platform. *Analytical chemistry* **2012,** *84* (24), 10817-10822.

112. Sulmann, S.; Kussrow, A.; Bornhop, D. J.; Koch, K. W., Label-free quantification of calcium-sensor targeting to photoreceptor guanylate cyclase and rhodopsin kinase by backscattering interferometry. *Scientific reports* **2017,** *7*, 45515.
113. Sulmann, S.; Dell'Orco, D.; Marino, V.; Behnen, P.; Koch, K. W., Conformational changes in calcium-sensor proteins under molecular crowding conditions. *Chemistry* **2014,** *20* (22), 6756-6762.
114. Polans, A. S.; Witkowska, D.; Haley, T. L.; Amundson, D.; Baizer, L., et al., Recoverin, a photoreceptor-specific calcium-binding protein, is expressed by the tumor of a patient with cancer-associated retinopathy. *Proceedings of the National Academy of Sciences of the United States of America* **1995,** *92* (20), 9176-9180.
115. Permyakov, S. E.; Cherskaya, A. M.; Senin, II; Zargarov, A. A.; Shulga-Morskoy, S. V., et al., Effects of mutations in the calcium-binding sites of recoverin on its calcium affinity: evidence for successive filling of the calcium binding sites. *Protein engineering* **2000,** *13* (11), 783-790.

Chapter 3: Longitudinal Pixel Averaging for Improved Compensation in Backscattering Interferometry

As published in *Optics Letters* volume 43, January 23, 2018.

Interferometry is one the most sensitive measurement approaches ever devised by humans. It has been used for measuring the distance to stars [116], determining the speed of light in a medium as with refractive index (RI) measurements, and, recently, a 2.5-mile long interferometer was used to confirm the existence of gravitational waves [117]. Various forms of interferometers have been employed in the arena of chemical/biochemical analysis, for example as detectors in separation science [106], tools for the study of molecular interactions [91], and for quantifying chemical or biochemical targets [92]. The types of interferometers used for these measurements include the Mach-Zehnder [100], Fabry Perot [118],Young [119], waveguiding [120], and a relatively novel, low-volume approach termed the backscattering interferometer (BSI) [63].

BSI is unique among interferometers, allowing ΔRI measurements at 10^{-7} RIU sensitivity in probe volumes from 4 nanoliters to as small as 250 picoliters. This level of sensitivity has enabled a wide array of chemical and biochemical investigations to be performed [10, 102]. While powerful and relatively simple, the optical configuration of BSI, consisting of a laser, an object (a microfluidic chip or capillary), a mirror, and a camera, has limitations. The single channel configuration of BSI negates direct comparison of sample and reference, adversely influencing reproducibility and throughput of biochemical determinations. As with the vast majority of interferometric methods, BSI also suffers from a significant sensitivity to temperature, with wavelength and pointing instability often causing drift and an increased noise floor. There have been several manifestations of a differential approach to BSI, all exhibiting varying levels of performance improvements. The most sensitive approach, ca. 10^{-9} ΔRI, consisted of two capillaries touching and tilted so as to direct the individual fringe patterns above and below the plane of illumination [103]. RI changes were quantified in the backscatter direction by measuring fringe position with matched bicell detectors. The capillaries were also contained within a

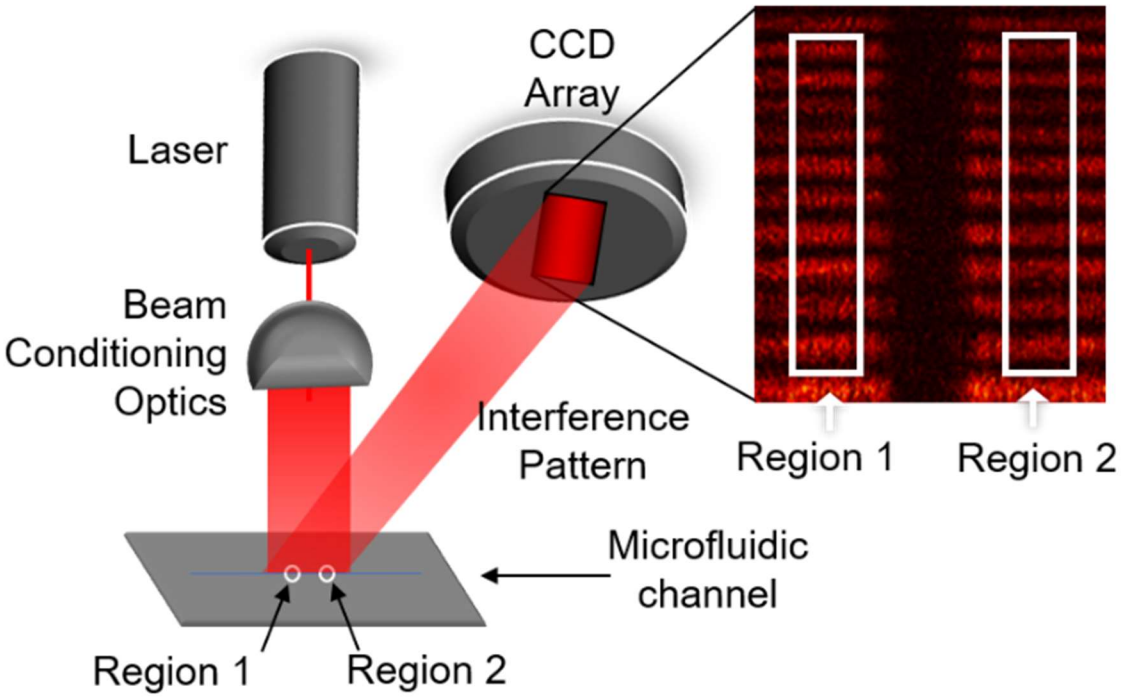

Fig. 3.1 Block Diagram of the Compensated Backscattering Interferometer

thermostatted chamber. Numerous factors made the tilted capillary approach challenging to set-up and align. More recently, we used a calcite polarizer to direct two equal intensity beams onto adjacent microfluidic channels in a single glass chip separated by 1 mm [104]. Here a CCD array was used to quantify fringe shift. This approach was also abandoned by our group after recognizing it was very difficult to align and that negligible compensation was provided by this configuration of BSI. Finally, in collaboration with Dr. Beiske at the University of Melbourne, we built an interferometer by illuminating two touching, co-linear capillaries with a single laser beam. In this case, we interrogated the predominantly single spatial frequency fringe pattern in the forward-looking direction [121].

Our research on numerous interferometer embodiments has taught us that subtle differences in the response function, due to optical misalignment, ultimately limits the level of compensation possible for temperature fluctuations, as well as laser pointing instabilities and intensity variations. Our modeling efforts have provided numerous insights [63] into BSI, such as how object size and shape influences signal. Yet due to limited resolution of the model and optical

complexity the interference phenomenon we have been unable to predict the relationship between compensation and alignment mismatch.

As a result of the works noted above, we began to investigate optical approaches that would inherently result in two nearly identical interferometers. After several additional attempts we discovered and recently reported on an approach to a compensated backscattering interferometer (CBSI) [122]. The CBSI, illustrated in **Fig. 3.1**, represents a unique optical approach to a nano-volume interferometer with significant compensation, thus providing insensitivity to temperature and source perturbations. Illuminating the microfluidic channel with a laser that is stretched along the axis of the channel produces a series of elongated interference fringes (**Fig. 3.1**). The stretched laser profile is achieved by passing a Helium Neon laser (632 nm wavelength, 800-micron spot size, Melles Griot, USA) through a collimating lens (Oz Optics, Canada) followed by two 4x expansion anamorphic prism pairs (Thorlabs, USA), resulting in a beam profile that is 12.8 mm in the stretched axis and 0.8 mm in the short axis.

Differential operation in CBSI is facilitated by separating the sample and reference solutions by an air gap or oil droplet, then comparing them directly with the expanded beam emanating from a common source. By placing a hole in the center of the microfluidic channel, the two solutions to be compared can be separated. Alternatively, an immiscible fluid or an air gap can separate the solutions. In either case, two regions of the same 'object' (microfluidic channel) are simultaneously interrogated by a common source. As demonstrated in this Letter, having two nearly identical interferometers by proper interrogation of the fringe patterns has enabled the simple optical train of CBSI to provide a high level of thermal compensation, a challenge widely encountered with interferometers.

While CBSI was easy to align, the initial level of compensation to $d\eta/dT$ perturbations was less than desirable. Upon further investigation we realized the slight imperfections in the manufacturing process of the microfluidic channel that serves as the interferometer can result in variations by up to 5% in depth/diameter. This variation can influence the distribution of the rays or laser energy that forms the interference pattern. The consequence is some non-uniformity in the RI response function between discrete regions of the channel.

We report here that interrogation of longer regions of the fringe pattern average out these imperfections, resulting in interference patterns that have increased "likeness" between multiple regions. **Fig. 3.2** demonstrates this dramatic improvement in fringe pattern likeness when the

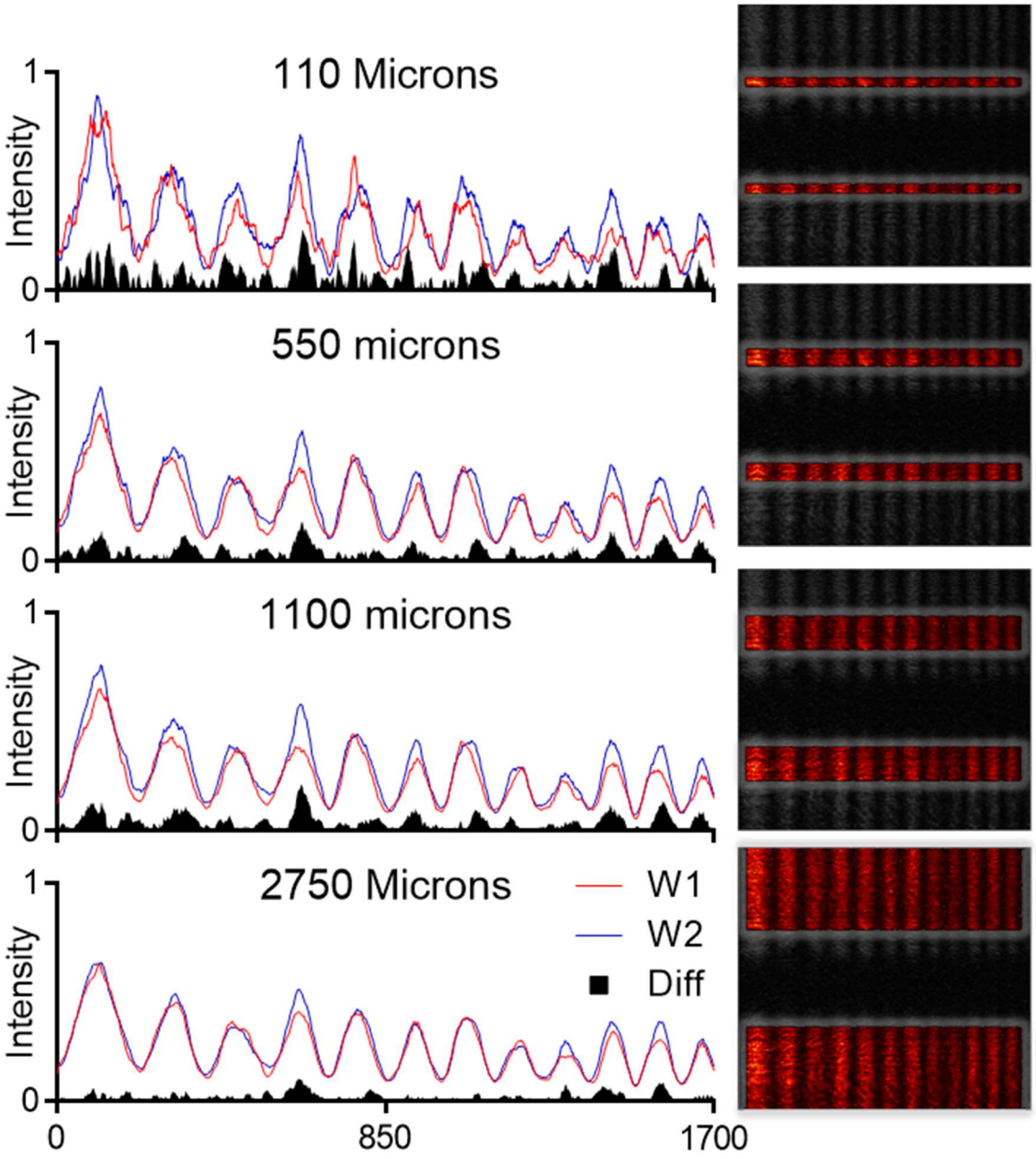

Fig. 3.2 Fringe pattern intensity profiles and differences as function of camera interrogation window (left). Camera image of fringes showing interrogation window.

signal is averaged over increasing spatial lengths of two fringe pattern regions. This averaging is accomplished using an in-house software program that allows us to increase the read width (number of camera pixels) for the fringe interrogation window (**Fig 3.1**). As with our previous design of BSI, we determine RI changes by quantifying spatial shift of the fringes by calculating

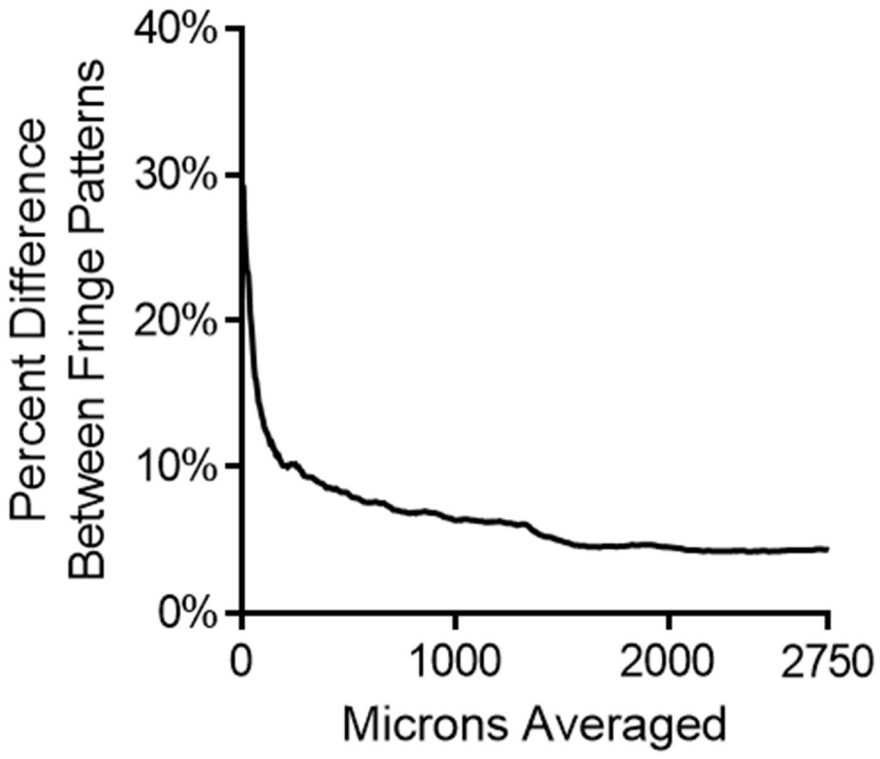

Fig. 3.3 Percent difference between fringe patterns as a function of averaged channel length.

an FFT of the windowed fringes, which allows the phase change to be determined with respect to time [91].

Fringe Likeness

A quantitative evaluation of fringe likeness versus interrogation length or camera pixel averaging is presented in **Fig. 3.3**. This observation is likely due to the intrinsic non-uniformities along the length the channel and slight differences in optical alignment of the laser along the channel. The camera used (Basler Aviator A2300, Basler, Germany) has 5.5 μM^2 pixels. In the transverse direction, there are roughly 150 pixels per fringe, which is well above the required Nyquist sampling frequency to transduce the signal. Therefore, small changes in pixel size or spacing should not affect this accuracy. This analysis indicates that there is little improvement in fringe pattern likeness after about 2000 microns or 360 pixels. Since performance improvements plateau and are likely a function of channel length, we predict that smaller pixels would yield a similar result if interrogating the same length of channel.

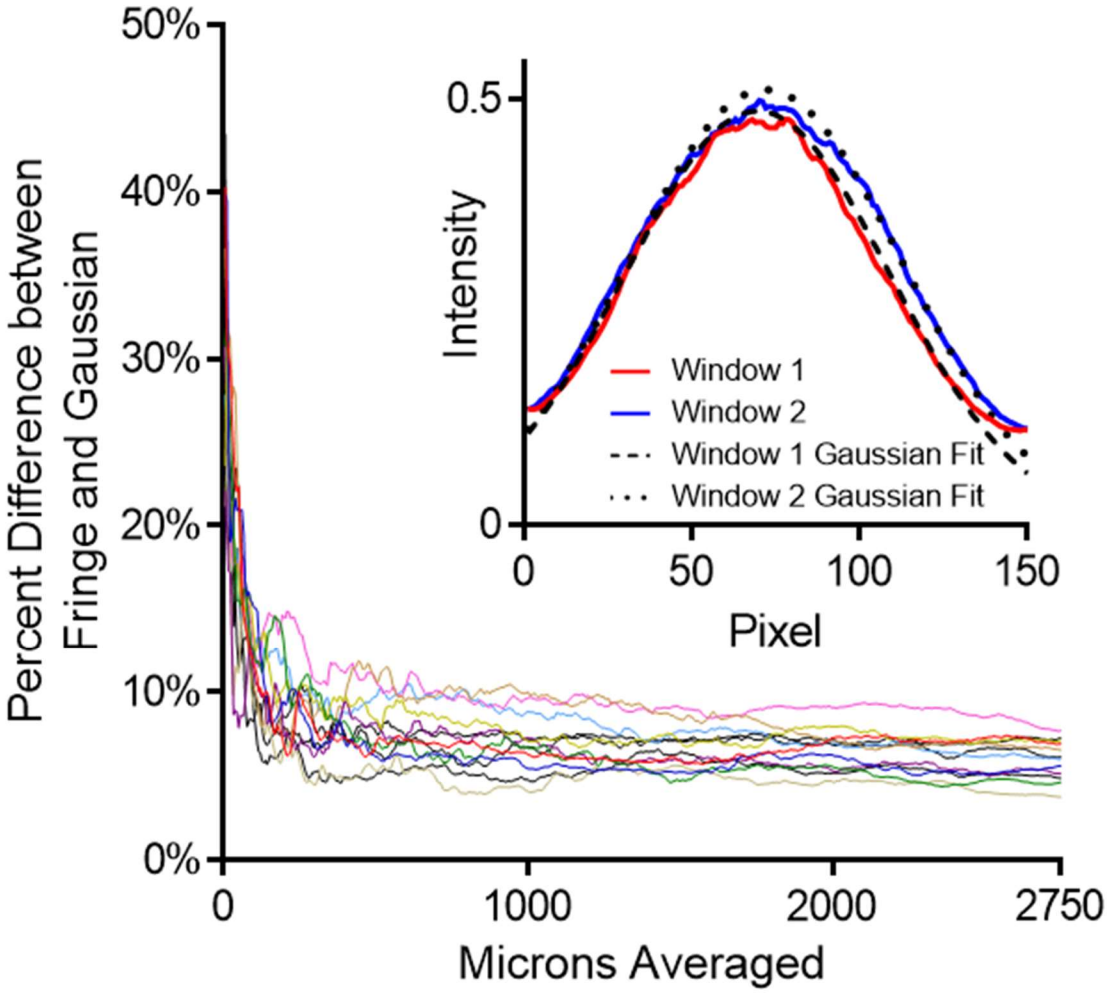

Fig. 3.4 Gaussian fit difference plot for 12 fringes, 6 in each interrogation window. Inset: Fringe is from 2750 microns averaged, 5th fringe from the left.

Regardless, the CBSI provides excellent compensation for environmental perturbations. When interrogating just 2mm of the channel, or about 360 pixels on the camera, the simple optical configuration of CBSI was able to provide two fringe patterns that were different by only 4.3%. As shown below, this level of 'likeness' provides excellent common mode noise rejection (CMNR) and allows for significant $d\eta/dT$ compensation.

Fringe Gaussianity

Another approach to access fringe uniformity after pixel averaging is to compare the fringes to a Gaussian distribution, which is the original shape of the beam used to illuminate the

optic (microfluidic channel). Thus, we expect that the fringe pattern would take on a Gaussian shape. Further, our previous modeling efforts have shown that the interference fringes resulting from BSI [63] exhibit a nearly Gaussian shape. **Fig. 3.4 inset** illustrates the characteristics of a sample and reference region fringe utilizing a 2.75mm window as compared to two Gaussians. Note the excellent correlation between the desired and the experimentally observed fringe shape. Taking this observation further, we performed Gaussian fit as a function of channel length. Since we typically interrogate multiple fringes, we calculated the normalized difference between 24 actual fringes (12 fringes in each of the two windows) and each fringe's fitted Gaussian, as a function of the number of averaged microns (length) along the channel. It is noteworthy that spatial averaging both increases sample/reference region fringe pattern likeness, but it also produces interference patterns that more closely resemble the ideal Gaussian fringe shapes predicted by past modeling efforts. This observation is quite interesting given that the energy distribution into the fringes is a complicated function with some fringes reporting the fluid RI, some reporting the fluid channel interface, and some being impacted by inconstancies in other parts of the chip (e.g. top and bottom surface).

Common Mode Noise Rejection

Next, we evaluated the general level of CMNR. While an extensive study of CMNR with respect to laser pointing and intensity instability was not performed here, we have shown that the two factors can contribute significantly to overall performance of BSI (unpublished). For example, under conditions where tight temperature control is maintained, the short and long-term base line offer a good indication of the level CMNR of for these parameters.

Recognizing the significant limitation of interferometers resulting from $d\eta/dT$ perturbations, we evaluated the level of compensation for water as a function of increased channel interrogation length. First, we introduced water into both detection regions of the microfluidic channel. Then using a high-resolution-Peltier-containing chip holder of in-house design and temperature controller (Wavelength Electronics, Bozeman, MT, USA), we increased the temperature of the microfluidic chip in 0.5°C increments from 25-27°C, while monitoring the resulting phase change.

Fig. 3.5 illustrates the dramatic reduction in temperature sensitivity that can be obtained by the CBSI optical configuration. As a shown in **Fig. 3.5A** when interrogating fringes over 550

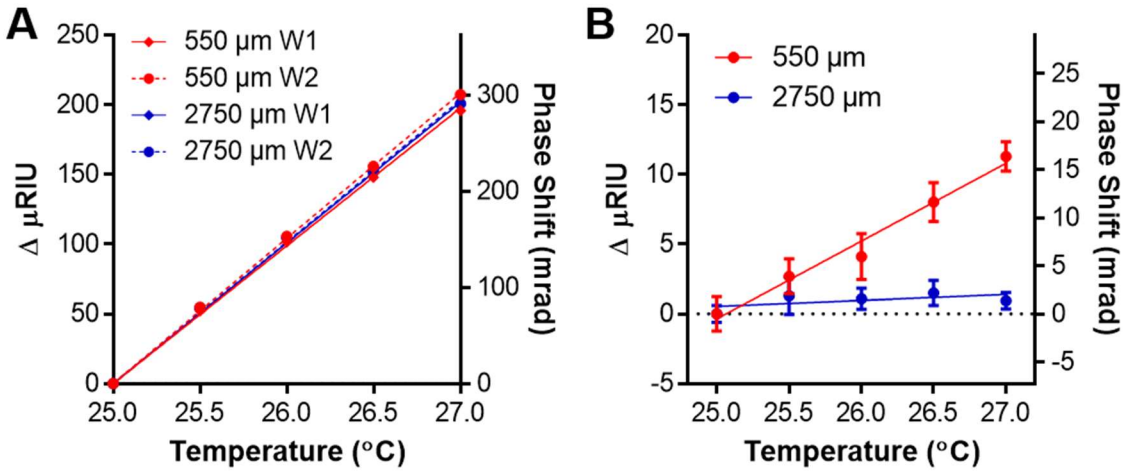

Fig. 3.5 CBSI compensation for water demonstrated by recording the phase change when raising the temperature over 2°C. A) Absolute phase shift reported by each window. B) Difference in phase between W1 and W2 for each window size.

microns (100 pixels) or 2750 microns (500 pixels) the interferometer exhibited the expected thermal response of 1.02×10^{-4} RIU/°C for the 2°C change. Next by recording the *difference between* the two windows (as in a sample and reference determination), the significant temperature response is greatly reduced or nearly abated. For example, the 550-micron windows produced a level of compensation corresponding to 5.8×10^{-6} RIU/°C, which corresponds to about a 50-fold reduction in sensitivity to the overall temperature change of 2°C. Additionally, the 0.55mm windowed difference approach reduced the short-term noise from 6.5×10^{-6} RIU (single window) to 1.2×10^{-6} RIU. By simply increasing the window size to 2750 microns, CBSI temperature compensation performance improved to a level 3.9×10^{-7} RIU/°C, an additional 15-fold improvement in rejection of dη/dT sensitivity. Putting this observation into context, when probing two 2.75mm adjacent sections of an unmodified, commercial micro-fluidic chip with an isotropically etched channel with dimensions of 100×210 µm, CBSI gives a 750-fold level of compensation for dη/dT perturbations. It is noteworthy that this level of performance was obtained on an interferometer with a probe volume of just 50nL. It should also be noted that all measurements presented here were obtained in the absence of any external electronic filtering. By applying a low pass filter with a 0.5 second time constant to the data output, the baseline noise (over 3 seconds) was reduced to a level of 3.1×10^{-8} RIU. In other words, a typical CBSI signal for the quantification of a 250pg/mL concentration of an analyte such as CYFRA 21-1 probed with a

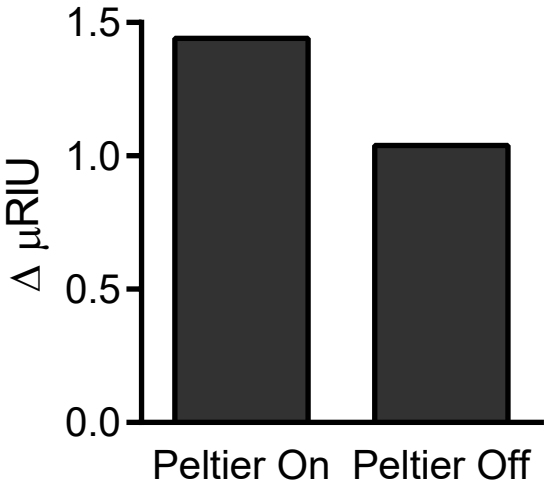

Fig. 3.6 Operation of CBSI **A)** with and **B)** without temperature regulation

monoclonal antibody is 25 mrad. So, the noise from a 2°C change in the room when using a 2.75mm window is just 2% of the binding signal.

Environmental Compensation

Does CBSI represent a differential interferometer that truly compensates for environmental noise? To answer this question, we compared the performance of CBSI operated with and without any external temperature regulation. **Fig. 3.6** illustrates that CBSI actually performs better in the absence of a temperature controller than when using a high-resolution Peltier. This is important because it is highly irregular to be able to perform an interferometric or RI determination since the large $d\eta/dT$ sensitivity dictates that vast majority of common laboratory instruments that are used to measure RI, require significant thermal regulation.

Finally, we present an analysis of glycerol to show the advantages of channel averaging (**Fig. 3.7**). Analyte detection was performed by measuring the phase shift between a reference solution (water) and sample solution (glycerol in water) using a 2000-micron fringe window, in the absence of external temperature regulation. Each data point is the average of 3 replicate measurements, with the graph showing that the error bars (standard deviation) are smaller than the symbols. For CBSI the slope is 14.46 ± 0.30 vs. 5.67 ± 3.17 milliradians per millimolar glycerol for the single channel, non thermostatted BSI. The standard deviation of the baseline noise over a 3 second period, in the absence of electronic filtering, is 0.68 milliradians, providing a 3-sigma

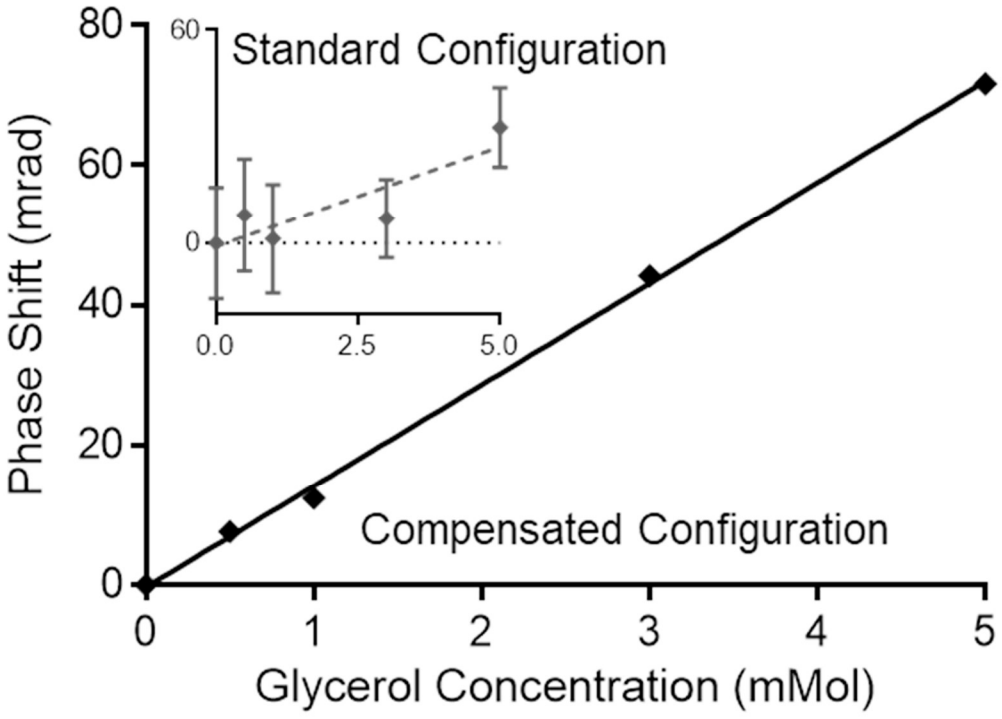

Fig. 3.7 CBSI detection of glycerol in water with no temperature regulation. Error bars are the standard deviation of 3 replicate measurements. Inset shows the same experiment performed on standard BSI.

detection limit of 0.16 millimolar glycerol (1.4×10^{-6} RIU). The inset shows the same experiment performed on a standard BSI which gives an LOD of ca. 7.4 mM glycerol. Note that in the absence of temperature regulation the standard BSI has very poor signal/noise.

Chapter 3 Conclusion

In summary, this work demonstrates that by averaging two larger regions of the backscattered and elongated fringe patterns produced in the CBSI optical configuration, significant compensation of environmental perturbations can be obtained in interferometric measurements.

The observation that CBSI is a highly compensated interferometer could pave the way to the development of a hand-held RI detector with 10^{-7} RIU sensitivity. Such a device, based on a diode laser, capillary or microfluidic cell, and a camera, would represent a significant advance in technology, providing a >1000-fold improvement in performance over existing commercial hand-held RI detectors.

10. Bornhop, D. J.; Latham, J. C.; Kussrow, A.; Markov, D. A.; Jones, R. D., et al., Free-solution, label-free molecular interactions studied by back-scattering interferometry. *Science* **2007,** *317* (5845), 1732-1736.
63. Swinney, K.; Markov, D.; Bornhop, D. J., Chip-scale universal detection based on backscatter interferometry. *Analytical chemistry* **2000,** *72* (13), 2690-2695.
91. Bornhop, D. J.; Kammer, M. N.; Kussrow, A.; Flowers, R. A., 2nd; Meiler, J., Origin and prediction of free-solution interaction studies performed label-free. *Proc Natl Acad Sci USA* **2016,** *113* (12), E1595-1604.
92. Olmsted, I. R.; Hassanein, M.; Kussrow, A.; Hoeksema, M.; Li, M., et al., Toward rapid, high-sensitivity, volume-constrained biomarker quantification and validation using backscattering interferometry. *Analytical chemistry* **2014,** *86* (15), 7566-7574.
100. Guha, B.; Gondarenko, A.; Lipson, M., Minimizing temperature sensitivity of silicon Mach-Zehnder interferometers. *Optics express* **2010,** *18* (3), 1879-1887.
102. Baksh, M. M.; Kussrow, A. K.; Mileni, M.; Finn, M. G.; Bornhop, D. J., Label-free quantification of membrane-ligand interactions using backscattering interferometry. *Nature biotechnology* **2011,** *29* (4), 357-U173.
103. Wang, Z.; Bornhop, D. J., Dual-capillary backscatter interferometry for high-sensitivity nanoliter-volume refractive index detection with density gradient compensation. *Analytical chemistry* **2005,** *77* (24), 7872-7877.
104. Morcos, E. F.; Kussrow, A.; Enders, C.; Bornhop, D., Free-solution interaction assay of carbonic anhydrase to its inhibitors using back-scattering interferometry. *Electrophoresis* **2010,** *31* (22), 3691-3695.
106. Markov, D.; Begari, D.; Bornhop, D. J., Breaking the $10^{(-7)}$ barrier for RI measurements in nanoliter volumes. *Analytical chemistry* **2002,** *74* (20), 5438-5441.
116. Monnier, J. D., Optical interferometry in astronomy. *Rep Prog Phys* **2003,** *66* (5), 789-857.
117. Ligo Scientific Collaboration, GW151226: Observation of Gravitational Waves from a 22-Solar-Mass Binary Black Hole Coalescence. *Physical review letters* **2016,** *116* (24), 241103.
118. Dancil, K. P. S.; Greiner, D. P.; Sailor, M. J., A porous silicon optical biosensor: Detection of reversible binding of IgG to a protein A-modified surface. *J Am Chem Soc* **1999,** *121* (34), 7925-7930.
119. Hradetzky, D.; Claas, M.; Holger, R., Interferometric label-free biomolecular detection system. *Journal of Optics A: Pure and Applied Optics* **2006,** *8* (7), S360.
120. Schmitt, K.; Schirmer, B.; Hoffmann, C.; Brandenburg, A.; Meyrueis, P., Interferometric biosensor based on planar optical waveguide sensor chips for label-free detection of surface bound bioreactions. *Biosens Bioelectron* **2007,** *22* (11), 2591-2597.
121. Durbin, B. M. Development of a compensated interferometric detector. Vanderbilt, Nashville, TN, 2015.
122. Bornop, D. J.; Kammer, M. N. Robust Interferometer and Methods of Using Same. 2016.

Chapter 4: Compensated Interferometric Reader Signal Extraction and Analysis

The compensated interferometric reader (CIR) capitalizes on a real-time differential measurement between a test sample and a reference solution to enable compensation and provide common mode noise rejection. This is accomplished by flowing alternating droplets of a test sample and reference solution through the capillary (which serves as the compensated interferometric optics) and recording the difference in interference patterns between two adjacent detection regions as a function of time. As described in Chapters 2 and 3, the interference patterns are quantified by taking the FFT of a set of 5 "fringes," and tracking the phase of these fringes as they shift position. This *phase shift* correlates with changes in the solution refractive index within the microfluidic chip/capillary.

Figure 4.1 shows the fundamental operation of the CIR's differential measurement for the simplest case: a droplet train consisting of a test sample drop and a reference drop, separated by a small oil gap, then a second test sample drop (a replicate measurement of the first test sample) also separated by an oil droplet. This droplet train flows through the capillary from left to right.

This example data consists of a test sample of 10 mM glycerol in water and a reference solution of water with no glycerol. In this example data, there are 5 key timepoints of interest, represented by the letters **A-E**. At time point **A**, the Test Sample 1 fully occupies ***both*** detection regions, as demonstrated in the top row (**A**) of the cartoon graphic at the top of **Fig. 4.1**. The result of this measurement is a difference in phase of 0, as shown on the plot at the bottom of **Fig. 4.1** in the blue-highlighted region under the heading **A**. As the droplets continue moving through the capillary, there is a transition period as Sample 1 moves out of detection region 1 and the oil drop passes through the detection region. This transition is seen on the plot as the slope upward between **A** and **B**. At time point **B**, Test Sample 1 fills detection region 2, and the reference solution fills detection region 1. The result of this differential measurement is the desired CIR signal, in this case a positive phase change. This result is shown on the phase shift/time graph during the time

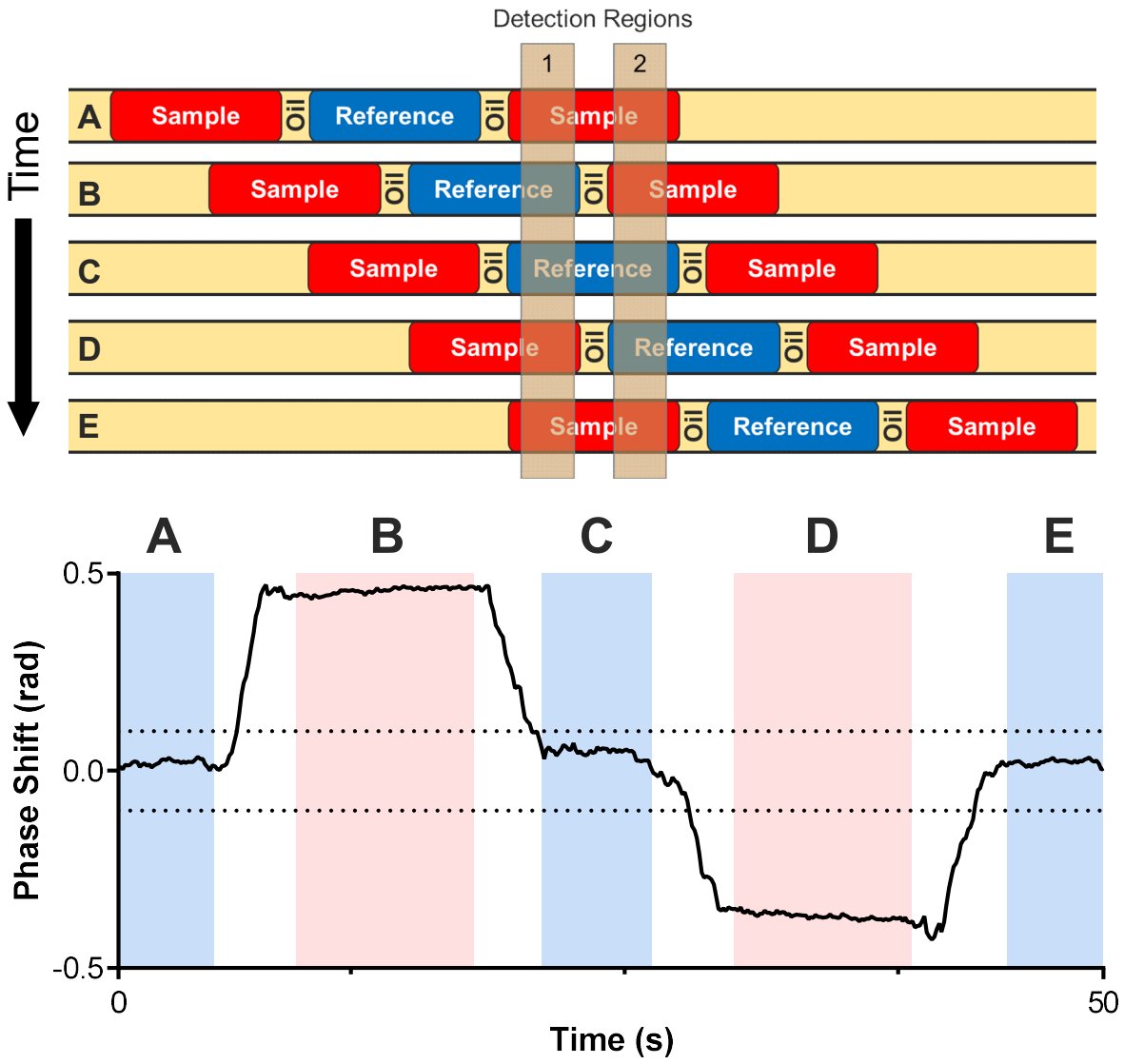

Fig. 4.1 The fundamental operation of the differential measurement as the droplet train moves through the two detection regions.

period marked in pink under the header **B**. Next the reference solution fills both detection regions and the phase returns to 0 (time **C**). At time **D**, now the *reference solution* fills detection region 2 and the *test sample* detection region 1, with the result being a phase change of equal magnitude as in **B**, but in the opposite direction. Then, following a transition period, test sample 2 fills both detection regions, producing a phase shift of 0, shown as time **E** in **Fig. 4.1**. There are 5 regions of interest here: **A** and **E** indicate when the sample fills both detection regions, and **C** indicates when the reference fills both detection regions. It is important to note that the flow is continuous,

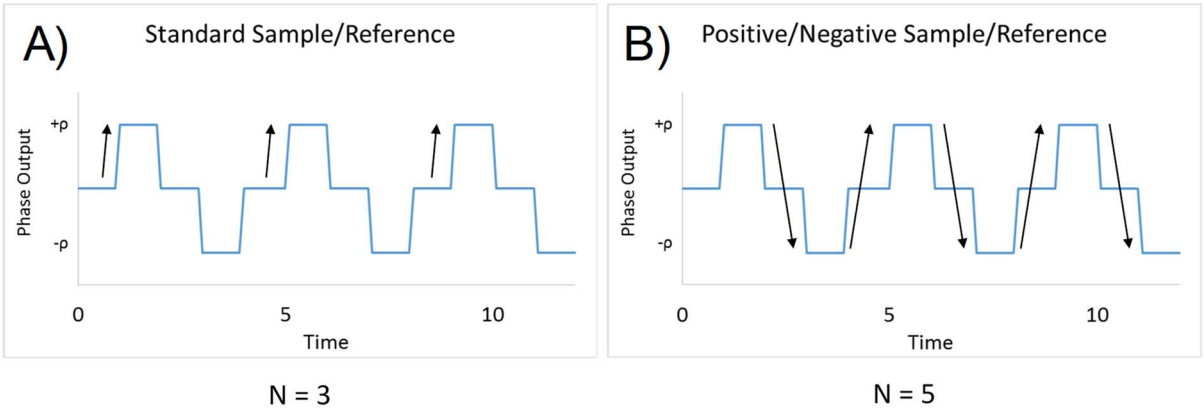

Fig. 4.2 A) Signal quantification by taking the difference between the phase shift and baseline results in an average value of +p with n=3, but quantification of the signal using the difference between phase shifts **B**) results in an average value of 2×p and an n=5.

and for the standard droplet size (1 µL) and flow speed (10 µL/min), each highlighted time section (**A-E**) corresponds to ~3 seconds.

The phase difference at time **A**, **C**, and **E** should be 0. Reasons for a non-zero measurement in regions **A**, **C**, and **E** are discussed in **Appendix C**. Times **B** and **D** report the differential signal, which is the data needed for the measurement. The average phase change over the duration of **B** is termed the "*test/reference* phase shift (+p)," while the average phase change over the duration of **D** is the "*reference/test* phase shift (-p)."

Figure 4.2 is a cartoon graphic of the data that would result from 3 test/reference solution pairs, resulting in 3 *test/reference* phase shifts (+p), 3 negative phase shifts *reference/test* phase shifts (-p), and 6 regions where the phase shift is 0. As demonstrated in **Fig. 4.2**, there are several methods that can be employed to obtain a value for the "signal." The first method, as demonstrated in **Fig. 4.2A**, is to calculate the phase shift as the *test/reference* solution phase shift's excursion from the baseline. Performing the Phase shift – baseline calculation results in an n=3, with an average phase shift of +p (denoted by the three vertical arrows in **Fig. 4.2A**). A similar phase shift – baseline calculation can also be performed by subtracting the *negative* going *reference/test* excursion (For example, **Fig. 4.1** region **D**, -p). Because the same test and reference sample are used to produce the alternating droplets, the phase shift from **Fig. 4.1** region **D** should have the same signal magnitude as region B with opposite sign. The second method, as demonstrated in **Fig. 4.2B**, is to take the *test/reference* phase shift and subtract it from the *reference/test* phase shift (corresponding to the difference of **D – E** in **Fig. 4.1**). This results in a signal with magnitude 2×p,

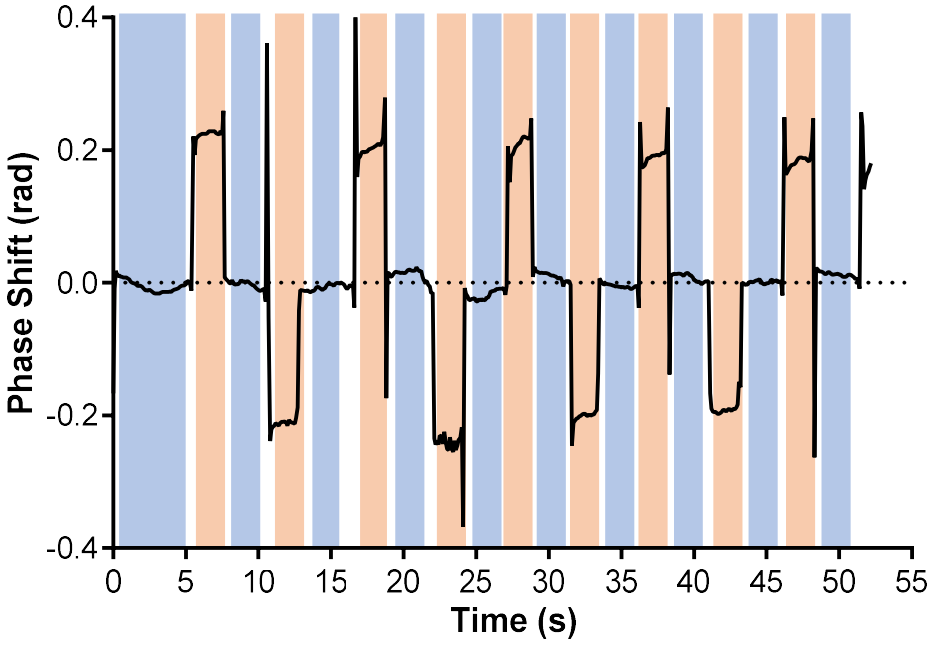

Fig. 4.3 Data resulting from 5 test/reference solution pairs consisting of 5 millimolar glycerol in water. The colors correspond to the colors in Fig. 4.1.

and an n=5, as denoted by the five alternating arrows in **Fig. 4.2B**. For example, if we apply the strategy described in **Fig. 4.2** to the data in **Fig. 4.1**, +p = 0.48, -p = 0.42, and 2×p = 0.90 radians.

A complete determination in the standard droplet train typically consists of 5 replicate pairs of test/reference droplets (10 droplets total). An example of a complete determination is displayed in **Fig. 4.3** for a sample pair consisting of 5 millimolar glycerol in water as the test sample and water with no glycerol as the reference. The data in **Fig. 4.3** has the same step-wise pattern correlating to regions **A**-**E** as in **Fig. 4.1**, and the regions are color coded the same way. The data in **Fig 4.3** can be tabulated in the +p method, the -p method, and the 2×p method, and these results are presented in **Fig. 4.4**. As demonstrated in **Fig. 4.4**, the +p and -p phase shift have approximately the same magnitude (0.214 vs. -0.201) with opposite sign, and similar standard deviation (0.017 vs. 0.021). The 2×p signal, however, is nearly double the +p and -p signal, while the noise (standard deviation) only increases by a factor of ~1.5. The result is a modest, but not insignificant, increase to signal-to-noise (14.3 vs. 12.1 and -9.8). Therefore the 2×p method is superior to the +p or -p method, and unless otherwise stated all further CIR signal determinations use the 2×p method.

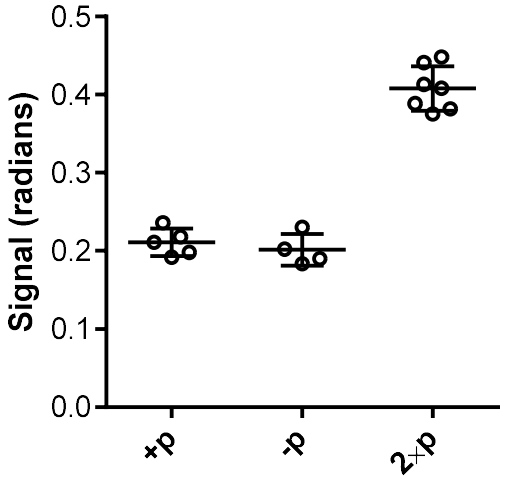

	+p	-p	2×p
Average	0.214	-0.201	0.408
Standard Deviation	0.017	0.021	0.028
S/N	12.1	-9.8	14.3

Fig. 4.4 The phase shift data in Fig. 4.3, analyzed according to the schema presented in Fig. 4.2. Quantifying the signal as 2×p provides an improvement in S/N over the +p and -p method.

It should be noted here that as demonstrated by the data in Figure 3, a 5 test/reference solution pair results in 19 regions, of which 10 will be "baseline." The first "baseline" is typically longer than the others, due to the first droplet in the standard droplet train configuration having a larger volume that the other droplets (described in more detail below). Following the initial long baseline, there will be 5 *test/reference* regions (+p, colored orange) and 4 *reference/tes*t regions (-p, colored orange).

The droplet train

The typical FSA-CIR assay consists of preparing a batch of samples that can be used to produce a droplet train. The current instrument incorporates a commercial Dropix droplet generator that employs a sample tray with 14 usable wells that are immersed in an oil bath. Droplets are made by the capillary moving between the oil and sample reservoir drawing up solutions that are separated by an oil droplet, while the syringe pump provides constant draw. With 14 wells available per tray, the standard assay consists of two rinse solutions and 6 test-solution/reference-solution pairs separated by oil, as presented graphically in **Fig. 4.5**. As shown in **Fig.4.5A**, the initial rinses are doubled.

An expanded view of a set of test/reference solution pairs is displayed in **Fig 4.5**, expressed by showing the time each droplet takes to traverse the detection region. The standard droplet train

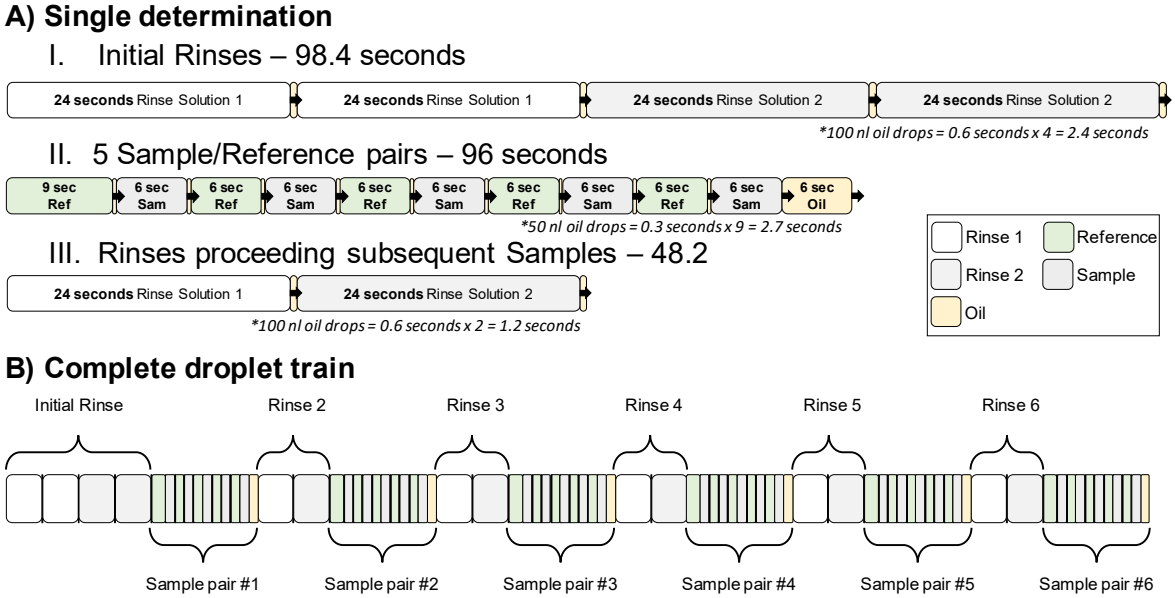

Fig. 4.5 Droplet train composition by length of time at a fixed point on the detector. A) A single determination consisting of 2 sets of duplicated 4 µL rinse solutions followed by 5 test/reference solution pairs. B) The standard droplet train consisting of 6 sample pair determinations.

begins with 2 initial rinses of 2×4 µL droplets of a rinse solution, typically water, followed by a second pair of 2 droplets of 4 µL of a 2nd rinse solution, typically buffer. The volumes and material used for the rinses can be larger in volume and consist of stronger solvents as needed by the assay. For example, a simple glycerol calibration curve in phosphate buffered saline (PBS) would use PBS as both rinse 1 and 2, but an experiment measuring antibody binding to vesicles may use chloroform as solution 1 and a 25% methanol solution as rinse 2. The combination of rinses can vary according to the experimental matrix (serum, plasma, urine, etc.) and the molecules present in solution (proteins, peptides, lipids, etc.).

The Dropix operating manual describes programing of the Dropix and guides the user on flow rate vs. droplet size. I have employed a syringe pump flow rate of 10 µL/min to generate the droplet train presented here. At this flow rate, the time each droplet takes to traverse in front of a point on the detector is calculated by dividing the volume by the flow rate. For example, the 1000 µL sample droplet moving at 10 µL/min spends 6 seconds in front of a point on the detector. The lengths of all drops used in the standard droplet train are presented in **Fig. 4.5**. The residence time of a droplet in the detection region is important to calculate, because the output of the interferometer registers or records the signal from the droplets as radians (fringe shift) vs. time.

The code to program the Dropix to deliver the standard droplet train is included in **Appendix C**.

Part III: Biomedical Applications

Chapter 5: Rapid assay development and quantification of two chemical nerve agents in serum

Adapted from a manuscript in preparation for submission to *Lab on a Chip*

During the siege of Khirra in 600 BCE, the Athenian army used hellebore to poison the city's water source, causing the defenders to become so weak with diarrhea that the Athenians beat them quite easily [123]. In the intervening two and a half millennia since, humanity has produced no shortage of advancements in the field of chemical warfare. In the modern era, several of the most widely used weapons of chemical warfare belong to the family of organophosphorus nerve agents (OPNAs). In the past century, OPNAs, specifically sarin gas, VX, and novichok agents were proliferated [124], with stockpiles produced by both the United States and the USSR during the cold war [125]. They were used against Iranian and Kurdish troops by Iraq during the Iran-Iraq war, and OPNAs affected both combatants and civilians during the Persian Gulf War [126]. Even within the past two decades, OPNAs were used in several high profile instances resulting in thousands of civilian exposures [127-129]. OPNAs are odorless and colorless molecules that block the binding site of acetylcholinesterase (AChE), therefore inhibiting the breakdown of acetylcholine [126]. The resulting buildup of acetylcholine leads to the inhibition of neural communication to muscles and glands and can lead to increased saliva and tear production, diarrhea, vomiting, muscle tremors, confusion, paralysis and even death [130-131]. Long-term effects of acute poisoning include neurological damage, psychiatric effects, dermatological conditions, sleeplessness, and low serum and erythrocyte AChE levels [130, 132]. While the onset of symptoms is often rapid, within minutes to hours, some symptoms can take much longer to present. Conventional tests for AChE activity lack the selectivity to identify the specific OPNA used, and testing is not always readily available at the site of an exposure. Diagnosis of exposure is typically based on symptoms and is often confirmed by measuring OPNA adducts to butyrylcholinesterase (BChE) in blood [125].

The effects from chronic, low level OP exposure are not typically as severe as high-level acute exposure [133-134], yet still include peripheral nervous system [135-137] and respiratory

damage [138], along with depression and cognitive impairment [139]. Organophosphates are still widely used in pesticides, and poisoning kills about 200,000 people annually worldwide [140]. OPNAs are odorless and colorless [141], making occupational OP exposure detection difficult by simple observational means. Since low level OPNA exposures do not typically evoke cholinergic symptoms such as lachrymation, salivation, meiosis, or muscle fasciculation, it is often difficult to diagnose exposure based upon these symptoms or cholinesterase activity without additional information from the exposure [142]. However, even intermediate exposure, resulting in non-specific, flu-like symptoms, represents a case where AChE inhibition never reaches a high enough level to produce quantifiable depression in activity [134]. In short, current detection methods based either on symptoms or cholinergic activity are insufficient to confirm chronic low/mid-level exposure from OPs.

Among the approaches used to detect OPNA exposure are those based on enzymatic activity or by detection of the OPNAs or their metabolites directly by ELISA, fluorescence [143-144], bead arrays [145], engineered-nanopore technologies [146], and label-free techniques, such as surface plasmon resonance (SPR), quartz-crystal microbalance [147], wave-guided interferometry [148], and mass spectrometry (MS) [149], Field deployable photometric dipstick assays do exist, but these methods are limited by sensitivity ranges between 10^{-7}-10^{-5} M [150], unreported false positives rates, matrix-dependent sample processing requirements [151], or interference from pigmented sample matrices such as blood. Two commonly used OPNA exposure quantification methods include liquid chromatography coupled to tandem mass spectrometry (LC-MS/MS) and the Test-mate ChE Assay [149, 152]. LC-MS/MS exhibits relatively high sensitivity and specificity, yet it is usually combined with a multi-step extraction/concentration procedure [149]. While powerful, this LC-MS/MS methodology is not field deployable. The Test-mate ChE assay has been shown to be a promising field-kit alternative to MS, with a transduction method based on measuring the activity of red blood cell AChE and plasma BChE using the modified Ellman method [153]. This kit produces results within 4 minutes requiring only 10 µL of blood [152]. While rapid, the Test-mate approach is still based on the OP target proteins, AChE or BChE, not the specific OP directly. Measurement of AChE activity for confirmatory testing requires routine measurements of baseline activity to account for intra- and inter- person variability [153]. Recently a wearable glove biosensor has been reported, where an electrochemical sensor is printed on a disposable nitrile glove enabling “swipe sampling” of

suspicious surfaces or agricultural products [154]. However, because utility is demonstrated by coating a surface with a 200 μM OP solution, it is difficult to assess the performance of this approach in terms of solution-phase biosensing. Development of alternative techniques are subject to challenges related to speed, reproducibility, cost, specificity, sensitivity, accessibility, or large sample volumes. Furthermore, the use of surface immobilization and labeling steps makes assay development and analyte validation arduous, slow, and expensive. Therefore, a free-solution method, particularly one that is label-free, enzyme-free, and compatible with complex matrices represents an innovative and beneficial alternative for next-generation detection methods.

The methodology reported here, is a free-solution assay (FSA) [91] combined with a compensated interferometer (CI) [155]. The FSA mix-and-read measurement can be used without relative mass dependency and in native environments, allows for accurate screening of therapeutics [156], improves *in-vitro/in-vivo* correlations for first-in-human dose estimates [157], investigating biological mechanisms of action [53], and quantifying protein biomarker targets [158]. Here we demonstrate that when combined with aptamer probes [159], FSA enables rapid development of assays that exhibit high sensitivity (pg/mL) and high specificity for the quantification of two OPNA acids (VX and GB) in serum.

Aptamers are short segments of RNA or single-strand DHA that can be quickly and inexpensively selected to bind to desired targets. They can serve as sensors[160], therapeutics [161], and cellular process regulators [162], as well as drug targeting agents [163-166]. The diversity of applications and the varied targets to which aptamers can bind (proteins, peptides, and small molecules) stem from the ability of aptamers to form complex three-dimensional shapes including both helices and single-stranded loops. Aptamers are selected *in vitro*, are easily stored and transported, and are stable for months to years, making them potential alternatives to antibodies or enzymes. Aptamers work particularly well in FSA because aptamers undergo a significant conformation change upon binding, resulting in a large FSA signal [91, 159]. An added benefit is that the aptamer-target signal is produced in absence of chemical modification or labeling. Using the aptamer-based FSA method, coupled with the CI, we screened aptamer probes by simply mixing and reading the magnitude of the interferometric signal. Label-free, solution-phase operation provided rapid selection of "the best-in-class" probe for the target in the matrix of interest. Once selected, the binding affinity of the probes were determined to estimate performance. Here aptamer K_D values for the best performing aptamers ranged from 16.1 ± 4.4

nM to 41.6 ± 8.3 nM allowing quantification of the target, GB acid or VX acid, at the level of 31 pg/mL (224 pM) and 29 pg/mL (231 pM) respectively in 25% serum. Cross-species selectivity for both serum assays was determined rapidly, by again using a mix-and-read screen. Response from the screens reported off-target, or interfering, signals well below the limit of quantification (LOQ) of the assay for the binding to the best-in-class aptamer probe. As such, the off-target concentration would need to be more than a thousand times higher than the target to produce quantifiable inaccuracy at the LOQ, and this is not the case.

Methods

Aptamer selection: All OPNA acid aptamers were selected by Base Pair Biotechnologies, Inc. (Pearland, TX, USA). Briefly, 2-aminoethyl monophosphonate (2-AEMP, Sigma Aldrich cat. SML0706) was covalently coupled through its primary amine group to aldehyde functionalized agarose resin (ThermoFisher Aminolink™ coupling resin, cat. 20381) using the manufacturer's recommended protocol for coupling and mild reduction using cyanoborohydride. A proprietary library of approximately 10^{15} unique natural DHA sequences were utilized for aptamer selection. Following three rounds of selection against the immobilized 2-AEMP, in the 4th round, we: 1) again applied the binding population of aptamers to the ligand-beads, 2) washed away weakly bound DHA species, and 3) subsequently split the pool of beads into two groups and offered one of the specific nerve agent metabolites in free solution as an elution agent and collected the resulting aptamer pool released from the beads. The eluted pools were then amplified by PCR, and the second, 5'-phosphorylated strand was digested away using lambda exonuclease. The resulting single stranded pools were then recombined for the next round of exposure to the 2-AEMP beads followed by specific elution using either VX- or GB-acid. This process of split-and-pool SELEX was repeated for 14 rounds. All binding and wash steps were performed in 1X PBS, 1% BSA, 1 mM $MgCl_2$, 0.02% baker's yeast tRNA, and 0.5% Tween-20. In the 4th round and onward, decreasing concentrations of the free target molecule were offered to obtain the tightest binders. After 14 rounds, the enriched aptamer pools were labeled with unique barcodes via PCR and sequenced using an Ion Torrent PGM next-generation sequencer (Thermo Fisher). For each target, bioinformatics analysis was used to choose aptamers for synthesis and functional screening in the described assay.

Aptamer preparation: The stock aptamers were reconstituted from the dried pellet to a concentration of 100 µM in a modified Phosphate Buffered Saline (PBS) containing 1 mM $MgCl_2$, 10 mM Tris HCl, and 0.1 mM EDTA with pH 7.5. All further dilutions used this PBS formulation. The stock aptamer solution was then diluted to 2 µM (the "Working Concentration") in PBS. Once diluted to the working concentration, the aptamers were refolded by heating the solution to 90°C for 5 minutes in a water bath, then cooled to room temperature for 15 minutes. This process ensures the aptamers were in their desired conformation following lyophilizing and shipping.

OPNA acid target solution preparation: Ethyl methylphosphonate (VX acid) with a molecular weight of 124.08 g/mol and density of 1.172 g/mL (9.4 M/L) was obtained from Synquest Laboratories (98% pure) in liquid form. A stock solution of 100 mM was prepared by diluting 10.59 µL into 989.41 µL of PBS. Isopropyl methylphosphonate (GB acid) with a molecular weight of 138.10 g/mol and density of 1.087 g/mL (7.87 M/L) was obtained from Sigma-Aldrich (98% pure) in liquid form. A stock solution of 100 mM GB acid was prepared by diluting 12.7 µL in 987.3 µL of PBS.

Aptamer Screening: Aptamers were screened in 25% pooled human serum / 75% buffer using the FSA method to determine the signal produced by the aptamers upon binding to the target. The pooled human serum used in this work was acquired from a commercial source and did not meet the definition of human subjects as specified in 45-CFR 46.102 (f). Six aptamers were screened for GB acid and five aptamers were screened for VX acid. The screen was performed by measuring the FSA signal for a high concentration of OPNA acid (500 nM) in the absence and presence of the aptamer at a concentration of 100 nM. These solutions were prepared by first diluting the stock aptamers 1:100 in PBS to obtain a 1 µM solution and diluting the OPNA metabolite targets 1:250,000 in PBS to obtain a 400 nM solution. The 400 nM OPNA solution was diluted in 100% pooled human serum to produce a 50% serum / 50 % PBS solution containing 200 nM of OPNA acid target. The 2 µM aptamer solution was diluted 1:2 in PBS to obtain a 1 µM aptamer solution. Then, 50 µL of the 200 nM OPNA acid solution was mixed with 50 µL of the 1 µM aptamer solution to obtain 100 µL of 500 nM aptamer + 100 nM OPNA acid to provide the binding sample. The reference sample was prepared by adding 50 µL of the 1 µM aptamer solution to 50 µL of a 50% serum / 50% PBS solution with no OPNA acid target. Following a 30-minute equilibration at room temperature, the phase shift between binding and reference solutions for each aptamer was measured using CI. Additionally, to correct for the potential contribution of

background to the signal from the OPNA acid target in the absence of binding, the phase shift between 100 nM OPNA acid and a blank 25% serum / 75% PBS solution was measured and subtracted from the aptamer-binding phase shift measurements.

Affinity Characterization: Binding affinity assays were performed in an end-point format as described previously [159]. To prepare affinity measurements in 25% serum / 75% PBS, a 7-point, 1:2 serial dilution of OPNA acid target was created in 50% serum / 50% PBS with concentrations ranging from 2000-31.25 nM (for VX203), with a 0 nM solution prepared containing only 50% serum / 50% PBS. A 400 nM aptamer solution was prepared by diluting the 2 µM working concentration 1:5 in PBS. Then 20 µL of each OPNA acid concentration was combined with 20 µL of the aptamer solution to create the binding sample. 20 µL of each OPNA acid concentration was combined with 20 µL of blank 50% serum / 50% PBS to create the reference sample. This resulted in binding and reference samples with final OPNA acid concentrations ranging from 1000-15.6 nM and a 0 nM concentration, and an aptamer concentration of 200 nM in the binding samples only with no aptamer in the reference samples, in 25% serum. The samples were allowed to incubate at room temperature for 1 hour, then the phase shift between each concentration's reference and sample was measured. The resulting phase shift, averaged over five replicates, was plotted vs. target concentration. The 0 nM concentration sample, containing only the aptamer, compared to the reference solution (no aptamer or target) provides a measure of the background signal contribution due to the aptamer and is subtracted from all concentrations. Dissociation constants were then calculated by fitting the data to a single-site saturation isotherm using Graphpad Prism™ according to the equation:

$$y = \frac{B_{max} \cdot X}{K_D + X} \qquad \textbf{Eq 5.1}$$

Cross Reactivity: To assess specificity, the best performing aptamer for each target was tested for its binding to the other targets. For example, the aptamer for GB acid was tested for non-specific binding to aptamers selected for VX acid, and vice versa. This determination was performed in 25% serum using a similar procedure to the screening experiments. Here we quantified the response for the interactions for both the target and off-target OPNA acid at 0 and 1000 nM, when incubated with the respective 500 nM aptamer.

LOQ Determinations and Unknown Quantification: Calibration curves were constructed in 25% serum / 75% PBS in a similar manner to the affinity determinations with the

goal of determining the assay analytical figures of merit. A 9-point, 2:1 serial dilution was prepared in 50% serum / 50% PBS ranging from 20 nM to 0.08 nM, with two additional concentrations at 100 and 200 nM, and a zero concentration with no OPNA acid target. The aptamer was prepared at a 1000 nM concentration in PBS. Then 20 µL of each OPNA acid concentration was combined with 20 µL of the aptamer solution to create the binding sample, and 20 µL of each OPNA acid concentration was combined with 20 µL of blank 50% serum / 50% PBS to create the reference sample. This resulted in 12 sample-reference pairs with concentrations ranging from 100 to 0 nM of the OPNA acid target, with 500 nM aptamer in the binding sample and no aptamer in the reference.

Test "unknowns" were prepared by spiking serum with a known concentration of the OPNA acid target, diluting to 50% serum in PBS, then combining equal amounts with a 1000 nM aptamer in PBS solution to serve as the binding sample and blank PBS to serve as reference. This resulted in a 25% serum solution with 500 nM aptamer in the binding sample and no aptamer in the reference.

The phase shift between sample and reference was fitted to the calibration curve to recover the concentration of spiked OPNA acid target.

Results & Discussion

Aptamer Screening: The ideal probe for a quantitative interaction assay would; 1) produce a large, reproducible signal, 2) have a high affinity to its target, and 3) exhibit little or no off-target interactions that could result in false-positive signals. One of the advantages of FSA over techniques such as ELISA is that probe-target performance can be evaluated quite rapidly using a mix-and-read screening approach. This approach is illustrated in **Fig 5.1**, showing how a single serum sample is split into two 10 µL aliquots, with one aliquot being combined with the probe aptamer at high concentration and the other aliquot combined with a refractive index-matched, non-binding control solution. Following a short incubation period, the FSA signal is quantified by measuring the binding sample and reference sample simultaneously in the compensated interferometer. Since FSA is matrix independent these screening determinations can be performed by simply quantifying the signal and signal/noise for a number of candidate probes in the desired milieu.

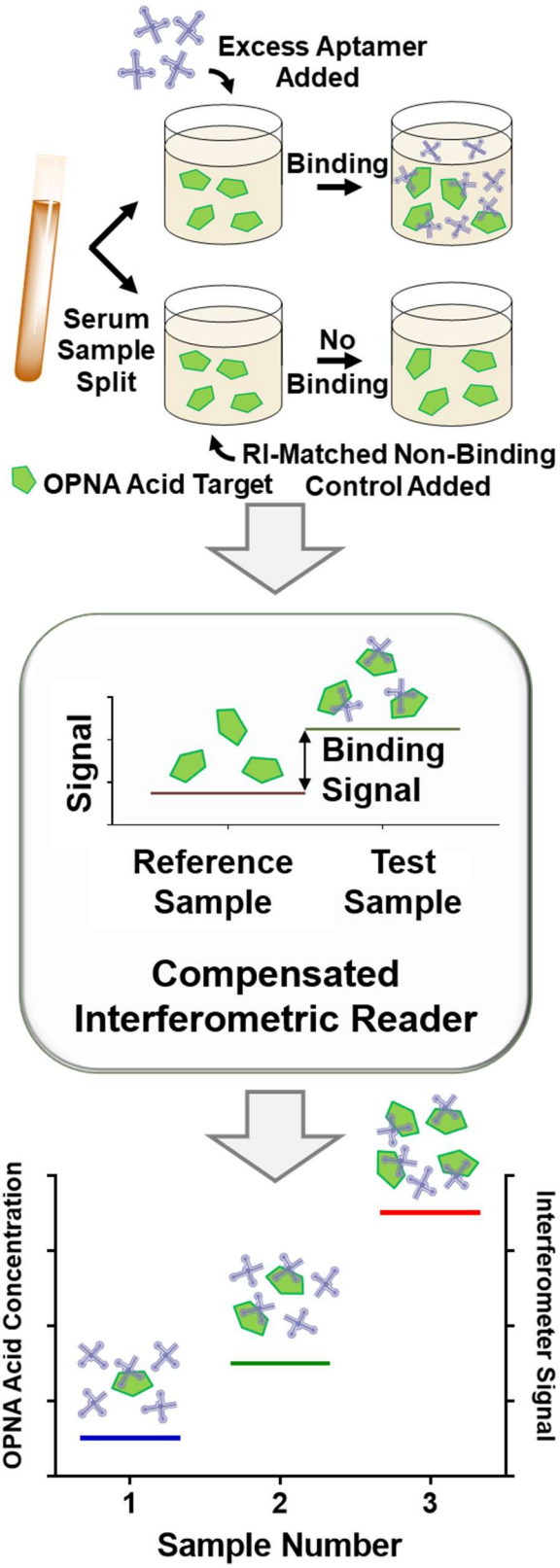

Fig. 5.1. The free solution assay (FSA) method

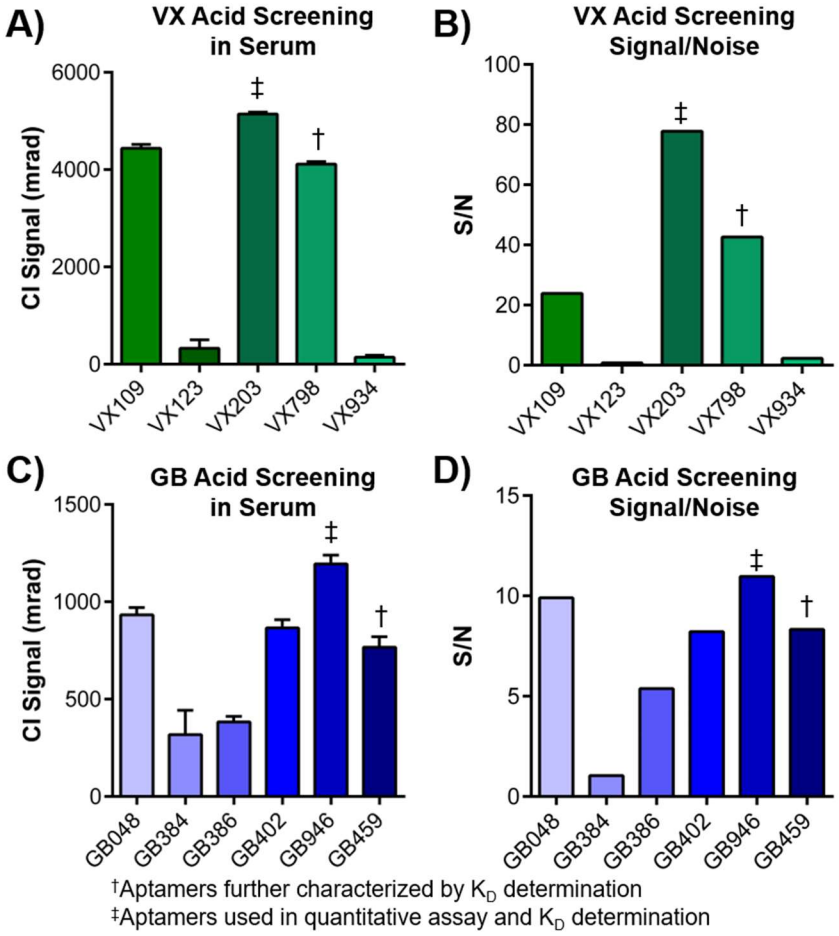

Fig. 5.2. Screening results in serum for 11 aptamers. **A**) CI signal and **B**) signal-to-noise for VX acid binding to five aptamers. **C**) CI signal and **D**) signal-to-noise for GB acid binding to six aptamers.

Figure 5.2 illustrates the results of the FSA-CIR screening experiments for our aptamer probes. Here a large concentration of the OPNA acid target (100 nM) was incubated with 500 nM of each aptamer in 25% serum (the binding sample), and 100 nM of the OPNA acid target was incubated with the 25% serum solution (the reference sample). This experiment is rapid, taking approximately 30 minutes to complete, including sample preparation, incubation and CI analysis times. From this simple approach we were able to identify which of the aptamer probes displayed the largest signal for each OPNA acid target. Hence, in less than an afternoon we were able to select the two most attractive aptamer-probe candidates for each OPNA acid target, from 11 starting species. In this way, our FSA method allowed for rapid identification of the best aptamer candidates for further investigation.

As illustrated in **Fig 5.2A and B** the best performing aptamers for VX acid were VX203 and VX798 (internal nomenclature), providing CI signals of 5143 ± 66 and 4113 ± 97 mrad, respectively. Screening results for the aptamers selected against GB acid are presented in **Fig 5.2C and D**. Here the highest screening signal (best candidates) were the GB946 and GB459 aptamers, with FSA-CI assay reporting signals of 1194 ± 107 mrad and 767 ± 92 mrad, respectively. Since FSA is a molecular interaction assay that measures conformation and hydration changes (solution molecular polarizability) [91], we have found that noise in the measurement (background) can vary with structure and solution-phase properties, including rearrangement and self-association. Therefore, to ensure we have selected the best candidates to move forward in our assay, we determined the S/N for each of the screening results (**Fig 5.2B** and **D**). When considering whether to use VX798 or V×109, the S/N provided an invaluable indicator of performance. While both aptamers gave similar absolute CI signals (4112 vs 4436 mrad), VX798 provided nearly double the S/N (42 vs 24) over V×109 so it was selected as the secondary candidate probe for further analysis. The GB acid aptamer screening produced one distinct frontrunner, both in terms of CI signal and S/N, the GB946 species. Yet several other aptamers (GB048, 402, and 459) looked promising during screening. In this case, a S/N determination did not produce a clear choice for the second GB acid aptamer to advance for further testing. Here we chose to advance the aptamer GB459 for further characterization because screening and S/N analysis in urine showed GB459 to be the most promising candidate (data not shown).

Aptamer Affinity Determinations: To ensure the aptamer probes exhibit high affinity, a property related to selectivity, we performed saturation isotherm binding assays. These measurements also provide insight as to the potential value of the assays in the context of target quantification. The saturation isotherms for each of the two best aptamer candidates, for each of the OPNA acid targets enabled binding affinity, K_D, to the ligand (OPNA acid) to be quantified. Our assay method has been used widely for K_D determinations [86, 167], consists of holding the aptamer concentration fixed at a value near the assumed K_D, and measures the binding signal of the OPNA acid to the aptamer as a function of concentration. As shown in **Fig 5.3,** aptamer OPNA acid affinity measurements all yielded $R^2 > 0.9$ and affinity values with K_Ds all in the nanomolar range. Specifically, the VX203 aptamer yielded a K_D of 35.1 ± 9.5 nM (**Fig 5.3A**), while the alternate aptamer probe (VX798) gave a K_D of 41.6 ± 8.3 nM (**Fig 5.3B)** both determined in 25% serum. From these two candidates, VX203 was selected as the probe for quantitative

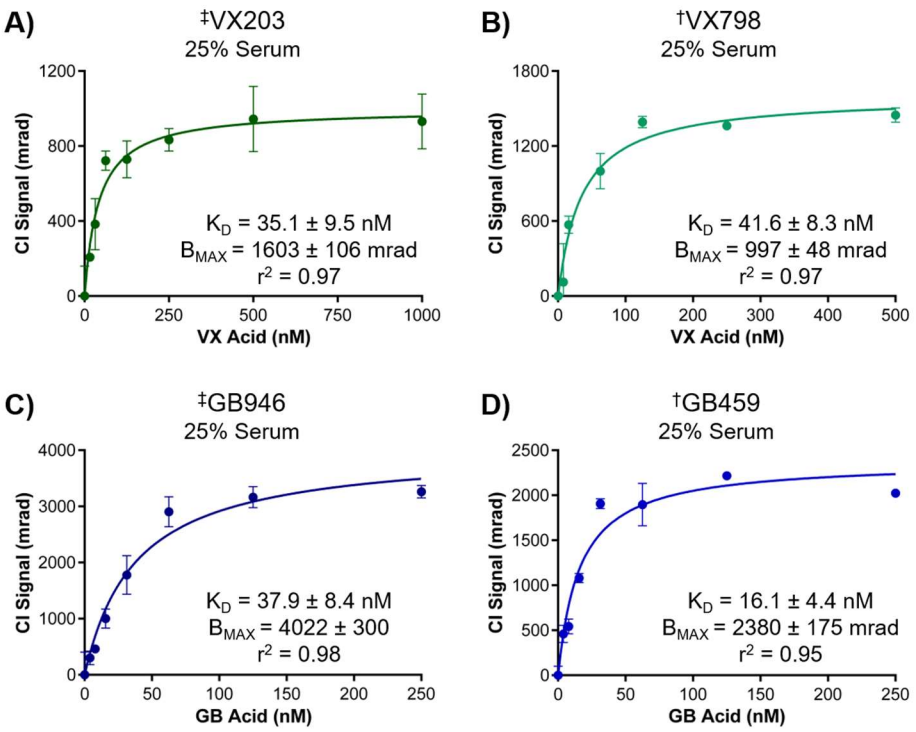

Fig. 5.3. Binding affinities in serum. Saturation isotherm for VX Acid binding the aptamer VX203 **A**) and the aptamer VX798 **B**) in serum. Binding affinity saturation isotherm for GB Acid binding the aptamer GB946 **C**) and the aptamer GB459 **D**) in serum.

assays on the merit of its larger signal and higher affinity (lower K_D). Evaluation of the GB aptamer candidates yielded affinities of 37.9 ± 8.4 nM (R^2 = 0.98) for GB946 (**Fig 5.3C**) and 16.1 ± 4.4 nM (R^2 = 0.95) for GB459 (**Fig 5.3D**). With both candidates yielding affinities in the 10's of nanomolar, GB946 was selected as the probe aptamer due to its larger signal (4022 mrad vs 2380 mrad). Results of these binding affinity measurements indicate that we have identified two excellent candidates upon which we can develop a high-quality serum assay for the VX and GB acids. Based on previous experience [158] and as shown below, candidate probes that have affinity values in the low nanomolar range often produce assays with pM or pg/mL sensitivity with good selectivity.

To confirm this hypothesis, we constructed calibration curves for the top two contenders for each target and then evaluated the assay performance with two unknowns to determine preliminary quantitative performance. **Figure 5.4** presents the result of these calibration investigations, illustrating that the FSA-CI assays provide excellent performance. Specifically, the LOQs, calculated as 3×standard deviation of replicate determinations/(calibration curve slope),

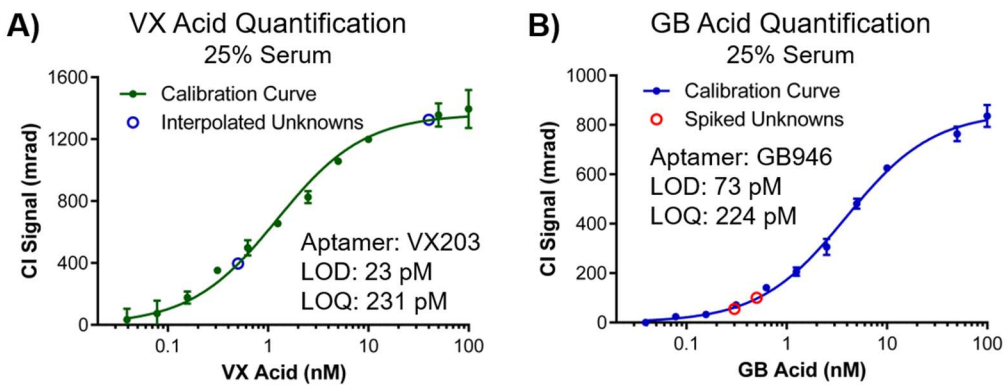

Fig. 5.4. Calibration curves for VX (A) and GB (B) acid quantification.

were determined to be 231 pM (29 pg/mL) and 224 pM (31 pg/mL) for the quantification of VX acid and GB acid respectively. Limits of detection (LODs), calculated as 3×instrument baseline standard deviation over 5-seconds/(calibration curve slope), of 23 pM (3 pg/mL) and 73 pM (10 pg/mL) for the targets in 25% serum. Our two-step, mix-and-read assay provides a dynamic range of ~2.5 orders of magnitude and requires just 10 µL of serum to perform the assay with >5 replicates per concentration for the standards and unknown sample. By comparison, the most widely used techniques for high-sensitivity OPNA exposure confirmation are based on mass spectrometric detection of OPNA acids [168-169], adducts to tyrosine [170], or BChE [171-172]. The protein adduct methods report a range of LODs from 18-97 pg/mL for tyrosine adducts to 350-4,000 pg/mL for BChE adducts. The LC-MS/MS LODs of OPNA acids in serum were previously reported as 400 pg/mL for GB acid and 500 pg/mL for VX acid from 50 µL lysed blood, serum, and plasma specimens. By comparison, we were able to quantify GB acid from 10 µL of serum at 30 pg/mL and avoided the protein precipitation, digestion, or extraction steps of the LC-MS/MS methods used above. Conventional LC-MS/MS quantification of OPNA acids and protein adducts remains an attractive option for confirmatory testing; however, the method described here yields a more than 130-fold improvement in sensitivity with a LOD of 2.9 pg/mL to current LC-MS/MS measurements of OPNA acids, at a fifth of the sample volume and without the need for time-consuming sample extraction steps or costly and bulky laboratory equipment.

As part of assay development, we tested "unknown" determination accuracy. Two test unknowns were prepared for each target using spiked blank serum. This data is overlaid upon the calibration curves (open circles) in **Fig 5.4** and shows recovery with an average error in the

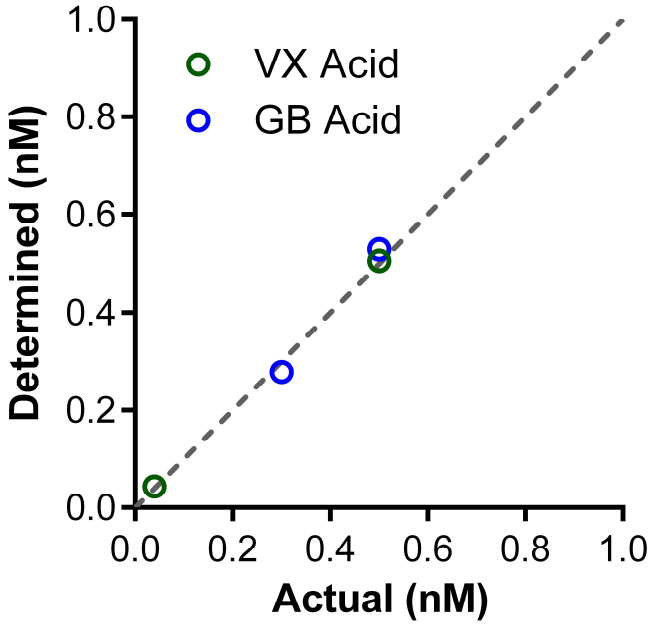

Fig. 5.5. "Unknown" quantification using the best-in-class aptamer provides high accuracy determinations.

determination of less than 6% (**Table 5.1**). More notably, when plotting the spiked concentration versus the determined concentration, as shown in **Fig 5.5**, the determined concentrations lie upon a straight line ($R^2 > 0.99$).

Finally, we performed screening assays to evaluate the specificity of the aptamer probes. In this experiment, we incubated the two top performing aptamers for each target with a high concentration of both targets (1000 nM). The results of these determinations are presented in **Figure 5.6**, which illustrates that for our two best aptamers, VX203 and GB946, the level of cross-reactivity is low. Specifically, VX203 and GB946 produced a signal at or below the LOQ for their respective off-targets (LOQ determined from **Fig 5.4**). Even the 2nd best performing aptamers produced a signal near the LOQ of the respective off-target quantification assay. For example, the LOQ for the VX assay was determined to be 231 pM, corresponding to a CI signal of 215 mrad. However, the 2nd best GB acid aptamer produced a signal of -487 mrad when incubated with the high concentration (1000 nM) of VX acid. Even if only considering the absolute magnitude of the signal, GB459 produced a signal only twice the VX acid assay LOQ despite a VX acid concentration of 4300 times higher than the LOQ. If both GB and VX acids were present in a

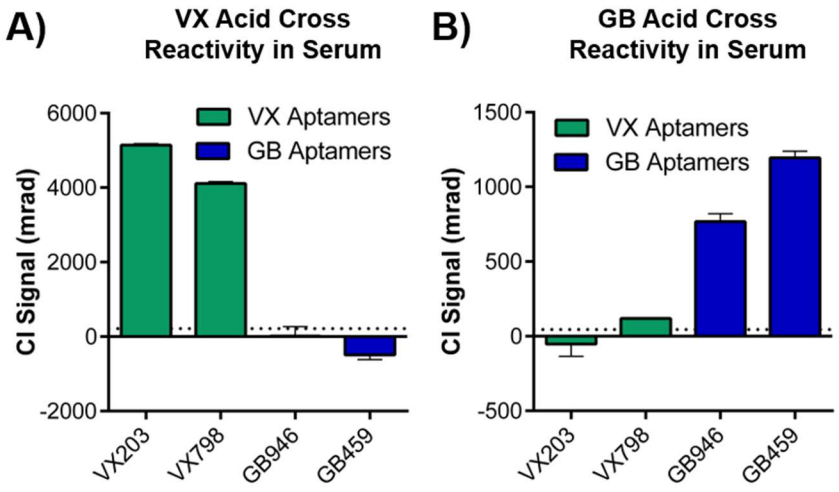

Fig. 5.6. Cross reactivity measurements tested the signal resulting from the best performing aptamers selected for both species incubated with VX acid (**A**) and GB acid (**B**).

sample at the concentration of the LOQ (231 pM), the presence of GB acid would only introduce an error of 9.5% in the quantification of VX acid. An additional metric of specificity uniquely available from the FSA method is signal directionality. In other words, when the GB acid aptamer binds VX acid, the result is a negative signal.

Likewise, the 2nd best aptamer for VX acid, VX798, produced a signal of 120 mrad when incubated with GB acid. The LOQ for the GB acid assay was determined to be 224 pM, which corresponded to a CI signal of 52 mrad. For a GB acid concentration of 4500 times the concentration of the VX acid LOQ, the VX acid aptamer only produced a signal equivalent to twice that of the GB acid LOQ. If both targets were present in equal concentration at the LOQ (224 pM), the presence of GB acid would result in a 9.9% error to the VX acid quantification.

These cross-reactivity results suggest that candidate probe aptamers would correctly report which nerve agent is present. As illustrated in **Fig 5.7**, VX acid and GB acid share remarkably

Table 5.1 Quantification of unknowns (values in pM)

Target	Spiked Concentration	Determined Concentration*	Error
VX Acid	500	506 ± 29	1%
VX Acid	40	43.6 ± 19	9%
GB Acid	300	279 ± 39	7%
GB Acid	500	530 ± 16	6%

*Average ± standard deviation of 6 replicates

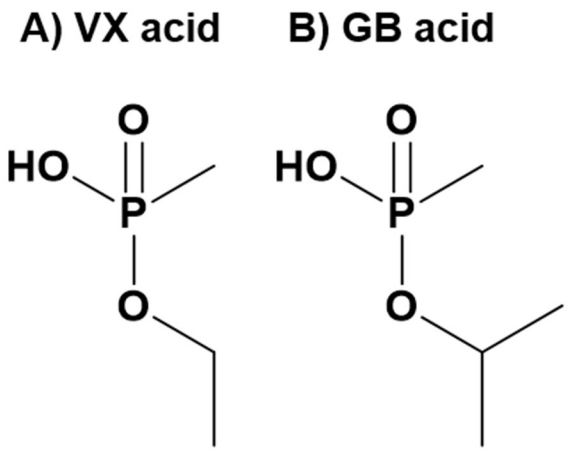

Fig. 5.7. Chemical structures of **A**) VX acid and **B**) GB acid.

similar chemical structures, differing by just one methyl group on the non-polar carbon chain. Given the size of the molecules and their structural similarity, the specificity of the aptamer probes (**Fig 5.6**) are even more noteworthy. There is a remote chance that the aptamer could interact with a different contaminant in the serum but given the magnitude of the K_D values and the outcome of the cross-reactivity experiments, the likelihood of this producing a quantifiable signal that leads to a false positive is minimal.

Chapter 5 Conclusion

FSA's mix-and-read format, combined with CI's simplicity, low cost, small size, low energy consumption, and high level of environmental compensation paves the way for the potential to develop a field deployable platform for diagnosing exposure to chemical warfare agents. Capitalizing on the unique transduction mechanism in FSA coupled with aptamer probes, we developed quantitative assays for VX acid and GB acid using CI that are more sensitive and considerably less complex than existing laboratory-based assays. The advantages of the FSA methodology using aptamers are the freedom from surface immobilization or aptamer probe labeling. Therefore, the aptamers can be employed in their native form, maximizing the FSA signal, while retaining their binding affinity and specificity to their target. Here we demonstrated the capability to rapidly develop quantitative assays for two important small molecule targets, the OPNA metabolites GB acid and VX acid. This work serves as an innovative first step toward a field deployable device that can identify the specific OPNA used at quantifiable levels, lower costs, greater sensitivity, and smaller sample volumes.

53. Luka, Z.; Moss, F.; Loukachevitch, L. V.; Bornhop, D. J.; Wagner, C., Histone Demethylase LSD1 Is a Folate-Binding Protein. *Biochemistry-Us* **2011,** *50* (21), 4750-4756.
86. Kussrow, A.; Enders, C. S.; Bornhop, D. J., Interferometric Methods for Label-Free Molecular Interaction Studies. *Analytical chemistry* **2012,** *84* (2), 779-792.
91. Bornhop, D. J.; Kammer, M. N.; Kussrow, A.; Flowers, R. A., 2nd; Meiler, J., Origin and prediction of free-solution interaction studies performed label-free. *Proc Natl Acad Sci USA* **2016,** *113* (12), E1595-1604.
123. Mayor, A., *Greek fire, poison arrows, and scorpion bombs : biological and chemical warfare in the ancient world*. 1st ed.; Overlook Duckworth: Woodstock, 2003; p 319 p.
124. Vucinic, S.; Antonijevic, B.; Tsatsakis, A. M.; Vassilopoulou, L.; Docea, A. O., et al., Environmental exposure to organophosphorus nerve agents. *Environmental Toxicology and Pharmacology* **2017,** *56*, 163-171.
125. Wiener, S. W.; Hoffman, R. S., Nerve Agents: A Comprehensive Review. *Journal of Intensive Care Medicine* **2004,** *19* (1), 22-37.
126. Holstege, C. P.; Kirk, M.; Sidell, F. R., CHEMICAL WARFARE: Nerve Agent Poisoning. *Critical Care Clinics* **1997,** *13* (4), 923-942.
127. Kyle, B. O., Aum Shinrikyo: Once and Future Threat? *Emerging Infectious Disease journal* **1999,** *5* (4), 413.
128. Rosman, Y.; Eisenkraft, A.; Milk, N.; et al., Lessons learned from the syrian sarin attack: Evaluation of a clinical syndrome through social media. *Annals of Internal Medicine* **2014,** *160* (9), 644-648.
129. Stone, R., U.K. attack puts nerve agent in the spotlight. *Science* **2018,** *359* (6382), 1314-1315.
130. A., B. M.; A., B. K., Review of health consequences from high-, intermediate- and low-level exposure to organophosphorus nerve agents. *Journal of Applied Toxicology* **1998,** *18* (6), 393-408.
131. Mangas, I.; Estevez, J.; Vilanova, E.; França, T. C. C., New insights on molecular interactions of organophosphorus pesticides with esterases. *Toxicology* **2017,** *376*, 30-43.
132. Talabani, J. M.; Ali, A. I.; Kadir, A. M.; Rashid, R.; Samin, F., et al., Long-term health effects of chemical warfare agents on children following a single heavy exposure. *Human & Experimental Toxicology* **2017,** *37* (8), 836-847.
133. Salvi, R. M.; Lara, D. R.; Ghisolfi, E. S.; Portela, L. V.; Dias, R. D., et al., Neuropsychiatric Evaluation in Subjects Chronically Exposed to Organophosphate Pesticides. *Toxicological Sciences* **2003,** *72* (2), 267-271.
134. Ray, D. E.; Richards, P. G., The potential for toxic effects of chronic, low-dose exposure to organophosphates. *Toxicology Letters* **2001,** *120* (1), 343-351.
135. Bowman, P. D.; Schuschereba, S. T.; Johnson, T. W.; Woo, F. J.; McKinney, L., et al., Myopathic changes in diaphragm of rats fed pyridostigmine bromide subchronically. *Fundamental and Applied Toxicology* **1989,** *13* (1), 110-117.
136. Baker, D. J.; Sedgwick, E. M., Single fibre electromyographic changes in man after organophosphate exposure. *Human & Experimental Toxicology* **1996,** *15* (5), 369-375.
137. Dési, I.; Nagymajtényi, L., Electrophysiological biomarkers of an organophosphorous pesticide, dichlorvos. *Toxicology Letters* **1999,** *107* (1), 55-64.
138. Hulse, E. J.; Davies, J. O. J.; Simpson, A. J.; Sciuto, A. M.; Eddleston, M., Respiratory Complications of Organophosphorus Nerve Agent and Insecticide Poisoning. Implications for

Respiratory and Critical Care. *American Journal of Respiratory and Critical Care Medicine* **2014,** *190* (12), 1342-1354.
139. Phillips, K. F.; Deshpande, L. S., Repeated low-dose organophosphate DFP exposure leads to the development of depression and cognitive impairment in a rat model of Gulf War Illness. *NeuroToxicology* **2016,** *52*, 127-133.
140. Gunnell, D.; Eddleston, M.; Phillips, M. R.; Konradsen, F., The global distribution of fatal pesticide self-poisoning: Systematic review. *BMC Public Health* **2007,** *7* (1), 357.
141. Ellison, D. H., *Handbook of chemical and biological warfare agents*. 2nd ed.; CRC Press: Boca Raton, 2008; p xxxv, 762 p.
142. Bloch-Shilderman, E.; Rabinovitz, I.; Egoz, I.; Yacov, G.; Allon, N., et al., Determining a threshold sub-acute dose leading to minimal physiological alterations following prolonged exposure to the nerve agent VX in rats. *Archives of toxicology.* **2018,** *92* (2), 873,892.
143. Viveros, L.; Paliwal, S.; McCrae, D.; Wild, J.; Simonian, A., A fluorescence-based biosensor for the detection of organophosphate pesticides and chemical warfare agents. *Sensors and Actuators B: Chemical* **2006,** *115* (1), 150-157.
144. Walton, I.; Davis, M.; Munro, L.; Catalano, V. J.; Cragg, P. J., et al., A Fluorescent Dipyrrinone Oxime for the Detection of Pesticides and Other Organophosphates. *Organic Letters* **2012,** *14* (11), 2686-2689.
145. Du, D.; Wang, J.; Wang, L.; Lu, D.; Smith, J. N., et al., Magnetic Electrochemical Sensing Platform for Biomonitoring of Exposure to Organophosphorus Pesticides and Nerve Agents Based on Simultaneous Measurement of Total Enzyme Amount and Enzyme Activity. *Analytical chemistry* **2011,** *83* (10), 3770-3777.
146. Wang, D.; Zhao, Q.; Zoysa, R. S. S. d.; Guan, X., Detection of nerve agent hydrolytes in an engineered nanopore. *Sensors and Actuators B: Chemical* **2009,** *139* (2), 440-446.
147. Funari, R.; Della Ventura, B.; Schiavo, L.; Esposito, R.; Altucci, C., et al., Detection of Parathion Pesticide by Quartz Crystal Microbalance Functionalized with UV-Activated Antibodies. *Analytical chemistry* **2013,** *85* (13), 6392-6397.
148. Zourob, M.; Simonian, A.; Wild, J.; Mohr, S.; Fan, X., et al., Optical leaky waveguide biosensors for the detection of organophosphorus pesticides. *The Analyst* **2007,** *132* (2), 114-120.
149. Knaack, J. S.; Zhou, Y.; Abney, C. W.; Jacob, J. T.; Prezioso, S. M., et al., A High-Throughput Diagnostic Method for Measuring Human Exposure to Organophosphorus Nerve Agents. *Analytical chemistry* **2012,** *84* (21), 9470-9477.
150. No, H.-Y.; Kim, Y. A.; Lee, Y. T.; Lee, H.-S., Cholinesterase-based dipstick assay for the detection of organophosphate and carbamate pesticides. *Anal Chim Acta* **2007,** *594* (1), 37-43.
151. Apilux, A.; Isarankura-Na-Ayudhya, C.; Tantimongcolwat, T.; Prachayasittikul, V., Paper-based acetylcholinesterase inhibition assay combining a wet system for organophosphate and carbamate pesticides detection. *EXCLI Journal* **2015,** *14*, 307-319.
152. Rajapakse, B. N.; Thiermann, H.; Eyer, P.; Worek, F.; Bowe, S. J., et al., Evaluation of the Test-mate ChE (Cholinesterase) Field Kit in Acute Organophosphorus Poisoning. *Annals of Emergency Medicine* **2011,** *58* (6), 559-564.e556.
153. Ellman, G. L.; Courtney, K. D.; Andres, V.; Featherstone, R. M., A new and rapid colorimetric determination of acetylcholinesterase activity. *Biochemical Pharmacology* **1961,** *7* (2), 88-95.

154. Mishra, R. K.; Hubble, L. J.; Martin, A.; Kumar, R.; Barfidokht, A., et al., Wearable Flexible and Stretchable Glove Biosensor for On-Site Detection of Organophosphorus Chemical Threats. *ACS sensors* **2017,** *2* (4), 553-561.
155. Kammer, M. N.; Kussrow, A. K.; Olmsted, I. R.; Bornhop, D. J., A Highly Compensated Interferometer for Biochemical Analysis. *ACS sensors* **2018**.
156. Tiefenbrunn, T.; Forli, S.; Baksh, M. M.; Chang, M. W.; Happer, M., et al., Small Molecule Regulation of Protein Conformation by Binding in the Flap of HIV Protease. *ACS chemical biology* **2013,** *8* (6), 1223-1231.
157. Wang, M. M.; Kussrow, A. K.; Ocana, M. F.; Chabot, J. R.; Lepsy, C. S., et al., Physiologically relevant binding affinity quantification of monoclonal antibody PF-00547659 to mucosal addressin cell adhesion molecule for in vitro in vivo correlation. *British Journal of Pharmacology* **2017,** *174* (1), 70-81.
158. Olmsted, I. R.; Hassanein, M.; Kussrow, A.; Hoeksema, M.; Li, M., et al., Toward Rapid, High Sensitivity, Volume-Constrained Biomarker Quantification and Validation using Backscattering Interferometry. *Analytical chemistry* **2014,** *in press*.
159. Kammer, M. N.; Olmsted, I. R.; Kussrow, A. K.; Morris, M. J.; Jackson, G. W., et al., Characterizing aptamer small molecule interactions with backscattering interferometry. *The Analyst* **2014,** *139* (22), 5879-5884.
160. Cho, E. J.; Lee, J. W.; Ellington, A. D., Applications of Aptamers as Sensors. *Annu Rev Anal Chem* **2009,** *2*, 241-264.
161. Kaur, G.; Roy, I., Therapeutic applications of aptamers. *Expert Opin Inv Drug* **2008,** *17* (1), 43-60.
162. Toulme, J. J.; Di Primo, C.; Boucard, D., Regulating eukaryotic gene expression with aptamers. *Febs Lett* **2004,** *567* (1), 55-62.
163. Chu, T. C.; Twu, K. Y.; Ellington, A. D.; Levy, M., Aptamer mediated siRNA delivery. *Nucleic Acids Res* **2006,** *34* (10).
164. Chu, T. C.; Marks, J. W.; Lavery, L. A.; Faulkner, S.; Rosenblum, M. G., et al., Aptamer : toxin conjugates that specifically target prostate tumor cells. *Cancer Res* **2006,** *66* (12), 5989-5992.
165. Chu, T. C.; Shieh, F.; Lavery, L. A.; Levy, M.; Richards-Kortum, R., et al., Labeling tumor cells with fluorescent nanocrystal-aptamer bioconjugates. *Biosens Bioelectron* **2006,** *21* (10), 1859-1866.
166. Cao, Z.; Tong, R.; Mishra, A.; Xu, W.; Wong, G. C., et al., Reversible cell-specific drug delivery with aptamer-functionalized liposomes. *Angewandte Chemie* **2009,** *48* (35), 6494-6498.
167. Kussrow, A.; Kaltgrad, E.; Wolfenden, M. L.; Cloninger, M. J.; Finn, M. G., et al., Measurement of monovalent and polyvalent carbohydrate-lectin binding by back-scattering interferometry. *Analytical chemistry* **2009,** *81* (12), 4889-4897.
168. Schulze, N. D.; Hamelin, E. I.; Winkeljohn, W. R.; Shaner, R. L.; Basden, B. J., et al., Evaluation of Multiple Blood Matrices for Assessment of Human Exposure to Nerve Agents. *J Anal Toxicol* **2016,** *40* (3), 229-235.
169. Hamelin, E. I.; Schulze, N. D.; Shaner, R. L.; Coleman, R. M.; Lawrence, R. J., et al., Quantitation of five organophosphorus nerve agent metabolites in serum using hydrophilic interaction liquid chromatography and tandem mass spectrometry. *Analytical and bioanalytical chemistry* **2014,** *406* (21), 5195-5202.

170. Crow, B. S.; Pantazides, B. G.; Quinones-Gonzalez, J.; Garton, J. W.; Carter, M. D., et al., Simultaneous Measurement of Tabun, Sarin, Soman, Cyclosarin, VR, VX, and VM Adducts to Tyrosine in Blood Products by Isotope Dilution UHPLC-MS/MS. *Analytical chemistry* **2014,** *86* (20), 10397-10405.
171. Carter, M. D.; Crow, B. S.; Pantazides, B. G.; Watson, C. M.; Thomas, J. D., et al., Direct Quantitation of Methyl Phosphonate Adducts to Human Serum Butyrylcholinesterase by Immunomagnetic-UHPLC-MS/MS. *Analytical chemistry* **2013,** *85* (22), 11106-11111.
172. Mathews, T. P.; Carter, M. D.; Johnson, D.; Isenberg, S. L.; Graham, L. A., et al., High-Confidence Qualitative Identification of Organophosphorus Nerve Agent Adducts to Human Butyrylcholinesterase. *Analytical chemistry* **2017,** *89* (3), 1955-1964.

Chapter 6: Quantitation of Opioids and the Prospect of Improved Diagnosis of Neonatal Abstinence Syndrome

Adapted from a manuscript in preparation

for submission to *Clinical Pharmacology & Therapeutics*

The United States is experiencing an opioid epidemic of unprecedented proportions, with ~100 Americans dying each day from an overdose, and an economic impact of ~$100B/year [173]. Newborns are innocent, yet frequently overlooked victims of this epidemic. Opioid use during pregnancy can result in addicted infants, who can suffer from Neonatal Abstinence Syndrome (NAS) [174]. This serious condition afflicts ~2% of all neonates born in the U.S. and is increasing rapidly [175]. It is not uncommon for newborns to be sent home with NAS, where they undergo withdrawal, exhibiting an inability to be comforted, continuous crying, difficulty breathing, diarrhea, fever, and seizures. Symptoms can intensify until treatment and if not diagnosed severe complications can arise. The unique pharmacokinetics in newborns, coupled with the limitations of existing assays, including poor sensitivity, complexity, long turnaround time, and lack of availability, points to a need for a non-invasive, rapid, sensitive and quantitative near-patient screening assay. As described here, the free-solution assay (FSA), performed on a novel benchtop reader, could address these limitations. The simplicity, high sensitivity, small urine volumes, and assay speed of our method can potentially expedite and extend clinical feedback and reach patients in birthing centers and the low resource hospitals in poor, rural communities that tend to be the loci of the opioid epidemic.

Accurately predicting which neonates have NAS is difficult, partly because expecting mothers often don't acknowledge their drug use and partly because testing is usually only performed after a newborn exhibits withdrawal symptoms (~36-48 hours after birth) [176]. While many insurers cover a 48-hour hospital stay for mothers and their infants allowing NAS to be detected, alternative birthing locations usually have shorter stays and reduced testing access.

Universal maternal testing could improve the identification of infants at risk for NAS [177], yet its success currently depends on access to Mass Spectrometry (MS) [178]. Since time to diagnosis is critical for clinical management of patients with NAS, the capability to accurately detect key analytes earlier and longer after birth could vastly improve care and clinical outcome. Varied metabolic rates in neonates further complicates therapeutic intervention for NAS and pain management, both best guided by testing [179], making rapid, quantitative clinical feedback a priority. We show here that the improved detection limits of aptamer-based FSA can both accelerate and extend the time needed to provide a quantitative measure of opioids in urine.

Urine is routinely collected during pregnancy and labor, and is a widely employed clinical matrix [180], making urine testing an attractive, non-invasive approach to opioid analysis. Yet, unhealthy or premature babies produce significantly less urine than the 1 mL/kg/hour produced in healthy newborns, increasing the time required to obtain a sufficient testing volume. Further, sample volume requirements (>100 µL) and time-to-results (24-48 hours, Mayo Clinic) make quantitative testing by LC-MS/MS less than optimal for patient management. The main alternatives to MS, the enzyme multiplied immunoassay technique (EMIT II) [181], or the cloned enzyme donor immunoassay (CEDIA) [182], are more rapid (1-2 hrs.), but still require 50-100 µL of urine and are not particularly sensitive or quantitiative (Table 1).

Here we report the specific opioid quantitation in 5 µL of urine, at the pg/mL level, by capitalizing on the marriage of three synergistic technologies; a unique label-free, solution-phase assay [91], high-affinity, high-selectivity DHA aptamers probes [159], and a recently developed compensated interferometer [183]. Our approach takes a total analysis time of ~1 hour, and depending on the target, provides opioid limits of quantification (LOQs) 5-275-fold better than LC/MS-MS and ~50-1000-fold better than EMIT or CEDIA.

Methods

The free solution assay method is shown pictorially in **Fig. 6.1** and has been described in detail elsewhere [91, 102]. Briefly the mix-and-read approach is based on preparing index matched solutions (splitting urine into two parts) and using one of these solutions as the reference and one as the binding sample for analysis by our interferometric reader.

Solution preparation is also described in detail in the SI, but consists of making stock aptamer and opioid solutions, either for binding assays or for target quantification. Aptamer

selection and characterization is described in detail in the SI, but briefly these opioid probes were selected using a modification of the Systematic evolution of ligands by exponential enrichment (SELEX) method of Nutiu et al [184]. This aptamer selection method is advantageous because it does not require immobilization of the target molecule and sequences binding the support matrix (beads) will not be further amplified. Reconstituting the aptamer from the dried pellet allowed a 100 µM stock solution to be prepared that was subsequently diluted to the working concentrations (**Table B.1**). To ensure the aptamers were in the desired conformation, the aptamers were refolded by heating the solution to 90°C for 5 minutes in a water bath, then cooled to room temperature for 15 minutes. For cross reactivity measurements (detailed in **Appendix B**), the stock aptamer solution was diluted to 2 µM before refolding.

Opiate target solution preparation followed normal analytical procedures described in detail in the SI. Briefly the six opioid targets and cortisol (Sigma-Aldrich) listed in **Table B.1** were obtained at 1 mg/ml (2.7 – 3.3 mM) in methanol. Working solutions of 27 - 32 µM (**Table B.1**, Column D) were prepared by diluting 10 µL of the opioid standard solution with 990 µL of PBS. Then the appropriate volume of the working solutions (**Table B.1**, Column E) were further diluted to give 200 nM opioid solutions. Care was taken to insure the 1% methanol in PBS solution was kept constant across all dilutions so that sample and reference solutions were index matched. The concentration of the target samples stayed below the 1 mM aqueous solubility limit. CIR calibration solutions consisted of glycerol solutions (0, 0.125, 0.25, 0.5, 1, and 2mM) dissolved in 50% urine / 50% PBS. PBS serves as the reference sample. Preparation of solutions used for aptamer affinity measurements, LOQ determinations for the opioid targets and the unknowns were all prepared as describe in the SI in 50% urine.

The CIR (Figure A.1) is described in detail in the SI. Briefly, the reader consists of a droplet generator, interferometer, and syringe pump. The interferometer is based on a laser, a fused silica capillary and a CCD camera. The laser – capillary interaction produces fringes that are directed onto the camera and proper windowing of the captured image using an in-house Labview™ program facilitates interrogation of adjacent regions of the capillary for differential comparison of sample and reference droplets. The positional shifts in the fringes within each of these two windows is proportional to molecular binding and is quantified by a fast Fourier transform (FFT) [185]. Droplet trains are generated directly in the capillary tube by a Mitos Dropix. The single section of capillary serves both as the reader cell and transfer line. The sample-

reference pairs were separated by a 40nL droplet of oil (Flourinert FC-40, Sigma-Aldrich). Prior to droplet train generation, the capillary was filled with PBS and the syringe pump operated at a flow rate of 10 μL/minute for 10 minutes to establish stable flow. Then the assay is run by introducing each sample/reference solution pair 5 times, followed by two PBS rinses of 4 μL. This process is repeated for each concentration, or unknown, completing a full dropix sample tray. An entire run requires ~14 minutes. Prior to the analysis of the next dropix sample tray the capillary tube is rinsed thoroughly with PBS. Glycerol calibration confirmed CIR performance with the desired values of; a) response ~0.110 radians/mM glycerol, b) injection reproducibility ~0.012 radians c) an LOQ of ~0.33 mM glycerol calculated as 3×(□□of 5 replicate measurements) / (slope).

Isothermal end-point binding affinity assays were performed on 1 nM solutions of the respective aptamer (to the opioid) in 50% Urine / 50% PBS, with a 7-point serial dilution series of the opioids ranging from 50 – 0.780 nM in the same matrix. The reference solution consisted of the same concentration of opioid (50 - 0.780 nM) incubated with a 50 % Urine / 50% PBS solution devoid of aptamer. Dissociation constants were quantified by performing 5 replicates at each opioid concentration, plotting the results (**Figure 6.3A and B.1**) and fitting the data to a single-site saturation isotherm using Graphpad Prism™. Further details of these determinations are found in the SI.

As described in detail in the SI, calibration curves for the opioid assays were obtained by creating a dilution series of the target at 0-100 nM in 50% Urine / 49.5% PBS / 0.5% Methanol with 1 nM aptamer, an RI matched reference and performing FSA-CIR analysis. The phase shift between binding and reference sample was measured using the CIR, and the response was fit with a saturation isotherm. The slope in the linear region was used to calculate the LOD (3×σ instrument baseline noise/slope) and the LOQ (3×σ (of replicate determinations)/slope). **Figure 6.3B and B.2** show the assay calibration curves for all 6 opioid targets.

Test “unknowns” were prepared by spiking blank human urine with the opioid target and performing the FSA measurement as described above and in the SI. Unknowns were prepared so that the “operator” remained blinded to the sample’s true concentration until after the determination was completed.

Aptamer specificity (cross-reactivity) was tested for each aptamer against their most common metabolite and cortisol. We performed cross-reactivity as described in detail in the SI,

briefly, high concentration solutions (2000 nM) of the target opioid, the metabolite, and cortisol were prepared in 50% Urine / 49%PBS / 1% methanol allowing the subsequent preparing of 1000 nM, 500 nM, and 0 nM solutions to be made. These were reacted with the target aptamer at 1000 nM aptamer in 50% Urine / 50% PBS and then assayed by CIR in an endpoint format.

Pharmacokinetic Modelling

Oxycodone and noroxycodone concentration-time profiles were calculated using a single-metabolite model where the primary opiate is eliminated via two pathways: 1) directly through urine excretion and 2) by metabolism to a single metabolite (**Figure B.7**). To calculate the urine concentration of oxycodone, it is necessary to first determine the serum concentration over time. Then the serum concentration is multiplied by the fraction eliminated through urine (f_r) and the renal clearance rate (CL_r) to obtain the urine elimination rate. The urine elimination rate is then divided by the total urine excretion rate (volume/hour), to obtain the urine concentration. A similar process is used to find the noroxycodone urine concentration,. The noroxycodone serum concentration was calculated using the oxycodone serum concentration and the fraction of oxycodone metabolized to noroxycodone.

The plasma concentration of oxycodone over time was calculated using a first-order decay, **equation 6.1** [186].

$$C(t) = ICe^{-kt} \qquad \textbf{Eq. 6.1}$$

Where *IC* is the initial concentration and *k* is the elimination rate constant. We chose two cases in our calculations for the initial concentration (IC). 1) The recommended analgesic doses (25 ng/mL [187] and 120 ng/mL [188]) for a newborn, and 2) a high concentration induced by illicit opiate use by the mother (300 ng/ml and the 2000 ng/ml) [189].

Equation 6.2 was used to determine *k* from the drug's half-life ($t_{1/2}$), an experimentally determined parameter.

$$k = \frac{ln(2)}{t_{1/2}} \qquad \textbf{Eq. 6.2}$$

The work of Valitalo *et-al* reported that the half-life of oxycodone in healthy neonates is about 4 hours, but can reach 8.8 hours in extremely preterm neonates [187]. For healthy newborns,

the half-life matures to about 2.1 hours, approximately the value in healthy adults, within the first 3-6 months of life [187].

Urine concentration of oxycodone: As illustrated in **Figure B.7** the urine oxycodone concentration is found by estimating the fraction (f_m) of oxycodone metabolized to noroxycodone and assuming the remaining oxycodone (f_r) is found (excreted) in the urine. The *rate* of oxycodone elimination through urine (dC_u/dt) is therefore dependent upon the plasma concentration (C) and the renal clearance (CL_r), and can expressed by **Equation 6.3**:

$$\frac{dC_u(t)}{dt} = f_r \cdot CL_r \cdot C(t) \qquad \textbf{Eq. 6.3}$$

The fraction of opioid eliminated through urine (not metabolized) is typically 5-11% in adults [190], but higher values have been reported for neonates [187, 191]. Because we did not consider other metabolites, for our calculations $f_r + f_m = 1$. Here we chose to use values of $f_m = 0.8$ and $f_r = 0.2$ based upon the published values for neonatal metabolite profiles [192]. Here it should be noted that very few reports exist that quantify neonate metabolite profiles or renal clearance (CL_r), and results are highly variable [191, 193-196]. We chose a value of 10 mL/min/kg because this represents an average value for (CL_r) [192, 197]. For subject weight we used 2 kg for a preterm neonate, 3.5 kg for a full-term neonate, and 7.2 kg for a 6 month old child [198]. Using these values provided an effective opioid renal clearance of 20 mL/min for a preterm neonate, 35 mL/min for a full-term neonate, and 72 mL/min for a 6-month-old.

We obtained the urine concentration of oxycodone over time by dividing the oxycodone elimination rate (Equation 4) by the rate of urine production. We used urine production rates of 0.5 mL/hr for a preterm neonate and 1 mL/hr for the full-term neonate and a child of age 6 months [199].

The serum concentration of noroxycodone (Cm) is dependent upon the rate of oxycodone metabolism and the rate of noroxycodone elimination in urine, which can be mathematically expressed as **equation 6.4**:

$$C_m(t) = f_m \frac{k \cdot IC}{k_m - k}(e^{-kt} - e^{-k_m t}) \qquad \textbf{Eq. 6.4}$$

As in **equation 6.2**, k is the elimination rate constant of oxycodone and IC is the initial oxycodone serum concentration. The metabolite has a half-life ($t_{m1/2}$) and extinction coefficient

(k_m). The limited available data on neonatal opioid metabolite half-lives suggests that $t_{1/2} \approx t_{\frac{m1}{2}}$ [187, 192]. Therefore, our calculations assumed k_m=k [197, 200].

The rate of noroxycodone elimination (the metabolite) in urine ($dC_{mu}(t)/dt$) was calculated **using Equation 6.4** in the same way it as for oxycodone, with appropriate parameters for CL_{mr} and f_{mr}. In healthy adults, a small fraction of noroxycodone is eliminated through metabolism to noroxymorphone. However, in the only published results of oxymorphone/noroxymorphone quantification in neonates, the concentration of both species was below the limit of quantification in many infants [192]. Therefore, we used $f_{mr} = 1$ (all noroxycodone is eliminated through urine, none is metabolized further). The value for renal clearance of primary drug was used as the renal clearance for noroxycodone ($CL_r = CL_{mr}$), due to the same observations that led us to use k_m=k [187, 192, 197, 200]. We calculated the urine concentration of noroxycodone over time in the same manner as we calculated the urine concentration of oxycodone over time, by dividing the rate of noroxycodone elimination by the rate of urine production.

Aptamer selection using SELEX

All opioid aptamers were selected by Base Pair Biotechnologies, Inc. (Pearland, TX, USA) using a modification of the method of Nutiu et al [184]. Briefly, random sequences in a single-stranded DHA library were hybridized to complementary DHA capture probes immobilized on magnetic beads. Sequences that interact with the target resulting in a structural change were released from the beads and thereby separated from non-binders. This aptamer selection method is advantageous because it does not require immobilization of the target molecule and sequences binding the support matrix (beads) will not be further amplified. Additionally, off-targets and/or background sample matrix can be applied to release non-specifically binding aptamers before elution using the desired target of interest. To avoid the potential risk for opioid contamination in "normal" pooled human urine, an ersatz urine formulation comprising 1X PBS, 300 mM urea, 6 mM creatinine, 0.05% Tween-20, and 1 mM $MgCl_2$ was used. After multiple rounds of positive and negative selection, the enriched aptamer pools were sequenced using an Ion Torrent PGM next generation sequencer (Thermo Fisher), and for each target, bioinformatics analysis was used to choose aptamers for synthesis and functional screening in the FSA assay.

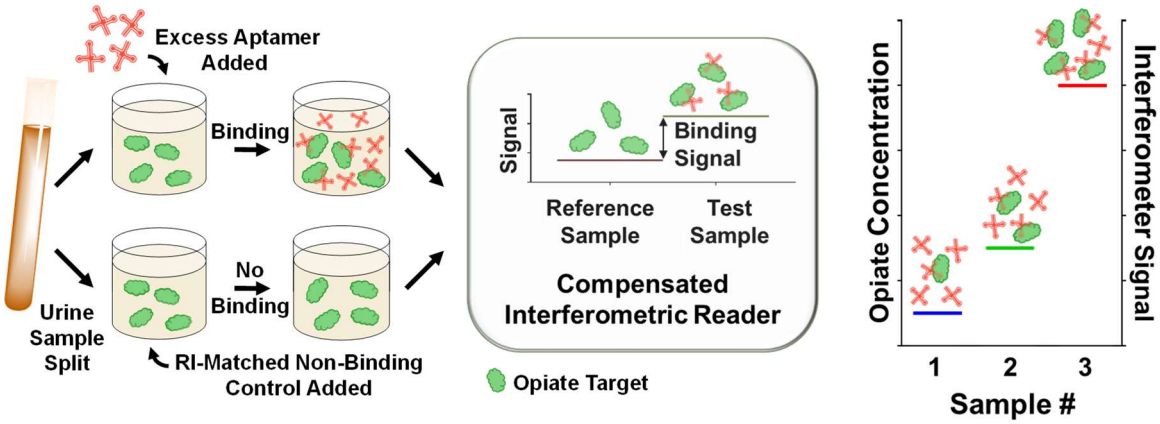

Fig. 6.1. Schematic of the free-solution assay (FSA) method.

Results and Discussion

Urine opioid quantification was accomplished using FSA, which is a universal sensing method based on measuring the predictable and reproducible binding-induced changes in the solution refractive index (RI)[91]. Complex milieu compatibility in the FSA mix-and-read approach is facilitated by performing the measurement on 'matched' sample-reference pairs and then comparing the signal for this pair of samples. As shown in **Figure 6.1** we take a small volume of urine, split into two aliquots and then process them to provide 'binding' and 'reference' solutions. To quantify a target, we add an excess of probe (DHA aptamer) to one of the aliquots, giving the "binding/test" sample, and to the other we add an RI matching solution (buffer) or "reference/control." Assay/instrument calibration solutions are prepared by first spiking blank urine with increasing concentrations of the opiate target, then splitting this sample into two aliquots and proceeding as described here and in **Appendix B**. These solutions are allowed to equilibrate and then introduced into adjacent wells of the droplet generator for analysis by the reader as pairs separated by an oil droplet. The difference in signal between sample–reference pairs provides a quantitative measure of target (e.g. concentration of aptamer-target complex), while allowing the matrix signal to be nullified. Since the probe is used in large excess relative to the target μM vs. nM) for quantification experiments, the RI signal due to the aptamer is essentially constant can be ignored.

The compensated interferometric reader (CIR), reported here for the first time, incorporates the compensated interferometer [183] and is shown to provide improvements in both speed and

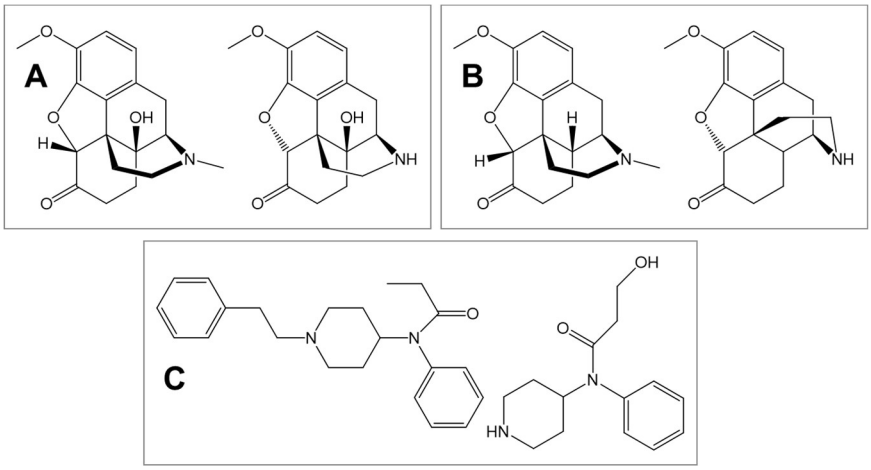

Fig. 6.2. Structures for target molecules: **A**) Oxycodone (left) and its major urinary metabolite, noroxycodone (right). **B**) Hydrocodone (left) and major urinary metabolite, norhydrocodone (right). **C**) Fentanyl (left) and its major urinary metabolite, norfentanyl (right).

signal-to-noise (S/N) over previous sensors [10]. The CIR described in detail in the SI, is a relatively simple device consisting of a sample introduction method (a commercial droplet generator (Mitos Dropix, Dolomite Microfluidics, UK), a diode laser (Lasermate, USA), a capillary flow cell (Polymicro, Molex, USA), a camera (Basler avA2300 2D CCD array, USA), and syringe pump (Figure 5.1 and B.5). In CIR an expanded laser beam illuminates the long axis of the capillary, producing elongated fringes that shift in proportion to the solution RI, which is proportional to analyte concentration. The simultaneous analysis of sample-reference pairs of 1.0 µL droplets separated by a 40 nL oil droplet in an uninterrupted fluid-droplet-train, speeds analysis time substantially over previous FSA measurement [201], while also conserving sample. Using a continuous section of fused silica capillary (250 µM ID×350 µM OD) as both the droplet train transfer line and the detector cell for the interferometer, and the appropriate settings for the droplet generator and syringe pump we were able to analyze 18 sample pairs in less than a total of 1 hour.

Our research also capitalizes on the value of employing DNA aptamer probe molecules for opioids in urine, by avoiding many of the issues associated with detecting small molecules by antibodies [159, 202]. DNA aptamers are advantageous because they can be made to bind with high selectively to small molecule targets, they don't require a cold train for storage/transport, are easily 'manufactured' using standard nucleic acid methods and can be selected in the matrix of interest (urine in our case) [184]. The aptamers selected here for the six opioid targets are

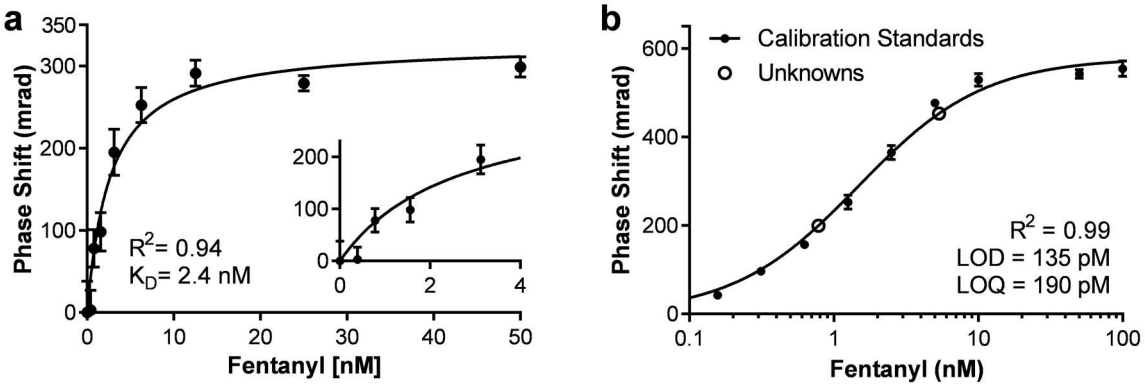

Fig. 6.3. A) Fentanyl aptamer K_D determination giving an affinity of 2.44 nM and $R^2 = 0.94$. Error bars show standard deviation of 7 replicates. **B**) Calibration curve for fentanyl.

displayed in **Figure 6.2**, were obtained using a combination of a multiplex version of "structure-switching" systematic evolution of ligands by exponential enrichment (SELEX) [203-204]. This version of SELEX is unique in the ability to minimize undesirable sequences through negative selection, providing improved target-binding selectivity. Once identified and prior to FSA-CIR testing, candidate aptamers were sequenced and modeled to provide a preliminary indication of how they might perform in our assay.

With aptamer candidates in hand, FSA-CIR was used to quantify the binding affinity to their cognate targets. **Figure 6.3A** displays a typical saturation isotherm obtained by our methodology for a fentanyl aptamer. These K_D determinations were performed in 50% urine/50% phosphate buffered saline (PBS) using the end-point assay described here, previously [91, 159], and in **Appendix B**. The quantification of the aptamer affinity provides an insight into opioid detection sensitivity. Constructing the assay such that the binding sample consists of urine solutions containing increasing concentrations of the target opioid (0-50 nM, e.g. ligand) with 1 nM aptamer (e.g. receptor) and reference solutions consisting of the individual opioid-containing urine/PBS solutions index matched and devoid of aptamer, enabled quantification of K_D. As illustrated in **Figure 6.3A**, based on seven replicate determinations by CIR for each sample-reference pair, results for affinity measurements are robust and reproducible. From these determinations we obtained high-quality dissociation constants upon fitting the binding curves to a single-site saturation isotherm using GraphPad Prism™. In all cases the aptamer probes had an affinity in the hundreds of picomolar to low-nanomolar range (**Table B.2**), with the K_D for fentanyl

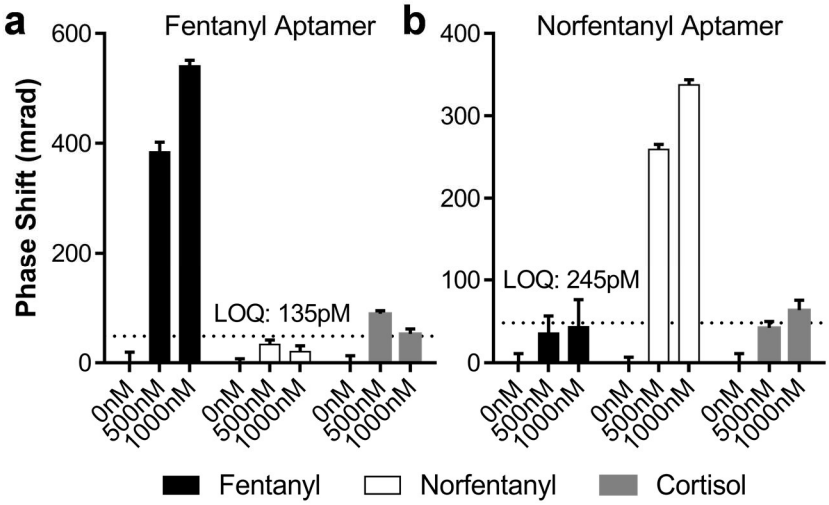

Fig. 6.4. Fentanyl and norfentanyl cross reactivity results. High specificity aptamers result in off target signals below the assay LOQ.

= 2.48 nM, norfentanyl = 0.93 nM, oxycodone = 0.66 nM, noroxycodone = 1.33 nM, hydrocodone = 4.49 nM and norhydrocodone = 0.72 nM. As shown below, K_D values in this range enable a mix-and-read approach using a single probe, as opposed to the typical sandwich method used in ELISA, that provides pg/mL sensitivity and excellent specificity for the target in urine.

Next, we determined the limits of detection (LODs) and LOQs for all of our opiate-aptamer assays. Here we define the LOD as 3×σ (5 sec. baseline noise)/(slope of the calibration curve) and the LOQ as 3×(σ for replicates)/slope. **Figure 6.3B** illustrates a typical calibration curve obtained by FSA-aptamer-CIR for an opioid in 50% urine (**Figure B.4**). When fitting the fentanyl calibration curve to a single-site saturation isotherm, we obtain a correlation coefficient, $R^2 = 0.99$, an LOD of 45 pg/mL (135 pM) and a dynamic operating range of ~2.5 orders of magnitude in concentration. As shown in **Table B.2**, all our opioid assays performed similarly to that for fentanyl, giving LODs ranging from ~28-81 pg/mL (90-245 pM) and LOQ's of 44-183 pg/ml (141-611 pM). The fentanyl assay is particularly important due to its recent explosion in use and abuse in the USA. The LOQ of 63 pg/mL for this assay is at least 5-fold better than the best value reported for the more time-consuming and complex LC-MS/MS assay [192].

Assay performance, regardless of methodology, can be impacted by undesirable off-target response [205-207]. Aptamer-based assays are no exception, with cross reactivity to non-target

species and matrix components a potential problem. First, outstanding LOQ values obtained here in urine, the lack of concentration dependent response for the matrix (data not shown) and the advantage of direct sample-reference comparison, indicates there is little matrix non-specific binding. Second, we focused on quantifying the level of cross-reactivity of the aptamer to its cognate target(s), the primary drug-metabolite, as well as the common biological signaling molecule cortisol. Cortisol was chosen because its widely found in urine, neonate levels have been correlated with opiate exposure and it is a known marker of stress [208]. Using FSA, we established the expected signal for samples containing large concentrations of the target, e.g. fentanyl, etc. (0 nM, 500 nM, and 1000 nM). Next, we quantified the signal urine from two interfering species spiked in ~100% urine, first from the most common metabolite, norfentanyl in this case, and next cortisol. In all assays we used 1000 nM of the 'target' aptamer. Here, the large concentration of the aptamer contributes measurably to the signal (bulk RI of the solution), therefore we zero CIR by subtracting this aptamer background signal. **Figure 6.4** illustrates the results of several target and off-target binding experiments. Notably, even at quite high concentration of the interfering species, all aptamer assays performed well, exhibiting off-target binding ranging from 0.03% to ~13% (**Table B.2**, **Figure B.3**). With 'cross-reactivity' signal magnitudes near or below the LOQ for the assay (**Figure B.3**), the *off-target* species concentration would need to be 4,000-10,000 times higher than the *target* concentration to introduce quantifiable inaccuracy into the LOQ. Here the norfentanyl aptamer exhibited the most undesired cross-reactivity, 12.9% for fentanyl. In this case it might be valuable to measure the ratio of target-to-metabolite in the clinical setting to correct for off-site binding. We acknowledge that to fully implement this assay clinically and predict potential false positives, it will be necessary to establish the magnitude of off-target binding for numerous other species. Yet, given the affinity of our aptamers and results for cortisol, we are confident that our multiple target assay will prove to be highly specific.

At the time of this research true clinical samples were not available from our collaborator, therefore we prepared spiked urine "unknowns." This was accomplished by adding the opioid targets to pooled human urine (Valley Biomedical) at concentrations between 250 pg/mL and 4 ng/mL (**Figure B.4**). Using the appropriate calibration curve for each target and the FSA-CIR measurement performed blinded by the operator from the unknown, we obtain concentrations for these test samples (**Table B.4**). Plotting these values versus the actual 'spiked' concentrations for

all assays results in a linear plot (R^2 = 0.996, **Figure B.4**). In all cases the assay provided quantification of the unknown target concentration with less than 6% error (**Tables B.2** & **B.3**). Interestingly, all unknowns evaluated here are 75-1000-fold below the standard clinical cut-off of 300 ng/ml [209], or 500-8000-fold below the Substance Abuse and Mental Health Services Administration (SAMHSA) drug-testing cut-off of 2000 ng/ml [210].

Table 6.1 shows that the aptamer-based FSA-CIR assay performed quite well compared to other methods. While gas chromatography has been used in the past, it has mostly given way to immunoassays for screening and LC-MS/MS for analyte confirmation/quantification. FSA-CIR is akin to immunoassay, in that it could be used as a screening tool, yet our free-solution method exhibits many differences, most important is that it is quantitative. EMIT® II Plus (Siemens) is qualitative or at best semi-quantitative (+/- 1.5 ng/mL) for opioid determinations. The Product Insert reports cut-offs in the 2-50 ng/ml range, and a very small 'quantitative' operating range of 5-20 ng/mL. CEDIA® (Thermo Scientific), has similar performance to the EMIT II Plus (CEDIA Product Insert). The aptamer-based FSA-CIR method is 50-1000-fold more sensitive than commercial immunoassays (**Table 6.1**) and is quantitative over about 2.5 decades. **Table 6.1** also illustrates that compared to LC-MS/MS methods, with LOQs of 10-50 ng/ml for hydrocodone, oxycodone, noroxycodone and Norhydrocodone [211] in urine, FSA LOQs in the pg/mL range are 1-3 *decades* more sensitive than LC-MS/MS. Even for the best MS-based assay reported [178], aptamer-based FSA is still 2-5-fold and 15-20-fold more sensitive for fentanyl and norfentanyl respectively, while requiring 20 times less sample. MS-based assays do provide the ability to directly measure multiple analytes with high specificity (depending on spectrometer resolution), yet the instrumentation is complicated, costly and impractical for the near-patient setting. Results presented here indicates the aptamer-based FSA-CIR represents attractive alternative.

In addition to the advantages of small volume and simplicity available with FSA, enhanced sensitivity has the potential to speed time-to-result and extend detection time, allowing previously unavailable pharmacokinetics. While the pharmacokinetics of opiates in neonates varies considerably [192], recent work by Valitalo [187] provides parameters that allows us to place reasonable bounds on expected neonate opiate lifetimes. Using their parameters for drug half-life and oxycodone as a representative case, we calculated opioid concentration in urine over time for preterm and healthy neonates. **Figure 6.5A** shows that for a preterm neonate ($t_{1/2}$ = 8.8 hr) and a very large initial concentration (IC) of drug, corresponding to a positive test result for illicit drug

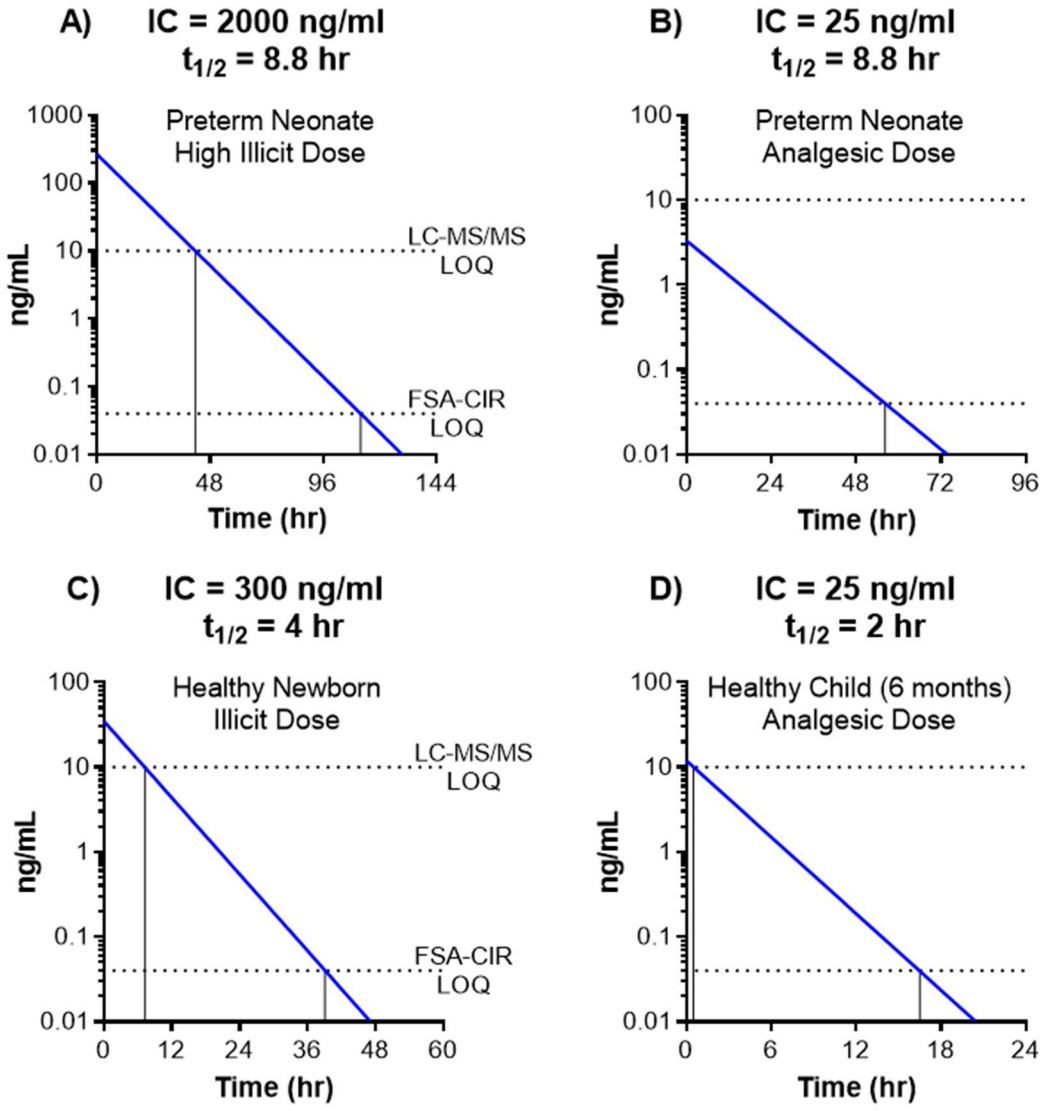

Fig. 6.5. Oxycodone concentration vs. time window in neonates for several representative cases, illustrating the increased time for detection that the lower LOQ of FSA-CIR provides over LC-MS/MS

use (2000 ng/ml), the presence of oxycodone would be unquantifiable after 43 hours by LC-MS/MS with an LOQ of 10 ng/mL. Yet, FSA-CIR, allows quantification of oxycodone for up to 112 hours following this level of opioid exposure, extending the detection window by nearly three days (70 hours). Assessing a more typical situation, for a recommended analgesic dose of 25 ng/ml in a preterm neonate, **Figure 6.5B** illustrates how the concentration of oxycodone never reaches

the LOQ for LC-MS/MS in urine. Currently, multiple blood draws are the only way to accurately detect this opiate under these conditions. However, with aptamer-based FSA-CIR, oxycodone urine levels are detectable for 56 hours, making urine analysis a viable option. In a full-term neonate ($t_{1/2}$ = 4 hr) exposed to an illicit level of 300 ng/ml, or a healthy child (age = 6 months, $t_{1/2}$ = 2 hr) exposed to an analgesic dose (25 ng/ml), **Figure 6.5C-D** show how improved LOQs can provide an extended period of 32 and 16 hours of accurate confirmatory testing to exposure as well as providing pain management feedback.

Measuring noroxycodone in neonates

Further addressing the pharmacokinetic variability found in young children, enhanced assay sensitivity and near-patient monitoring of the primary opioid metabolite could allow more accurate titration of analgesics. Using a simple model for metabolism (**Figure B.7**) [187], our and the LC-MS/MS LOQ values for noroxycodone, we construct plots that illustrate this opportunity. Based on an 80% fraction metabolized, our concentration vs. time plots (**Figure 6.6**) show several things.

In a neonate pain management setting, for safe and effective drug administration it would be desirable to have dose titration and monitoring on a case-by-case basis. Here we show that the improved sensitivity of our assay has the potential to accurately quantify both the primary opioid and its metabolites providing a vehicle toward the proper assessment of metabolic rates, and therefore administration, dosage and interval [195, 212].

To illustrate the value of improved LOQs for the target drug or metabolite we capitalized on our calculations to construct the concentration versus time plots shown in **Figure 6.6** for four representative pharmacokinetic cases. In **Fig. 6.6A** the urine concentration over time for both oxycodone (blue) and noroxycodone (red) for a *low analgesic dose* (25 ng/mL serum concentration) is presented for a preterm neonate using an oxycodone half-life of $t_{1/2}$ = 8.8. In this instance, the concentration of noroxycodone rises above the LOQ for FSA-CSI quickly, being detectable after a few minutes, but never rises above the LOQ of LC-MS/MS.

Using the recommended analgesic dose in a preterm neonate, (IC = 120 ng/mL serum concentration), produces the results shown in **Figure 6.6B**. Here the noroxycodone concentration does rise above the LOQ for LC-MS/MS, but only after 2.4 hours. Under this scenario, limited

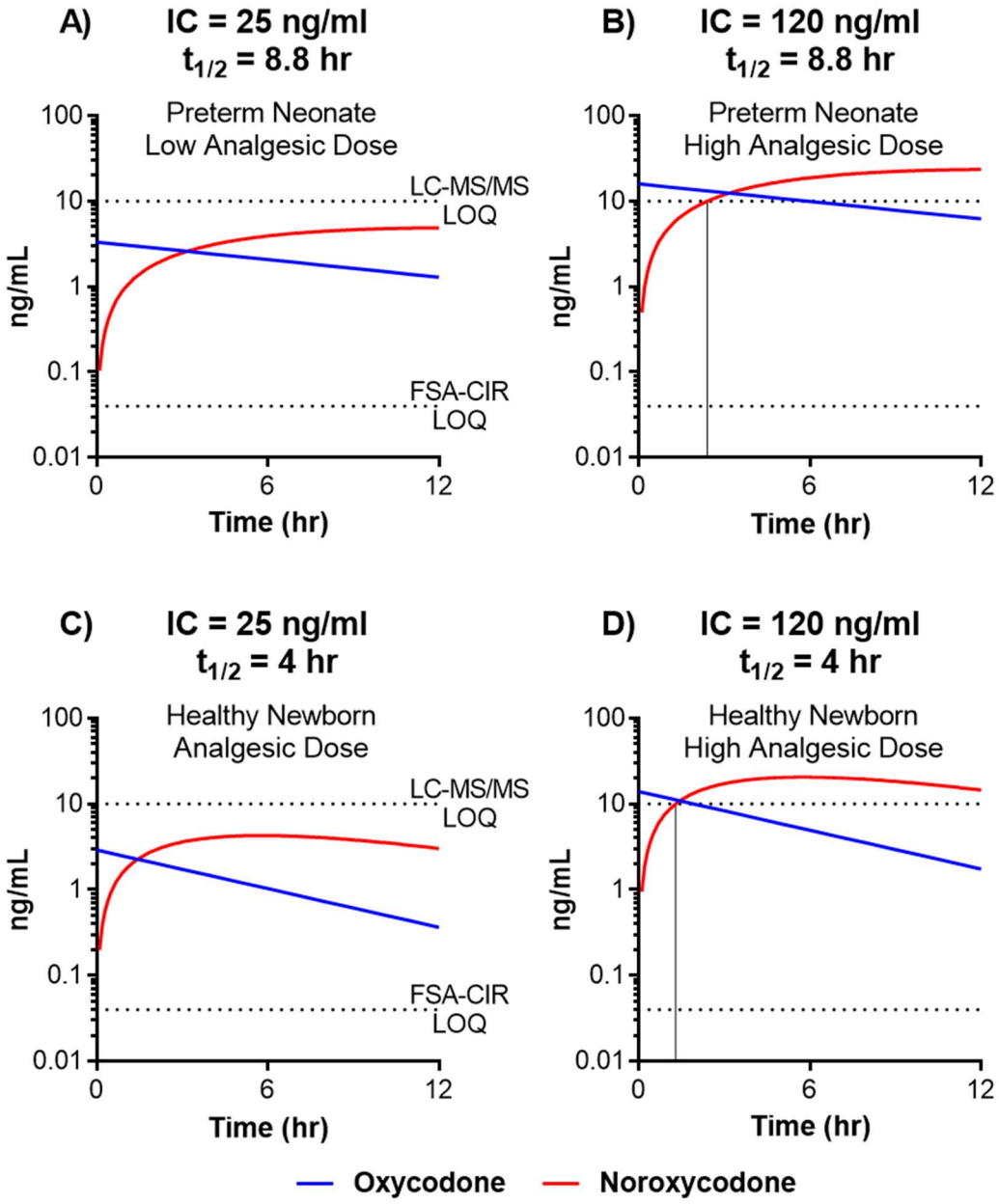

Fig. 6.6. Oxycodone and Noroxycodone urine concentrations over time for several cases. IC denotes the initial plasma concentration.

drug sensitivity provided by LC-MS/MS leads to an interval not fast enough to allow accurate feedback for proper drug dosing every couple of hours of a neonate undergoing pain management.

Full-term "healthy" newborns being administered an IC = 25 ng/mL (**Fig. 6.6C**) represents a similar case to that shown in **Fig 6.6A**. Again, for the lower dose of drug, neither the noroxycodone nor the oxycodone are at a concentration quantifiable by LC-MS/MS (**Fig. 6.6C**).

Yet, FSA-CIR would be able to quantify noroxycodone accurately after only a few minutes. For the higher dose of drug, IC = 120 ng/mL (**Fig. 6.6D**), the concentration of metabolite rises above the LC-MS/MS LOQ only after 1.3 hours. Further, the oxycodone level drops below the detection limit for MS/MS in this period of time. In both cases, for full-term infants, aptamer-based FSA-CIR can accurately quantify noroxycodone only a few minutes after administration. These LOQ comparisons illustrate how FSA can potentially provide a simple screen for earlier opiate detection, be used to extend the period of detection and enable the ability to quantify/identify opioids for a longer period after birth.

Results of our calculations, illustrated in **Fig. 6.6**, correlate with the results published by Kokki *et al.*, where they found oxycodone concentrations remained above ~10 ng/mL for ~1-3 hours in healthy children (age 6-91 months), following administration of a high analgesic dose. As for noroxycodone, when quantified at approximately 1 hour after administration, only in a few cases (4) was it was determined to above 10ng/ mL, yet in in the majority of cases it never surpassed 10 ng/mL [200].

Chapter 6 Conclusion

Here we demonstrate how improved sensitivity can positively impact both confirmatory testing of NAS and dose-titration for neonates undergoing pain management. Using a single-metabolite model for oxycodone metabolism and excretion, we put bounds on the expected range of lifetimes of both the drug and metabolite in plasma and the subsequent concentration in urine. For detection of exposure to illicit use, aptamer-based FSA-CIR enables an extended window for confirmatory testing between 2-4 days in neonates past the average onset time of NAS symptoms. By the time NAS symptoms have presented in neonates (48-72 hours), residual oxycodone concentration levels are too low for confirmation by LC-MS/MS. In the pain-management setting, aptamer-based FSA-CIR would enable quantification of metabolite after a shorter period and therefore provide more accurate information for dosing.

In conclusion, we report a small volume urine assay for oxycodone, hydrocodone, fentanyl, noroxycodone, norhydrocodone, and norfentanyl with excellent LODs and LOQs. The aptamer-based FSA-CIR approach, coupled with high affinity DHA aptamer probes represents a potential solution for the need to quantify opioids at high sensitivity, non-invasively on small sample volumes. The method reported here is rapid when compared to currently available methods and

exhibits accuracy of better than 95% across a wide range of opioid concentrations. Even with the use of a commercial droplet generator, a relatively low-cost system can be configured in a bench-top format, making it compatible with the near-patient setting. The simplicity of the reader and recent demonstration of temperature controller-independent operation [183], point to the potential for developing a hand-held digital reader. Enabled by highly selective aptamers, an understanding of the signal transduction mechanism for FSA, and the capability to predict signal magnitude using the molar refractometry [91], this novel technology has the promise to revolutionize near-patient screening in a variety of contexts, particularly for neonatal opioid quantification.

10. Bornhop, D. J.; Latham, J. C.; Kussrow, A.; Markov, D. A.; Jones, R. D., et al., Free-solution, label-free molecular interactions studied by back-scattering interferometry. *Science* **2007,** *317* (5845), 1732-1736.
91. Bornhop, D. J.; Kammer, M. N.; Kussrow, A.; Flowers, R. A., 2nd; Meiler, J., Origin and prediction of free-solution interaction studies performed label-free. *Proc Natl Acad Sci USA* **2016,** *113* (12), E1595-1604.
102. Baksh, M. M.; Kussrow, A. K.; Mileni, M.; Finn, M. G.; Bornhop, D. J., Label-free quantification of membrane-ligand interactions using backscattering interferometry. *Nature biotechnology* **2011,** *29* (4), 357-U173.
159. Kammer, M. N.; Olmsted, I. R.; Kussrow, A. K.; Morris, M. J.; Jackson, G. W., et al., Characterizing aptamer small molecule interactions with backscattering interferometry. *The Analyst* **2014,** *139* (22), 5879-5884.
173. Florence, C. S.; Zhou, C.; Luo, F.; Xu, L., The Economic Burden of Prescription Opioid Overdose, Abuse, and Dependence in the United States, 2013. *Medical care* **2016,** *54* (10), 901-906.
174. Pryor, J. R.; Maalouf, F. I.; Krans, E. E.; Schumacher, R. E.; Cooper, W. O., et al., The opioid epidemic and neonatal abstinence syndrome in the USA: a review of the continuum of care. *Archives of disease in childhood. Fetal and neonatal edition* **2017,** *102* (2), F183-F187.
175. Tolia, V. N.; Patrick, S. W.; Bennett, M. M.; Murthy, K.; Sousa, J., et al., Increasing incidence of the neonatal abstinence syndrome in U.S. neonatal ICUs. *The New England journal of medicine* **2015,** *372* (22), 2118-2126.
176. Wachman, E. M.; Schiff, D. M.; Silverstein, M., Neonatal Abstinence Syndrome: Advances in Diagnosis and Treatment. *Jama* **2018,** *319* (13), 1362-1374.
177. Wexelblatt, S. L.; Ward, L. P.; Torok, K.; Tisdale, E.; Meinzen-Derr, J. K., et al., Universal maternal drug testing in a high-prevalence region of prescription opiate abuse. *The Journal of pediatrics* **2015,** *166* (3), 582-586.
178. Eckart, K.; Rohrich, J.; Breitmeier, D.; Ferner, M.; Laufenberg-Feldmann, R., et al., Development of a new multi-analyte assay for the simultaneous detection of opioids in serum and other body fluids using liquid chromatography-tandem mass spectrometry. *J Chromatogr B* **2015,** *1001*, 1-8.
179. Aukes, D. I.; Roofthooft, D. W. E.; Simons, S. H. P.; Tibboel, D.; van Dijk, M., Pain Management in Neonatal Intensive Care: Evaluation of the Compliance With Guidelines. *The Clinical journal of pain* **2015,** *31* (9), 830-835.
180. Mundt, L. A.; Graff, L.; Shanahan, K., *Graff's textbook of routine urinalysis and body fluids*. 2nd ed.; Wolters Kluwer/Lippincott Williams & Wilkins Health: Philadelphia, 2011; p xxii, 330 p.
181. Luzzi, V. I.; Saunders, A. N.; Koenig, J. W.; Turk, J.; Lo, S. F., et al., Analytic performance of immunoassays for drugs of abuse below established cutoff values. *Clin Chem* **2004,** *50* (4), 717-722.
182. Kohler, K. M.; Hammer, R.; Riedy, K.; Auwarter, V.; Neukamm, M. A., Evaluation of CEDIA and DRI Drugs of Abuse Immunoassays for Urine Screening on a Thermo Indiko Plus Analyzer. *Journal of clinical laboratory analysis* **2017,** *31* (1).
183. Kammer, M. N.; Kussrow, A. K.; Bornhop, D. J., Longitudinal pixel averaging for improved compensation in backscattering interferometry. *Optics letters* **2018,** *43* (3), 482-485.

184. Nutiu, R.; Li, Y., In vitro selection of structure-switching signaling aptamers. *Angewandte Chemie* **2005,** *44* (7), 1061-1065.
185. Bornhop, D. J.; Kammer, M. N.; Kussrow, A.; Flowers, R. A., 2nd; Meiler, J., Origin and prediction of free-solution interaction studies performed label-free. *Proc Natl Acad Sci U S A* **2016,** *113* (12), E1595-1604.
186. Houston, J. B.; Taylor, G., Drug Metabolite Concentration-Time Profiles - Influence of Route of Drug Administration. *British journal of clinical pharmacology* **1984,** *17* (4), 385-394.
187. Valitalo, P.; Kokki, M.; Ranta, V. P.; Olkkola, K. T.; Hooker, A. C., et al., Maturation of Oxycodone Pharmacokinetics in Neonates and Infants: a Population Pharmacokinetic Model of Three Clinical Trials. *Pharm Res* **2017,** *34* (5), 1125-1133.
188. Pacifici, G. M., Metabolism and pharmacokinetics of morphine in neonates: A review. *Clinics* **2016,** *71* (8), 474-480.
189. Yazdy, M. M.; Desai, R. J.; Brogly, S. B., Prescription Opioids in Pregnancy and Birth Outcomes: A Review of the Literature. *Journal of pediatric genetics* **2015,** *4* (2), 56-70.
190. Poyhia, R.; Seppala, T.; Olkkola, K. T.; Kalso, E., The pharmacokinetics and metabolism of oxycodone after intramuscular and oral administration to healthy subjects. *British journal of clinical pharmacology* **1992,** *33* (6), 617-621.
191. Pokela, M. L.; Anttila, E.; Seppala, T.; Olkkola, K. T., Marked variation in oxycodone pharmacokinetics in infants. *Paediatric anaesthesia* **2005,** *15* (7), 560-565.
192. Kokki, M.; Heikkinen, M.; Valitalo, P.; Hautajarvi, H.; Hokkanen, J., et al., Maturation of oxycodone pharmacokinetics in neonates and infants: Oxycodone and its metabolites in plasma and urine. *British journal of clinical pharmacology* **2017,** *83* (4), 791-800.
193. Kart, T.; Christrup, L. L.; Rasmussen, M., Recommended use of morphine in neonates, infants and children based on a literature review .1. Pharmacokinetics. *Paediatric anaesthesia* **1997,** *7* (1), 5-11.
194. Encinas, E.; Calvo, R.; Lukas, J. C.; Vozmediano, V.; Rodriguez, M., et al., A predictive pharmacokinetic/pharmacodynamic model of fentanyl for analgesia/sedation in neonates based on a semi-physiologic approach. *Paediatric drugs* **2013,** *15* (3), 247-257.
195. Ku, L. C.; Smith, P. B., Dosing in neonates: special considerations in physiology and trial design. *Pediatric research* **2015,** *77* (1-1), 2-9.
196. Davis, P. J.; Stiller, R. L.; Cook, D. R.; Brandom, B. W.; Davin-Robinson, K. A., Pharmacokinetics of sufentanil in adolescent patients with chronic renal failure. *Anesthesia and analgesia* **1988,** *67* (3), 268-271.
197. Kokki, H.; Rasanen, I.; Reinikainen, M.; Suhonen, P.; Vanamo, K., et al., Pharmacokinetics of oxycodone after intravenous, buccal, intramuscular and gastric administration in children. *Clinical pharmacokinetics* **2004,** *43* (9), 613-622.
198. Pomerance, H. H., Nelson Textbook of Pediatrics. *Archives of pediatrics & adolescent medicine* **1997,** *151* (3), 324.
199. Jones, M. D., Jr.; Gresham, E. L.; Battaglia, F. C., Urinary flow rates and urea excretion rates in newborn infants. *Biology of the neonate* **1972,** *21* (5), 321-329.
200. Kokki, H.; Rasanen, I.; Lasalmi, M.; Lehtola, S.; Ranta, V. P., et al., Comparison of oxycodone pharmacokinetics after buccal and sublingual administration in children. *Clinical pharmacokinetics* **2006,** *45* (7), 745-754.
201. Kussrow, A.; Baksh, M. M.; Bornhop, D. J.; Finn, M. G., Universal sensing by transduction of antibody binding with backscattering interferometry. *Chembiochem : a European journal of chemical biology* **2011,** *12* (3), 367-370.

202. Cheng, S.; Shi, F.; Jiang, X.; Wang, L.; Chen, W., et al., Sensitive detection of small molecules by competitive immunomagnetic-proximity ligation assay. *Analytical chemistry* **2012,** *84* (5), 2129-2132.
203. Nutiu, R.; Li, Y., Structure-switching signaling aptamers. *J Am Chem Soc* **2003,** *125* (16), 4771-4778.
204. Jackson, G. W. Methods for simultaneous generation of functional ligands. 2012.
205. Backmund, M.; Meyer, K.; Von Zielonka, M.; Eichenlaub, D., Ofloxacin causes false-positive immunoassay results for urine opiates. *Addict Biol* **2000,** *5* (3), 319-320.
206. Baden, L. R.; Horowitz, G.; Jacoby, H.; Eliopoulos, G. M., Quinolones and false-positive urine screening for opiates by immunoassay technology. *Jama-J Am Med Assoc* **2001,** *286* (24), 3115-3119.
207. French, D.; Wu, A.; Lynch, K., Hydrophilic interaction LC-MS/MS analysis of opioids in urine: significance of glucuronide metabolites. *Bioanalysis* **2011,** *3* (23), 2603-2612.
208. Jacobson, S. W.; Bihun, J. T.; Chiodo, L. M., Effects of prenatal alcohol and cocaine exposure on infant cortisol levels. *Development and psychopathology* **1999,** *11* (2), 195-208.
209. Milone, M. C., Laboratory testing for prescription opioids. *Journal of medical toxicology : official journal of the American College of Medical Toxicology* **2012,** *8* (4), 408-416.
210. Administration, S. A. a. M. H. S. Drug-Free Workplace Guidelines and Resources. https://www.samhsa.gov/workplace/resources.
211. French, D., The challenges of LC-MS/MS analysis of opiates and opioids in urine. *Bioanalysis* **2013,** *5* (22), 2803-2820.
212. Anand, K. J.; Hall, R. W.; Desai, N.; Shephard, B.; Bergqvist, L. L., et al., Effects of morphine analgesia in ventilated preterm neonates: primary outcomes from the NEOPAIN randomised trial. *Lancet* **2004,** *363* (9422), 1673-1682.

Chapter 7: Preclinical Evaluation of a Free Solution Assay for the Quantification of a Candidate Lung Cancer Biomarker CYFRA 21-1

Adapted from a manuscript in preparation for submission to Science Translational Medicine

Lung cancer is the leading cause of cancer-related deaths in the United States [213]. Low dose chest CT screening programs that target high-risk individuals (e.g., individuals 55-75 years of age with a smoking history of at least 30 pack-years and who have smoked within the last 15 years) can reduce the relative risk for lung cancer-specific mortality by 20% in the context of a randomized clinical trial [214]. There is a growing movement to implement this life saving screening into routine practice, with endorsements from the U.S. Preventive Services Task Force [215], the vast majority of professional societies [216], and a willingness from payers to provide reimbursement [215-216]. Yet, numerous challenges still need to be navigated for early detection of lung cancer to implement this service and to provide significantly improved outcomes. Among those are: a) how can we position a biomarker prior to chest CT screening to decrease the cost and rates of false positive tests; b) how to address the diagnosis of lung cancer among indeterminate pulmonary nodules (IPNs); and c) how to detect recurrence after therapy. The availability of a rapid, high sensitivity detection method to improve the quantification of biomarkers has the potential to aid in improving individualized management of indeterminate pulmonary nodules (IPNs) in lung cancer patients.

Redefining the value of strong candidate biomarkers could produce changes in the guidelines for the management of indeterminate pulmonary nodules, for disease monitoring and for the early detection of cancer in the preclinical period. Our approach addresses how current clinical blood biomarker strategies are too insensitive to enable detection of a developing tumor within the first decade of tumor growth [217] and mirrors what was accomplished when a *high sensitivity* version of the CRP assay was demonstrated. Because of improved sensitivity, the *h*-CRP test, performed widely today, allowed the repurposing of an otherwise nondiscriminatory

biomarker, transforming it into a clinically useful target for determining initial status of a patient with a suspect cardiac event [218-220]. Others have taken this tactic of addressing biomarker value by attempting to increase the sensitivity of the assay [221-222]. While promising results have been obtained, there is no definitive report that shows significant improvement in positive predictive value (PPV) and diagnostic likelihood ratio (DLR) values for lung cancer from a single protein lung cancer biomarker.

Numerous approaches have been reported to quantify biomarkers for the study of pathogenesis in cancer, albeit their clinical translation has been problematic. Among the most common methods are enzyme-linked immunosorbent assays (ELISA) [223], electrochemiluminescence (ECL) [224-226], and bead array technologies [227]. Label-free techniques, such as surface plasmon resonance (SPR) [228-229], quartz-crystal microbalance [230], wave-guided interferometry [231-232], and mass spectrometry (MS) have been employed for biomarker quantification, but have yet to provide an improvement in diagnostic power [233]. Although MS has been exceedingly valuable in the biomarker discovery phase [234-235], instrumentation complexity and difficulty with quantification make its use in clinical screening unattractive [236]. Multiplexed MRM/MS targeted assays using stable-isotope-labeled peptide standards for accurate quantitation are showing promise as clinical diagnostic assays [237], but complexity and low-throughput remain as challenges.

Newly emerging platforms have reported single-molecule sensitivity. These techniques capitalize principally on one of two approaches, yet still employ a fluorescence sandwich assay based on multiple chemical steps. One approach is a microparticle-based assay that is analogous to ELISA. The technique, named Singulex, uses a capture and separation step to yield a bead with the fluorescently labeled target, then by limiting the probe volume to a few femtoliters in a manner similar to confocal microscopy uses single molecule counting technology to obtain high sensitivity for biomarker targets [238]. Simoa (Single Molecule Array) from Quanterix is a technology that exploits the advantages of digital assays by employing a sandwich assay on beads which are each collected in wells formed at the end of a coherent fiber optic or similar small volume receptacle [239-240]. Both techniques have deficiencies, related to speed, reproducibility, cost, and/or accessibility. SOMALOGIC has taken a different approach to quantifying serum proteins, employing aptamers, which are stands of DHA or RNA selected to bind selectively with the target [241]. Their detection approach capitalizes on a slow ‘off-rate’ for one of the complexes formed

to separate the sample from background [242]. While this aptamer-probe method has shown promise [243], multiple (as many as 10) sample handling and labeling steps, combined with relatively complicated instrumentation has impeded the wide dissemination of the technology for biomarker quantification.

In general, platforms that require either surface immobilization and/or labeling steps can make assay development and species validation arduous, slow, and expensive. Given these observations, we have chosen to explore the potential to do biomarker quantification label-free and in free-solution. The Free-Solution Assay (FSA) presented here appears to represent a viable alternative [91] to many of the existing and emerging assays. FSA is a mix-and-read approach that is assay agnostic, highly sensitive, rapid, and matrix independent. It will be shown here that when FSA is combined with a newly demonstrated compensated interferometric reader (CIR), reported here for the first time, it is possible to quantify a protein biomarker rapidly in serum samples at levels significantly lower than the gold standard approach (50 pg/mL vs. 500 pg/mL for ECL).

With the overall objective to improve the detection methods for the early diagnosis of lung cancer among indeterminate pulmonary nodules (IPNs), we hypothesized that, as with *h*-CRP, this lower limit of quantitation (LOQ) could transform biomarker utility. In doing so it would be possible to redefine the detectable concentrations of one of the best candidate serum biomarkers for lung cancer, CYFRA 21-1, thereby significantly improving its clinical utility by increasing the discriminatory power of the biomarker. CYFRA 21-1 has a long history of being investigated as a potential lung cancer biomarker [223, 244-245]. Yet, to date, insufficient sensitivity and specificity has limited the value of CYFRA 21-1 in clinical practice. Even so, CYFRA 21-1 concentration appears to correlate with disease progression [246-248]. The diagnostic utility of CYFRA 21-1 in lung cancer has been restricted by the low constitutive expression in healthy individuals (2.4 ng/mL), a value which is well below the typically reported ELISA limit of quantification (LOQ) values typically reported as 4 ng/ mL, and near the typically reported limit of detection (LOD) of 1 ng/mL [249]. Our preliminary observations with backscattering interferometry (BSI) showed that our FSA, based on a single antibody probe to CYFRA 21-1 and read by an interferometer, can provide up to 40-fold LOQ improvements for serum biomarker quantification, when compared to established enzyme-linked immunosorbent assays (ELISAs) [92]. Here we build on these observations, reporting a new higher throughput interferometric

reader with enhanced signal-to-noise (S/N) performance, and the application of our FSA to quantify CYFRA 21-1 in a clinically relevant patient population.

Methods

Study Design The objectives of this study were to evaluate the performance of the free-solution assay method (FSA), measured by the compensated interferometric reader (CIR), as an ultrasensitive, volume constrained, biomarker quantification platform and to demonstrate it can be used to improve the utility of the protein biomarker CYFRA 21-1 for lung cancer diagnosis through improved sensitivity. The FSA-CIR method was used to quantify the level of CYFRA 21.1 in 225 patient serum samples. CYFRA 21-1 is a well-studied fragment of cytokeratin 19 that is widely regarded as a potential diagnostic biomarker for lung cancer. This is a case control study design of archival blood specimens. The patient cohort was selected from samples available in the Vanderbilt Thoracic Biorepository. The study was approved by the Internal Review Boards at both Vanderbilt University and Vanderbilt University Medical Center.

Blinding of group allocation was achieved by relabeling of the samples with an internal ID number (randomly assigned with numbers 1-225) after being pulled from the biorepository and before being delivered for measurement by FSA-CIR. The samples were run in the order of increasing ID number. Two separate CIR instruments were used to analyze the samples, and samples were split randomly between the two instruments. There was no correlation between sample ID# and patient histology, cancer staging, gender, smoking history, age of the patient at time of sample collection, or age of the sample at time of measurement.

Materials and Reagents: Unless otherwise specified, reagents were purchased from Sigma-Aldrich, and lab disposables were purchased from Fisher. Deionized water (DI H_2O) was used to prepare all aqueous solutions. Pooled human serum was obtained from Valley Biomedical. CYFRA 21.1 was obtained from DRG International. The CYFRA 21.1 monoclonal antibody (clone XC4, product # MBS850246) was obtained from MyBioSource.

The Mitos Dropix was obtained from Dolomite Microfluidics through their US distributor, Blacktrace. The capillary interface to the Dropix was fabricated in house. To avoid non-specific adsorption of proteins and plasticizer leaching sample-well-trays were machined from PEEK at the Vanderbilt Physics and Astronomy Machine Shop. Capillary mounting blocks were machined

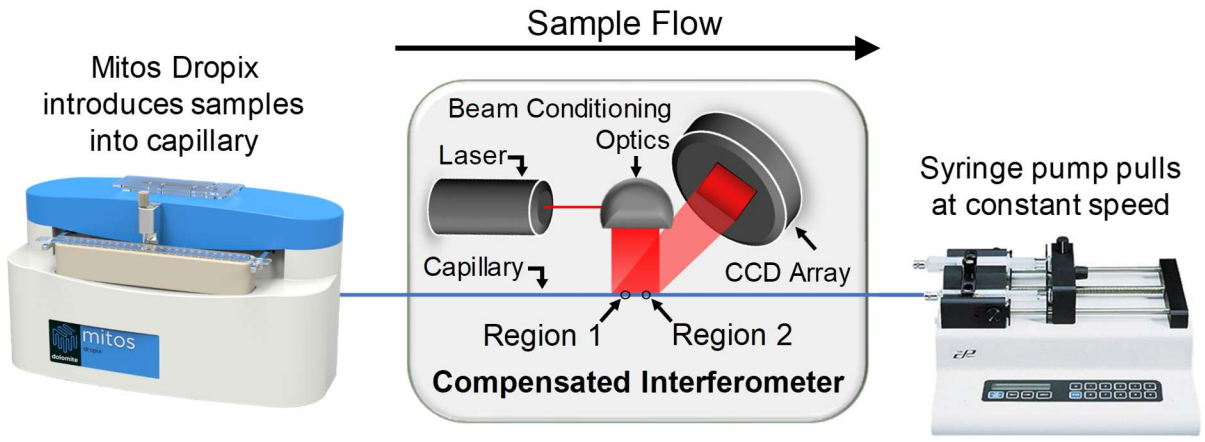

Fig. 7.1 Workflow of the compensated interferometric reader. Block diagram of the CIR, showing droplet generator (left), laser and fringe detector (center), and syringe pump (right).

from aluminum at the Vanderbilt Physics and Astronomy Machine Shop and black-anodized by Mid-Western Anodizing, Milwaukee, WI. Capillary was obtained from Molex.

Compensated interferometric reader setup, signal transduction, and calibration

The CIR, illustrated in **Figure 7.1**, is a unique nano-volume interferometric sensor consisting of a laser, a fused silica capillary and a CCD camera. The laser beam is conditioned in a manner to be elongated along the central axis of the capillary by passing the light through a pair of spherical lenses (Lasermate, USA). This expansion results in a beam profile that is ~12.8 mm in the long axis and ~0.8 mm in the short axis. Upon illumination of the capillary, a series of high contrast elongated interference fringes are produced from the laser-capillary interaction. These fringes are directed onto the 2D CCD, which is used to quantify the position of these fringes as a function of time. Proper windowing of the 2D CCD array, using an in-house LabVIEW™ program, facilitates interrogation of two nearly adjacent regions of the fringes, and thus the capillary, for differential reader operation allowing the optical train to function as a compensated interferometer. When properly aligned so that the fringe patterns of the two regions are matched, the result is two nearly identical interferometers enabling operation in the absence of active temperature control, as well as compensation for wavelength wander and laser intensity instability [155]. The positional shifts in the fringes from each of these two windows is quantified by a fast Fourier transform (FFT) [91] allowing for calculation of the phase change as a function of time.

The difference in the phase readout between the two windows provides a relative measure of refractive index (RI).

Capillary preparation and mounting: Capillary tubing (350 µm outer diameter / 250 µm inner diameter) was obtained in a 20-meter spool from Polymicro (Molex, USA). A 1-meter length of the capillary was separated from the spool by careful scoring of the capillary using the sharp edge of a freshly snapped silicon wafer [250]. An anodized black aluminum block (3x3 inches by ½ inch thick) served as a mounting block for the capillary. A shallow V-Groove (100 µm deep) etched into the block provides alignment and support for the capillary. A hole was drilled through the mounting block where the laser impinges on the capillary to reduce scattered light. Prior to mounting the capillary upon the aluminum mounting block, the capillary interior was silanized using Sigmacote® according to the following protocol: Using the syringe pump, 1mL of water was drawn through the capillary at a rate of 200 µL/min. Then the capillary is dried out by pulling 10 mL of air through the tube at a rate of 1 mL/min. Next, Sigmacote® (300 µL) was pulled through the capillary at a rate of 50 µL/min, followed by another air-drying step at a rate of 1 mL/min. After drying, the capillary was wetted by flowing DI H_2O (500 µL) at a rate of 50 µL/min through the tube. The water-filled capillary was then placed into an oven at 150°C for 30 minutes to dry and complete the silanization. The coated capillary was then mounted on the Al block, which was mounted to two perpendicular translation stages (Newport 423 linear aluminum stage driven by Newport SM-25 Vernier Micrometer) to allow precise alignment of the capillary relative to the incoming beam.

CIR Alignment: The diode laser was attached to the optical bench so as to give a 35 cm beam path to the capillary. The interaction of the beam with the capillary produces a series of interference "fringes" which are directed onto the CCD array mounted 5 cm from the capillary. Beam – capillary alignment was achieved by translating the capillary so that it was centered with respect to both the short and long axis of the beam. Proper alignment was attained when the interference fringes exhibited a nearly single spatial frequency, uniform intensity and a high-contrast ratio (>0.9) as calculated from the maximum intensity / minimum intensities.

Syringe Pump Setup: A Chemyx® Nexus 3000 Syringe pump operated in so as to pull fluids was affixed with a Hamilton Gastight® 1001 syringe. The syringe was interfaced to the capillary using a LabSmith Luer-Lock to capillary adaptor. Using a Hamilton syringe with an

inner diameter of 4.610 mm and volume of 1000 µL allowed continues operation for ~100 minutes at a typical operating flow rate of 10 µL/min.

Droplet Train Generation: The Mitos Dropix was interfaced to the interferometer so that droplet trains were formed directly in the capillary, allowing a single section of capillary to serve as both the reader detection cell and the transfer line. Here the interface was accomplished by feeding the capillary through a sample hook of in-house design. This approach provides for uninterrupted, unperturbed droplet generation and flow. It also reduces the potential for sample loss. Droplet trains were produced by this sample hook/capillary assembly moving up and down between two "reservoirs" while the pump pulls fluid. One of the reservoirs was an open tray containing oil (Fluorinert FC-40, Sigma-Aldrich), serving to separate the droplets, the other was a PEEK tray consisting of 24 bottomless wells where the sample and reference solutions reside. Hook sample-well dwell time and solution flow rate determines droplet volume and spacing. Prior to droplet train generation, the capillary was filled with PBS and the syringe pump operated at a flow rate of 10 µL/minute for 10 minutes to establish a stable flow through the system.

Next the Dropix was programmed using its onboard control software provided by Dolomite Microfluidics to produce a droplet train with the appropriate droplet order, volume, and spacing. The program facilitates droplet train generation by timing the movement of the sample-collection hook between the reservoirs containing the samples and the oil bath. Sample hook dwell time in each appropriate reservoir is determined by the droplet volume, spacing, and flow rate in the capillary. Here a single determination consists of a droplet train of 1000nL of sample and reference solutions separated by 40nL of oil. Sample and reference solutions (18 µL) were loaded into adjacent wells in the sample tray. Typically, the first sample/reference pair in the droplet train was preceded by 4 x 4 µL droplets of PBS, each separated by 100nL of oil, to serve as a rinse. For all determinations using the CIR, the sample/reference pairs were introduced five times for a total of 10 droplets. Following the analysis of each group of sample/reference droplet pairs a 500nL droplet of oil and 2 x 4 µL droplets of PBS separated by 100nL of oil was used to rinse and prepare the capillary for the next sample/reference pair. When operating the CIR, a total of 6 sample/reference solution pairs can be analyzed sequentially from a single tray. The entire droplet train, consisting of all six sample pairs and the required rinses, takes about 14 minutes to run. After an entire tray was run, the capillary was rinsed with PBS for 3 minutes to prepare the CIR for a new PEEK tray containing 6 new sample pairs. A total of 6 sample trays, including all rinses,

can be sampled before the syringe needs to be emptied and the capillary rinsed thoroughly with PBS (500 µL at 50 µL/min). No quantifiable noise or change in reader response was detected due to emptying the syringe and restarting the pump.

CIR signal transduction: As the droplet trains traverse the detection region, the resulting interferometric fringe patterns were captured on the CCD array and processed in real time. Windows of the fringes from each detection region measuring 200 pixels long×1200 pixels wide were selected for analysis using our in-house software running under a LabVIEW^{TM} program (National Instruments). A set of 5 fringes with a nearly single-spatial frequency, defined as a Fast Fourier Transform (FFT) power spectrum with a ratio of 4:1 or greater (dominant frequency to neighboring frequencies), was selected from each detection region. Measuring the FFT phase of the dominant frequency as a function of time provides a quantitative measure of the fringe shift which can be correlated to the change in RI for the sample and reference windows. The difference in phase change between the two regions when the sample/reference droplets were in their respective window provides a readout for the interferometer.

CIR Calibration: Device performance and instrument response was evaluated using solutions of glycerol in 25% pooled serum / 75% PBS. This was accomplished by generating a calibration curve using solutions containing 0, 0.125, 0.25, 0.5, 1, and 2mM glycerol in serum/PBS, with Serum/PBS used as the reference sample. For each glycerol concentration, 18 µL of glycerol (sample) and 18 µL of serum/PBS (reference) were loaded into adjacent wells in the Dropix tray and their relative response measured with the CI allowing a calibration curve of concentration vs. response to be constructed. Using this experimental data and the calibration curve we determine the response (sensitivity) of the instrument (target value >0.110 radians/mM glycerol). We also measure the reproducibility of replicate measurements enabling the calculation of the standard deviation (target value <0.012 radians) and the limit of quantification (LOQ) which is calculated as 3×σ / slope of the calibration curve for 5 replicate measurements. Glycerol calibration curves must produce LOQs of 0.33 mM glycerol or less. In terms of RIU sensitivity, using the dη/dC value for glycerol of 1.05×10^{-5} RIU/mM, this corresponds to an LOQ of 3.4 µRIU. To determine the LOD the baseline noise was determined as the standard deviation of the phase shift over the duration of a single measurement (~1 second). Here we found this value to typically be on the order of 0.0042 radians giving an LOD that was 0.111 mM glycerol or 1.16 µRIU. Based upon our past experience, this sensitivity was more than adequate to perform free-solution

molecular interaction studies [91, 201]. When the values noted above are not obtained, capillary rinsing and refinement of the optical alignment is often necessary.

Free Solution Assay Methods

Calibration curves were prepared by spiking several aliquots of a 50% pooled human serum / 50% PBS solution with concentrations of the biomarker target CYFRA 21.1 ranging from 0.024 ng/mL to 25 ng/mL. Each serum aliquot was combined with a solution containing the probe antibody to produce the binding sample. To produce an RI-matched, nonbinding reference sample, each serum aliquot is combined with a "blank" solution containing buffer with no antibody. Following a 1-hour incubation at ambient temperature (22 °C) on a shaker (300 rpm), the sample and reference solutions were loaded onto the droplet generator and measured by the CIR in order of increasing concentration. A single site saturation isotherm was fitted to the resulting phase shifts according to the equation:

$$Y = B_{max} \times X/(K_D + X) \qquad \textbf{Eq. 7.1}$$

where Y is the phase shift at concentration of X (in ng/mL), B_{max} is the maximum signal at saturation, and K_D is the dissociation constant. Calibration curves consisted of 11 concentrations of biomarker, with 2:1 serial dilution resulting in concentrations ranging from 24 pg/mL to 25 ng/mL and a concentration devoid of CYFRA 21.1 biomarker to serve as a "zero" concentration. Then, the CYFRA 21.1-spiked serum (20 µL) was added to PBS (20 µL) to form the reference sample, and CYFRA 21.1-spiked serum (20 µL) was added to PBS containing 2 µg/mL probe antibody (20 µL) to form the binding sample. Final sample compositions were 25% serum in PBS, with 1 µg/mL antibody is the binding sample. Following the initial validation studies (explained below), calibration curves consisted of 5 concentrations of biomarker (5:1 serial dilution resulting in concentrations ranging from 25 ng/mL to 40 pg/mL) and a zero concentration.

Patient serum samples were measured by preparing binding and reference sample pairs according to the following procedure: Each serum sample was thawed on an Eppendorf thermomixer (300 RPM) at 20 °C for 20 minutes, then homogenized by aspiration with a 75 µL mixing volume using a hand pipetter. Then, 10 µL of the patient serum was added to 30 µL of PBS to form the "reference" sample, and 10 µL of the patient serum was added to 30 µL of solution containing the probe antibody (1.5 µg/mL) to form the "binding" sample. Samples were incubated at ambient temperature (22 °C) using shaking (300 rpm) for 1.5 hours before measurement with

FSA-CIR. Final samples were 40 μL with a composition of 25% patient serum, 75% PBS buffer, with 1 μg/mL probe antibody in the binding sample. Sample and Reference (18 μL of each) were loaded into adjacent wells in the droplet generator sample-well-tray.

After measurement with FSA-CIR, the phase shift for each patient serum sample was fit to the calibration curve to determine the concentration of CYFRA 21-1 using Graphpad Prism.

Spiked "unknowns" were prepared by adding a known quantity of the CYFRA 21-1 biomarker to pooled serum, then processing the samples in the same manner as patient samples.

After the initial determination of the patient cohort we performed the assay on a set of twenty samples (10 controls, 5 adenocarcinoma, 5 squamous cell carcinoma) randomly selected and blinded by our clinical collaborators. Aliquots of these samples (200 μL) were subjected to an additional freeze-thaw cycle and measured in the same manner as the full cohort, then subjected to *another* freeze-thaw cycle and measured. Coefficients of Variations (CVs) of the replicate measurements were calculated as standard deviation / average.

Patient characteristics

Cases and control samples were selected from our thoracic biorepository to meet the following criteria. Samples need to have been enrolled in our indeterminate pulmonary nodule cohort by chest CT. All nodules must have been ascertained by either a tissue diagnosis or a 2 year follow up with no evidence of growth. The 225 patient samples were selected to include roughly equal proportion of four histology groups (no cancer, adenocarcinoma, squamous cell carcinoma, and small cell carcinoma). Samples were selected to maintain an even distribution of gender, smoking history, and nodule size across all four histology groups.

Serum sample collection and storage:

Patient serum samples were collected according Vanderbilt Thoracic biorepository Standard Operating Procedures THO 0136, THO 0398, and THO 1078, corresponding to different research studies. For all three studies, the serum sample collection followed the same format. Patient blood sample (10 mL) was collected via venipuncture. Patient blood was then allowed to clot at room temperature for 30 minutes, then centrifuged. Centrifuge protocol was as follows: 15 minutes at 1000g at 4°C for THO 1078; 15 minutes at 2000g at 0-4°C for THO 0398 and THO 0136. The supernatant (serum) was aliquoted into several Eppendorf cryovials: two aliquots of 1 mL, and the remaining serum in 50 μL aliquots. All aliquots were labeled with a Lung ID and

barcode number and immediately stored at -80°C. Time between venipuncture sample collection and sample freezing in the -80 was kept to under 2 hours. Samples were stored in the same -80°C freezer until they were pulled for this study, but were not thawed until the time of measurement by FSA-CIR. All standard operating procedures are available online (Massion lab Website).

Results: FSA-CIR provides high sensitivity analysis of serum protein.

Several advances have enabled the breakthrough lung cancer biomarker results reported here. The first is the demonstration of the one of the first truly compensated interferometers [155]. This benchtop interferometric sensor is based on a simple optical train that consists of a diode laser, an object (capillary tube), and a camera and allows the elimination of the high-resolution temperature controller typically needed for such devices [183]. Further simplifying the device compared to other interferometric sensors [86], is the use of an inexpensive diode laser for illumination of the capillary flow cell. In work parallel to that reported here we have begun to reduce the compensated interferometer to practice, having constructed a beta test unit with ultimate goal of translating the technology to the commercial sector.

Here we married the compensated interferometer with a modified droplet generator (Mitos, Dropix), and an inexpensive syringe pump to construct a compensated interferometric reader (CIR) (**Fig. 7.1**). CIR, reported here for the first time, uses a fused silica capillary tube for seamless sample droplet train generation and analyte quantification. The ability to use of a capillary is noteworthy, because it has been shown to have sensitivity advantages over chip-based optics [63, 251]. Also, as a consequence of our unique compensation method, which eliminates the need for high resolution thermal regulation of the flow cell, the instrument is greatly simplified and can in theory be battery operated. Furthermore, the continuous transfer line approach used here provides for effective, smooth, uninterrupted sample droplet production. Collectively, when compared to previous sensor designs [86], the CIR provides significantly increased throughput, streamlined data collection and analysis, and constrains sample size to less than 1µL.

CIR represents a unique biomarker detection approach that functions by having samples drawn into and through the capillary by a syringe pump (**Fig. 7.1**) and having those droplets traverse the detection region of the interferometer. In short, comparison of sample – reference pairs, separated by a droplet oil allows the quantification of the target biomarker. Specifically, the laser illuminates the capillary with an expanded beam that is reflected/refracted by the tube

producing an elongated interference fringe pattern. Comparison of positional shifts in the adjacent regions of this reflected beam pattern (fringes), when a train of sample and reference solution droplets traverses through the beam, provides a measure of the antibody-biomarker target complex. In other words, protein biomarkers are quantified by interrogating two regions of the backscattered light that is directed onto a CCD camera and using an in-house image processing software to measure the difference phase change in the fringe patterns for the sample and reference. This process is similar to that described previously, and involves performing a Fourier Transform, to quantify relative positional shift in the fringes [91].

Recognizing the advantages of microfluidics for sample handling and the need for turn-key operation in translation, we chose to use a slightly modified, commercially available droplet generator (Mitos, Dropix). Multi-well biocompatible, low non-specific adsorption, sample holders unique to our laboratory ensured that replicate sample analyses by CIR provided high analysis precision.

The two nearly *identical interferometers* [155] used in our CIR represents a unique optical detection approach with unprecedented noise rejection from temperature fluctuations and laser pointing-intensity instabilities. The combination of this noise rejection and the inherent performance of the interferometer, results in an ultra-sensitive reader capable of detecting probe-target binding in ultra-small sample volumes of serum. Here CIR facilitated direct interrogation of adjacent sample/reference droplets of 0.8µL, separated by 40nL droplet of oil, enabling rapid serum protein biomarker quantification with excellent sensitivity. CIR is, to our knowledge, the only nanoliter-volume interferometer based on a battery-operated diode laser with no need for a high resolution temperature controller [86]. These developments should pave the way for its use in a clinical lab and the near-patient setting.

Establishment of a CYFRA 21-1 assay

Fig. 7.2 illustrates the workflow used to perform an assay with FSA. A small volume of serum is split into two aliquots and then processed to provide 'binding' and 'reference' solutions. To quantify a target, we add an excess of antibody probe to one of the aliquots, giving the "binding/test" sample, and to the other we add a refractive index (RI) matching solution (buffer) or "reference/control." Solutions are allowed to equilibrate and are introduced into adjacent wells of the droplet generator for analysis by the interferometer as pairs separated by an oil droplet. The

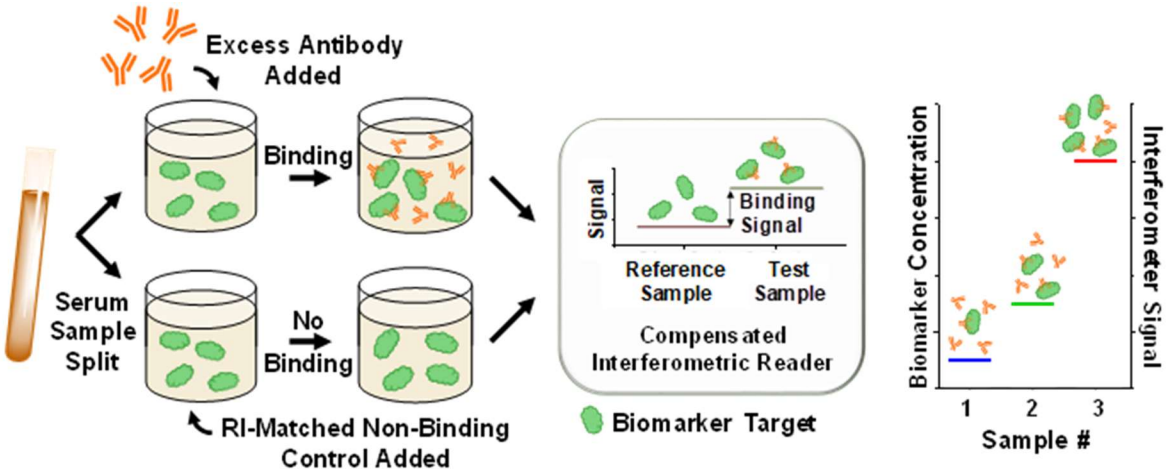

Fig. 7.2 Schematic of the Free-solution assay method

difference in signal between the sample–reference pair provides a quantitative measure of target (e.g. concentration of antibody-target complex), while allowing the matrix signal to be nullified. As noted above the scientific principal for FSA is based on binding-induced changes in molecular conformation and hydration producing predictable and reproducible changes in the solution dipole moment [91].

As a first step toward testing our hypothesis that lowered LOQs for serum protein markers can improve performance of the increase their clinical utility as lung cancer biomarkers we established the analytical performance of FSA-CIR for quantifying CYFRA 21-1. We show here that using a commercial antibody to CYRFA 21-1 we were able obtain high quality calibration curves over multiple days that gave an average LOQ of 40pg/mL in 25% serum. **Fig. 7.3** presents a summary of these results, showing the calibration curves for 9 serum CYFRA 21-1 assays, the 95% confidence interval for these curves and the response for the spiked serum samples that served as 'unknown' test standards. These calibration curves gave correlation coefficients of R^2 = 0.98-0.99 (**Fig. 7.3**). Using FSA-CIR we were able to easily process 20 samples/hour. Analyzing 0.8 µL/droplets we could operate at a modest throughput of 50 serum samples per day, obtaining intra-assay CVs of 6.2% for five replicate measurements and an inter-assay CV of 9.5% for four-day replicate determinations. The LOQs reported here are ~2-fold better than those published recently for a complicated, chemically intensive immunoassay, reported to give an LOQ of 80pg/mL [252],

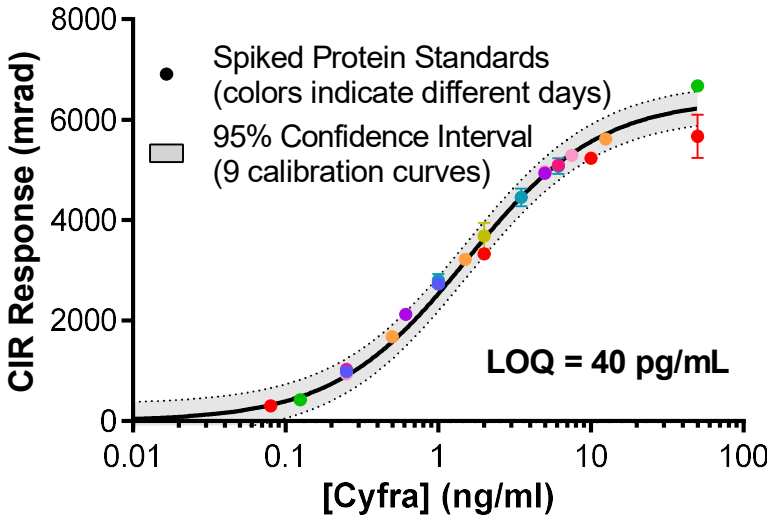

Fig. 7.3 Cyfra 21-1 calibration curve performance for nine independent assays and results for spiked protein standard unknowns.

and 10-fold better than the ~500pg/mL LOQ for the gold-standard Roche Cobas commercial electro-chemiluminescence assay (ECL) for CYFRA-21-1 [253].

As a test of assay accuracy, we prepared 'unknowns' by spiking CYFRA 21-1 in to serum, then quantified the unknowns using FSA-CIR. **Figure 7.3** shows that, barring just two exceptions, FSA-CIR provided a highly quantitative result for these determinations, with the percent difference ranging from 0.4% to 25%. While the 10ng/mL sample gave a 32% difference, the determined value still fell with the 95% confidence interval (grey region, **Fig. 7.3**) and represents an error in CYFRA 21-1 that would not impact classification as it is well above the traditional case vs. control cut-off of around 2-4 ng/mL. It should be noted that the one outlier that showed a 77% difference at a concentration of 50ng/mL was a test solution prepared at a concentration outside the normal operating range for the assay intended to show the response of a very high concentration. Furthermore, a concentration of 50ng/mL is also well above the range of CYFRA 21-1 values that would impact the diagnostic go-no-go decision tree for ranking a patients IPN as benign or malignant. Overall, within the linear range of the calibration curve (0 to 4 ng/mL), FSA-CIR provided an average percent difference between actual and determined concentration of 10.9%.

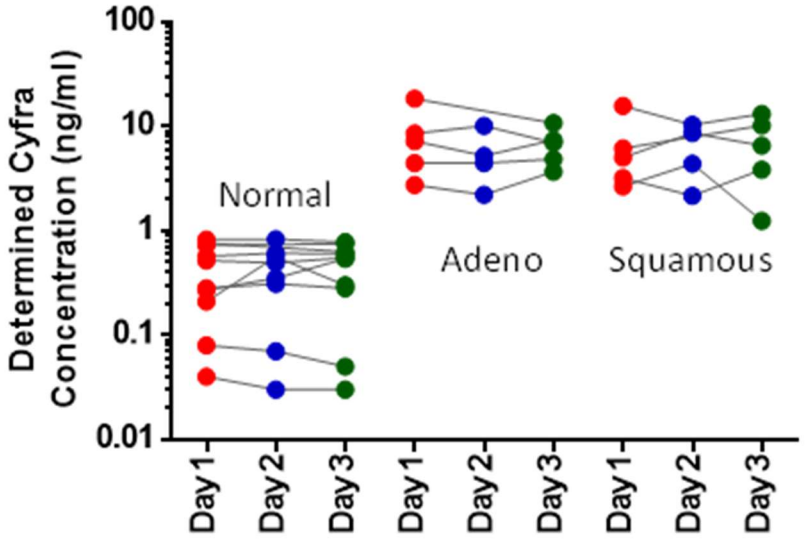

Fig. 7.4 Reproducibility of the assay across 3 independent (freeze-thaw) experiments.

Robustness of the assay

To test the robustness of the assay, serum samples were submitted to the following treatments: measures repeated on different days, measured by different operators, and measurement following multiple freeze and thaw cycles. Again, these samples consisting of 10 controls, 5 adenocarcinomas, 5 squamous cell carcinomas were blinded to the FSA-CIR operator, having been randomly selected. **Fig. 7.4** illustrates the results of this experiment, showing that the FSA-CIR biomarker quantification method is robust and repeatable with respect to sample freeze-thaw cycles. The average CV for all sample determinations over three days and 2 extra freeze-thaw cycles was found to be 21.1%. While additional, more extensive tests of sample handling are necessary before formal translation to the clinic, the fact that we observed relatively small changes in the patient CYFRA 21-1 biomarker concentrations for these 20-blinded patient samples indicates that assay is robust over a 3-day period and that at least two freeze-thaw cycles can be tolerated.

Testing of the assay in a case control study

With a mix-and-read assay and a bench-top reader in hand, we performed preclinical evaluation to address the two questions key to our hypothesis. 1) As with the introduction of a

Table 7.1 Patient Characteristics

	No Cancer	ADC	SCC	SCLC
	N=75	N=45	N=44	N=61
Age	59.2 ± 12.7	65.2 ± 8.0	65.8 ± 7.8	63.9 ± 8.9
Gender (%)				
Male	40 (53)	26 (58)	29 (66)	36 (59)
Female	35 (47)	19 (42)	15 (34)	25 (41)
Smoking (%)				
Current	20 (27)	7 (16)	11 (25)	20 (33)
Ex	54 (72)	38 (84)	33 (75)	38 (62)
Never	1 (1)	0 (0)	0 (0)	3 (5)
Pack Years	41.1 ± 30.3	50.1 ± 31.3	53.9 ± 23.5	63.7 ± 32.8
Nodule Size (cm)	2.5 ± 1.6	2.7 ± 1.7	2.7 ± 2.0	3.6 ± 2.6
Path Staging (%)				
IA-IB	0 (0)	33 (73)	34 (77)	0 (0)
IIA-IIB	0 (0)	12 (27)	10 (23)	0 (0)
IIIA-IV	0 (0)	0 (0)	0 (0)	0 (0)
Limited	0 (0)	0 (0)	0 (0)	33 (54)
Extensive	0 (0)	0 (0)	0 (0)	28 (46)

high sensitivity *CRP* assay [218], can a lower LOQ versus the gold standard approach allow CYFRA 21-1 to become a clinically useful biomarker? 2) Can increasing biomarker sensitivity improve the discriminatory power of the biomarker? To address these questions, we quantified CYFRA 21-1 in serum samples from a cohort of patients with incidentally found indeterminate pulmonary nodules. The cohort consisted of 225 individuals including 75 with nonmalignant nodules, 45 adenocarcinomas (stages 1 and 2), 44 squamous cell carcinomas (stages 1 and 2) and 61 small cell lung cancers (limited and extensive stages), (**Table 7.1**) as determined by biopsy and histology. The FSA-CIR quantified level of CYFRA 21-1 grouped by histology is shown in **Fig. 7.5**, with the limit of quantification of FSA-CIR and of ELISA denoted by dotted lines.

Next we tested our biomarker diagnostic performance against clinical predictors [254]. Here we predicted risk for lung cancer for each patient based on the Gould model [255]. Our preliminary data suggest a strong improvement to risk prediction when combining the FSA-CIR measurement with the Gould model over the Gould model alone. This improved performance is

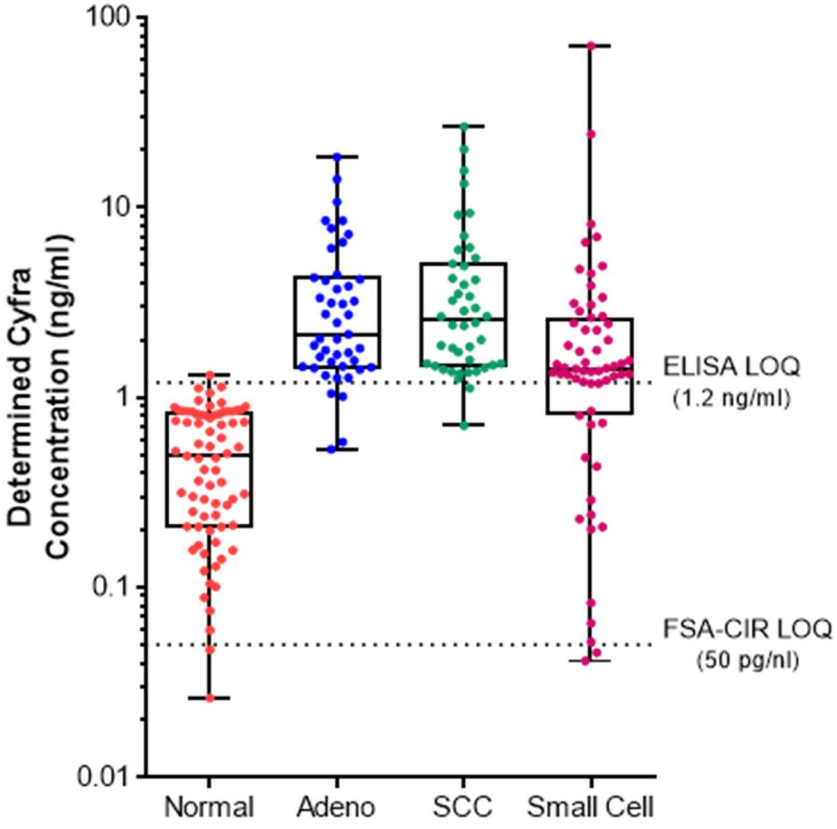

Fig. 7.5 Measurement of Cyfra 21.1 by F-CBSI across individuals with benign lung nodules (normal), Stages 1, 2 lung squamous (SCCs), Adenocarcinomas (ADCs) and all stages small cell carcinomas (SCLCs).

demonstrated by the receiver operating characteristics (ROC) curves shown in **Fig. 7.6**. The area under the curve (AUC) increases from *0.62* based on the Gould model to *0.94* when combining Gould with CYFRA 21-1 measured by FSA-CIR. Using a cutoff of 1.19 ng/mL CYFRA 21-1 for all tumors provides a positive predictive value (ppv) of *99%* (**Table 7.2**) and a positive diagnostic likelihood ratio (DLR+) of 64. The optimal cutoff is lowest for adenocarcinoma, at 1.01 ng/mL, with sensitivity and specificity both above 90%. The best performing population in this cohort was squamous cell carcinoma, with a cutoff of 1.12 ng/mL providing sensitivity of 98% and specificity of 97%. Even small cell lung cancer, traditionally not correlated with elevated CYFRA 21-1 levels, reported excellent discrimination, with an optimal cutoff of 1.19 ng/mL providing a sensitivity of 75% and specificity of 99%.

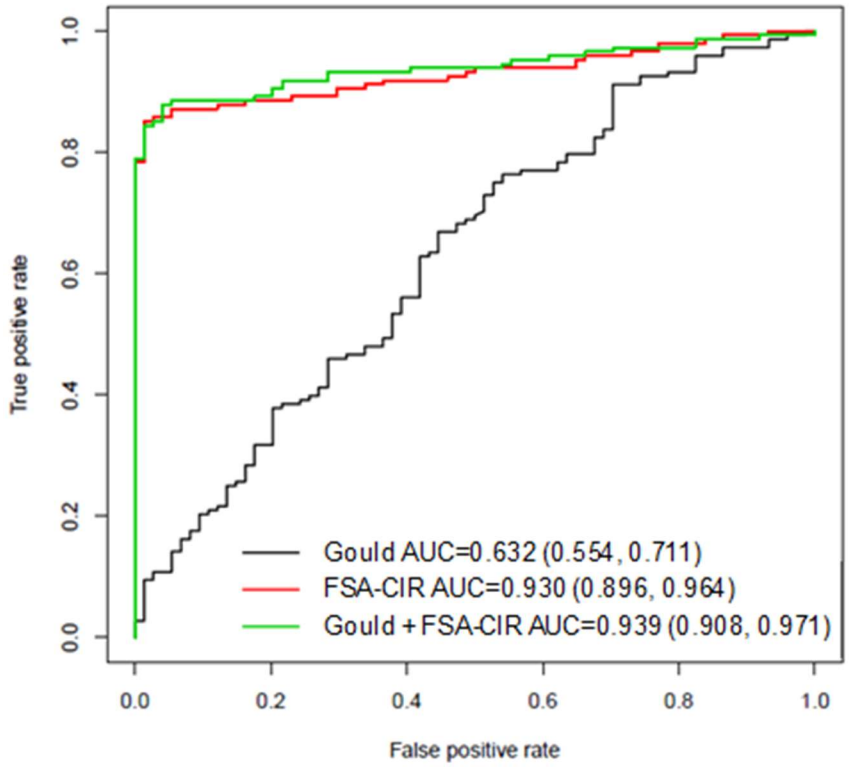

Fig. 7.6 ROC curve illustrating added value of FSA-CIR over clinical parameters and nodule size for the diagnosis of IPNs. N=225 lung cancers.

Table 7.2 Diagnostic properties of CYFRA 21-1 by CBSI. PPV, positive predictive value; NPV, negative predictive value; DLR, diagnostic likelihood ratio; FP, false positive; FN, false negative.

	All tumors	**ADC**	**SCC**	**SCLC**
Cutoff	1.19	1.01	1.12	1.19
Sensitivity.	0.85	0.93	0.98	0.75
Specificity.	0.99	0.95	0.97	0.99
PP V	0.99	0.91	0.96	0.98
NPV	0.77	0.96	0.99	0.83
DLR (+)	64	17.5	36.6	56.6
DLR (-)	0.15	0.07	0.02	0.25
False Positives	1	4	2	1
False Negatives	22	3	1	15
Optimal Criterion	0.84	0.88	0.95	0.74

PPV = Positive Predictive Value, NPV = Negative Predictive Value, DLR (+) = Postiive Diagnostic Likelehood Ratio, DLR (-) = negative Diagnostic Likelehood Ratio

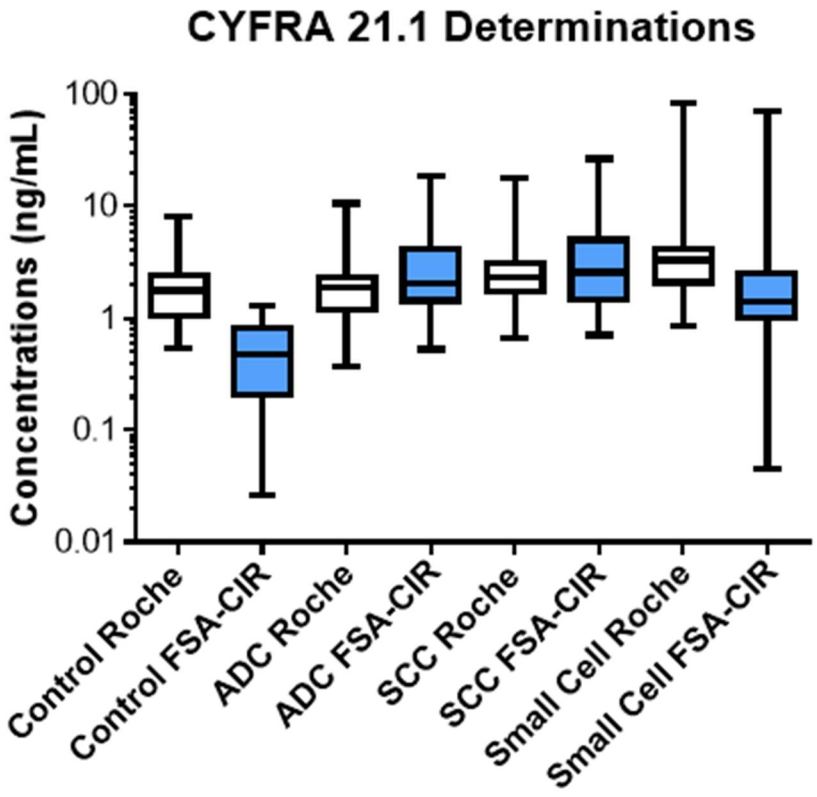

Fig. 7.7 Box plots illustrate Cyfra 21-1 measurements by FSA and Roche across individuals with indeterminate lung nodules, Stages 1, 2 lung squamous (SCCs), Adenocarcimonas (ADCs) and all stages small cell carcinomas (SCLCs).

Comparison of FSA-CIR to ECL

An independent analysis was then performed on aliquots of the same serum samples by a Clinical Laboratory Improvement Amendments (CLIA) approved lab at the University of Maryland, using the gold-standard Roche Cobas 601 module procedure, an electro-chemiluminescence (ECL) technology. These results are displayed in a box plot, along with the FSA-CIR findings (**Fig. 7.7**). With our FSA-CIR, 98/225 patient samples were below 1.2 ng/mL for the gold-standard ELISA technique. More importantly, the figure shows that the FSA-CIR analysis gave a clear separation of cases and controls for this patient cohort.

Discussion

Lung cancer continues to be one of the most difficult disease to diagnose. Challenges to early detection include: a) how to diagnosis patients with IPNs; b) how to determine recurrence

after therapy; and c) how to position biomarker use prior to chest CT screening to improve clinical outcomes. Here we tested a hypothesis that by virtue of lower LOQs afforded by FSA-CIR measurements it was possible to redefine the concentration of the candidate biomarker CYFRA 21-1 in the control population of patients diagnosed with IPNs. As with the *h*-CRP test, we pondered if a >10-fold better serum biomarker LOQ would lead to enhanced separation between cases and controls, thereby improving the diagnostic utility of the biomarker. Data shown here for a 225-patient cohort, that indicates it is possible to improve the clinical performance of CYFRA 21-1. To my knowledge this is first report where a single biomarker of lung cancer exhibited performance metrics of 85% specificity, 99% sensitivity, and a positive predictive value of 99% for all tumors.

Furthermore, the patient cohort was independently analyzed by a CLIA laboratory using the Roche ECL assay for the CYRFA 21.1 biomarker. In this head-to-head comparison of FSA-CIR with ECL, our assay methodology outperformed the gold standard in diagnostic testing for CYFRA 21-1 assay, providing a clear and quantifiable separation of cases and controls. This performance advantage was a result of a 10-fold improvement in sensitivity by FSA-CIR when compared to the FDA approved ECL method offered by Roche. Interestingly, in the probe volume defined by the laser capillary interaction of 40 nL, at the LOQ of 50 pg/mL there is ~2 femtomoles (2×10^{15} moles of target present). Also we are confident that we can further improve the sensitivity of FSA-CIR, given a recent report, where we able to use our assay method to quantify 120 protein-target molecules in a tissue matrix [90].

Chapter 7 Conclusion

In this report we have shown that combining a newly demonstrated interferometer with a droplet generator and a syringe pump results in a relatively simple, microfluidic reader, the CIR. When combining this reader with FSA a label-free, solution-phase assay the result is a potentially revolutionary platform for biomarker validation and diagnosis for numerous reasons: **1**) Its label-free (no fluorescence or radiolabeling) making it rapid, cost effective, and allowing the use of unaltered or minimally processed patient samples; **2**) Analyses can be performed on <1 μL sample aliquots allowing multiple replicates to be performed on quantity-limited samples; **3**) The simultaneous comparison of sample and reference solutions allows matrix insensitive operation and ensures assay specificity; **4**) Sensitivity of the FSA-CIR exceeds that of many, more

complicated competing technologies and can be further improved; **5**) The optical engine of CIR is simple, consisting of a diode laser, capillary tube, and camera, and due to the unique compensation performance, it was possible to eliminate the need for a high-resolution temperature controller, paving the way for the construction of a benchtop or even battery-operated hand-held reader; **6**) When combined with FSA, CIR is highly modular (assay agnostic) allowing for quantitation of a wide array of interactions (antibodies to DHA to small molecules), providing the ability to rapidly test additional potential serum biomarkers with numerous probe variations.

In summary, employing a single monoclonal antibody as the detection probe, our preliminary FSA-CIR CYFRA 21-1 data reported an improvement of ROC AUC from 0.63 for the Gould model to 0.94 using the Gould model + CYFRA 21-1 measured by FSA-CIR in a 225-patient cohort. Furthermore, the use of CYFRA 21-1 enabled a +DLR of 64 using a cutoff of 1.19 ng/mL. The improvements in biomarker predictive capability illustrated here are among the best reported, particularly for a single biomarker. Results shown here using our FSA-CIR method to quantify serum CYFRA 21-1 indicates it is possible to redefine cases from controls, where the Roche ECL Cobas assay could not. While a more stringent clinical validation from additional (external and independent) datasets are needed, our results suggest it may be possible to address a major hurdle in the management of patients with lung cancer by implementing an improved non-invasive testing protocol in the clinical setting.

63. Swinney, K.; Markov, D.; Bornhop, D. J., Chip-scale universal detection based on backscatter interferometry. *Analytical chemistry* **2000,** *72* (13), 2690-2695.
86. Kussrow, A.; Enders, C. S.; Bornhop, D. J., Interferometric Methods for Label-Free Molecular Interaction Studies. *Analytical chemistry* **2012,** *84* (2), 779-792.
90. Wang, M.; Kussrow, A. K.; Ocana, M. F.; Chabot, J. R.; Lepsy, C. S., et al., Physiologically relevant binding affinity quantification of monoclonal antibody PF-00547659 to mucosal addressin cell adhesion molecule for in vitro in vivo correlation. *British journal of pharmacology* **2017,** *174* (1), 70-81.
91. Bornhop, D. J.; Kammer, M. N.; Kussrow, A.; Flowers, R. A., 2nd; Meiler, J., Origin and prediction of free-solution interaction studies performed label-free. *Proc Natl Acad Sci USA* **2016,** *113* (12), E1595-1604.
92. Olmsted, I. R.; Hassanein, M.; Kussrow, A.; Hoeksema, M.; Li, M., et al., Toward rapid, high-sensitivity, volume-constrained biomarker quantification and validation using backscattering interferometry. *Analytical chemistry* **2014,** *86* (15), 7566-7574.
155. Kammer, M. N.; Kussrow, A. K.; Olmsted, I. R.; Bornhop, D. J., A Highly Compensated Interferometer for Biochemical Analysis. *ACS sensors* **2018**.
183. Kammer, M. N.; Kussrow, A. K.; Bornhop, D. J., Longitudinal pixel averaging for improved compensation in backscattering interferometry. *Optics letters* **2018,** *43* (3), 482-485.
201. Kussrow, A.; Baksh, M. M.; Bornhop, D. J.; Finn, M. G., Universal sensing by transduction of antibody binding with backscattering interferometry. *Chembiochem : a European journal of chemical biology* **2011,** *12* (3), 367-370.
213. Siegel, R. L.; Miller, K. D.; Jemal, A., Cancer Statistics, 2015. *Ca-Cancer J Clin* **2015,** *65* (1), 5-29.
214. Aberle, D. R.; Adams, A. M.; Berg, C. D.; Black, W. C.; Clapp, J. D., et al., Reduced Lung-Cancer Mortality with Low-Dose Computed Tomographic Screening. *New Engl J Med* **2011,** *365* (5), 395-409.
215. Moyer, V. A.; Force, U. S. P. S. T., Screening for lung cancer: U.S. Preventive Services Task Force recommendation statement. *Ann Intern Med* **2014,** *160* (5), 330-338.
216. Wiener, R. S.; Gould, M. K.; Arenberg, D. A.; Au, D. H.; Fennig, K., et al., An Official American Thoracic Society/American College of Chest Physicians Policy Statement: Implementation of Low-Dose Computed Tomography Lung Cancer Screening Programs in Clinical Practice. *American Journal of Respiratory and Critical Care Medicine* **2015,** *192* (7), 881-891.
217. Hori, S. S.; Gambhir, S. S., Mathematical model identifies blood biomarker-based early cancer detection strategies and limitations. *Sci Transl Med* **2011,** *3* (109), 109ra116.
218. Rifai, N.; Ridker, P. M., High-sensitivity C-reactive protein: a novel and promising marker of coronary heart disease. *Clin Chem* **2001,** *47* (3), 403-411.
219. Ridker, P. M.; Rifai, N.; Clearfield, M.; Downs, J. R.; Weis, S. E., et al., Measurement of C-reactive protein for the targeting of statin therapy in the primary prevention of acute coronary events. *The New England journal of medicine* **2001,** *344* (26), 1959-1965.
220. Chaturvedi, A. K.; Caporaso, N. E.; Katki, H. A.; Wong, H. L.; Chatterjee, N., et al., C-reactive protein and risk of lung cancer. *Journal of clinical oncology : official journal of the American Society of Clinical Oncology* **2010,** *28* (16), 2719-2726.

221. Chen, Z. H.; Liang, R. L.; Guo, X. X.; Liang, J. Y.; Deng, Q. T., et al., Simultaneous quantitation of cytokeratin-19 fragment and carcinoembryonic antigen in human serum via quantum dot-doped nanoparticles. *Biosens Bioelectron* **2017,** *91*, 60-65.
222. Li, J.; Skeete, Z.; Shan, S. Y.; Yan, S.; Kurzatkowska, K., et al., Surface Enhanced Raman Scattering Detection of Cancer Biomarkers with Bifunctional Nanocomposite Probes. *Analytical chemistry* **2015,** *87* (21), 10698-10702.
223. Pastor, A.; Menendez, R.; Cremades, M.; Pastor, V.; Llopis, R., et al., Diagnostic value of SCC, CEA and CYFRA 21.1 in lung cancer: a Bayesian analysis. *European Respiratory Journal* **1997,** *10* (3), 603-609.
224. Wang, J.; Ahmad, H.; Ma, C.; Shi, Q. H.; Vermesh, O., et al., A self-powered, one-step chip for rapid, quantitative and multiplexed detection of proteins from pinpricks of whole blood. *Lab Chip* **2010,** *10* (22), 3157-3162.
225. Fan, R.; Vermesh, O.; Srivastava, A.; Yen, B. K. H.; Qin, L. D., et al., Integrated barcode chips for rapid, multiplexed analysis of proteins in microliter quantities of blood. *Nature biotechnology* **2008,** *26* (12), 1373-1378.
226. Garcia-Cordero, J. L.; Maerkl, S. J., A 1024-sample serum analyzer chip for cancer diagnostics. *Lab Chip* **2014**, DOI: 10.1039/c1033lc51153g.
227. Lee, H. J.; Kim, Y. T.; Park, P. J.; Shin, Y. S.; Kang, K. N., et al., A novel detection method of non–small cell lung cancer using multiplexed bead-based serum biomarker profiling. *The Journal of Thoracic and Cardiovascular Surgery* **2012,** *143* (2), 421-427.e423.
228. Lee, H. J.; Nedelkov, D.; Corn, R. M., Surface plasmon resonance imaging measurements of antibody arrays for the multiplexed detection of low molecular weight protein biomarkers. *Analytical chemistry* **2006,** *78* (18), 6504-6510.
229. Teramura, Y.; Iwata, H., Label-free immunosensing for alpha-fetoprotein in human plasma using surface plasmon resonance. *Analytical biochemistry* **2007,** *365* (2), 201-207.
230. Huang, C. S.; Chaudhery, V.; Pokhriyal, A.; George, S.; Polans, J., et al., Multiplexed Cancer Biomarker Detection Using Quartz-Based Photonic Crystal Surfaces. *Analytical chemistry* **2012,** *84* (2), 1126-1133.
231. Cunningham, B.; Li, P.; Lin, B.; Pepper, J., Colorimetric resonant reflection as a direct biochemical assay technique. *Sensor Actuat B-Chem* **2002,** *81* (2-3), 316-328.
232. Cunningham, B. T.; Laing, L., Microplate-based, label-free detection of biomolecular interactions: applications in proteomics. *Expert Rev Proteomics* **2006,** *3* (3), 271-281.
233. Guerra, E. N. S.; Rêgo, D. F.; Elias, S. T.; Coletta, R. D.; Mezzomo, L. A. M., et al., Diagnostic accuracy of serum biomarkers for head and neck cancer: A systematic review and meta-analysis. *Critical Reviews in Oncology / Hematology* **2016,** *101*, 93-118.
234. Biosystems, A. Protein Biomarker Discovery, Verification and Validation.
235. Mischak, H.; Schanstra, J. P., CE-MS in biomarker discovery, validation, and clinical application. *Proteom Clin Appl* **2011,** *5* (1-2), 9-23.
236. Diamandis, E. P., Biomarker validation is still the bottleneck in biomarker research. *Journal of internal medicine* **2012,** *272* (6), 620-620.
237. Gillette, M. A.; Carr, S. A., Quantitative analysis of peptides and proteins in biomedicine by targeted mass spectrometry. *Nat Methods* **2013,** *10* (1), 28-34.
238. Gilbert, M.; Livingston, R.; Felberg, J.; Bishop, J. J., Multiplex single molecule counting technology used to generate interleukin 4, interleukin 6, and interleukin 10 reference limits. *Analytical biochemistry* **2016,** *503*, 11-20.

239. Rissin, D. M.; Kan, C. W.; Campbell, T. G.; Howes, S. C.; Fournier, D. R., et al., Single-molecule enzyme-linked immunosorbent assay detects serum proteins at subfemtomolar concentrations. *Nature biotechnology* **2010,** *28* (6), 595-599.
240. Rissin, D. M.; Kan, C. W.; Song, L. N.; Rivnak, A. J.; Fishburn, M. W., et al., Multiplexed single molecule immunoassays. *Lab Chip* **2013,** *13* (15), 2902-2911.
241. Gold, L.; Ayers, D.; Bertino, J.; Bock, C.; Bock, A., et al., Aptamer-Based Multiplexed Proteomic Technology for Biomarker Discovery. *PloS one* **2010,** *5* (12).
242. Russell, T. M.; Green, L. S.; Rice, T.; Kruh-Garcia, N. A.; Dobos, K., et al., Potential of High-Affinity, Slow Off-Rate Modified Aptamer Reagents for Mycobacterium tuberculosis Proteins as Tools for Infection Models and Diagnostic Applications. *J Clin Microbiol* **2017,** *55* (10), 3072-3088.
243. Chen, C.; Zhou, S.; Cai, Y.; Tang, F., Nucleic acid aptamer application in diagnosis and therapy of colorectal cancer based on cell-SELEX technology. *npj Precision Oncology* **2017,** *1* (1), 37.
244. Barak, V.; Goike, H.; Panaretakis, K. W.; Einarsson, R., Clinical utility of cytokeratins as tumor markers. *Clin Biochem* **2004,** *37* (7), 529-540.
245. Takada, M.; Masuda, N.; Matsuura, E.; Kusunoki, Y.; Matui, K., et al., Measurement of cytokeratin 19 fragments as a marker of lung cancer by CYFRA 21-1 enzyme immunoassay. *British Journal Of Cancer* **1995,** *71*, 160.
246. Molina, R.; Filella, X.; Augé, J. M.; Fuentes, R.; Bover, I., et al., Tumor Markers (CEA, CA 125, CYFRA 21-1, SCC and NSE) in Patients with Non-Small Cell Lung Cancer as an Aid in Histological Diagnosis and Prognosis. *Tumor Biology* **2003,** *24* (4), 209-218.
247. Molina, R.; Marrades, R. M.; Augé, J. M.; Escudero, J. M.; Viñolas, N., et al., Assessment of a Combined Panel of Six Serum Tumor Markers for Lung Cancer. *American Journal of Respiratory and Critical Care Medicine* **2016,** *193* (4), 427-437.
248. Integrative Analysis of Lung Cancer, E.; Risk Consortium for Early Detection of Lung, C., Assessment of lung cancer risk on the basis of a biomarker panel of circulating proteins. *JAMA Oncology* **2018**, e182078.
249. Pujol, J. L.; Molinier, O.; Ebert, W.; Daurès, J. P.; Barlesi, F., et al., CYFRA 21-1 is a prognostic determinant in non-small-cell lung cancer: results of a meta-analysis in 2063 patients. *British Journal Of Cancer* **2004,** *90*, 2097.
250. Roeraade, J., Cutting of Glass and Fused-Silica Capillaries. *J High Res Chromatog* **1983,** *6* (3), 140-144.
251. Tarigan, H. J.; Neill, P.; Kenmore, C. K.; Bornhop, D. J., Capillary-scale refractive index detection by interferometric backscatter. *Analytical chemistry* **1996,** *68* (10), 1762-1770.
252. He, A.; Liu, T. C.; Dong, Z. N.; Ren, Z. Q.; Hou, J. Y., et al., A novel immunoassay for the quantization of CYFRA 21-1 in human serum. *Journal of clinical laboratory analysis* **2013,** *27* (4), 277-283.
253. Muzyka, K., Current trends in the development of the electrochemiluminescent immunosensors. *Biosens Bioelectron* **2014,** *54*, 393-407.
254. Atwater, T.; Cook, C. M.; Massion, P. P., The Pursuit of Noninvasive Diagnosis of Lung Cancer. *Semin Resp Crit Care* **2016,** *37* (5), 670-680.
255. Gould, M. K.; Ananth, L.; Barnett, P. G.; Cooperative, V. A. S., A clinical model to estimate the pretest probability of lung cancer in patients with solitary pulmonary nodules. *Chest* **2007,** *131* (2), 383-388.

Chapter 8: CIR Analysis Tools

To facilitate translation of the CIR platform to the broader community, I have encoded the data analysis strategy presented in **Chapter 4** into a set of tools that enable a user to easily analyze their data. The CIR analysis program is a LabVIEW^{TM} virtual instrument (VI) that processes the raw phase-over-time data into averaged values that are then exported to excel. A brief overview of the program is presented in **Fig. 8.1**. The data is loaded into the program (step 1), then the user must select the region of the data containing the 5-replicate test/reference solution droplets for the first test/reference solution pair (step 2). The program then partitions this trace into "solution samples" and "oil" (step 3-5), at which point the user updates a table containing the averaged values to be exported (step 6). The user then repeats steps 2-5 for the rest of the solution pairs in the droplet train.

The program user interface (**Fig. 8.2**) is arranged so that the user works from top to bottom. The top graph shows the phase shift/time data for the entire droplet train. The operator then uses the green and blue cursors to select the region of interest, which will then be displayed in the middle graph. The bottom graph shows the selected data overlaid with the average values for each droplet pair, as depicted by the large red dots. These values are then added to a table for export to excel, and the process is repeated for all test/reference sample pairs in the droplet train. A complete step by step tutorial for this program is included in **Appendix C**.

Once the averages for all droplet pairs have been tabulated, the operator can export the averaged values for further analysis in the paired CIR Excel Template.

Data workup using the CIR Excel Template

The CIR analysis program exports the data in the form of a tab delineated spreadsheet, consisting of 19 columns and 6 rows (for a standard droplet train consisting of 6 test/reference pairs). The 19 data points per row correspond to the averages of the 19 regions as described in **Fig. 4.3** and **Fig. 8.2**. However, the final data required for biochemical analysis are the 2×p signals

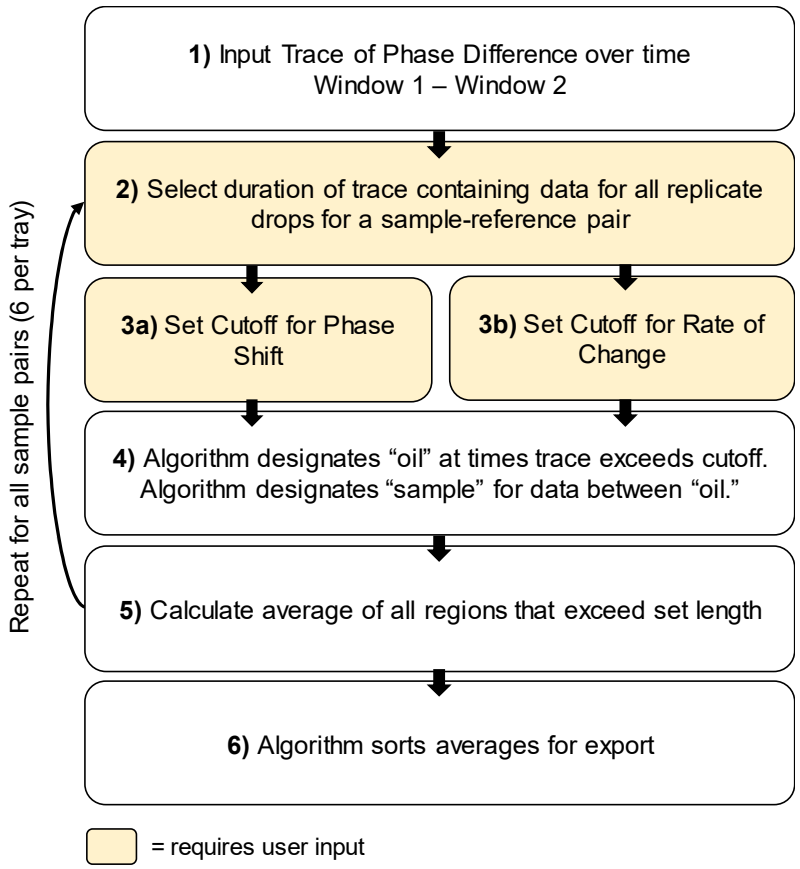

Fig. 8.2 CIR Analysis Algorithm Flow Chart.

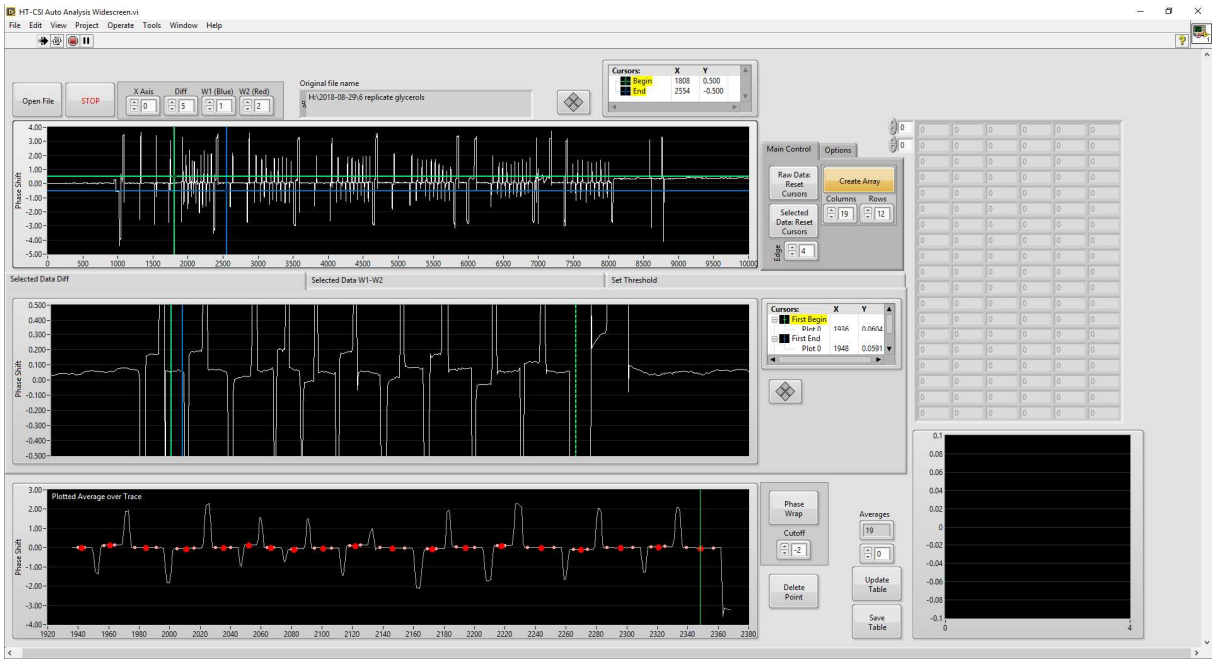

Fig. 8.1 CIR analysis program user interface.

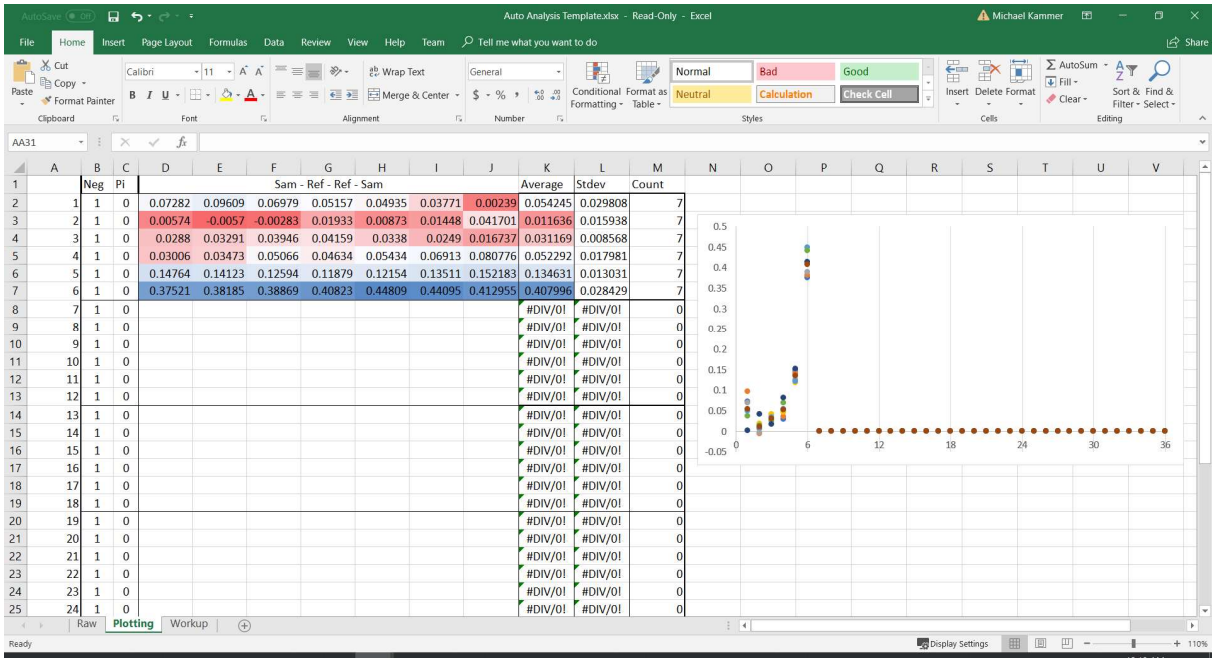

Fig. 8.3 The CIR Excel Template is a companion to the CIR Analysis program. Each row contains all replicate values for a 5 test/reference solutions droplet train. The 2×p values are listed in columns D – J, and these are plotted on the graph on the right. Column K contains the final averaged phase shift for each droplet pair.

(**Fig. 4.4**). To expedite this last step of analysis, I have prepared an Excel Template spreadsheet that converts the CIR Analysis program output into a list of 2×p averages with standard deviations.

The CIR Excel Template has 3 "sheets," as denoted by the three tabs on the bottom left of **Fig. 8.3**. The first is titled "Raw," and this is where the operator pastes the sheet of averages from the CIR analysis (further explained in **Appendix C**). The second sheet (displayed in **Fig. 8.8**) is titled "Plotting." This sheet is the primary point of interaction for the user working with the CIR Excel Template. Each row contains all replicate 2×p values for a 5 test/reference solution droplet train (the standard configuration, as described above) in column D-J. Each row in column K has the average of the replicate values in that row. Column L has the standard deviations of the replicate values in that row, and column M contains the number of replicate values. The standard droplet train contains 6 test/reference solution pairs per run, therefore this sheet is vertically delineated with a black line every six rows for ease of navigation. The 2×p values are automatically colored based on their relative value, with the lowest numbers colored red and the highest numbers colored blue. The coloration is a useful aid in quickly spotting troublesome data

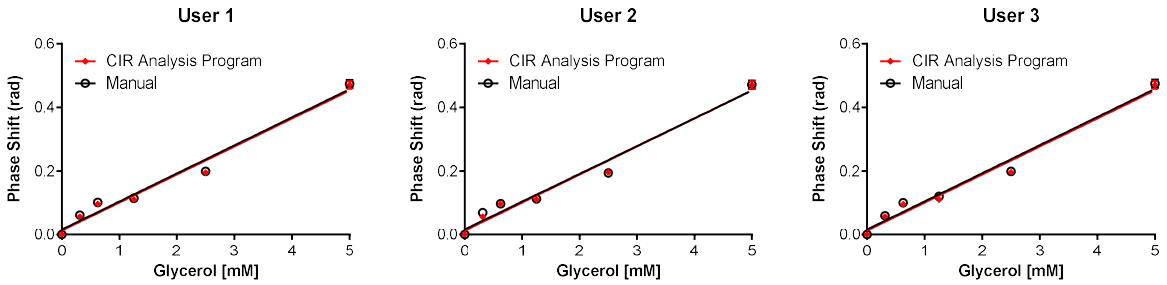

Fig. 8.4 Comparison of the same experimental CIR data when analyzed manually and when using the CIR analysis program, repeated by three independent users. There is excellent agreement between manual and automated analysis for all users.

or outliers. For example, row 2, columns D through J contain the 2×p values for the first concentration, which have an average of 0.0542. The value in row 2, column J is 0.002, nearly two standard deviations from the mean, and could be a statistical outlier. The values in row 2, columns D to I are colored lightly, but the value in 2J is a dark red. This coloration aids the user in quickly finding which values may be outliers. If all numbers in a row are colored similarly (for example, the values in row 7 are all a similar shade of blue) there are no outliers.

For the example data displayed in **Fig 8.3,** a single *tray* of 6 sample pairs has been pasted into the file, and therefore only rows 1-6 show are filled while rows 7-24 are empty. Rows 7-24 will automatically populate when the user pastes data into the corresponding location in the "raw" sheet.

On the right side of the "plotting" sheet is a plot of the replicate 2×p values. The X-axis for the plot is column A, which is initially numbered in increasing integers, starting with 1. For concentration dependent data, the values in column A can be replaced with the concentration of each sample pair, which will alter the plot to display a common dose-response curve.

Column B (Neg) and C (Pi) of the "plotting" sheet are used only when troubleshooting in advanced situations, and are described in detail in **Appendix C**.

The third sheet is entitled "Workup," and requires no input by the user. This sheet contains formulas that perform calculations in the background. The full function of each section of this template is described in detail in **Appendix C**.

After pasting the data in the Spreadsheet template, the operator can then adjust the plot to display the data appropriately, perform curve fitting, or copy the values in columns K-M (titled Average, Stdev, and Count) to paste into a 3rd party curve fitting or plotting program.

Comparison of Analysis Software vs Manual Averaging

Figure 8.4 displays the results of analysis by 3 independent users when analyzing the same raw data using both the CIR analysis program (displayed as the colored diamonds) and by manually averaging the regions (displayed as the open circles). For all 3 users, there is nearly perfect overlap between the manual analysis (open circles) and CIR Analysis Program (diamonds), which implies the CIR analysis program processes the data accurately. The linear fit of the data is plotted for both analyses, and due to the perfect overlap, the linear fits are indistinguishable.

The analytical figures of merit for all 6 analyses (3 users, manual vs. auto) are presented in **Table 8.1**. It is interesting to note here that while the response function (slope) shows good agreement across all three users and both analysis methods, the fitted y-intercept shows good agreement between the three users, but there is a discrepancy between auto (0.013, 0.012, and 0.012) and manual (0.016, 0.016, 0.016). An explanation for this discrepancy in slope is that while the CIR analysis program selects all data points between "oil," a human user biases the selected data to the middle of each data region when manually selecting the data to average.

The same data presented in **Fig. 8.4** can be used to determine the reproducibility of analysis across users. **Figure 8.5** shows the standard deviation of the three independent measurements as calculated for the six sample pairs (0, 0.31, 0.625, 1.25, 2.5, and 5 mM glycerol). Each data point represents the standard deviation of the three averages. For example, when analyzing the 0.31 mM glycerol data manually, User 1 calculated the average as 0.0614 rad, User 2 calculated 0.0687 rad, and User 3 calculated 0.05919. The standard deviation of these three independent analyses is 0.0050 rad. This calculation is performed for the manual analysis and for the CIR analysis program analysis. As demonstrated by **Figure 8.5**, there is less variability (lower standard deviations) in analyses across the three users when using the CIR analysis program vs. when performing the

Table 8.1 Comparison of manual vs CIR Analysis Program

	User 1		**User 2**		**User 3**	
	Auto	Manual	Auto	Manual	Auto	Manual
Slope	0.088 ± 0.007	0.088 ± 0.007	0.088 ± 0.007	0.087 ± 0.007	0.088 ± 0.007	0.088 ± 0.007
Y-Int	0.013	0.016	0.012	0.016	0.012	0.016
R^2	0.9775	0.9762	0.9784	0.9729	0.9783	0.9777
LOQ	0.532	0.574	0.520	0.551	0.517	0.620

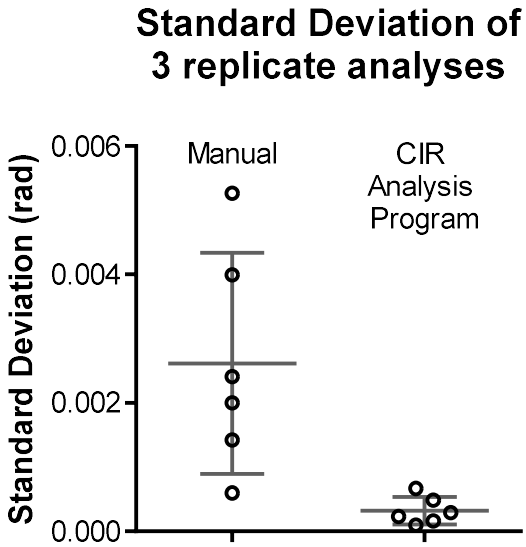

Fig. 8.5 Standard deviation of the analysis of the same data across 3 independent users.

analysis manually. While the CIR Analysis Program minimizes the discrepancy between users, it should be noted that this discrepancy is already very small and unlikely to significantly affect manually analyzed data. Even the largest discrepancy (0.005 radians) correlates to ~3×10^{-7} RIU, which is below the typical detection limit for the device (~5×10^{-7} RIU). Given the breadth of results we have obtained previously with the CIR and the small magnitude of error that is inherent to manual analysis (below the detection limit of the device), it is reasonable to assume that manually analyzing assay data has not significantly impacted the accuracy of past CIR results.

The CIR Analysis Program enables much faster analysis of raw CIR data. To analyze the data presented in **Fig. 8.4**, the three users spent 19, 18, and 22 minutes to analyze the data manually. But when using the CIR analysis program, the users spent 2, 3, and 2.5 minutes. This is an average of approximately 17 minutes in time savings when analyzing a 6-sample-pair tray's data. For example, when analyzing the CIR data for a 225-patient sample cohort and the associated controls and calibration curves (which would amount to an extra 75 sample pairs), data analysis using the CIR Analysis Program would save 12.9 hours when compared to analyzing the data manually.

The advantages to using the data analysis program include ease of use, time savings, and making the technology more translatable so that an unskilled user can use the CIR.

Conclusion

This chapter has presented the strategy employed in a set of tools I have created for analysis of CIR data, and presented a preliminary validation of these tools. The CIR analysis program enables a user to quickly convert the raw CIR phase/time data into a set of averages. These averages are then imported into the CIR Excel Template, which parses the data into a set of average and standard deviation values, which can be used for further data analysis in Excel or in 3rd party applications (such as Graphpad Prism or Origin). Three users analyzing the same data demonstrated good correlation between their manual analysis and analysis using the CIR analysis program, with good agreement in the analysis across all three users.

Conclusions and Future Directions

Here I have described advances to the theory, instrumentation, and applications of the free-solution molecular interaction assay. I have also demonstrated an ultra-sensitive interferometric reader. The studies contained here represent major advancements in understanding the mechanism for signal generation for free-solution assay (FSA) and demonstrating the utility of the assay methodology. Furthermore, I implemented a compensated interferometric reader that enables FSA for studies in biomarker validation, small molecule quantification and pharmacologic mechanism of action studies. The methods presented here represent an emerging technique with the potential to revolutionize drug discovery, medicine, biomedical engineering, and analytical chemistry. The work presented here showcases improvements to the theory, instrumentation, and biomedical applications for this potentially revolutionary platform technology.

Chapter 1: Chapter 1: Origin and prediction of free-solution interaction studies performed label-free**,** adapted here from Proceedings of the National Academy of Sciences, Volume 113, presents the operational parameters for the free-solution assay and a first pass at defining the response function, or FreeSRF, was developed on a diverse training set and provided excellent accuracy and predictability for the systems studied. Supporting information for this chapter is included in **Appendix A.**

However, based on insights gained recently, I hypothesize that building training sets for specific molecular species (i.e. aptamer-small molecule, protein-antibody, etc.) and for specific sample matrices (i.e. aqueous vs non-aqueous, polar vs nonpolar solvents, etc.) will further improve the prediction accuracy for these specific types of interactions, while adding to the understanding of the mechanism of free-solution interaction assays. I also postulate that these improvements in the understanding of FreeSRF signal transduction will lead to intelligent probe design and therefore the ability to design specific molecular probes that capitalize on the FSA mechanism to provide larger signals and improved assay sensitivity. In our initial model, we used surface area and radius of gyration as our markers of change in conformation/hydration, but there

may be other physical parameters from molecular structures that add improved performance to the model, for example change in surface charge, ordered vs disordered sidechains, and hydrogen bond formation/breaking.

Similarly, a first principles approach describing the mechanism for free solution assays, beginning from Maxwell's equations of light propagation and interaction with matter, is expected to further improve our understanding of FreeSRF. The Clausius Mossotti relation and an effective medium theory approximation such as the Maxwell-Garnett mixing formula are both currently being investigated, with promising preliminary results.

In **Chapter 2: Chapter 2: A Highly Compensated Interferometer** for Biochemical Analysis, adapted here from ACS: Sensors Volume 3, I presented the compensated interferometer, an improved interferometric sensing approach that facilitates high sensitivity nano-volume refractive index (RI) measurements and molecular interaction assays without a temperature controller.

Chapter 3: Chapter 3: Longitudinal Pixel Averaging for Improved Compensation in Backscattering Interferometry, adapted here from Optics Letters Volume 43, expanded upon the work in Chapter 2 by defining the channel interrogation properties needed to achieve true compensation between the two RI sensing regions.

Chapter 4: CIR Data Analysis Methods provides a technical description of the signal extraction mechanism employed to convert the raw phase shift/time data collected by the CIR to a useful format.

Chapter 5: Rapid assay development and quantification of two chemical nerve agents in serum describes research to demonstrate an important biomedical application of the compensated interferometer. This chapter, adapted here from a manuscript submitted to Lab on a Chip, presents a strategy for developing highly sensitive, highly specific quantitative assays for organophosphorus nerve agents in serum by combining the FSA method with the compensated interferometric reader and aptamer probes. In this work, FSA-CIR provided sensitivity better than the current gold standard mass spectrometry-based methods without the need for multiple extraction steps, costly equipment, or derivatization/immobilization steps. The research shows that the assay method is rapid, robust, quantitative, and highly sensitive in a complex matrix. Supporting information for this chapter, including CIR setup, in depth methods, and a description of the pharmacokinetic calculations is included in **Appendix B**.

Chapter 6: Chapter 6: Quantitation of Opioids and the Prospect of Improved Diagnosis of Neonatal Abstinence Syndrome represents another biomedical application that significantly improves on the current mass-spec based method, which is time-consuming, expensive and has limited performance. In this work I demonstrated assays for quantitating three opioid targets (oxycodone, hydrocodone, and fentanyl) and their primary urinary metabolites (noroxycodone, Norhydrocodone, norfentanyl). Again, I used aptamer probes (DHA) to demonstrate the potential of FSA-CIR. In addition to developing assays for use in urine, defining the analytical figures of merit, performing spiked unknown determinations, and interrogating specificity, or cross reactivity, I performed pharmacokinetic modeling. These modeling efforts showed that the level of opioid target in neonatal urine samples would be below the detection limits of current methods before symptoms arose in the patient. The significantly improved limits of quantification (LOQs) provided by FSA over current methods extend the window in which the level of opioid in neonatal urine samples would be detectable. These improvements in detection limits over current gold standard methods provided by FSA point to the potential to do confirmatory testing of neonate opioid exposure for a longer time period than existing methods and well-after the onset of neonatal abstinence syndrome symptoms. Similarly, the pharmacokinetic modeling efforts indicate that FSA could be valuable in the neonatal pain management setting.

Chapter 7: Preclinical evaluation of a free solution assay for the quantification of a candidate Lung Cancer Biomarker CYFRA 21-1 presents third biomedical application I explored with FSA-CIR. Here I performed a preclinical evaluation of the potential lung cancer serum biomarker CYFRA 21.1 in a blinded 225-patient cohort. The overall goal of this investigation was to improve the capability for diagnosis of lung cancer by addressing the need for an accurate diagnostic biomarker. The hypothesis of this ongoing study is that by virtue of lower LOQs provided by FSA-CIR measurements it will be possible to redefine the concentration of the candidate serum biomarker CYFRA 21-1 in the control population of patients diagnosed with IPNs. Results from FSA-CIR presented in this chapter showed that by using a single monoclonal antibody as the probe, it was possible to obtain a 40-fold improvement in assay sensitivity over the current gold-standard method, electrochemiluminescence (ECL), which greatly increased the discriminatory power of the biomarker. If these preliminary observations hold true for additional patient cohorts and a more rigorous clinical analysis, this avenue of use for FSA and CIR could

lead to a paradigm shift in how lung cancer patients are managed, possibly improving diagnosis of this otherwise difficult to detect disease.

Chapter 8: **CIR Analysis Tools** describes the algorithm used in the Auto Analysis Program I wrote in LabVIEW™, which is intended to simplify system operation. A step-by-step tutorial that teaches how to operate this program is included in **Appendix C**. Additionally, a troubleshooting guide covering several other aspects of CIR setup and function not included elsewhere are presented in **Appendix D**.

While the research included in my dissertation has been focused on target quantification, there are equally impressive opportunities in affinity characterizations, specifically for first-in-human-dose estimation for therapeutic candidate molecules. Results from several projects I participated in that are not included in this dissertation have demonstrated the use of FSA-CIR to obtain in-vivo/in-vitro affinity correlations in serum, cell-derived vesicles, and tissue-derived vesicles. Such measurements can be performed in a matter of days using the FSA method. Other experiments not included in this dissertation showed the potential for direct measurement of multi-site binding, where each binding event produces a RI signal that is unique in both magnitude and direction. Studies of multi-site binding are still in the preliminary stage but show promise for the unperturbed study of complex binding systems. No other small-volume technique, optical or otherwise, can accurately measure binding affinities in native conditions without labeling or surface immobilization of the constituents of sample.

The Redpoint Prototype

While completing the projects presented in this dissertation, I also participated in an academic-industry collaboration aimed at making the compensated interferometer a viable commercial reader or benchtop interaction photometer. The platform, named Redpoint, shown in **Fig 9.1**, was developed in conjunction with Biotex, Inc. (Houston, TX) and represents a nearly mature instrument with relatively mature graphical user interface that guides the user through the process of performing a binding assay, screening assay, or target quantification experiment. This first generation Redpoint device was based upon the chip configuration (as detailed in **Chapters 2 & 3**) and provided excellent RI sensitivity, but was difficult to use due to a less than optimum sample introduction method based on manual pipetting and the need for capillary action to draw the sample into the chip. Chip clogging was found to be an issue as well. Even so, several users

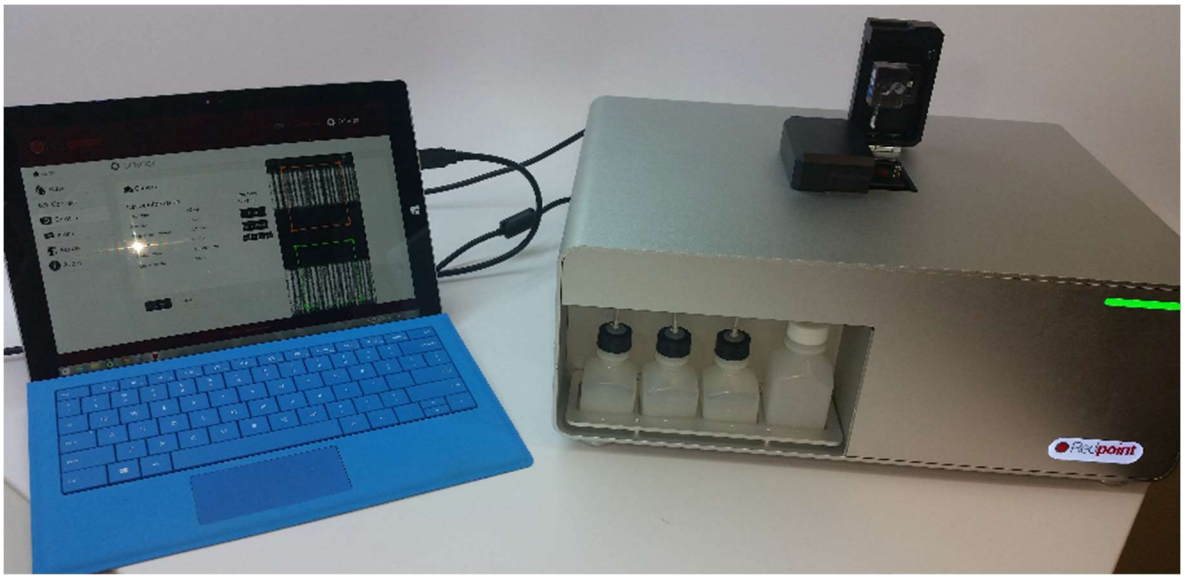

Fig. 9.1 The Redpoint Platform developed in collaboration with Biotex, Inc, represents a fully functional prototype benchtop interaction photometer based upon the compensated interferometer.

were able to perform binding experiments on the platform, demonstrating its functionality and illustrating the potential of the methodology. Redpoint also contained a series of pumps, rinse bottles, tubing, and valves to rinse the microfluidic chip after each sample was measured. Upon demonstrating compensation (Chapter 2 and 3) it became apparent the best course of action for the next generation interferometric reader would be to replace the chip with disposable capillaries. This approach would simplify the user interface and capitalize on the signal/noise improvement provided by the capillary over the chip (as detailed in Chapters 5, 6, and 7). The core Redpoint optical train remains intact though, as does the operating software.

Future Device Improvements

Since Redpoint (and CIR) is based on a low power diode laser, capillary, and a camera to capture the fringes, the optical train opens the door to a miniaturized version of the detector. Elimination of the temperature controller, as possible with the compensated interferometer also greatly simplifies the instrument design paving the way for rapid deployment in the wider scientific community.

I conceptualize Redpoint Gen 2 being designed to function as reader that can rapidly interrogate a series of single-use capillaries, with a simple sample introduction strategy that

requires the user to simply dip the capillary into the sample solution (for example, a patient blood or urine sample) drawing up the premixed sample/reference with capillary action, followed by insertion of the capillaries into the reader. This sample introduction strategy is expected to facilitate rapid, easy use particularly suited to end-users who have not been trained in analytical chemistry techniques, such as nurses in the near-patient setting, which will expedite translation of the technology from lab to clinic.

In the long term I fully anticipate that CI can be miniaturized into a hand-held device or built in a manner that would allow integration into a smartphone attachment with a slot for the disposable capillary and that uses the smartphone's camera, battery, and processing power to run the interferometer.

Similarly, I envision a benchtop version of the CIR, coupled with a droplet generator and automated sample preparation robotics which would enable fully automated automation. In this embodiment of the technology, a "snap in/snap out" disposable capillary cassette would enable easy capillary replacement between experiments, and capillaries that are pre-coated with various surface chemistries (silanized, hydrophobic, or hydrophilic) would allow the end user to tailor the device to the needs of their experiments. The "front end" sample preparation would be handled by a robotic automated pipetter, relieving the end user from the repetitive and precise pipetting steps currently required. Data analysis would also be automated by combining the strategy provided in **Chapters 4 and 8** and **Appendix C** with an internal timer to match data to the corresponding sample. A device incorporating these features could enable free solution assay binding affinities or target quantification where the end user needs only to pipette an approximate amount of sample into a 96 well plate, load the well plate into the device, and let the device handle everything else.

The Future: Applications

Armed with a volume constrained, highly sensitive biosensor based upon the FSA-CIR technology, development of a highly sensitive, highly specific quantitative test requires only the development of a probe (aptamer, antibody, small molecule, or another molecular probe). The possible areas of use are nearly endless, with multiple multi-billion-dollar products within reach.

As discussed in **Chapter 5**, FSA-CIR assays using aptamer probes could provide a field deployable chemical nerve agent detection strategy, applicable to both environmental testing and human exposure testing in blood or urine.

The results from **Chapter 6** demonstrates how an FSA-CIR opioid/opioid metabolite detection strategy could enable low-resource clinical management for neonates at risk of neonatal abstinence syndrome. To progress towards the goal of low resource opioid detection, we have continued our already fruitful collaboration with Base Pair Biotechnologies to further expand the opioid quantification assays to encompass several other high-profile opioid targets, then build the assay and device into an integrated, easy-to-use kit for neonatal abstinence syndrome diagnosis in low-resource hospitals and birthing centers.

Capitalizing on the promising results of our CYFRA 21-1 quantification in lung-cancer studies presented in **Chapter 7**, we aim to increase the number of samples measured by FSA-CIR. Contingent upon validation in individual sample cohorts, we envisage a clinical trial at the Vanderbilt University Medical Center with Dr. Pierre Massion. In this trial, which is currently being designed, patients presenting indeterminate pulmonary nodules will have their level of CYFRA21-1 quantified in a blood sample using the compensated interferometer. The level of CYFRA 21-1 in the patient's blood will then be incorporated into a risk model to aid clinicians in the patient management decision-making process.

Because CYFRA 21-1 is a marker of epithelial inflammation, it could be a useful biomarker in early detection of other carcinomas, such as pancreatic, ovarian, colon, prostate, and breast. Additionally, there are other potential biomarkers that may provide added sensitivity and specificity for detecting lung cancer, and/or allow the clinician to predict response to therapy. I have begun preliminary investigation into the evaluation of Cancer Antigen 125 (CA-125), and plan to move forward with studies of other potential biomarkers including human epididymis protein (HE4), neuron-specific enolase (NSE) and progastrin-releasing peptide (ProGRP) in lung cancer.

Longitudinal studies of biomarker levels may provide added insight, especially among high-risk patients or patients with comorbidities. The improved sensitivity of FSA-CIR over current methods could demonstrate a change in a patient's biomarker levels over time that corresponds to changing risk. The Vanderbilt Thoracic Biorepository has already begun identifying candidate patients for longitudinal studies for which serum samples have been banked,

and the laboratory of Dr. Pierre Massion is designing a study with these samples. As new candidate biomarkers immerge, or previously studied biomarkers show promise for repurposing, we will be in a position to rapidly develop assays with FSA-CIR and evaluate them in a clinical context.

Another important potential application for FSA-CIR is in the detection of infectious disease, especially in low-resource areas of the world. FSA has already demonstrated quantification of plasmodium-host protein interactions on intact, unmodified erythrocytes to study the pathogenesis of malaria [256], and has also been shown to be useful for antibody-antigen quantification for the serological diagnosis of infectious disease [257]. The combination of a low-cost, field deployable detector with a mix-and-read assay would result in a valuable tool for doctors in the developing world. Even in the developed world, viral detection is not employed widely in the clinic, and this leads to over-prescription of antibiotics. Viral RNA hybridization-induced secondary structure alterations have been quantified using the FSA method, suggesting that this approach might be useful for detecting viral biomarkers of infection [258].

In conclusion, the free solution assay method measured by a volume-constrained compensated interferometer represents a powerful tool with many potential uses that can impact human health, quality of life, and healthcare costs. With the simplicity, ease of use, and wide applicability of the method, it is not hard to imagine that the Free Solution Assay method measured by a compensated interferometric reader could be a widely used laboratory technique.

256. Saetear, P.; Perrin, A. J.; Bartholdson, S. J.; Wanaguru, M.; Kussrow, A., et al., Quantification of Plasmodium-host protein interactions on intact, unmodified erythrocytes by back-scattering interferometry. *Malaria journal* **2015,** *14*, 88.
257. Kussrow, A.; Enders, C. S.; Castro, A. R.; Cox, D. L.; Ballard, R. C., et al., The potential of backscattering interferometry as an in vitro clinical diagnostic tool for the serological diagnosis of infectious disease. *The Analyst* **2010,** *135* (7), 1535-1537.
258. Adams, N. M.; Olmsted, I. R.; Haselton, F. R.; Bornhop, D. J.; Wright, D. W., The effect of hybridization-induced secondary structure alterations on RNA detection using backscattering interferometry. *Nucleic Acids Res* **2013,** *41* (9), e103.

Appendix A: Supporting information for Chapter 1: Origin and prediction of free-solution interaction studies performed label-free

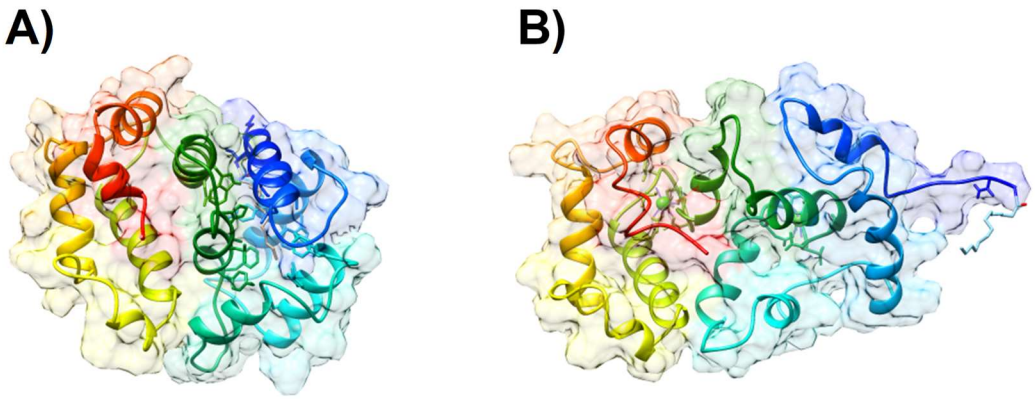

Fig. A.1 Comparison of structures of recoverin before and after Ca^{2+} binding. **A)** Compact conformation of Ca^{2+}-free recoverin showing the myristoyl group sequestered in a hydrophobic pocket and **B)** Ca^{2+}-loaded form in a more extended conformation, where the myristoyl is solvent-exposed.

Modeling and Background

In 1991 a group from Pharmacia [33] showed SPR response was linear with surface concentration of protein (ng/mm^2) for adsorbed species, and introduced the refractive index increment (RII), which was defined as dη/dC in ml/g. They further illustrated that the RI of the surface layer was:

$$\eta_{layer} = \eta_{liquid} + (d\eta/dC)_{dextran}\, Cdextran + (d\eta/dC)_{protein}\, C_{protein} \qquad \textbf{Eq. .1}$$

In addition, the thickness of the protein at the surface, represented by a closely packed protein crystal was calculated. In the absence of values for solvent content and specific volume, they used Matthews report [34] that indicated the fractional solvent content for globular protein

crystals ranged from 30-78% to show the extreme values gave a surface thickness range of 60 and 200nm.

Others have expanded on these observations. In 1998 Sinclair Yee and co-workers [31] showed that the Lorenz-Lorenz equation can be reduced to:

$$\eta_{soln} = f_j\eta_j + f_k\eta_k = f_j(\eta_j - \eta_k) + \eta_k \qquad \textbf{Eq. .2}$$

where *f* is the volume fraction of the species. Using a literature derived value for protein specific volume [259-260] (0.77 mL/g) in Error! Reference source not found., Yee showed that $\eta_{protein} - \eta_{buffer} = 0.234$ RIU. They noted: "since in those solutions $\eta_{buffer} = 1.336$ RIU, (we obtain) $\eta_{protein} = 1.57$ RIU for the *water-free* (unreacted) protein. This value is very close to the index of refraction measured for crystalline proteins of 1.60 RIU, a finding confirmed by Schuck [35]. Importantly these values are greater than those estimated for "adsorbed protein films" using ellipsometric approaches assuming a single optical thickness, since the film volume includes a great deal of water [31, 36-37]. Yee et. al. referred to that part of the film that "are made of protein material itself, *not water*". They also noted, "we believe this approach, which n*eglects the intermixed solvent* in the adlayer, is more direct and general for quantitative analysis of adsorbate coverages for proteins and adsorbates in general."[31] It was also reported that the volume of a functional group can be estimated from its geometry (bond lengths, angles) and van der Waals radii of its atoms or can it can be treated as a parameter and determined by fitting the equation to known RIs. One can also measure η_a in cases where very thick adlayers can be grown. By simply measuring the maximum response for an infinitely thick ($>> l_d$) adlayer, one gets $R_{max} = m(\eta_a - \eta_s)$. Since the slope of the calibration plot, *m*, and the RI of the solvent are known, one can solve for η_a.

In 2000, Davis and Wilson reported on an approach to determine the RII of small molecules for correction of SPR data [39]. They too employed the formalism of a concentration weighted RII and predicted the maximum (BIACORE) SPR instrument response for binding of a single ligand:

$$RU_{obs} = \eta * X = X\,[(\delta\eta/\delta C)_{ligand}\, C] \qquad \textbf{Eq. .3}$$

where RU_{obs} is the observed instrument response in resonance units after blank subtraction, η is the refractive index at the surface which increases as ligand binds to immobilized macromolecule, *X* is a factor to convert η to RU_{obs}, $(\delta\eta/\delta C)_{ligand}$ is the refractive index increment

(RII) of the bound ligand, and *C* is the concentration of ligand bound at the biospecific surface in mass/volume. In a plot of Δη versus concentration they showed that the RII range for small molecules can be quite large (0.15 – 0.34), and that the value measured for the protein BSA corresponded well with literature values of 0.17 – 0.18. They predicted the maximum SPR instrument (BIACORE) response for binding of a single ligand to be:

$$(RU_{pred})_{max} = RUM * (MWL/MWM) * (\delta\eta/\delta C)L / (\delta\eta/\delta C)M \qquad \textbf{Eq. .4}$$

$(RU_{pred})_{max}$ is the predicted maximum instrument response in resonance units for binding at a single site, RU_M is the experimental amount of macromolecule immobilized on the chip in resonance units, MW_L is the molecular weight of the ligand, MW_M is the molecular weight of the immobilized macromolecule, $(\delta\eta/\delta C)_L / (\delta\eta/\delta C)_M$ is the RII of the macromolecule. The relative mass was also shown to be an important parameter in predicting the maximal signal flow injection gradient SPR systems [40].

Shortly after this report, a group in Brazil [40] showed that flow injection gradient SPR systems exhibit the same response as previously reported and that the expression:

$$C_{ligand} = \Delta\theta/X(\delta\eta/\delta C)_{ligand} \qquad \textbf{Eq. .5}$$

could be used to determine the RII of the ligand/molecule and macromolecule solutions, where *C* is concentration of molecules adsorbing over surfaces, Δθ shift detected and X is the instrument calibration constant.

The existing paradigm described above is based on a model that defines the response for RI sensing methods as being proportional to the mass or concentration weighted change in RI. Critical to our point is that this supposition *does not* take into account the possibility that signal change may be impacted by significant conformation and hydration changes upon chemical or biochemical transformation (folding, binding, changes in waters of hydration).

The Free-Solution Signal in the Absence of a Mass Change

Using the titration and incubation DHA:DHA duplexes with trifluoroethanol (TFE), an established method for converting the duplex structure [58-59], we induced the transition from the B-form to A-form (**Figure A.3**). We then monitored these structural transformations with circular dichroism (CD), ellipticity at 270nm, and BSI [57]. As illustrated in **Figure A.3A**, the CD analysis confirmed the predicted structural transition in the DHA:DHA duplex. Correcting for the bulk RI

change in the solvent, we also found that, as the DHA:DHA duplex adopted a more A-form, both the ellipticity signal and the free-solution change in RI increased significantly (**Figure A.3B**). This correlation is of particular importance, because the ellipticity signal reports film thickness and is widely accepted method to determine conformation changes [261]. Collectively, the results confirm that the free-solution readout reports a structural transformation in the DHA duplex.

Heuristic Model for the Free-Solution Response Function

Our first attempt at modeling the free-solution assays was heuristic and based on the assumption that binding-induced change in hydrodynamic radius dominated the signal for CaM interactions. The preliminary calculations utilized the PDB structural information to estimate the radius of gyration (R_{gyr}) and solvent accessible surface area (SASA) of the bound and unbound species (ΔR_{gyr} and ΔSASA). A simple multivariable linear equation was obtained that relates the interferometry signal in phase, to change in R_{gyr} and SASA for the CaM system ($\Delta BSI = 1.0 + 2.6\times10^{-4}\ \Delta SASA + 0.054\ \Delta R_{gyr}$). **Figure A.4A** shows the correlation between the predicted and experimental values for free-solution interaction studies of CaM binding Ca^{2+}, Ca^{2+}-CaM – TFP, Ca^{2+}-CaM – calcineurin, Ca^{2+}-CaM – M13 peptide. Calcineurin – CaM data spread (purple) is rather large due to a wide range of values for SASA for structures with close R_{gyr} values. The surprisingly good correlation ($R^2 = 0.88$) between the actual and predicted signal magnitude for these binding events encouraged us to further our investigation.

Figure A.4B presents the results from our unsegregated model, which uses a wide range of χ values (all of those evaluated), but with a modest Spearman correlation coefficient (ρ_s=0.853), a nonparametric measure of statistical dependence between variables indicating that the relationship is not random.

Mass Balance Equation Calculations

To calculate the ΔRIU of the test samples, the concentration of product must first be calculated using the mass balance equation. A binding system's dissociation constant (KD) is related to the concentration of free protein [P], free ligand [A] and bound complex [PA] by the mass-balance equation:

$$K_D = \frac{[P][A]}{[PA]} \qquad \textbf{Eq. .6}$$

Since the total amount of protein and ligand can be defined as:

$$[P]total = [P]free + [PA] \quad \textbf{Eq. .7}$$

$$[A]total = [A]free + [PA] \quad \textbf{Eq. .8}$$

These equations can be solved for amount of free protein and free ligand as:

$$[P]_{free} = [P]_{tot} - [PA] \quad \textbf{Eq. .9}$$

$$[A]_{free} = [A]_{tot} - [PA] \quad \textbf{Eq. .10}$$

The equation for KD can then be rewritten as:

$$K_D = \frac{([P]_{tot} - [PA])([A]_{tot} - [PA])}{[PA]} \quad \textbf{Eq. .11}$$

This can be rearranged to a quadratic in the following manner:

$$K_D[PA] = ([P]_{tot} - [PA])\,([A]_{tot} - [PA]) \quad \textbf{Eq. .12}$$

$$K_D[PA] = [P]_{tot}[A]_{tot} - [A]_{tot}[PA] - [P]_{tot}[PA] + [PA]^2 \quad \textbf{Eq. .13}$$

$$0 = [PA]^2 - [A]_{tot}[PA] - [P]_{tot}[PA] - K_D[PA] + [P]_{tot}[A]_{tot} \quad \textbf{Eq. .14}$$

$$0 = [PA]^2 - ([P]_{tot} + [A]_{tot} + K_D)[PA] + [P]_{tot}[A]_{tot} \quad \textbf{Eq. .15}$$

The concentration [PA] can then be solved for by using the quadratic equation:

$$[PA] = \frac{([P]_{tot} + [A]_{tot} + K_D) \pm \sqrt{([P]_{tot} + [A]_{tot} + K_D)^2 - 4[P]_{tot}[A]_{tot}}}{2} \quad \textbf{Eq. .16}$$

This result will yield two outcomes, only one of which will be physically relevant, which is used to calculate the amount of complex present in a binding assay based upon known concentrations of the protein, ligand, and the KD.

Calculation of dη/dc signal

Here we perform a quantitative comparison of the convention and FreeSFR when used to predict/measure a refractive index change for a binding event. According to Qian et. al., the mass weighted refractive index increment (RII) for a protein complex is:

$$\frac{d\eta}{dc}_{complex} = (1\text{-}W_r)\frac{d\eta}{dc}_{ligand} + W_r\frac{d\eta}{dc}_{receptor} \quad \textbf{Eq. .17}$$

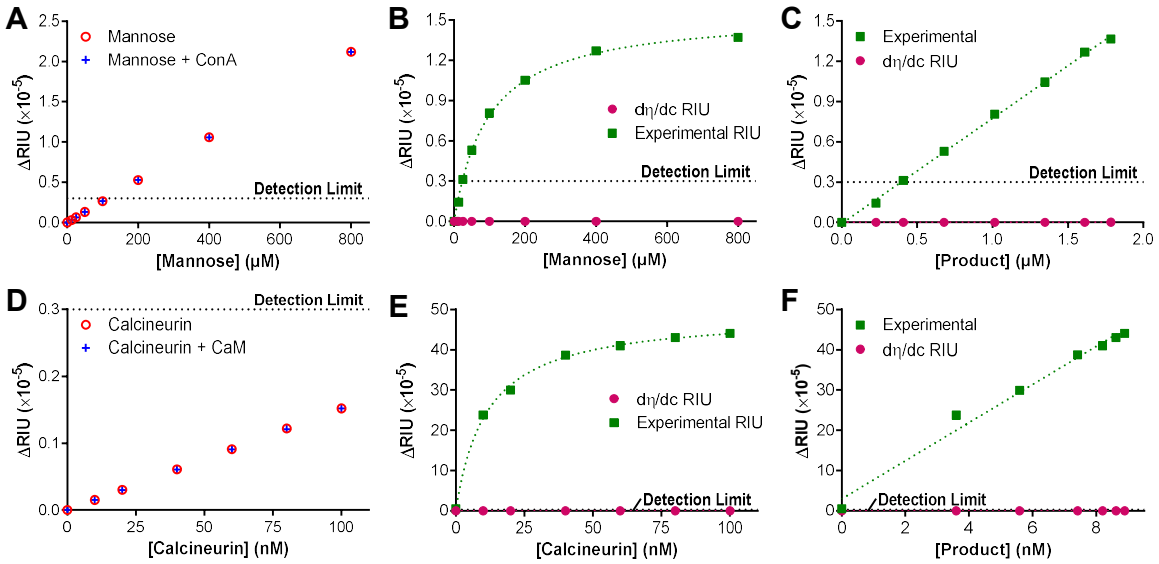

Fig. A.2 Determination of the predicted dη/dc ΔRIU. Plots show the calculated dη/dc for the reference (O) and test (+) samples for **A)** the Concanavalin A – Mannose system and **D)** the Calmodulin – Calcineurin system. Plots **B)** and **E)** show the predicted $d\eta/dc_{complex}$ signal (●) compared with the experimentally observed signal (■) for ConA-mannose and Calmodulin-calcineurin, respectively. Plots **C)** and **F)** show the predicted $d\eta/dc_{complex}$ signal (●) compared with the experimentally observed signal (■) versus product concentration for ConA-mannose and Calmodulin-calcineurin.

where W_r is the mass percentage of the receptor in the complex [262]. For our example calculation we use the mannose binding to Concanavalin A (ConA) system. The refractive index increment (RII) values used was 0.146 ml/g [40] for mannose and 0.190 ml/g for ConA [35]. Using a molecular weight for mannose of 180 Daltons and 26.5 kDa for ConA and equation **A.17**, the calculated mass weighted RII for the binding system ($d\eta/dc_{complex}$) is 0.1897 ml/g.

The RII values were then used to predict the refractive index change in both the reference and test sample solutions. The references are samples that do not contain the receptor (ligand alone), so ΔRIU calculated by multiplying the RII by the concentration of ligand (**Eq A.18**).

$$\Delta RIU_{reference} = RII_{ligand} \times [ligand] \qquad \textbf{Eq. .18}$$

To calculate the ΔRIU of the test samples, the concentration of product must first be calculated using the mass balance equation as described above (**Eq. A.7 – A.12**). From there the amount of receptor and ligand left in solution can be calculated as:

$$[receptor] = [receptor]_{initial} - [product] \qquad \textbf{Eq. .19}$$

$$[\text{ligand}] = [\text{ligand}]_{\text{initial}} - [\text{product}] \qquad \textbf{Eq. .20}$$

Using these concentration values and the RII's, the maximum ΔRIU of the binding samples can be calculated as:

$$\Delta RIU_{test} = RII_{product} \times [\text{product}] + RII_{receptor} \times [\text{receptor}] + RII_{ligand} \times [\text{ligand}] \qquad \textbf{Eq. .21}$$

These values were plotted versus *ligand* concentration (**Figure A.2A**) and illustrate that, while three of the reference and test samples are predicted to give measurable RI signals using BSI, the ΔRIU for these samples will be very similar.

In order to further illustrate our point, the ΔRIU predicted for the $d\eta/dc_{complex}$, which is the *difference* between the reference and test samples at the same *ligand* concentration, was plotted versus ligand concentration in **Figure A.2B.** The plot also presents the *experimentally measured* binding signal produced by BSI (**Figure A.2B**), clearly showing the difference in measured signal and that predicted by the current theory. This example shows that we are in agreement with the statement [65]: "that it would be in conflict with the *conventional* theory to expect a protein binding event would produce a measurable RI change expected by pure dη/dc considerations."

Additional calculations are illuminating. For the Mannose – ConA system, the concentration of complex at maximum binding was found to be 1.79 μM (4.76×10^{-5} g/mL) or a maximum ΔRIU of 1.4×10^{-8}. This value is considerably below the detection limit of most RI detectors (ca. 10^{-6}). In another calculation, we set the experimental ΔRIU equal to the difference between the ΔRIU of the test sample and the ΔRIU of the reference sample at the highest concentration, we find that the RII of the ConA-mannose complex would need to be 3164.1 mL/g to generate the experimental signal. The RII calculated using the Qian equation is 0.1897 mL/g.

Plotting the calculated ΔRIU versus *product concentration*, along with the actual ΔRIU measured by BSI for this binding event (**Figure A.2C**), further illustrates the dramatic disconnect between the signal predicted from dη/dc considerations and that measured by our interferometer. In this case, the conventional model predicts a signal that it is 3 orders of magnitude below the experimentally measured ΔRIU.

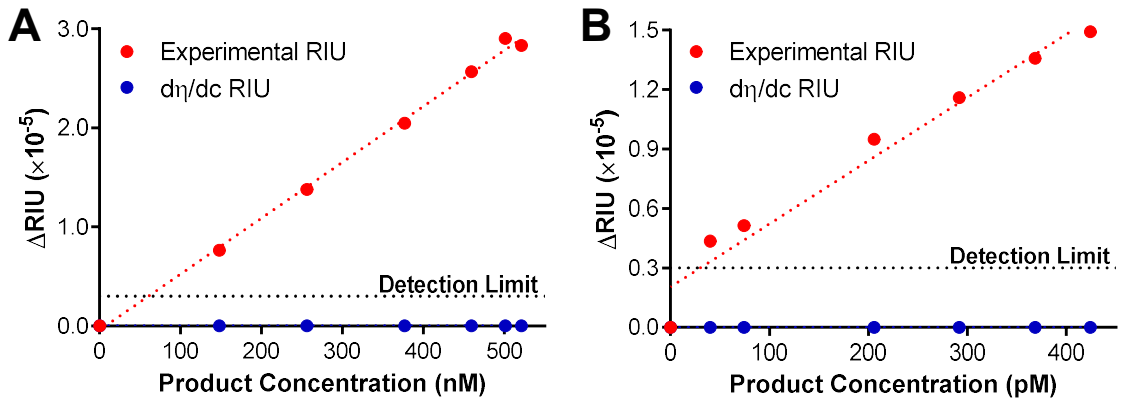

Fig. A.3 Comparison of Experimental and Modeled dη/dc Signal. Plots showing the experimental BSI signal in RIU with the calculated dη/dc signal for **A)** Recoverin binding Ca^{2+}; and **B)** Carbonic Anhydrase II binding dansylamide.

These calculations were repeated for the calmodulin - calcineurin assay. **Figure A.2D-F** illustrates similar results are obtained for the protein-protein binding pair. Here, even though the ligand is much larger in mass (and absolute RI), the ΔRIU of the reference (calcineurin) and the test samples, (**Eq. A.17 – A.21**), are below the detection limits of the instrument. We attribute this result to the use of considerably lower concentrations of the ligand. As before, the FreeSRF (binding) signal quantified by the interferometer was large and reproducible at ΔRIU (4.41×10^{-4}).

Figure A.3 presents the results for performing the calculations show in **Eq. A.17 – 21** for two other binding systems. According to Zhao et. al, large proteins (<10kDa) exhibit a RII of 0.190 with a Gaussian standard deviation of 0.003 mL/g [35], so this value was used for all species that met that criteria. In all cases, a 0.003 mL/g deviation produced minimal change in the final mass weighted refractive index change calculation. This result is principally due to the large differences between the masses of the species. For the small molecule dansylamide, no RII information was available, so the RII of 0.2 mL/g was used, which is a common RII for small molecules. Regardless, no RII value in the range of 0.1 mL/g to 0.5 mL/g produced an RI change large enough to be detected by current RI techniques.

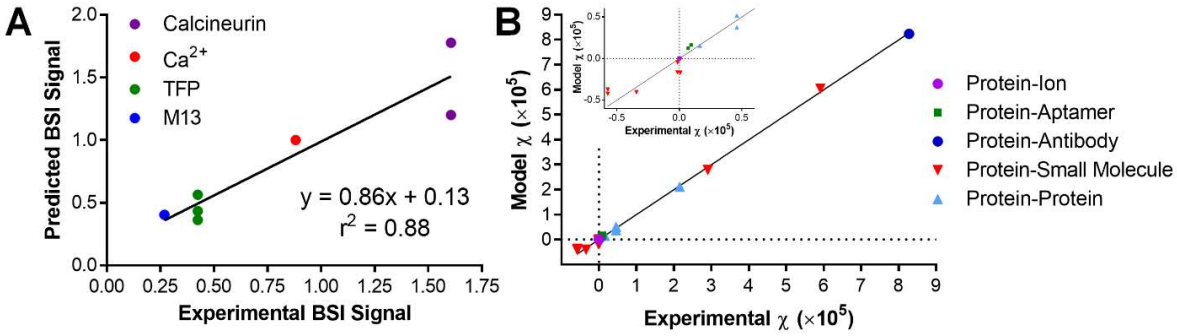

Fig. A.4 A) Predicted versus BSI experimental values for the CaM binding system. **B**) Plots showing correlation of χ_{exp} and χ_{model} of the unsegregated learning set.

Experimental Parameters for Effective Free-Solution Measurements

Free-solution assays must be prepared to purposely minimize the difference in RI between the sample and the reference (and/or control). The procedure is illustrated in **Figure A.6** and, in short, the sample and reference are prepared from the same matrix (buffer, serum, urine, RBCs, etc.). A fixed concentration solution of the receptor is prepared in the matrix and then combined with the ligand dilution series, which is typically prepared in buffer. Reference solutions are matrix solutions, devoid of the receptor/target that have been combined with the dilution series. For cells, cell- or tissue-derived samples (e.g. vesicles, membrane fractions, lipoparticles, etc.), the reference sample consists of a preparation with the receptor either absent from the matrix or inactivated (expression knocked out, chemically blocked, etc.). Test samples are prepared by combining the dilution series with the receptor-in-matrix solutions. Reference and test samples are then allowed to reach equilibrium, often on ice when proteins are evaluated, and then introduced sequentially into the interferometer. The difference in fringe position (shift) between the reference and test sample reports the binding/interaction in a concentration dependent manner.

In an attempt to enable others to successfully perform free-solution assays with an in interferometer and avert reports stating; "…we are not able to reproduce the protein A–IgG binding results by Bornhop et al. performed with a reported detection limit of 10^{-6} RIU…" [65], we note that three conditions are critical to the success of a free solution assays. 1) Care must be taken when preparing the solutions. It is essential that the RI of the sample and reference composition are matched. While we have not found it to be necessary to dialyze as recommended in ITC [263],

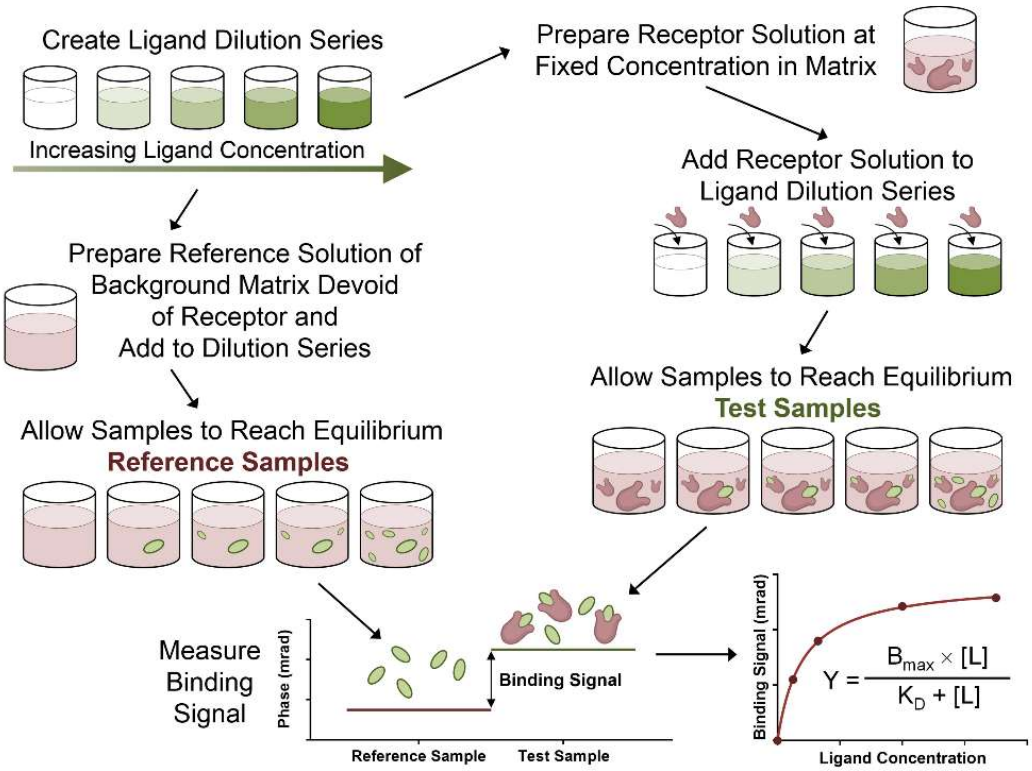

Fig. A.5 Illustration of the procedure for using BSI to measure a binding affinity.

the test and reference and/or control samples must be reasonably well index matched. If 2% DMSO is to be used, ***both*** the reference and the test solutions must have the same amount (2%) of DMSO. 2) Protein DHA and other types of samples denature over time or can be altered as a consequence of environmental conditions. None have an indefinite shelf life. Free-solution assay reports functional transformations, and the absence of tethering or a surrounding structure like a dextran to orientate the protein, makes it critical they are operational. Even *one* freeze-thaw cycle or the length and/or environment used during equilibration can impact the performance of the assay. Experience has taught us that the presence of the correct band on a Western is not necessarily an indicator the protein is unadulterated. 3) To insure the signal is not from surface interactions, we establish a baseline for the matrix with replicate injections. Then after *each consecutive injection*, we reestablish that baseline by rinsing the channel prior to collecting the next datum. This procedure helps to ensure that the binding signal is emanating from the change in composition of the solution and not adoption to the walls. Any sample-to-sample baseline excursion would be reporting a change in the optical path length for the interferometer such as the

RI of the solution or the effective channel diameter. Channel rinses, and to a lesser extent coatings, serves to improve replicate assay reproducibility by minimizing the contribution of non-specific binding. A wide variety of rinse solutions have been found to be successful, ranging from simply buffer to light acid/base to Piranha, to methanol and chloroform. Since the chip is the optics, the baseline shift from sample to sample to can be used to determine if something has been adsorbed to the surface and when it has been removed.

The importance of #3 cannot be over emphasized, since others have questioned the validity of our BSI protein binding studies [65], suggesting that using "channels etched in glass chips…could affect protein interactions. It was also stated that, "It is well known that protein adsorbs to…surfaces" and since "BSI is sensitive towards RI change of both bulk and surface layers…we believe that unspecific binding of proteins could produce erroneous signals." It is true that BSI can detect RI changes in either the bulk or the surface [264-267], in fact we and others have employed this unique property to compare affinities derived from free-solution and surface-immobilized formats for the same species [9, 60]. Yet, after >7 years of operation, more than 30 users running numerous blinded samples on multiple different instruments, provide significant evidence that our procedures are enabling *free solution* measurements.

We often work at nM-pM concentrations, a regime where the neither the ligand nor probe exhibits a quantifiable response. In this case, there is no dη/dC response expected, yet procedures always include the dη/dC determination for a dilution series of the ligand. This procedure allows for compensation of species with higher RI values that would potentially skew the saturation isotherm [10, 20].

Free-solution measurements do quantify solution-phase RI changes, thus effective, long-term environmental control is needed to succeed. Since dη/dT is large for fluids, temperature control of the sample/chip is required at the level of a couple millidegrees C. Accomplishing this level of thermal stability consists isolating the optical train, using a high-performance Peltier controller and thermoelectric device (TE) and a chip mount with a large thermal mass and designed to have intimate contact with TE and the chip [10, 20].

Though sensitivity of RI to pressure (dη/dP) is about 10-fold less than dη/dT, pressure perturbations will impact the measurement performance if not constrained. Since end-point assays involve sequentially introducing the samples into a microfluidic channel, often followed by rinses, we have developed a somewhat unique injection methodology aimed toward minimizing sample-

to-sample pressure (dη/dP-induced) differences. While effective, simplifying the macro-to-micro interface, while constraining the required volume, has been one of the most challenging aspects of deploying our method into other laboratories. The current manual approach, optimized empirically, works by having a drop is dispensed onto the channel inlet and a applying a controlled vacuum to the channel outlet for a fixed time period. This semi-automated approach is effective, but still requires the operator to develop injection skills. The level of difficulty is modest, but as with GC injections to this day, manual sample introduction requires practice. Repetition and multiple repeats of the assay aid to mitigate the contribution of injection to error in the assay. Improved sample introduction methods are currently under intense investigation.

Alignment and Fringe Selection

Physics of fringe production and selection are intertwined, because 'poor' alignment is really *miss-alignment and leads to a different fringe profile (beam energy distribution)*. Free-solution assay success with our interferometer, is dependent on a general understanding of the optical train that reports the signal. In the Bornhop interferometer, "***the chip is the optics***", so in addition to obtaining high-quality chips (Micronit, NL), proper optical alignment is essential. There are several criteria for success and significant deviation from this configuration changes the optical train resulting in fringe patterns different from those we have characterized. A) The Gaussian laser beam should consist of nearly parallel rays that *evenly* overfill the channel and impinge on chip at an angle near to 90° (**Fig. 1.1**). The best angle is 90° direct backscatter configuration, but to prevent light reentering the laser cavity and to direct the fringes onto the camera, we have found that ±7° angle is acceptable. If the chip/capillary is not in maxima of the Gaussian profile the intensity profile will change significantly with different fringes reporting optical path length changes other than those desired. Optimization here is easily accomplished by translating the beam or chip so as to obtain equal intensity on both sides of the centroid. B) Tilt of the incoming beam should be avoided as it leads to a different "object" being interrogated or serving as the interferometer. The result of this type of miss-alignment leads to a different fringe profile with fringes becoming distorted or slanted. C) As reported elsewhere [268], placing the object (chip/capillary) in a region of beam divergence or convergence will distort the fringes in a manner similar to adding a modest power lens. In our experience this configuration will degrade performance using the regions of interest (ROI) we have previously characterized. D) Fringe

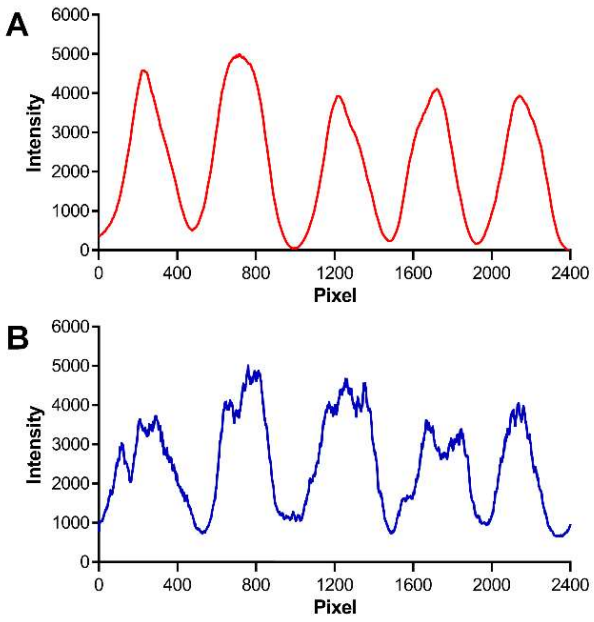

Fig. A.6 A) An example of a fringe pattern with a good alignment. Fringes are smooth, Gaussian shaped, evenly spaced, high contrast, and with similar intensities. **B)** An example of a fringe pattern with poor alignment. Fringes have a high frequency noise, have lost the Gaussian shape, and have a lower contrast ratio.

quality is also of paramount importance to obtaining high ΔRI performance. Well-shaped fringes (**Figure A.6A**) have found that contrast ratios approaching ca. 98% should be obtained for the fringes of interest. Poor contrast indicates reduced interferometer finesse, so as with and interferometer the result is diminished sensitivity (**Figure A.6B**).

A fully physical description of BSI and quantitative analysis of fringe production are beyond the scope of this communication, with excellent discussion found in the literature [63, 251, 269], yet a summary is provided here. Since fringe position (shift) reports the RI, proper selection is imperative. With reference to **Figures 1.1 and A.7** it can be easily recognized that the fringes are not equivalent in their physical origin and thus their response. BSI is a multi-modal interferometer with several dominate frequencies, all mixing as a result of reflection and refraction from the surfaces of the chip. There is low frequency component emanating from the top and bottom surface reflections, a middle frequency (the one we employ) principally from a combination of the rays combining after reflecting from all surfaces and traversing the channel. The other frequencies are potentially of interest but have not been as well characterized. To illustrate the complexity of BSI, **Figure A.7** presents optical ray traces of the optical train using

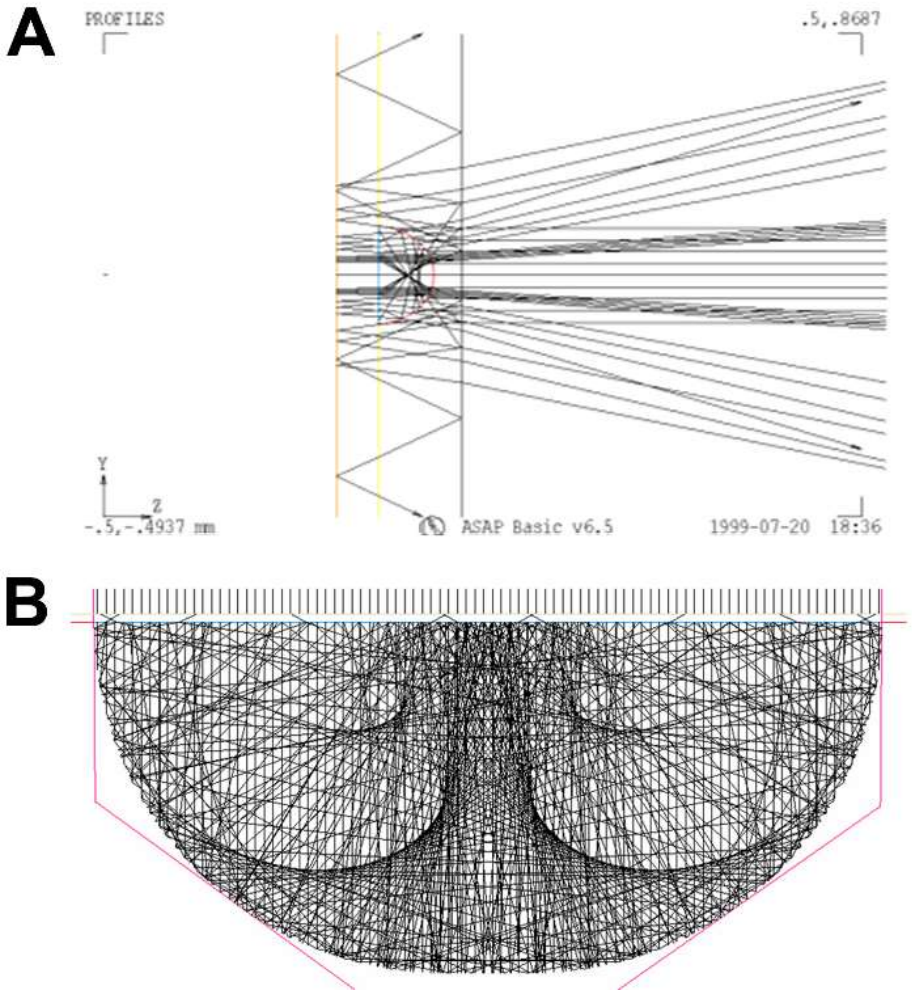

Fig. A.7 Optical modeling of the beam path. **A)** Ten parallel rays are impinged on the chip from the right are allowed to refract and reflect and exit to the right interfering. Reprinted with permission from Ref 63. Copyright 2000 American Chemical Society. **B)** Optical ray trace of a semicircular channel in a microfluidic chip.

ASAP® modeling software. **Figure A.7B** presents a higher resolution modeling outcome, showing, as empirical evidence suggests [63, 251], that the Bornhop multimodal interferometer has an optical path-length, greater than the dimensions of the channel. Note that **Figure A.7B** more clearly shows that there is significant optical energy (numbers of rays) concentrated in the central part channel, predominantly interrogating the bulk solution. Others take a grazing angle path, principally reporting RI changes at the channel surface. Simply put, not all fringes emanate from the same region of the object (chip, capillary, capillary in an enclosure etc.), and as a consequence they don't all exhibit a strong free-solution signal. There is added complexity to the

system since quite a bit of signal mixing occurs, resulting in fringes that respond to both the surface and the bulk RI changes. Therefore, selection of the appropriate fringes is necessary to obtain robust free-solution signals. Since we have yet to identify a pure frequency, a desirable outcome results only from combining assay procedures (see above), with prudent alignment guided by empirical evidence.

Using a chip with a 210 μm×100 μm semicircular channel isotropically etched in a 0.7mm substrate and covered with a 1.1mm thick top-plate produces fringes that are ca. #6-14 from the centroid that exhibit a nearly single spatial frequency (**Figure 1.1**). As described in detail previously [61], we perform a Fast Fourier Transform (FFT), within a LabView program, facilitating the time dependent collection of the position of fringes in radians.

Using this same chip, we determine the probe volume by calculating the volume of fluid within the intersection of the beam and the channel. The cross-sectional area of channel is two quarter circles connected by a 10 μm wide rectangle (width of the etch mask) and can be calculated by:

$$A = \frac{\pi r^2}{2} + 10r \qquad \textbf{Eq. .22}$$

where r is the etch radius of the channel in μm. Our channels have an etch radius of 100 μm, yielding a cross sectional area of 16708 μm^2.

This area is then multiplied by the beam diameter (d) to determine the probe volume. Our beam diameter is 450 μm and results in a probe volume of 7.5nL.

The BSI Signal is Not Calorimetric

Under conservative conditions we used the reaction between IgG and P_A [10], the Gibbs free energy, and heat energy equation to predict a temperature change of ~1.09×10^{-5} K. For 100% energy transfer to an RI change, 1 μM of the IgG-P_A pair, normally analyzed at nM concentrations, would induce a 1.09×10^{-9} RIU signal in water. This value is two orders of magnitude smaller than the BSI detection limit of 1 $\times10^{-7}$ RIU and a decade below the system noise floor of $\Delta RI = 10^{-8}$ [270]. Having applied this calculation to the entirety of binding pairs within the model, the largest RI change that could be induced upon binding is no greater than the system noise, with a majority of the ΔRI values predicted being several orders of magnitude lower than the instrument LOD.

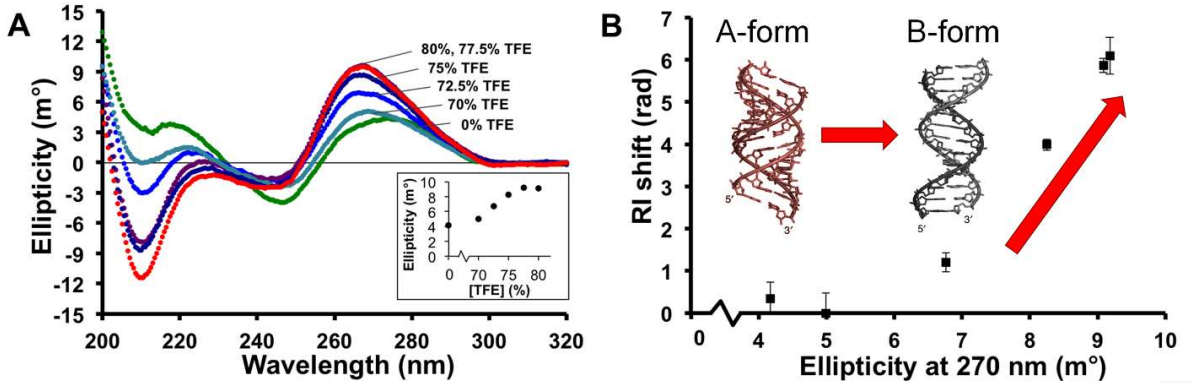

Fig. A.8 A) CD spectra of the DHA duplex Inset: A-form to B-form transition monitored at 270 nm by ellipticity. **B)** Correlation for BSI signal and ellipticity. Adapted from Ref 57 with permission of Oxford University Press.

Therefore, it is reasonable to infer that the heat of reaction cannot be a significant contributor to the RI signal reported in free-solution assays.

Stop-flow kinetic binding studies offered further validation that the heat of reaction is not the source of the free-solution signal [10], showing an absence of signal decay due to conduction to a heat sink. Environmental temperature drift can and does produce spurious signals, but this annoyance can be corrected for with careful instrument design and system temperature control. Virtually all assays performed since 2008 have been run as end-point determinations, with samples prepared, mixed, allowed to equilibrate (up to 10 hours) and then read by the interferometer. The end-point scenario excludes calorimetric contributions to the signal.

Table A.1 Comparison of Experimental and Predicted RIU Change

	Receptor	Ligand	K_D (M)	BSI ΔRIU	Predicted ΔRIU	
					Large Model	Small Model
Large	IL-2 Antibody	Interleukin-2	2.59E-11	8.17E-05	2.13E-06	2.23E-09
	β2AR	Alprenolol	5.50E-10	1.51E-05	3.33E-05	3.54E-08
	β2AR	Isoproterenol	1.52E-09	7.45E-06	4.25E-05	4.95E-08
	Basigin	Rh5	1.08E-06	2.33E-05	2.30E-02	3.46E-05
	Carbonic Anhydrase II	Acetazolamide	1.06E-08	2.87E-05	4.50E-05	2.56E-08
	Carbonic Anhydrase II	Acetazolamide	1.06E-08	2.87E-05	3.96E-05	3.04E-08
	Calmodulin	Calcineurin	1.14E-08	4.90E-04	4.26E-05	9.66E-08
	Calmodulin	Calcineurin	1.14E-08	4.90E-04	5.88E-05	1.11E-07
	Calmodulin	M13	9.87E-09	8.76E-05	1.52E-05	6.95E-08
	Thrombin	Bock	5.96E-09	1.90E-05	9.70E-06	4.84E-08
	Thrombin	Tasset	3.84E-09	1.45E-05	4.78E-06	3.00E-08
	Carbonic Anhydrase II	Benzene Sulfonamide	5.68E-07	1.38E-05	9.53E-04	2.65E-06
	Carbonic Anhydrase II	Benzene Sulfonamide	5.68E-07	1.38E-05	2.62E-04	3.24E-06
	Carbonic Anhydrase II	Sulfanilamide	1.76E-06	3.92E-05	2.99E-03	8.15E-06
	Carbonic Anhydrase II	Dansylamide	4.45E-07	1.72E-05	1.81E-03	1.15E-06
Small	Calmodulin	TFP	7.82E-06	1.56E-04	1.42E-02	5.75E-05
	Calmodulin	TFP	7.82E-06	1.56E-04	1.85E-02	6.15E-05
	Calmodulin	TFP	7.82E-06	1.56E-04	1.37E-02	5.72E-05
	Carbonic Anhydrase II	Sulpiride	5.90E-06	3.11E-05	6.00E-04	3.55E-05
	Calmodulin	Calmodulin-Ca2+	1.82E-05	2.89E-04	1.10E-02	1.03E-04
	HIV PR	Pepstatin 1F1N	5.30E-06	3.04E-05	2.24E-02	7.28E-06
	HIV PR	Pepstatin 1F1	1.45E-05	4.52E-05	7.18E-02	1.04E-05
	Concanavalin A	Mannose*	9.63E-05	1.55E-05	4.46E-01	1.39E-04
	Concanavalin A	Mannose*	9.63E-05	1.55E-05	5.21E-01	7.38E-05
	Concanavalin A	Glucose*	3.44E-04	1.46E-05	2.21E+00	4.41E-05
	Concanavalin A	Glucose*	3.44E-04	1.46E-05	1.97E+00	1.60E-04
	Recoverin	Ca^{2+}	7.35E-07	4.42E-05	2.06E-03	5.74E-06

Table A.2 Comparison of Experimental and Modeled BSI Signal

	Ligand Concentration (M)	**ρ_{exp} Experimental BSI signal (mrad)**	***C* (M)***	**ρ_{model} Predicted BSI signal (mrad)**	**Percent Error**
Carbonic Anhydrase	0.00	0.00	0.00	0.00	0.0%
	3.90×10^{-8}	-3.81	4.07×10^{-11}	-2.37	37.8%
	7.80×10^{-8}	-4.57	7.52×10^{-11}	-4.38	4.1%
	1.56×10^{-7}	-5.91	1.31×10^{-10}	-7.62	29.0%
	3.12×10^{-7}	-9.68	2.07×10^{-10}	-12.09	24.9%
	6.25×10^{-7}	-14.32	2.93×10^{-10}	-17.10	19.4%
	1.25×10^{-6}	-17.89	3.70×10^{-10}	-21.55	20.5%
	2.50×10^{-6}	-21.36	4.25×10^{-10}	-24.78	16.0%
Recoverin	0.00	0.00	0.00	0.00	0.00%
	2.50×10^{-7}	9.73	1.90×10^{-7}	12.20	25.43%
	5.00×10^{-7}	17.71	3.29×10^{-7}	21.12	19.25%
	1.00×10^{-6}	29.39	4.50×10^{-7}	31.06	5.69%
	2.00×10^{-6}	36.17	5.03×10^{-7}	37.88	4.75%
	4.00×10^{-6}	40.93	5.23×10^{-7}	41.33	0.97%
	8.00×10^{-6}	40.11	5.32×10^{-7}	42.97	7.13%

*Solution to the mass balance equation

Table A.3: Compiled List of PDB Structures Used for Calculations

	Receptor	Ligand	Bound PDB ID	Unbound PDB ID
Large	IL-2 Antibody	Interleukin-2	4YUE	1M4C and 1F8T
	β2AR	Alprenolol	3NYA	2RH1
	β2AR	Isoproterenol	2Y03	2RH1
	Basigin	Rh5	4U0Q	3I84 and 4WAT
	Carbonic Anhydrase II	Acetazolamide	1ZSB	1CA2
	Carbonic Anhydrase II	Acetazolamide	1YDA	1CA2
	Calmodulin	Calcineurin	2R28	1OSA
	Calmodulin	Calcineurin	2F2O	1OSA
	Calmodulin	M13	1CDL	1OSA
	Thrombin	Bock	1HUT	3U69
	Thrombin	Tasset	4I7Y	3U69
	Carbonic Anhydrase II	Benzene Sulfonamide	4JSA	1CA2
	Carbonic Anhydrase II	Benzene Sulfonamide	2WEJ	1CA2
	Carbonic Anhydrase II	Sulfanilamide	2NNG	1CA2
	Carbonic Anhydrase II	Dansylamide	1OKL	1CA2
Small	Calmodulin	TFP	1CTR	1OSA
	Calmodulin	TFP	1LIN	1OSA
	Calmodulin	TFP	1A29	1OSA
	Carbonic Anhydrase II	Sulpiride	1G4O	1CA2
	Calmodulin	Calmodulin-Ca2+	1OSA	1CFD
	HIV PR	Pepstatin 1F1N	4EJK	5HVP
	HIV PR	Pepstatin 1F1	4EJD	5HVP
	Concanavalin A	Mannose*	5CNA	1JBC
	Concanavalin A	Mannose*	1I3H	1JBC
	Concanavalin A	Glucose*	1CJP	1JBC
	Concanavalin A	Glucose*	1GIC	1JBC
	Recoverin	Ca^{2+}	1OMV	1REC

Table A.4 Calculated Structural Components

	Receptor	Ligand	Bound Radius of Gyration (Å)	Unbound Radius of Gyration (Å)	Bound Surface Area ($Å^2$)	Unbound Surface Area ($Å^2$)
Large	IL-2 Antibody	Interleukin-2	28.11	38.98	24399.8	26849.7
	β2AR	Alprenolol	28.84	29.21	22944.5	22633.3
	β2AR	Isoproterenol	22.00	21.43	17028.6	15726.8
	Basigin	Rh5	29.56	19.19	25215.0	27363.2
	Carbonic Anhydrase II	Acetazolamide	17.40	17.40	11420.8	11549.7
	Carbonic Anhydrase II	Acetazolamide	17.35	17.40	11490.0	11549.7
	Calmodulin	Calcineurin	21.68	22.45	9457.7	10129.7
	Calmodulin	Calcineurin	21.43	22.45	9645.2	10129.7
	Calmodulin	M13	16.5	22.45	8965.9	10129.7
	Thrombin	Bock	17.82	17.76	12849.4	12684.2
	Thrombin	Tasset	17.67	17.76	12791.4	12684.2
	Carbonic Anhydrase II	Benzene Sulfonamide	17.39	17.40	11775.4	11549.7
	Carbonic Anhydrase II	Benzene Sulfonamide	17.53	17.40	11948.8	11549.7
	Carbonic Anhydrase II	Sulfanilamide	17.41	17.40	11772.7	11549.7
	Carbonic Anhydrase II	Dansylamide	17.41	17.40	11448.1	11549.7
Small	Calmodulin	TFP	15.78	22.45	8977.8	10129.7
	Calmodulin	TFP	15.54	22.45	9046.4	10129.7
	Calmodulin	TFP	15.54	22.45	8960.0	10129.7
	Carbonic Anhydrase II	Sulpiride	17.61	17.40	12001.4	11549.7
	Calmodulin	Calmodulin-Ca2+	22.45	20.29	10129.7	10290.8
	HIV PR	Pepstatin 1F1N	17.34	17.22	10160.4	9556.4
	HIV PR	Pepstatin 1F1	17.60	17.22	10069.7	9556.4
	Concanavalin A	Mannose*	17.19	17.32	10559.5	10303.9
	Concanavalin A	Mannose*	17.08	17.32	10447.5	10303.9
	Concanavalin A	Glucose*	17.17	17.32	10310.7	10303.9
	Concanavalin A	Glucose*	17.19	17.32	10405.4	10303.9
	Recoverin	Ca^{2+}	18.30	16.50	12014.0	10333.0

Table A.5 Model Fitted Parameters

ρ	Number of systems	R^2	Spearman ρ_S	Average Residuals	A $\left(\frac{RIU}{MÅ^2}\right)$	B $\left(\frac{RIU}{MÅ^2}\right)$	C $\left(\frac{RIU}{MÅ}\right)$	D $\left(\frac{RIU}{MÅ}\right)$	E $\left(\frac{RIU}{M}\right)$
All	25	0.986	0.853	20248.88	8.04	23.63	-6617.55	29031.93	-96478.05
Small	11	0.991	0.936	2.28	0.05	0.026	-16.05	25.62	-713.38
Large	14	0.998	0.979	9441.28	60.42	23.66	-7529.18	29830.00	-25460.48

9. Olmsted, I. R.; Kussrow, A.; Bornhop, D. J., Comparison of Free-Solution and Surface-Immobilized Molecular Interactions Using a Single Platform. *Anal Chem* **2012,** *84* (24), 10817-10822.
10. Bornhop, D. J.; Latham, J. C.; Kussrow, A.; Markov, D. A.; Jones, R. D., et al., Free-solution, label-free molecular interactions studied by back-scattering interferometry. *Science* **2007,** *317* (5845), 1732-1736.
20. Kussrow, A.; Enders, C. S.; Bornhop, D. J., Interferometric Methods for Label-Free Molecular Interaction Studies. *Anal Chem* **2012,** *84* (2), 779-792.
31. Jung, L. S.; Campbell, C. T.; Chinowsky, T. M.; Mar, M. N.; Yee, S. S., Quantitative Interpretation of the Response of Surface Plasmon Resonance Sensors to Adsorbed Films. *Langmuir* **1998,** *14* (19), 5636-5648.
33. Stenberg, E.; Persson, B.; Roos, H.; Urbaniczky, C., Quantitative-Determination of Surface Concentration of Protein with Surface-Plasmon Resonance Using Radiolabeled Proteins. *J Colloid Interf Sci* **1991,** *143* (2), 513-526.
34. Matthews, B. W., In *The Proteins III*, Academic Press: New York, 1977; pp 403-590.
35. Zhao, H.; Brown, P. H.; Schuck, P., On the Distribution of Protein Refractive Index Increments. *Biophys J* **2011,** *100* (9), 2309-2317.
36. Golander, C. G.; Kiss, E., Protein Adsorption on Functionalized and Esca-Characterized Polymer-Films Studied by Ellipsometry. *J Colloid Interf Sci* **1988,** *121* (1), 240-253.
37. Haussling, L.; Ringsdorf, H.; Schmitt, F. J.; Knoll, W., Biotin-Functionalized Self-Assembled Monolayers on Gold - Surface-Plasmon Optical Studies of Specific Recognition Reactions. *Langmuir* **1991,** *7* (9), 1837-1840.
39. Davis, T. M.; Wilson, W. D., Determination of the refractive index increments of small molecules for correction of surface plasmon resonance data. *Anal Biochem* **2000,** *284* (2), 348-353.
40. Tumolo, T.; Angnes, L.; Baptista, M. S., Determination of the refractive index increment (dn/dc) of molecule and macromolecule solutions by surface plasmon resonance. *Anal Biochem* **2004,** *333* (2), 273-279.
57. Adams, N. M.; Olmsted, I. R.; Haselton, F. R.; Bornhop, D. J.; Wright, D. W., The effect of hybridization-induced secondary structure alterations on RNA detection using backscattering interferometry. *Nucleic Acids Res* **2013,** *41* (9), e103.
58. Ivanov, V. I.; Minchenk.Le; Minyat, E. E.; Frankkam.Md; Schyolki.Ak, Bbar to Abar Transition of DNA in Solution. *J Mol Biol* **1974,** *87* (4), 817-833.
59. Kypr, J.; Kejnovska, I.; Renciuk, D.; Vorlickova, M., Circular dichroism and conformational polymorphism of DNA. *Nucleic Acids Res* **2009,** *37* (6), 1713-1725.
60. Pesciotta, E. N.; Bornhop, D. J.; Flowers, R. A., Back-Scattering Interferometry: A Versatile Platform for the Study of Free-Solution versus Surface-Immobilized Hybridization. *Chemistry-an Asian Journal* **2011,** *6* (1), 70-73.
61. Markov, D.; Begari, D.; Bornhop, D. J., Breaking the 10(-7) barrier for RI measurements in nanoliter volumes. *Anal Chem* **2002,** *74* (20), 5438-5441.
63. Swinney, K.; Markov, D.; Bornhop, D. J., Chip-scale universal detection based on backscatter interferometry. *Analytical chemistry* **2000,** *72* (13), 2690-2695.

65. Jepsen, S. T.; Jorgensen, T. M.; Zong, W.; Trydal, T.; Kristensen, S. R., et al., Evaluation of back scatter interferometry, a method for detecting protein binding in solution. *The Analyst* **2015,** *140* (3), 895-901.
251. Tarigan, H. J.; Neill, P.; Kenmore, C. K.; Bornhop, D. J., Capillary-scale refractive index detection by interferometric backscatter. *Analytical chemistry* **1996,** *68* (10), 1762-1770.
259. Darnell, J. E.; Lodish, H.; Baltimore, D., *Molecular Cell Biology*. Scientific American Books: New York, 1990.
260. Leslie, T. E.; Lilley, T. H., Aqueous-Solutions Containing Amino-Acids and Peptides .20. Volumetric Behavior of Some Terminally Substituted Amino-Acids and Peptides at 298.15 K. *Biopolymers* **1985,** *24* (4), 695-710.
261. Fasman, G. D.; Schaffha.B; Goldsmit.L; Adler, A., Conformational Changes Associated with F-1 Histone-Deoxyribonucleic Acid Complexes - Circular Dichroism Studies. *Biochemistry-Us* **1970,** *9* (14), 2814-&.
262. Qian, R. L.; Mhatre, R.; Krull, I. S., Characterization of antigen-antibody complexes by size-exclusion chromatography coupled with low-angle light-scattering photometry and viscometry. *J Chromatogr A* **1997,** *787* (1-2), 101-109.
263. Velazquez-Campoy, A.; Freire, E., Isothermal titration calorimetry to determine association constants for high-affinity ligands. *Nat Protoc* **2006,** *1* (1), 186-191.
264. Latham, J. C.; Markov, D. A.; Sorensen, H. S.; Bornhop, D. J., Photobiotin surface chemistry improves label-free interferometric sensing of biochemical interactions. *Angew Chem Int Edit* **2006,** *45* (6), 955-958.
265. Markov, D. A.; Swinney, K.; Bornhop, D. J., Label-free molecular interaction determinations with nanoscale interferometry. *J Am Chem Soc* **2004,** *126* (50), 16659-16664.
266. Sorensen, H. S.; Larsen, N. B.; Latham, J. C.; Bornhop, D. J.; Andersen, P. E., Highly sensitive biosensing based on interference from light scattering in capillary tubes. *Appl Phys Lett* **2006,** *89* (15).
267. Kussrow, A.; Kaltgrad, E.; Wolfenden, M. L.; Cloninger, M. J.; Finn, M. G., et al., Measurement of Monovalent and Polyvalent Carbohydrate-Lectin Binding by Back-Scattering Interferometry. *Anal Chem* **2009,** *81* (12), 4889-4897.
268. Bornhop, D. J., Microvolume Index of Refraction Determinations by Interferometric Backscatter. *Appl Optics* **1995,** *34* (18), 3234-3239.
269. Sorensen, H. S. Self Calibrating Interferometric Sensing. PhD, Technical University of Denmark, Roskilde, 2006.
270. Bornhop, D. J.; Latham, J. C.; Kussrow, A.; Markov, D. A.; Jones, R. D., et al., Materials and Methods are available as supporting material on *Science* online. *Science* **2007**.

Appendix B: Supporting Information for Chapter 6: Quantitation of Opioids and the Prospect of Improved Diagnosis of Neonatal Abstinence Syndrome

The Compensated Interferometric Reader

The compensated interferometric reader (CIR), illustrated in **Figure B.1**, consists of a compensated interferometer [155], a droplet generator and a syringe pump.

Syringe Pump Setup: A Chemyx® Nexus 3000 Syringe pump pulling a Hamilton Gastight® 1001 syringe provides constant flow through the capillary at 10 µL/min. The syringe was interfaced to the capillary using a LabSmith Luer-Lock to capillary adaptor. Using a Hamilton syringe with an inner diameter of 4.610 mm and volume of 1000 µL gives a total flow time of about 100 minutes.

Droplet Train Generation: The Mitos Dropix was interfaced to the interferometer so that droplet trains were formed directly in the capillary (350 µm OD / 250 µm ID, Polymicro, Molex, USA), allowing a single section of capillary to serve as both the reader cell and the transfer line. Droplet trains were produced by a sample hook/capillary moving up and down between two

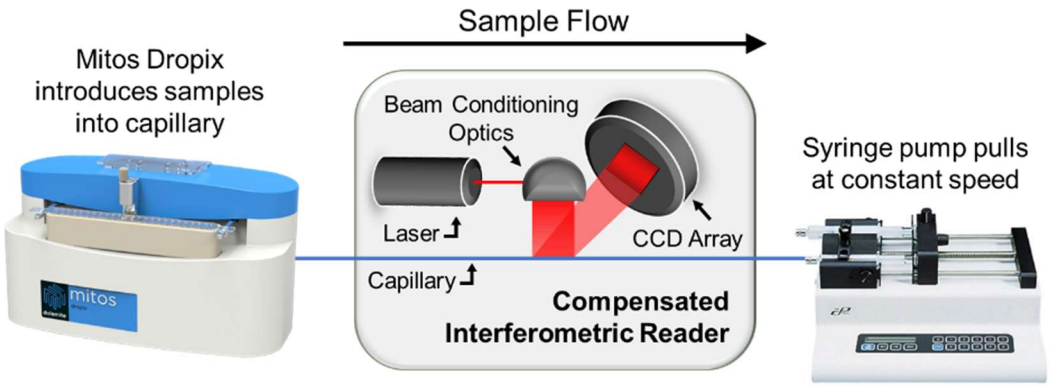

Fig. B.1 Reader consisting of a droplet generator for sample introduction, compensated interferometer (diode laser, capillary cell and camera) and syringe pump.

"reservoirs" while the pump pulls fluid. One of the reservoirs was an open tray containing the oil (Fluorinert FC-40, Sigma-Aldrich) used to separate the droplets, the other was a PEEK tray consisting of 24 bottomless wells where the sample and reference solutions reside. Hook sample-well dwell time and solution flow rate determines droplet volume and spacing. The Dropix system was programmed using the built-in software.

Sample and reference solutions were loaded into adjacent wells in a Dropix sample well tray (20 µL of each). A single determination consists of a droplet train of 1000nL of sample and reference solutions separated by 40nL of oil. The first sample/reference pair was preceded by 4 x 4 µL droplets of PBS, each separated by 100nL of oil. For all determinations using the CIR, the sample/reference pairs were introduced five times for a total of 10 droplets. Following the analysis of each group of sample/reference droplet pairs a 500nL droplet of oil and 2 x 4 µL droplets of PBS separated by 100nL of oil was used to rinse and prepare the capillary for the next sample/reference pair. An entire droplet train, consisting of all six sample pairs and the required rinses, takes about 14 minutes to run through the CIR. Assays requiring more than 6 determinations were performed by running multiple trays sequentially. After an entire tray was run, the capillary was rinsed with PBS for 3 minutes before beginning the next tray.

CIR Calibration: Device performance and instrument response was evaluated using solutions containing 0, 0.125, 0.25, 0.5, 1, and 2mM glycerol in PBS in 50% urine / 50% PBS. PBS serves as the reference sample. Using the calibration curve we establish that the response function of the instrument is ~0.110 radians/mM glycerol, the reproducibility of replicate measurements (standard deviation) for like glycerol concentrations is <0.012 radians, and the limit of quantification LOQ values <0.33mM. The LOD was determined by measuring ~3 seconds of baseline noise of the phase shift and was ~0.111mM glycerol. Based upon our past experience, this sensitivity is more than adequate to perform free-solution molecular interaction studies [185, 201].

Aptamer selection

All opioid aptamers were selected by Base Pair Biotechnologies, Inc. (Pearland, TX, USA) using a modification of the SELEX method of Nutiu et al [184]. To avoid the potential risk for opioid contamination in "normal" pooled human urine, an ersatz urine formulation comprising 1X PBS, 300 mM urea, 6 mM creatinine, 0.05% Tween-20, and 1 mM $MgCl_2$ was used. After multiple

rounds of positive and negative selection, the enriched aptamer pools were sequenced using an Ion Torrent PGM next generation sequencer (Thermo Fisher), and for each target, bioinformatics analysis was used to choose aptamers for synthesis and functional screening in the FSA assay.

Free Solution Assay Methods

Aptamer solution preparation: The aptamer stock solutions were prepared by reconstituting the aptamer dried pellet to a concentration of 100 μM in a modified Phosphate Buffered Saline (PBS) containing 1 mM $MgCl_2$, 10 mM Tris HCl, and 0.1 mM EDTA with pH 7.5. All further dilutions used this PBS formulation. The stock aptamer solution was then diluted to 1 μM (working concentration) in PBS. Once diluted to the working concentration (**Table B.1**), the aptamers were refolded by heating the solution to 90°C for 5 minutes in a water bath, then cooled to room temperature for 15 minutes. This process ensures the aptamers were in their desired conformation. For cross reactivity measurements (detailed below), stock aptamer solution was diluted to 2 μM before refolding.

Opiate target solution preparation: The six opioid and metabolite targets and cortisol, listed in **Table B.1**, were obtained from Sigma-Aldrich at 1 mg/ml in methanol. For all targets, stock solutions were prepared at a concentration of 2.7 – 3.3 mM. Care was taken to insure the concentration of the target samples stayed below the 1 mM aqueous solubility limit. To prepare analysis samples, 10 μL of the opioid standard solution was added to 990 μL of PBS, creating working solutions of 27 and 32 μM (**Table B.1**, Column D). The resulting solvent composition of the working solutions was 99% PBS and 1% methanol. Next, a volume of the working solution (**Table B.1**, Column E) was diluted to 200 nM with 1% methanol in PBS. The 1% methanol in PBS solution was kept constant across all target dilutions to ensure that solutions in the free-solution measurements were index matched.

Table B.1. Opioid targets and their dilution concentrations.

A) Target	B) Molecular Weight	C) Stock Concentration	D) Working Concentration	E) Dilution Volume of Target	F) Dilution Volume of 1% Methanol/PBS
Oxycodone	315.36 g/mol	3.17 mM	31.7 µM	6.33 µL	993.67 µL
Noroxycodone HCl	337.80 g/mol	2.96 mM	29.6 µM	6.44 µL	993.56 µL
Hydrocodone	299.36 g/mol	3.34 mM	29.9 µM	6.70 µL	993.30 µL
Norhydrocodone HCl	321.80 g/mol	3.11 mM	31.1 µM	6.43 µL	993.57 µL
Fentanyl	336.47 g/mol	2.97 mM	29.7 µM	6.73 µL	993.27 µL
Norfentanyl Oxalate	322.36 g/mol	3.10 mM	31.0 µM	6.45 µL	993.55 µL
Cortisol	362.46 g/mol	2.76 mM	27.6 µM	7.24 µL	992.76 µL

Aptamer characterizations: Binding affinity assays were performed in an end-point format: First, a 100 nM solution of each target was prepared in 50% Urine / 49.5% PBS / 0.5% Methanol by adding 100 µL of the 200 nM target (prepared above) to 100 µL of pooled human urine (Valley Biomedical). Second, a 7-point serial dilution series was prepared from the 100 nM target solution by diluting the solution in half at each step with 50% urine / 49.5% PBS / 0.5% methanol. This dilution series resulted in 7 concentrations ranging from 100 – 0.780 nM. A "zero" concentration consisted of 100 µL of 50% urine / 49.5% PBS / 0.5% methanol. The corresponding aptamer to the target was then diluted from the 1 µM working concentration to give a solution of 2 nM aptamer in 50% Urine / 50% PBS. An RI-matched control solution was then prepared with 50% urine and 50% PBS. For each concentration in the target dilution series, 10 µL of the diluted target was combined with 10 µL of the 2nM aptamer to produce the binding sample, while 10 µL of the diluted target was combined with 10 µL of the RI-matched control solution to produce the reference sample. The final aptamer concentration in the binding samples was 1nM, and the final target concentration ranged from 0 – 50 nM. For each concentration, the binding and reference samples were measured with the CIR in quintuplicate. The averaged phase shift for 5 replicates was plotted vs. target concentration (**Figure B.2**).

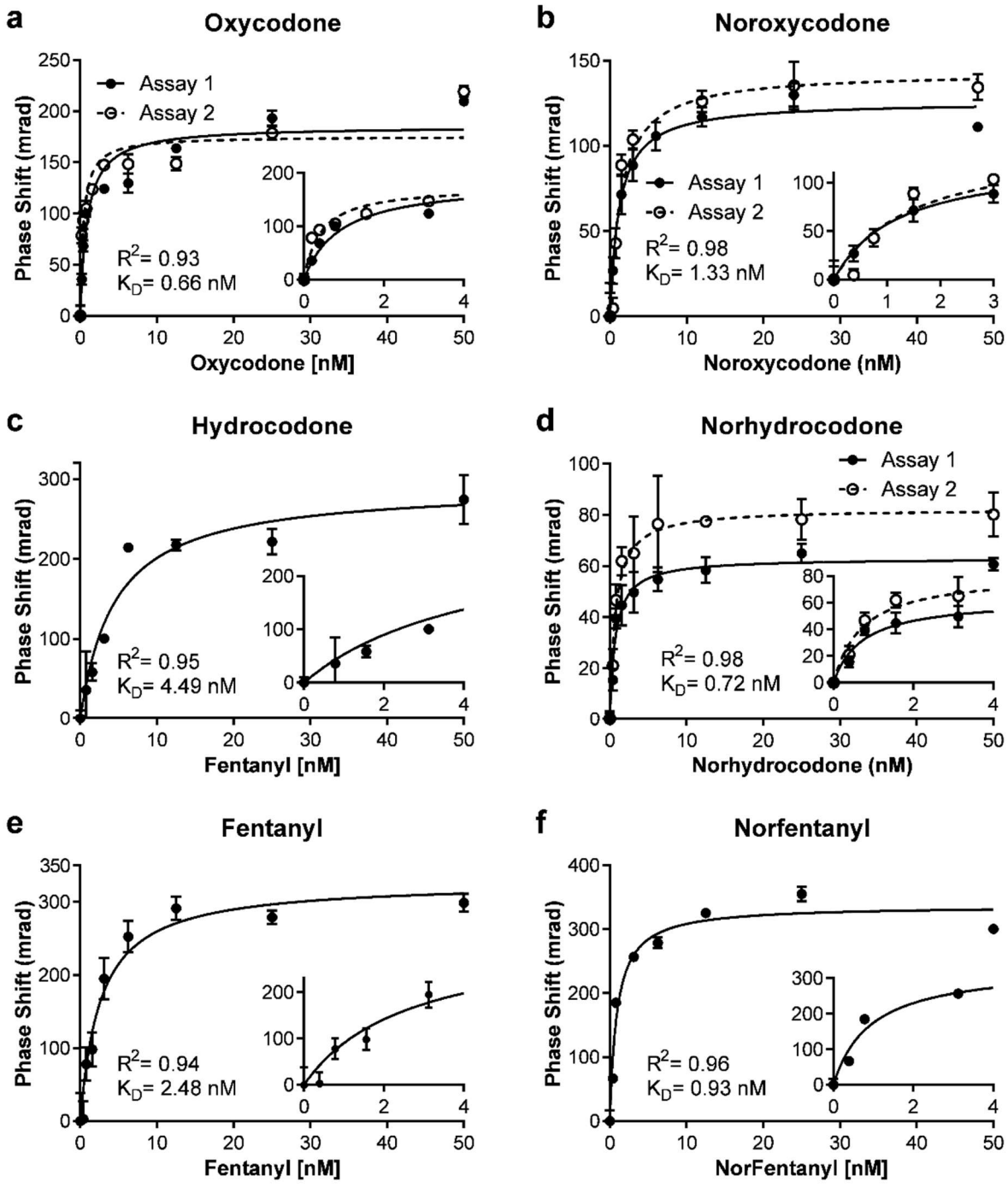

Fig. B.2 Saturation isotherms for each target and its best performing aptamer.

Dissociation constants were then calculated by fitting the data to a single-site saturation isotherm using Graphpad Prism™ according to the equation:

$$y = \frac{B_{max} \cdot X}{K_D + X} \qquad \textbf{Eq. B.1}$$

Figure B.2 shows the saturation isotherm for all six opioid target-aptamer K_D determinations, and these results are presented in **Table B.2**.

Day-to-day reproducibility was evaluated for three targets (Oxycodone, Noroxycodone, and Norhydrocodone) by rerunning the assay on subsequent days. For these three determinations, we calculated the percent difference (mean/standard deviation) for both signal magnitude (B_{MAX}) and affinity (K_D), obtaining a value of 13.6% for B_{MAX} and 24.5% for K_D. Based on these results we determined additional K_D determinations unnecessary for hydrocodone, fentanyl, and norfentanyl.

Opioid Quantification

Calibration curves were prepared by creating a dilution series of the target (opioid) at concentrations ranging from 0-200 nM in 50% Urine / 49.5% PBS / 0.5% Methanol. Aptamer solutions of 2 µM were prepared in 50% Urine / 50% PBS. The binding sample was prepared by combing 10 µL of the target each concentration of the target dilution series with 10 µL of 2 µM aptamer solution. To produce the reference solution, 10 µL of each target dilution was combined with 10 µL of the RI-matching control solution. The final aptamer concentration in the binding samples was 1 µM, and the final target concentration ranged from 0–100 nM.

Table B.2. Performance summary for opioid assays.

Target	Kd (nM)	LOD (pg/ml)	LOQ (pg/ml)	Off Target Signal[a]	Quantification Error
Fentanyl	2.48	45	63	4%	5.5%
Norfentanyl	0.93	81	94	13%	5.6%
Oxycodone	0.66	28	44	0%	4.4%
Noroxycodone	1.33	72	183	8%	2.4%
Hydrocodone	4.49	45	159	0%	1.6%
Norhydrocodone	0.72	42	84	11%	4.1%

[a] Determined versus the target opioid's metabolite or parent compound

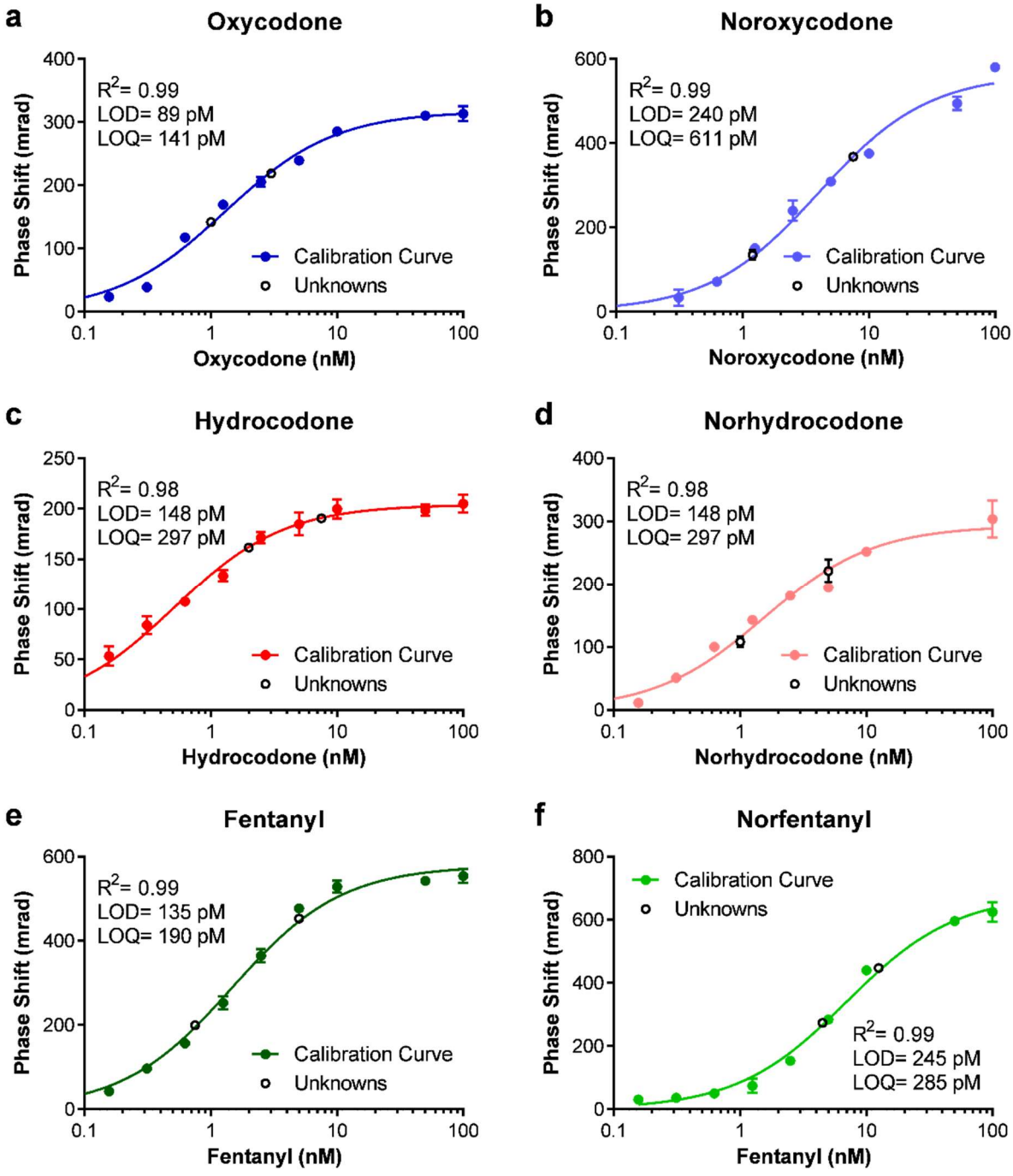

Fig. B.3 Calibration curves for the six opioid targets.

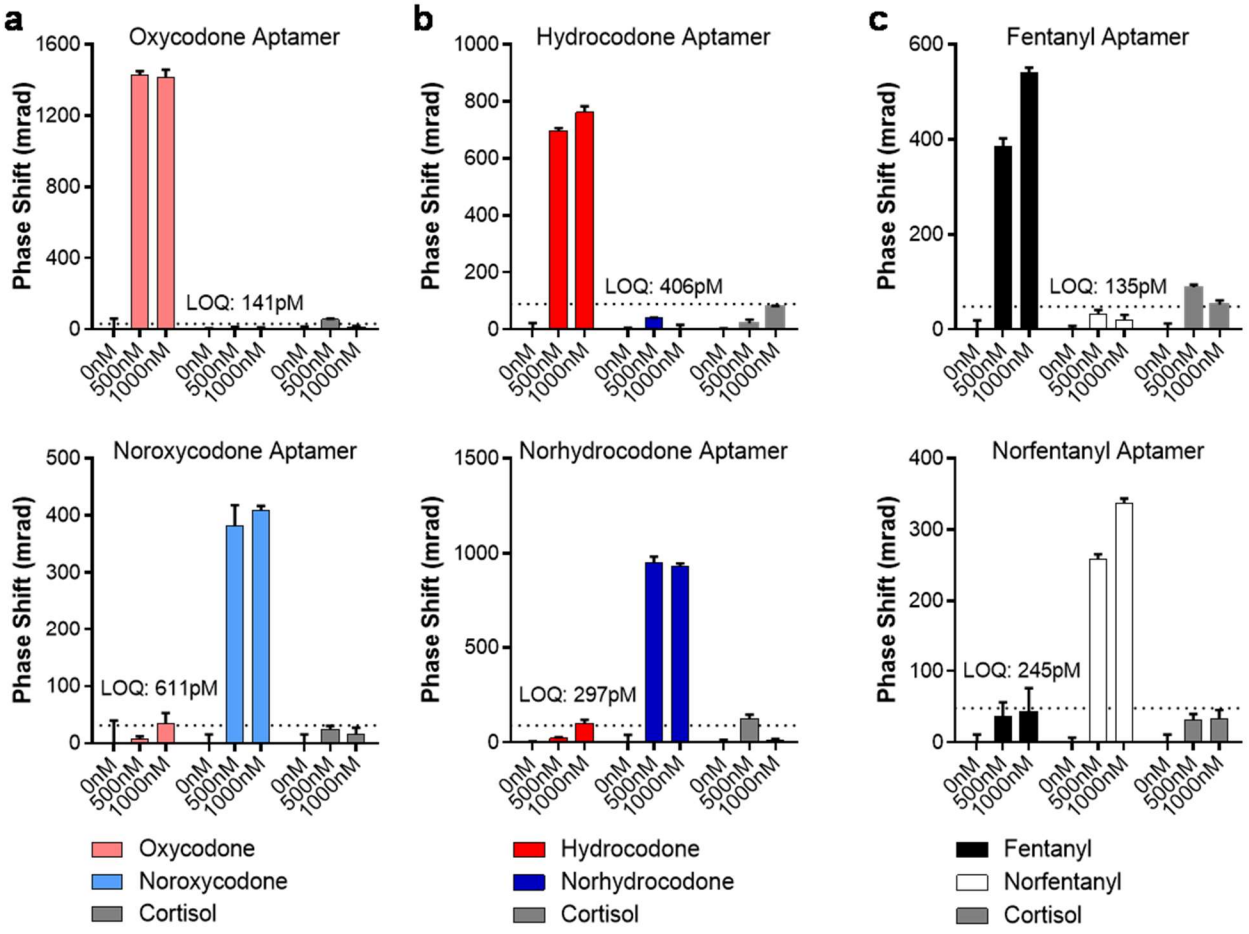

Fig. B.4 Cross-reactivity Studies for 6 aptamer probes vs. their target, off-target, and cortisol.

The phase shift between binding and reference sample was quantified with CIR by fitting the response to a saturation isotherm. The slope in the linear region of this curve was used to calculate the LOD (3×σ of the instrument baseline noise/slope) and the LOQ (3×σ of replicate measurements/slope). **Figure B.3** shows the assay calibration curves for all 6 opioid targets.

Cross-Reactivity Measurements

Specificity studies were performed for each of the aptamers to the target metabolite and cortisol. For example, the aptamer for oxycodone was tested for non-specific binding to noroxycodone and cortisol, and binding of the noroxycodone aptamer to oxycodone and cortisol.

Binding samples consisted of a 2000 nM target solution prepared from the working concentration (**Table B.1, Column D**), in 50% Urine / 49%PBS / 1% methanol. A 50 µL volume

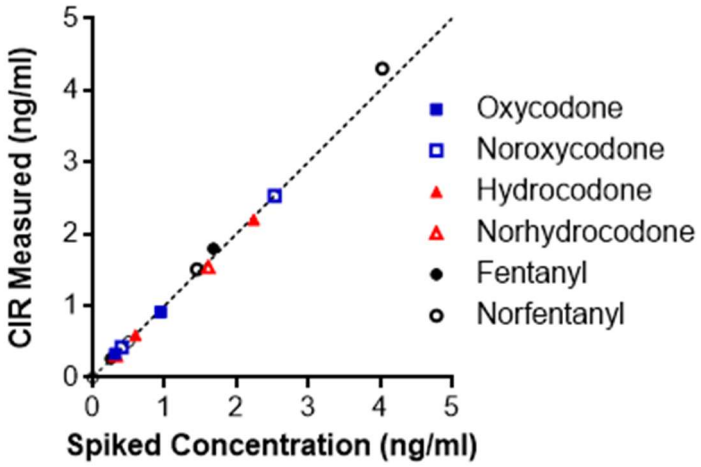

Fig. B.5 FSA-CIR quantification of unknowns, providing <5% error for all species in spiked unknown measurements.

of this solution was further diluted in 50 µL of 50% Urine / 49% PBS / 1% methanol to produce a 1000 nM solution. A solution containing 2000 nM aptamer in 50% Urine / 50% PBS was prepared from the stock aptamer solution. Then, 10 µL of the aptamer was incubated with 10 µL of 0 nM, 1000 nM, and 2000 nM of the target, resulting in final solutions containing 1 µM aptamer and 1000 nM, 500 nM, and 0 nM target in a solution of 50% urine / 49.5% PBS / 0.5% methanol.

Reference samples were prepared by adding 10 µL of a 50% urine / 50% PBS solution to 10 µL of 0 nM, 1000 nM, and 2000 nM of the target, giving final solutions containing 1000 nM, 500 nM, and 0 nM target in 50% urine / 49.5% PBS / 0.5% meth.

Sample-reference pairs were measured with CIR with the results from these determinations presented in **Figure B.4**. In all cases, the response for the aptamers' designated targets was quite large, while the signal for the off-target species and cortisol were at or below the assay's LOQ. The dotted line in **Figure B.4** represents the LOQ values for each aptamer assay.

Quantification of Unknowns

Test "unknowns" were prepared by spiking blank human urine with the opioid target. Then, 10 µL of the unknown was combined with 10 µL of 2 µM aptamer probe in PBS to create the binding sample. The reference sample was created by combining 10 µL of the unknown sample with 10 µL of PBS devoid of aptamer. All unknowns were prepared by a lab member other than

the "operator," with the operator blinded to the sample's true concentration. The signal for the unknowns were fit to the calibration curve to determine the concentration. All unknowns were measured within the linear region of the calibration curves. The percent error was calculated as $\%\, error = \frac{measured - tru}{true}$. The unknowns are plotted as open circles in overlaid upon the calibration curves in **Figure B.3**. The results are summarized in **Table B.3 and Figure B.5** and illustrate the excellent correlation between the true and unknown values.

Table B.3. Quantification of Unknowns (values in ng/ml).

Target	Unknown 1		Unknown 2		Average Error
	Spiked	Measured	Spiked	Measured	
Fentanyl	0.25	0.26	1.68	1.80	5.5%
Norfentanyl	1.45	1.51	4.03	4.31	5.6%
Oxycodone	0.32	0.33	0.95	0.91	4.4%
Noroxycodone	0.41	0.42	2.53	2.53	2.4%
Hydrocodone	0.60	0.59	2.25	2.20	1.6%
Norhydrocodone	0.32	0.31	1.61	1.54	4.1%

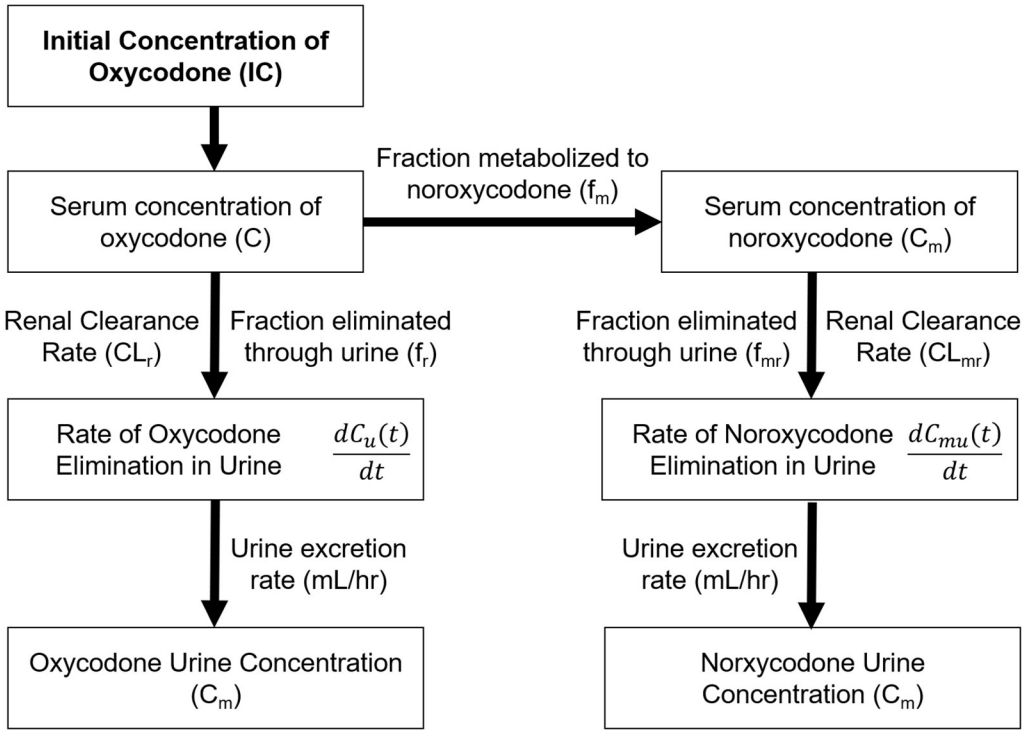

Fig. B.6 Single metabolite model of drug elimination.

Pharmacokinetic Modelling

Oxycodone and noroxycodone concentration-time profiles were calculated using a single-metabolite model where the primary opioid is eliminated via two pathways: 1) directly through urine excretion and 2) by metabolism to a single metabolite and then excretion through urine. As shown below, to calculate the urine concentration of a drug (for example, oxycodone), it is necessary to first determine the serum concentration over time. This is calculated using a first-order decay, **Eq. B.2.**[186]

$$C(t) = ICe^{-kt} \qquad \textbf{Eq. B.2}$$

Where *IC* is the initial concentration and *k* is the elimination rate constant. We chose two cases in our calculations for the initial concentration (IC). 1) The recommended analgesic doses (25 ng/mL [187] and 120 ng/mL [188]) for a newborn, and 2) a high concentration induced by illicit opiate use by the mother (300 ng/ml and the 2000 ng/ml) [189].

Equation B.3 was used to determine k from the drug's half-life ($t_{1/2}$), an experimentally determined parameter.

$$k = \frac{ln(2)}{t_{1/2}} \qquad \textbf{Eq. B.3}$$

From the work of Valitalo *et-al* reported half-life values for oxycodone depends on numerous factors. In healthy neonates it is about 4 hours, but can reach 8.8 hours in extremely preterm neonates [187]. For healthy newborns, the half-life decreases to about 2.1 hours, a value that is approximately the same as that observed in healthy adults [187]. Here we calculated k for all cases, from $t_{1/2}$ = 8.8 to 2.1

With k in hand we used **Eq. B.2** to calculate the serum concentration of drug (oxycodone).

Urine concentration of oxycodone: As illustrated in **Fig. B.6** the *urine* oxycodone concentration is found by estimating the fraction (f_m) of oxycodone metabolized to noroxycodone and assuming the remaining oxycodone (f_r) is found (excreted) in the urine. The *rate* of oxycodone elimination through urine (dC_u/dt) is therefore dependent upon the serum concentration (C) and the renal clearance (CL_r), and can expressed by **Eq. B.4**:

$$\frac{dC_u(t)}{dt} = f_r \cdot CL_r \cdot C(t) \qquad \textbf{Eq. B.4}$$

It should be noted that, the fraction of opioid eliminated through urine (not metabolized) is widely agreed upon to be 5-11% in adults [190]. However, higher values have been reported for neonates, with some being as high 20% [187, 191]. Here we chose to use a value $f_r = 0.2$ based upon the published values for neonatal metabolite profiles [192]. Because we did not consider other metabolites, in our calculation $f_r + f_m = 1$, which would make $f_m = 0.8$.

While few reports exist that quantify neonate metabolite profiles, there are indications that choosing a value of 10 mL/min/kg for renal clearance (CL_r), represents a relevant value [191, 193-196]. For subject weight we used 2 kg for a preterm neonate, 3.5 kg for a full-term neonate, and 7.2 kg for a 6 month old child [198]. Using these body mass values we obtained opioid renal clearance values of 20 mL/min for a preterm neonate, 35 mL/min for a full-term neonate, and 72 mL/min for a 6 month old.

To obtain the urine concentration of oxycodone as a function of time, (see **Fig. 6.5 and B.7, blue line**) we divide the oxycodone elimination rate determined by using **Eq. B.4,** by the rate

of urine production. Here we used urine production rates of 0.5 mL/hr for a preterm neonate and 1 mL/hr for both a full-term neonate and a 6 month old child [199].

Now to determine the *urine noroxycodone*, the *serum* noroxycodone (primary metabolite) concentration must be found. This value (Cm) is dependent upon the rate of oxycodone metabolism and the rate of noroxycodone elimination in urine, mathematically expressed as **Eq. B.5**:

$$C_m(t) = f_m \frac{k \cdot IC}{k_m - k}(e^{-kt} - e^{-k_m t}) \qquad \textbf{Eq. B.5}$$

Where k is the elimination rate constant of the drug (oxycodone) and IC is the initial oxycodone serum concentration, f_m fraction of oxycodone metabolized to noroxycodone, k_m the elimination rate constant of the metabolite (noroxycodone), and ($t_{m1/2}$) is the metabolite half-life. While there is limited available data on the exact neonatal opioid metabolite half-life, the existing literature suggests that $t_{1/2} \approx t_{m1/2}$, in other words the parent drug and metabolite both exhibit similar half-lives [187, 192]. Therefore, our calculations assumed k_m=k [197, 200]. Using these values and **Eq. B.5** we obtained the serum concentration of noroxycodone.

With the serum values in hand we can now calculate the rate of noroxycodone elimination (the metabolite) in *urine* ($dC_{mu}(t)/dt$). These values were calculated using **Eq. B.4** in the same way as for oxycodone, using the appropriate parameters for CL_{mr} and f_{mr}. In healthy adults, a small fraction of noroxycodone is eliminated through metabolism to noroxymorphone. However, in the only published results of oxymorphone/noroxymorphone quantification in neonates, the concentration of both species was below the limit of quantification [192]. Therefore, we used $f_{mr} = 1$ (all noroxycodone is eliminated through urine, none is metabolized further). The value for renal clearance of primary drug was used as the renal clearance for noroxycodone ($CL_r = CL_{mr}$), due to the same observations that led us to use k_m=k [187, 192, 197, 200]. We then calculated the urine concentration of noroxycodone over time by dividing the rate of noroxycodone elimination by the rate of urine production.

155. Kammer, M. N.; Kussrow, A. K.; Olmsted, I. R.; Bornhop, D. J., A Highly Compensated Interferometer for Biochemical Analysis. *ACS sensors* **2018**.
184. Nutiu, R.; Li, Y., In vitro selection of structure-switching signaling aptamers. *Angewandte Chemie* **2005,** *44* (7), 1061-1065.
185. Bornhop, D. J.; Kammer, M. N.; Kussrow, A.; Flowers, R. A., 2nd; Meiler, J., Origin and prediction of free-solution interaction studies performed label-free. *Proc Natl Acad Sci U S A* **2016,** *113* (12), E1595-1604.
186. Houston, J. B.; Taylor, G., Drug Metabolite Concentration-Time Profiles - Influence of Route of Drug Administration. *British journal of clinical pharmacology* **1984,** *17* (4), 385-394.
187. Valitalo, P.; Kokki, M.; Ranta, V. P.; Olkkola, K. T.; Hooker, A. C., et al., Maturation of Oxycodone Pharmacokinetics in Neonates and Infants: a Population Pharmacokinetic Model of Three Clinical Trials. *Pharm Res* **2017,** *34* (5), 1125-1133.
188. Pacifici, G. M., Metabolism and pharmacokinetics of morphine in neonates: A review. *Clinics* **2016,** *71* (8), 474-480.
189. Yazdy, M. M.; Desai, R. J.; Brogly, S. B., Prescription Opioids in Pregnancy and Birth Outcomes: A Review of the Literature. *Journal of pediatric genetics* **2015,** *4* (2), 56-70.
190. Poyhia, R.; Seppala, T.; Olkkola, K. T.; Kalso, E., The pharmacokinetics and metabolism of oxycodone after intramuscular and oral administration to healthy subjects. *British journal of clinical pharmacology* **1992,** *33* (6), 617-621.
191. Pokela, M. L.; Anttila, E.; Seppala, T.; Olkkola, K. T., Marked variation in oxycodone pharmacokinetics in infants. *Paediatric anaesthesia* **2005,** *15* (7), 560-565.
192. Kokki, M.; Heikkinen, M.; Valitalo, P.; Hautajarvi, H.; Hokkanen, J., et al., Maturation of oxycodone pharmacokinetics in neonates and infants: Oxycodone and its metabolites in plasma and urine. *British journal of clinical pharmacology* **2017,** *83* (4), 791-800.
193. Kart, T.; Christrup, L. L.; Rasmussen, M., Recommended use of morphine in neonates, infants and children based on a literature review .1. Pharmacokinetics. *Paediatric anaesthesia* **1997,** *7* (1), 5-11.
194. Encinas, E.; Calvo, R.; Lukas, J. C.; Vozmediano, V.; Rodriguez, M., et al., A predictive pharmacokinetic/pharmacodynamic model of fentanyl for analgesia/sedation in neonates based on a semi-physiologic approach. *Paediatric drugs* **2013,** *15* (3), 247-257.
195. Ku, L. C.; Smith, P. B., Dosing in neonates: special considerations in physiology and trial design. *Pediatric research* **2015,** *77* (1-1), 2-9.
196. Davis, P. J.; Stiller, R. L.; Cook, D. R.; Brandom, B. W.; Davin-Robinson, K. A., Pharmacokinetics of sufentanil in adolescent patients with chronic renal failure. *Anesthesia and analgesia* **1988,** *67* (3), 268-271.
197. Kokki, H.; Rasanen, I.; Reinikainen, M.; Suhonen, P.; Vanamo, K., et al., Pharmacokinetics of oxycodone after intravenous, buccal, intramuscular and gastric administration in children. *Clinical pharmacokinetics* **2004,** *43* (9), 613-622.
198. Pomerance, H. H., Nelson Textbook of Pediatrics. *Archives of pediatrics & adolescent medicine* **1997,** *151* (3), 324.
199. Jones, M. D., Jr.; Gresham, E. L.; Battaglia, F. C., Urinary flow rates and urea excretion rates in newborn infants. *Biology of the neonate* **1972,** *21* (5), 321-329.

200. Kokki, H.; Rasanen, I.; Lasalmi, M.; Lehtola, S.; Ranta, V. P., et al., Comparison of oxycodone pharmacokinetics after buccal and sublingual administration in children. *Clinical pharmacokinetics* **2006,** *45* (7), 745-754.
201. Kussrow, A.; Baksh, M. M.; Bornhop, D. J.; Finn, M. G., Universal sensing by transduction of antibody binding with backscattering interferometry. *Chembiochem : a European journal of chemical biology* **2011,** *12* (3), 367-370.

Appendix C: CIR Analysis Program Tutorial

I have shown in chapters 5, 6, and 7 that the free-solution assay (FSA) and the compensated interferometric reader can be used effectively for a plethora of biomedical research and preclinical applications. This appendix is intended to be an overview of the operation and trouble-shooting procedures for a data analysis program which is intended to simplify system operation.

Figure C.1 shows an example of the raw data collected while operating the CIR, a spreadsheet of radians vs time. The first three rows consist of 1) The date of data collection, 2) the time data collection began, and 3) the time data collection terminated. Row 5 contains headers for the data columns, with the data arranged as follows: A is time, B is window 1 phase, and C is W2 phase. Column D contains the bounds for the camera windows. Column F contains the difference output. This raw data can be plotted in excel, although selecting regions to average for further analysis is inefficient in Excel. Interpretation of these traces can be unintuitive. For this reason, as part of my recent efforts I have been working on automating data collection. Thus far I have a program that saves the data as a tab-delineated spreadsheet, which can be opened in any common spreadsheet or text program for easy plotting, curve fitting, or other analysis.

	A	B	C	D	E	F
1	8/29/2018					
2	11:15:54 AM					
3	11:20:17 AM					
4						
5	Time	W1(rad.)	W2(rad.)	W1, W2 C	W2-W1	
6	(sec.)	0.82c/mm	0.82c/mm			
7	0	0.681311	1.524318	0	0.436002	0.032206
8	1.673	0.684543	1.523839	0	0.436002	0.028495
9	1.786	0.68754	1.524014	2330	0.436002	0.025674
10	1.903	0.690906	1.524565	200	0.436002	0.022859
11	2.019	0.693778	1.517712	0	0.436002	0.013133
12	2.118	0.696202	1.517659	2130	0.436002	0.010656
13	2.238	0.698212	1.52508	2330	0.436002	0.016068
14	2.353	0.701561	1.529944	2330	0.436002	0.017582
15	2.451	0.703201	1.529835	0	0.436002	0.015833
16	2.566	0.705245	1.528426	0	0.436002	0.01238
17	2.685	0.706807	1.526915	0	0.436002	0.009307
18	2.803	0.709034	1.527688	0	0.436002	0.007854
19	2.903	0.710781	1.528618	0	0.436002	0.007036
20	3.032	0.712218	1.530428	0	0.436002	0.007408
21	3.134	0.713002	1.531196	0	0.436002	0.007393
22	3.251	0.714384	1.531193	0	0.436002	0.006008
23	3.368	0.714696	1.527164	0	0.436002	0.001668
24	3.467	0.7154	1.530925	0	0.436002	0.004724
25	3.562	0.715902	1.533279	0	0.436002	0.006576
26	3.698	0.717139	1.532261	0	0.436002	0.004321
27	3.8	0.717395	1.530183	0	0.436002	0.001987
28	3.916	0.717894	1.530304	0	0.436002	0.001609

6 replicate glycerols

Fig. C.1 Raw data output: The data collection program saves the data as a tab-delineated spreadsheet, which can be opened in any common spreadsheet or text-editing program.

Auto analysis program

As with any LabVIEW VI, the Auto Analysis program will run when it is first launched. However, if the program is not running, click the top left button with a right-facing arrow icon (**Fig C.2**). The program can also be stopped at any time by clicking the button with red-lettered "STOP." The program can then be started again with no interruption by clicking the right-facing arrow again. On older computers, it can be helpful to stop the program when not using it, then restart it when needed. The auto-analysis program can slow down the performance of other programs on the computer but will not do so when stopped. **NOTE**: stopping the program using the red stop sign in the top left (next to the "run" arrow) will cause errors, and the program may cease to function correctly when restarted. If this happens, simply close the Auto Analysis program and reopen it.

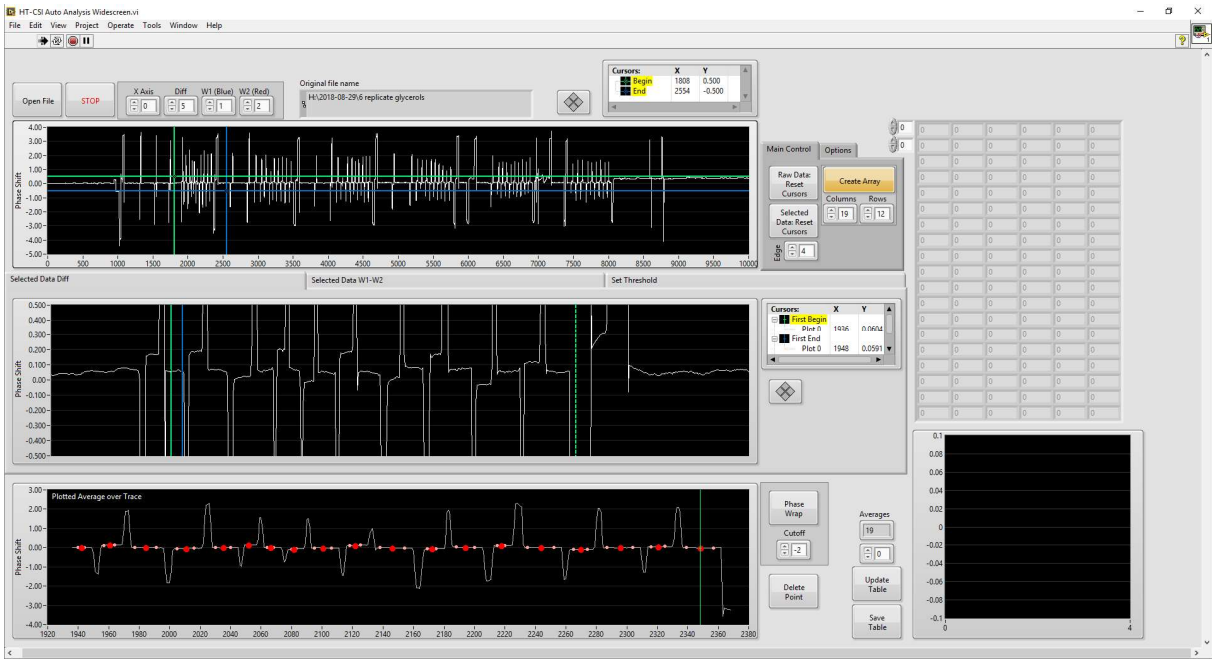

Fig. C.2 Auto analysis program user interface.

Step 1: Load data

To begin (**Step 1**), the user loads the desired raw data by clicking the "Open File" button and selecting the raw data from the dialog box (**Fig. C.3**). To the right of this button is an area where the column corresponding to the appropriate data can be adjusted. For standard operation, these values never need to be changed, but future updates to the analysis protocol may warrant analysis of different columns within the raw data output structure. Briefly, time (X axis) will be column 0, Window 1 and 2 will be column 1 and 2, respectively, and the differential readout will be column 5.

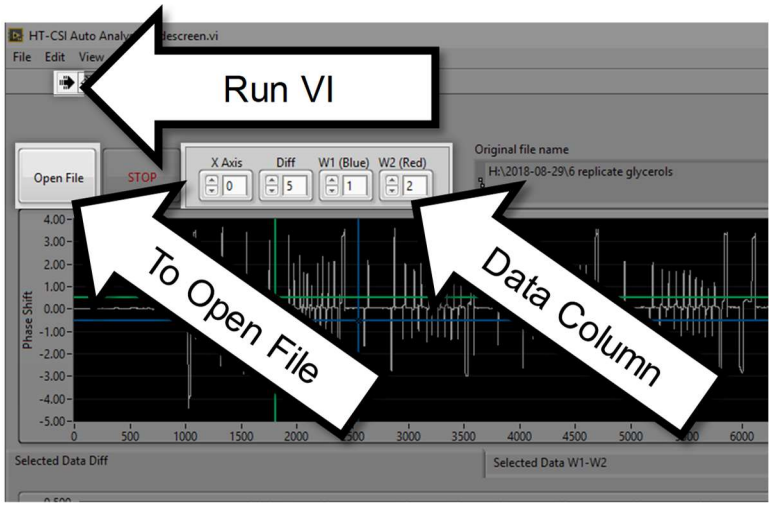

Fig. C.3 The program will run when launched, but if the program is stopped or paused, click the arrow to run. To load data, click the "Open File" button and a dialog box will appear. Select the raw data to be analyzed. For standard operation, there is no need to adjust the "Data column" inputs.

Step 2: Select Region of Data for analysis

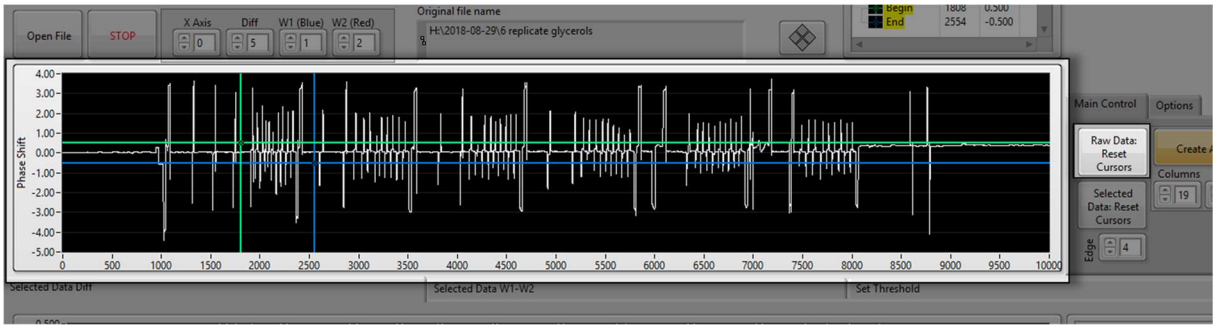

Fig. C.4 Use the blue and green cursors to select the phase data from the concentration to be analyzed. Reset the location of these cursors using the "Raw Data Reset Cursor" button.

Once the data is loaded, the next step is to select the duration of data containing the first 5-replicate measurements of the first test/reference solution pair. To do this, use the pointer to click and drag the green and blue cursors to surround the desired data region, as illustrated in Fig 4.12. **NOTE:** The green cursor should go to the left and top of the data region with the blue cursor on the right and bottom. If the cursors are not visible, then they are outside of the bounds of the graph. The cursors can be reset to their default position by clicking the "Raw Data Reset Cursors" button to the right of the top plot **(Fig. C.4**).

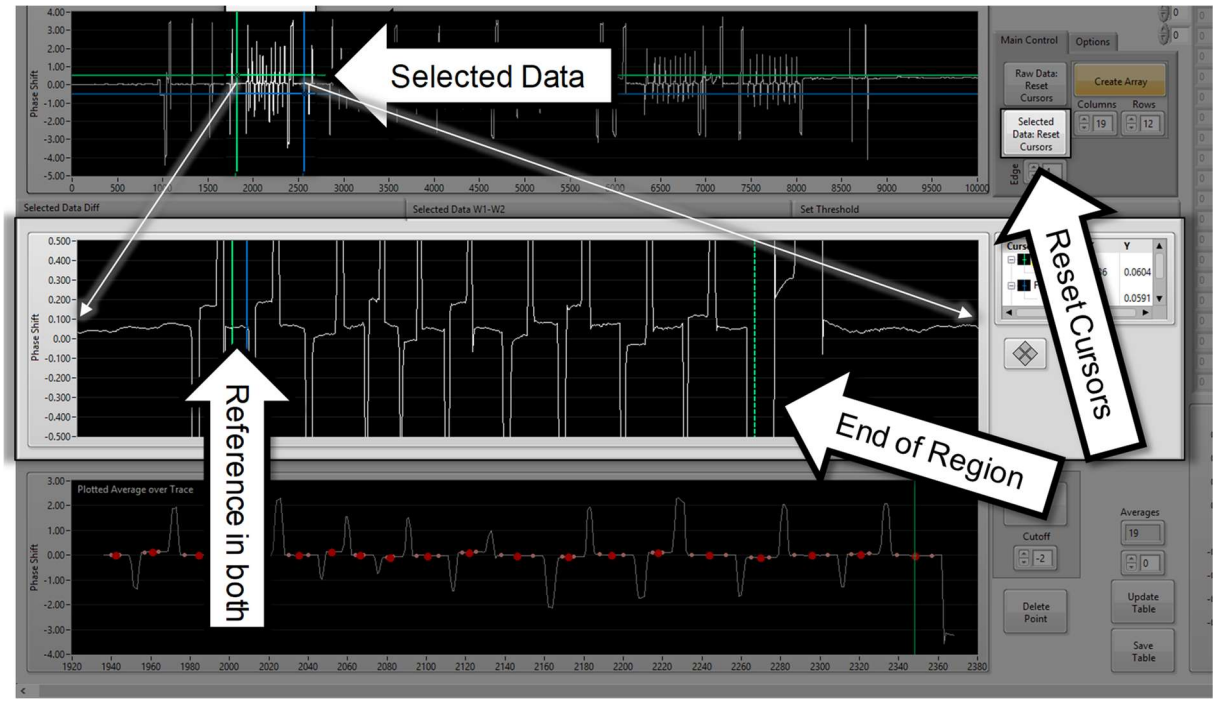

Fig. C.5 The middle window shows a zoomed in view of data selected in the top panel.

The middle window shows a zoomed-in view of the data selected in the top panel. The top panel's cursors control the bounds for this graph. The blue and green cursors in the middle graph will control how the program discriminates "solution" and "oil" regions of the trace and can be moved with the pointer. The first cursor (from the left, solid green) should be placed at the beginning of the first flat region at a phase shift of 0 after the long rinse. This is the region of the trace where the reference solution is in both windows. Ensure the cursors is placed within the flat region (it is ok to miss the first few data points to err on the side of caution). The second cursor (solid blue) should be placed just before the end of this same flat region. As shown in Figure 13, there will be 19 flat regions between "Reference in both" and "End of Region." The dotted green cursor should be placed after the last flat region. In most cases, the middle plot will look like it contains no data here, because the oil will cause a phase-shift excursion large enough to be off the scale of this plot. If the cursors are not within this window, they can be reset to a default value within this window by clicking the "Selected Data Reset Cursors" button (**Fig. C.5**).

The first two cursors will correspond to the duration when the first reference drop is in front of both window 1 and window 2. Large excursions from this baseline that exceed the cutoff

(detailed below) will be denoted as "oil." The last cursor denotes the end of this solution pair's replicate droplets, so no data after this cursor will be considered when the program averages and arranges the data for output. Behind the scenes, here the program will average the data points between the green and blue cursors and that value will be the "baseline."

If the difference data is confusing or the start/end location of the droplets is difficult to discern, the second tab on this middle window (Selected Data W1-W2) contains a plot of the individual windows overlaid (**Fig. C.6**). There are no controls on this tab, and the cursors cannot be moved from this tab; they reflect the location of the cursors in the first tab (Selected Data Diff). This tab can be useful to aid the user in discriminating where the first and last droplets begin and end.

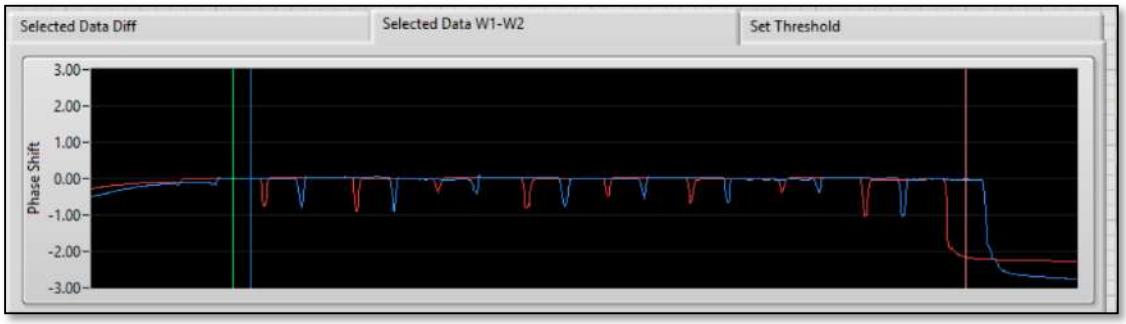

Fig. C.6 Use the tabs at the top of this middle window to switch between a plot of the difference data (**Fig. C.5**), or the raw data for both windows (window 1 is in blue, window 2 is in red). This is not necessary for analysis, but this is a useful plot to aid the user determine where the data begins and ends.

Step 3: Set cutoff threshold

To discriminate between usable data and oil, the program uses a cutoff with a user-adjustable threshold (**Fig. C.7**). Two criteria (with two independently adjustable thresholds) are used here: 1) the absolute magnitude of the difference signal relative to the baseline and 2) the rate of change of the signal. Any time point where either the absolute magnitude or rate of change exceed their respective cutoff value is denoted as a "gap," and this is illustrated on this graph as any time point with a blue background. The operator adjusts the level of the threshold by clicking the horizontal line with the pointer, then dragging it up or down vertically.

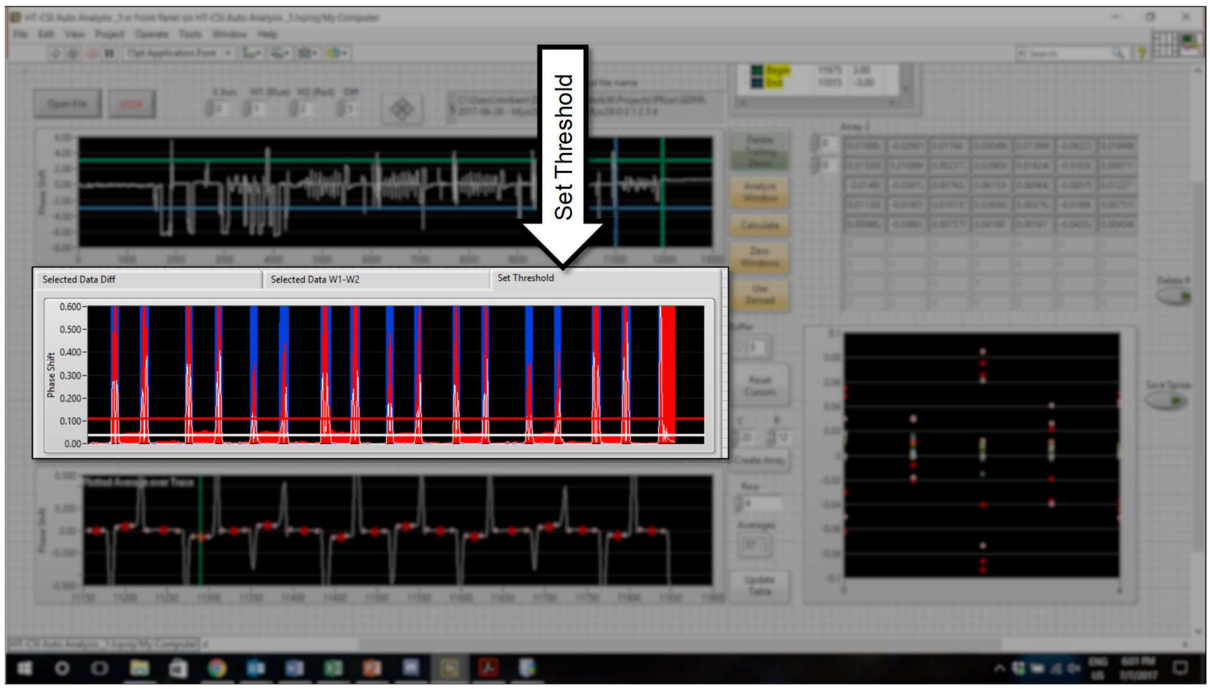

Fig. C.7 Select the "Set Threshold" tab to display a plot of cutoff criteria. The vertical blue bars show where the algorithm has "cut" data. This should correspond to data containing oil. Raise or lower the horizontal red and white bars to change the threshold parameters.

The absolute magnitude of the signal is displayed on the plot as the solid red area, as explained in **Fig. C.8**. The tall, sharp red peaks correspond to the time when oil passes through either window, as the FC-40 oil used to separate solutions has a much different RI than the aqueous solutions. Areas with a red arrow correspond to where the same test or reference solution fully fills both W1 and W2, therefore the difference is 0. Areas marked with a white arrow correspond to a test solution in W1 and reference solution in W2, or vice versa, where the signal magnitude is appreciable (~0.2 radians). The cutoff for this threshold can be adjusted by moving the red horizontal bar using the pointer. If you cannot see the red bar, click the "Reset Threshold Cursors" button to the right

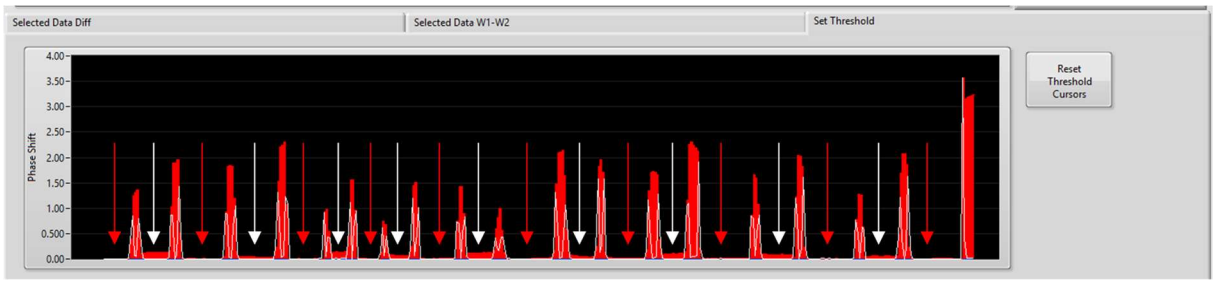

Fig. C.8 Cutoff threshold tab explanation: Areas with a red arrow correspond to where the same sample or reference fully fills both W1 and W2, therefore the difference is 0. Areas marked with a white arrow correspond to a sample in W1 and reference in W2, or vice versa, where the signal magnitude is appreciable (~0.2 radians). The tall peaks in between arrows correspond to where the oil separates sample drops.

The second criteria is rate of change, calculated using **Eq. C.1**:

$$Rate\ of\ Change = \frac{|X_t - X_{t-1}|}{t} \qquad \textbf{Eq. C.1}$$

Where the rate of change is calculated as the absolute value of the difference between each data point (X_t) and the data point at the previous time (X_{t-1}). The threshold cutoff for rate of change works similarly to the threshold for absolute magnitude and is controlled by the white horizontal bar.

In the vast majority of cases, either the magnitude or rate of change cutoff will suffice to properly partition the data, however in some cases one may miss the "gap" between solutions. For this reason, both are included.

The threshold values are set appropriately when a solid blue vertical bar completely fills the space between test/reference solution plateaus (**Fig. C.9**). An example of the cutoff threshold set too high, too low, and properly configured is displayed in **Fig C.10**.

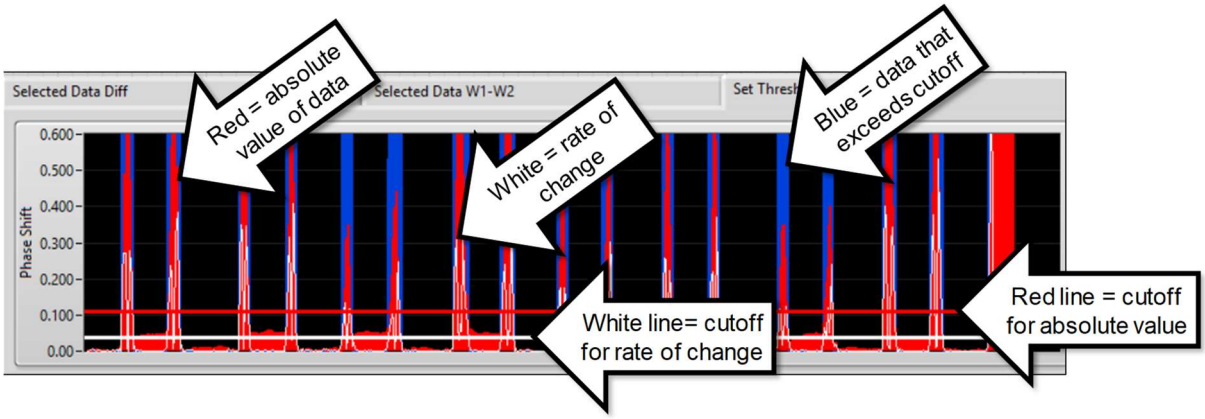

Fig. C.9 Cutoff threshold explanation

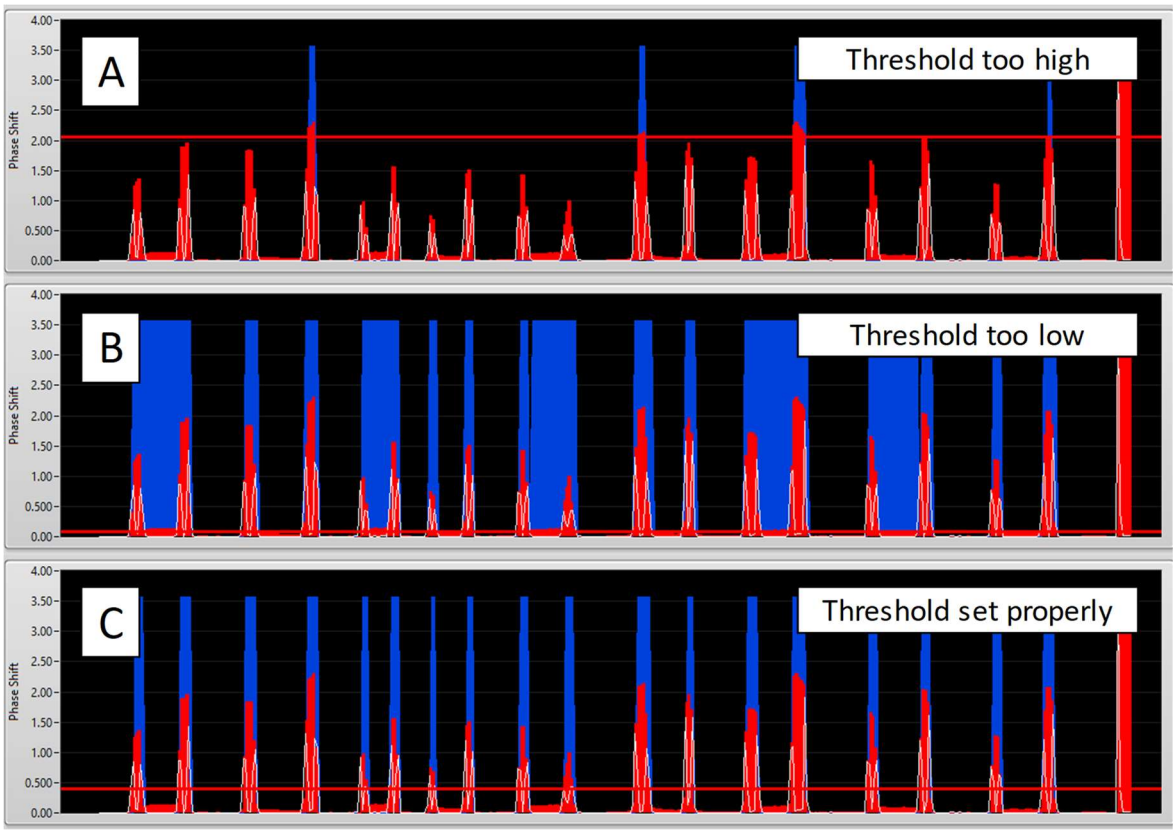

Fig. C.10 Cutoff threshold example. The vertical blue bars represent where the signal value has exceeded the cutoff, and therefore where the program has decided there is a "gap" between sample/reference measurements. In panel A, the threshold bar is set too high, and most of the "gaps" are missed. In panel B, the threshold bar is set too low, and therefore the program counts some of the Sample-Reference data regions as "gaps." Panel C shows the threshold in the "goldilocks" zone where all "gaps" exceed the threshold but none of the usable data does.

Step 4: Data partition and averaging

The program decides where the data of interest are based on the spaces between the "gaps" (the blue regions in **Fig. C.10**). All data points between two gaps are averaged together, and this represents the average value of a single differential measurement. When all cursors and thresholds are set properly, a 5 test/reference-sample pair train will be partitioned into 19 averages, and these values will be plotted in the bottom panel window as displayed in **Fig. C.11**.

In this bottom panel, the large red dot indicates the calculated average value for its segment of data. Each red dot's X value corresponds to the middle of its region's time, and the Y value is the average phase shift over that time period. The smaller pink dots indicate where that region begins and ends (**Fig. C.11**).

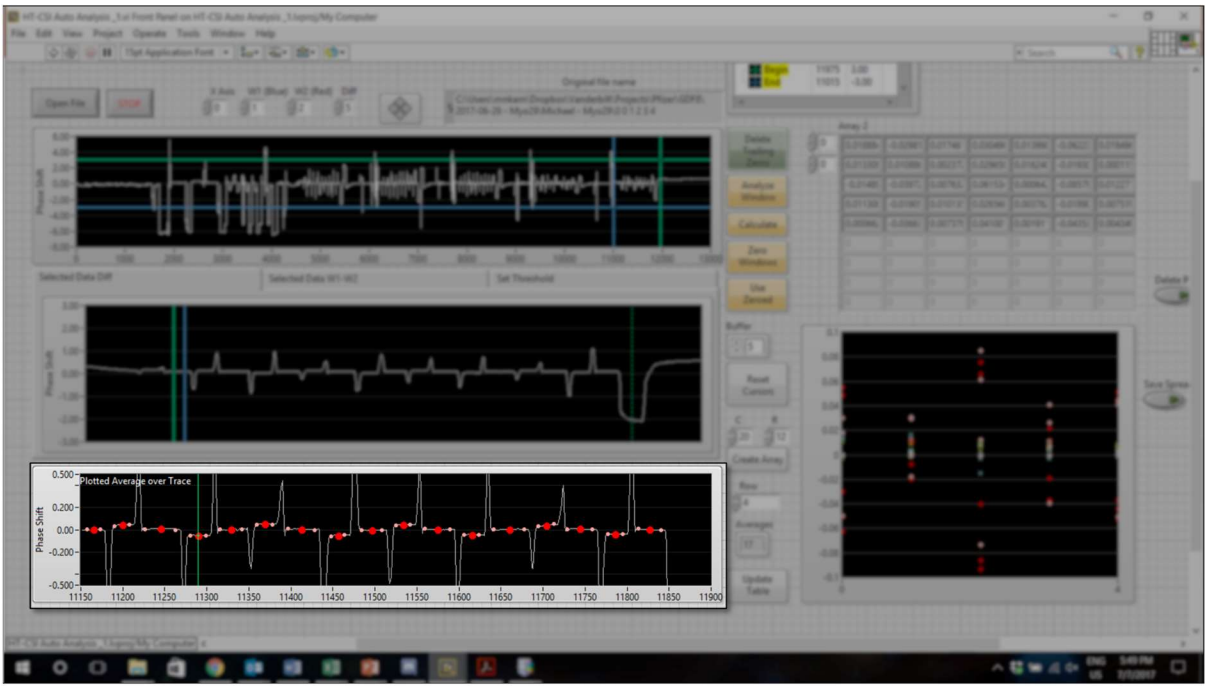

Fig. C.11 The data is partitioned into sample-reference regions according to the cutoff criteria then averaged over the length of a sample-reference measurement.

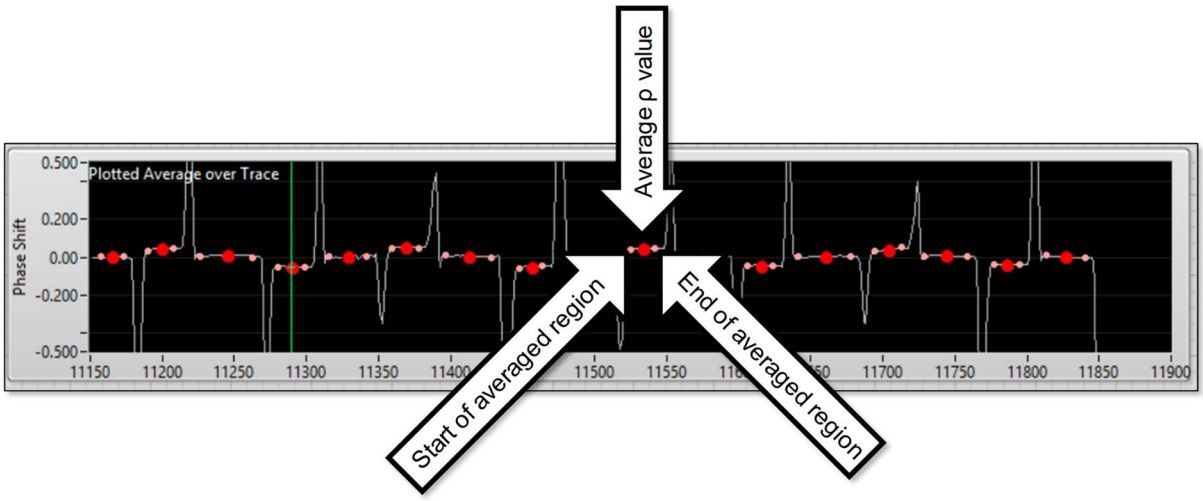

Fig. C.12 The large red dots are plotted in the center of each averaged data region. The red dots' X axis value is the average time of that region, and the Y value is the average phase shift of that region. The smaller pink dots indicate the start and end of the data region that is averaged.

If all red dots are present and in the correct location, then it is time to tabulate and save the data.

Fig. C.13 Clicking "Update Table" saves the averages to the table on the right. These values are plotted as a scatter dot plot underneath this table.

Step 5: Tabulation of averages

If the large red dots are placed correctly, click "Update Table" to save the averages into a table. Repeat steps 2-5 for all test/reference solution pairs (standard of 6 per tray). If the large red dots are placed incorrectly, adjust threshold cutoff (step 3) or the initial reference bounds (step 2).

Appendix D: CIR Setup and Troubleshooting

This appendix contains a compilation of setup and troubleshooting procedures that cover several aspects of CIR operation that were not detailed elsewhere.

Capillary setup for CIR operation

Capillary Coating Procedure

These steps are best performed with the capillary mounted on the CIR while watching the fringes.

1. Flow 1mL of DI H_2O (200 µL/min)
    a. At this point the fringes will be high contrast and uniform
2. Flow 100 µL of 1mM NaOH, followed by 500 µL DI H_2O (200 µL/min)
3. Flow 100 µL of 1mM H_2SO_4, followed by 1mL of DI H_2O (200 µL/min)
    a. At this point the fringes will still be high contrast and uniform
4. Flow 300 µL of Sigmacote (50 µL/min)
    a. Fringes will become blurry, not well defined, "wiggly"
5. Flow several full syringe volumes of air through the capillary to dry it (pull quickly by pump or by hand)
    a. Fringes will disappear, except briefly when small drops of Sigmacote move through
6. Flow 1mL DI H_2O, followed by 50 µL of 1mM NaOH (200 µL/min)
    a. Fringes will become slightly more uniform, but will still be "wiggly"
7. Flow 1mL DI H_2O (200 µL/min)
    a. Fringes should return to high contrast, uniform. If they do not, flow some Fluorinert through capillary, followed by more water.
8. Begin Assay once fringes return to high contrast/uniform and are stable over 30 seconds while pulling water at 200 µL/min

The capillary should be re-aligned using the matrix you will run assays in (buffer, serum, etc.). At this point the capillary is ready to begin assays.

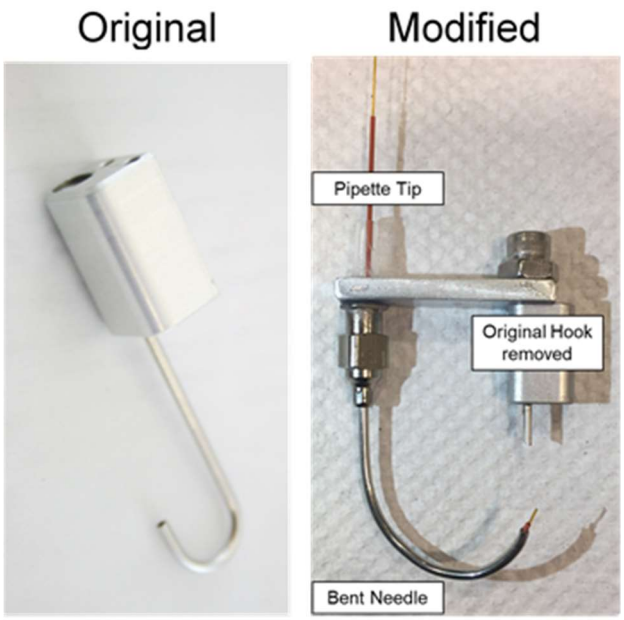

Fig. D.1 The unmodified and modified Dropix Sample Collection Hook.

Capillary/Dropix Interface

The sample collection Hook: The Dropix sample hook guides the tube/capillary through the oil reservoir and into the bottom of the sample well tray, guided by the Dropix. The inner diameter (0.8 mm) holds the tubing secure so that there is no movement of the opening of the tubing relative to the sample hook during operation. The original sample hook was designed for flexible FEP tubing and makes a very tight 180° turn with a radius of ~2.5 mm.

The HT-CSI system requires a single piece of uninterrupted capillary from sample collection to detection. The turn in the original hook was too tight to allow capillary through without breaking. The hook was modified to enable capillary (450 µM OD) to pass through

The original hook is removed using strong wire cutters or a Dremel tool with cutting attachment. This leaves the hook fitting without the hook.

To facilitate capillary handling, a 12-gauge blunt needle is bent (using a C-Clamp and a 1" OD metal pipe). Then, the needle is attached to the hook fitting by a 1" steel "arm" bolted into the hook fitting by ¼"-20. The needle is secured to the arm using a pipette tip and superglue.

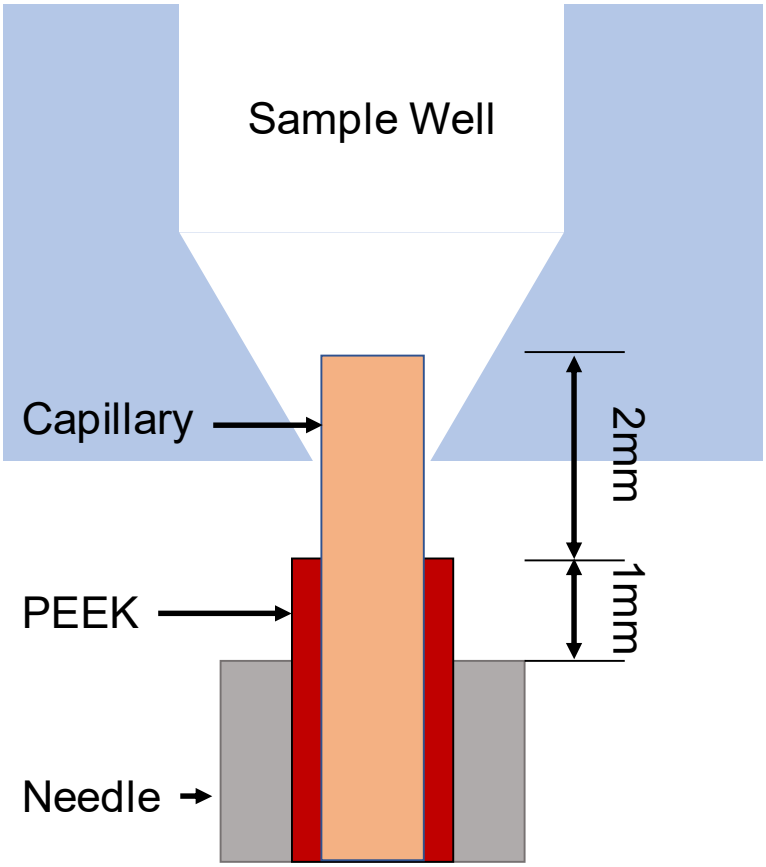

Fig. D.2 Schematic of the tip of the sample collection hook, peek tubing, and capillary opening.

The sample collection end of the needle should be cut off (using Dremel cutting tool) to allow 2mm of clearance between the needle and the bottom of the sample tray when both are installed on the Dropix, and the Dropix is in the "Up" configuration (collecting sample).

A length of 1/16" OD / 0.02" ID PEEK tubing is inserted into the bent needle so that ~1.5" extends from the top of the ensemble and 1mm extends from the sample collection opening. The PEEK is necessary to firmly secure the capillary, and to ensure that ragged/uneven/dented portions of the steel tube do not damage the capillary as it is slide through the needle tubing.

Capillary is slid through the needle until 2mm extends past the tip of the PEEK. This means the capillary will extend 3mm past the end of the needle. When the Dropix is in the "Up" configuration, the capillary will extend 1mm into the sample well.

If the needle does not extend far enough, the Capillary may "shift" it's relative location and miss sample wells.

If the needle extends too far, the needle can hit the sample well tray. This will either:

1) Bump the tray, knocking it from the Dropix rack, causing the Dropix to miss collection of all subsequent drops OR even knock the tray off the device completely, spilling samples everywhere. 2) Cause the *needle* to enter the sample well. This can cause the sample to "run" down the needle (losing all sample into the oil bath), or cause sample to reside inside the tip of the needle, between the needle and the PEEK tubing. This sample can then interact with sample in subsequent wells causing carryover between samples

If the capillary does not extend far enough, some or all samples will be missed by the capillary, resulting in no sample drop introduction to the CIR system

If the capillary extends too far, as the hook moves from one well to the next, the end of the capillary will not lower enough to clear the bottom of the sample well. The capillary tip can then break off as it hits the bottom of the sample well tray

If the PEEK extends too far, the PEEK can enter the sample well, collecting sample in the "collar" between the PEEK and capillary. This sample can be introduced to subsequent wells, causing carryover between wells.

If the PEEK does not extend far enough to fully cover the opening of the needle, the capillary can scrape against the needle and crack/break/score and snap off

The circular opening to the capillary must be flat, uniform, and free of obstructions/cracks.

Obstructions and cracks can impede droplet flow (causing irregular flow speed), cause droplet breakup (turbulent flow), or harbor sample that will cause carryover in subsequent sample wells.

The capillary should be prepared by light scoring with a freshly broken edge of silicon wafer, then gentle bending of the capillary to snap off the edge. This should be done *after* the capillary is pushed through the needle, as the capillary opening is easily broken while inserting through needle.

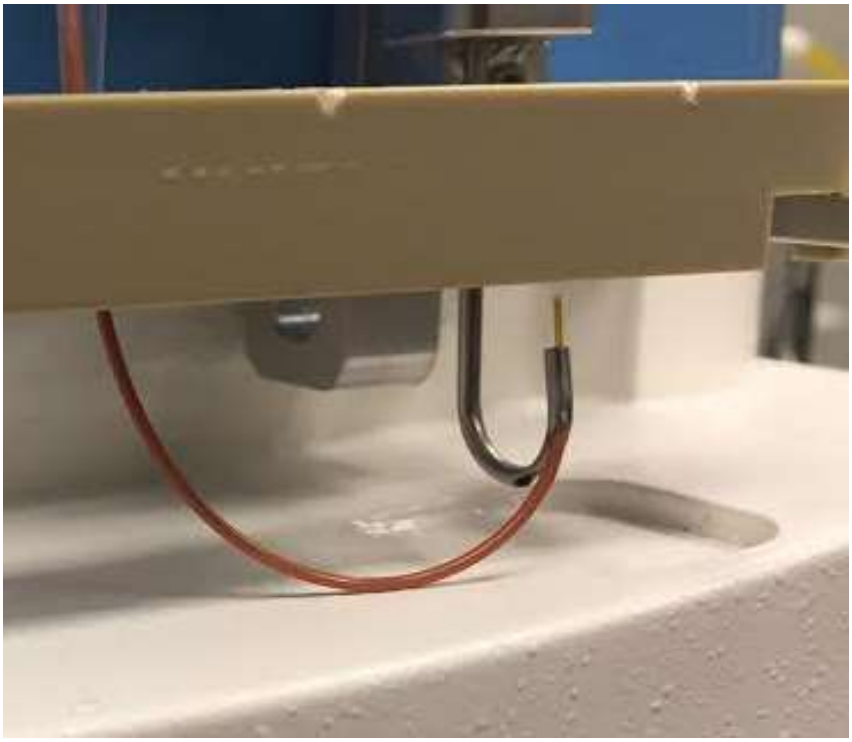

Fig. D.3 To adjust the capillary height, place the sample collection hook on the dropix with the oil bath removed. Then, snap a sample well tray into place and ensure a 1mm gap between the opening of the capillary and the bottom of the tray while the dropix is in the "down" (resting) position.

Capillary/Hook placement

The orange peek tubing should stop right where the metal tube hook does, and the capillary should extend upwards from this until it is 1mm below the sample wells. CHECK THIS BEFORE EVERY ASSAY.

The tip of the capillary can become damaged/moved during regular use. Score-off the first ~3 mm of capillary at the start of each new assay if the capillary is not replaced.

Once hook and capillary are in place, run the WELL TEST Dropix protocol which will rapidly move the capillary into and out of each sample well. The capillary should not move during this test, if it does, reset the capillary, adjust its location, and try again. Do this before placing the hook in the oil bath.

Changing the capillary between assays

1. Remove old capillary
    a. Unscrew Luer-Lock connection to syringe, empty syringe into waste
    b. Gently tug on capillary to remove it from Dropix sample collection hook
    c. Unscrew mounting plates holding capillary in v-groove
    d. Discard old capillary in glass waste
2. Prepare New Capillary
    a. Cut a 65cm length of capillary from the spool by gently scoring the capillary with the sharp edge of a shard from a shattered silicon wafer
    b. Connect one end of capillary to syringe through Luer-Lock
    c. Apply capillary coating
        i. Flow 1mL of water through the capillary at a rate of 200 µL/min
        ii. Flow 300 µL of hydrophobic coating through capillary at a rate of 50 µL/min for
        iii. Pull air through the capillary by hand for 3 full syringes
        iv. Flow 500 µL of water through the capillary at a rate of 50 µL/min
        v. At this point, flowing water through capillary should not cause more fringe drift. If it does, continue flowing water through at 50 µL/min until fringes no longer drift
3. Mount Capillary
    a. Lay capillary across the mounting block, ensuring it rests flatly in the groove. Screw mount plates down gently to hold capillary in place.
    b. Thread open end of capillary through the Dropix sample collection hook and mount sample collection hook on the Dropix robotic arm
4. Align Capillary
    a. Ensure the capillary is in the center of the stretched laser beam profile where the beam intensity is uniform
        i. The resulting fringes should be straight and with uniform intensity along the length of the capillary. If they are not, ensure the mounting plates are flat with even amounts of pressure, ensure the capillary is not twisted or bent.

IMPORTANT NOTE: Never touch the region of the capillary where the laser impinges. Any contact, with any material, will result in scratches/smudges on the capillary surface that will result in SEVERELY reduced interference fringe contrast ratio and uniformity.

Sample well tray preparation and cleaning.

The 24-well sample trays are milled from solid PEEK by CNC (Computer Numeric Control machining) to ensure biocompatibility. Before each use, the trays are washed by submersion with agitation for 5 minutes in each of the following, and rinsed with water between each: Methanol, Acetone, Chloroform, 10mM NaOH, 10mM Sulfuric Acid. The trays are then dried in an oven at 80°C for at least 30 minutes and allowed to cool to room temperature before use.

Standard Tray Wash Procedure

1. After use, keep trays in a soapy water bath until ready to clean (they can stay in this bath for up to 1-2 days)
2. Prepare 5 glass jars with the following solutions:
    a. Methanol, Acetone, Chloroform, 1mM Sulfuric Acid, 1mM Sodium Hydroxide
3. To begin cleaning
    a. Rinse trays under flowing tap water for 1 minute
    b. Shake off excess water, then place trays into glass jar with Methanol. Close the jar and gently swirl for 1 minute.
    c. Remove trays, rinse, and repeat step 2 for Acetone, Chloroform, Acid, and Base
    d. Rinse trays in DI water for 1 minute
    e. Place trays in warm oven (80°C) to dry for at least 30 minutes. Trays can be stored in the oven for several days before use. For longer storage times, trays can be kept in a sealed container at room temperature. Suggested storage vessels include Tupperware and Ziplock bags.
    f. Trays should be cooled to ambient temperature before use.

Oil Bath Preparation

To fill the oil bath to the proper level before an assay, the following steps are recommended. With no sample well strip in place, snap the hook onto the Dropix Guide. Fill the oil bath so that the oil is ~1 mm above the top of the capillary. NOTE: This will fill the oil bath to higher than the MITOS recommended amount. Proper oil level is achieved when there is no meniscus resulting from the capillary above the oil level (**Fig. D.4**). Ensure to replenish the oil after each assay.

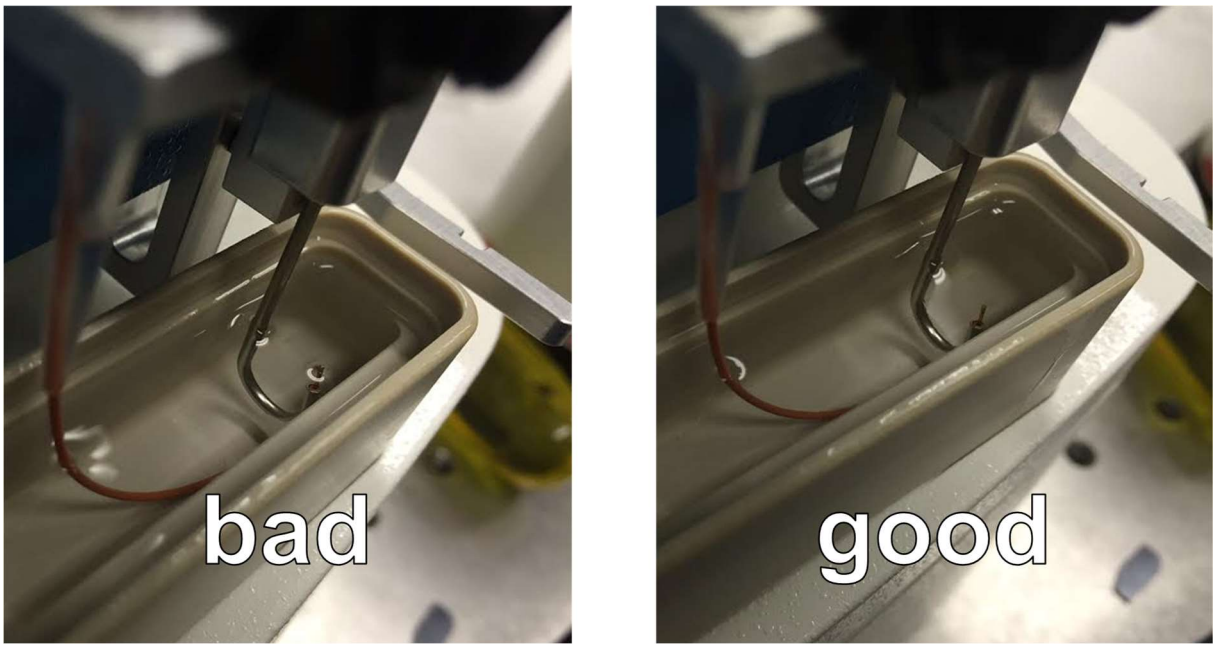

Fig. D.4 Incorrect and correct filling of the dropix oil bath.

Diode laser mount and power supply

The CIR uses a low-cost diode laser with integrated beam-conditioning optics to produce the elongated laser profile. The diode laser used in the experiments in this dissertation is produced by Lasermate (model PLP6395AH). A diode laser's wavelength and intensity are very sensitive to the supplied current, so to ensure wavelength and intensity stability, we powered the diode laser using an Acopian A5MT1200 high precision linear regulated power supply.

The diode laser was mounted using a C-Clamp collar-style housing manufactured at the Vanderbilt Physics and Astronomy Machine Shop (**Fig. D.5**). This housing was designed to fit onto a standard optical mounting.

Using the Acopian power supply, this diode laser has a lifetime of about 6 months of continuous use, although the lifetime can be significantly shorter if the diode laser is not handled with care. Diode Laser End of Life (EOL) is signified by laser flickering, dimming, or non-uniformity in the beam profile.

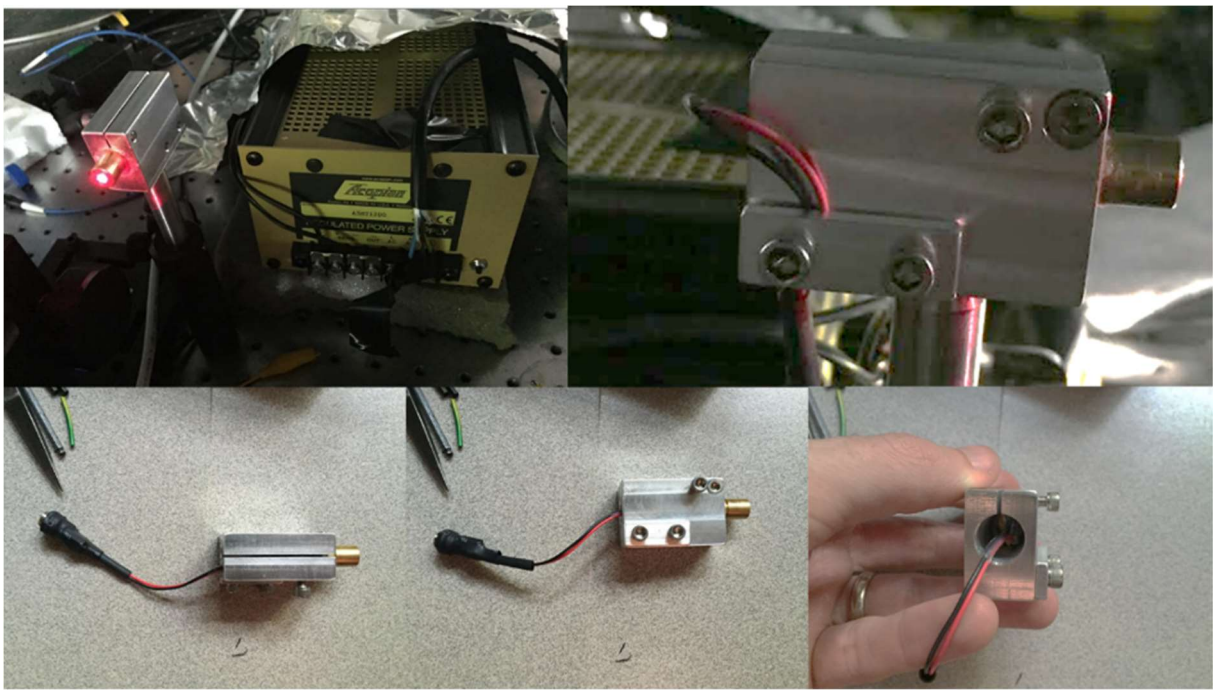

Fig. D.5 Diode laser power supply and housing/mount.

Arduino Power Supply

In several iterations of the instrument, the diode laser is powered by an Arduino UNO microcontroller board. The diode laser is powered by the Arduino's built in power converter, which produces a stable 5v output. The Arduino power circuit is modified by the addition of 3×100 nF capacitors across the leads, and a potentiometer for power output control (**Fig. D.6**).

To prepare the Arduino UNO to power the diode laser:

1. Solder these connections to the Arduino shield:
    a. Three capacitors in parallel soldered across ground/5V
    b. Potentiometer soldered across Ground/5V
    c. 2 1x4 connectors to attach Leads to laser
    d. 1 1x8 connector to connect Ground/5V to shield
2. Attach shield to Arduino Using connectors
3. Attach Leads to laser
    a. Black = Ground
    b. Red = 5V after Potentiometer
4. Dial in appropriate current using potentiometer
    a. "Appropriate" current is lowest current that produces strong, uniform beam. During initial setup, current can be turned to 100% (turn the potentiometer all the way down) to produce bright beam.
    b. Once beam is impinging on capillary (after alignment of the mirrors, camera), introduce liquid solution (water or buffer) and adjust the potentiometer until bright, high contrast, stable fringes. This is typically at ~95% (turn potentiometer all the way down, then back off slightly).

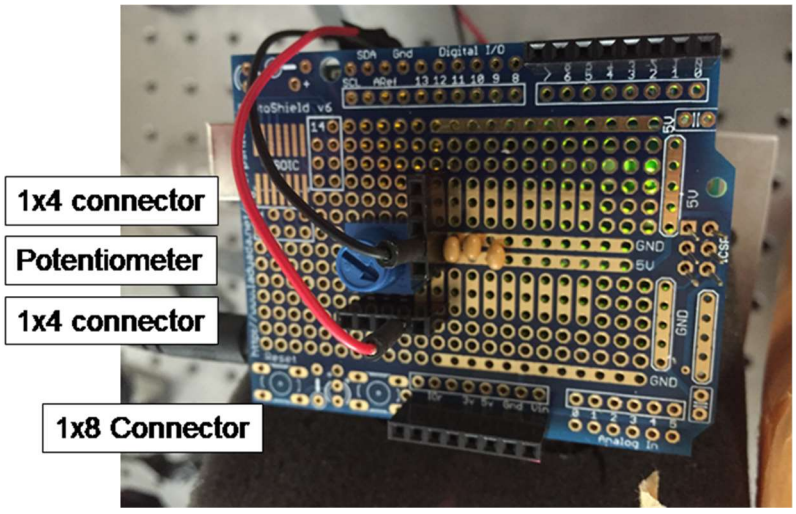

Fig. D.6 Arduino UNO used as the Diode laser power supply

Data collection program

These steps describe the process used by the Data collection program. This has been implemented in both the CIR analysis program developed in LabVIEW™ and in a commercial prototype, Redpoint.

1. Acquire Camera image
2. Partition camera image into two discrete windows
    a. This is hard coded to be the 500 pixels at either end of the camera image
    b. The fringes from these 500 pixels are averaged to create the fringe signal for each window
3. Selection of fringes from fringe pattern for both windows for Fourier Transform
    a. The user selects a set of 5 fringes from the signal for each window. These fringes are selected during alignment and this window is locked in for the duration of the experiment (all samples in a binding curve OR all samples in a calibration curve and all unknowns to be measured and fit to the curve).
    b. This selection goes from the top of the first fringe to the top of the 5^{th} fringe
    c. The 5 fringes for both windows are Fourier Transformed. The phase for the dominant frequency is recorded for both windows, and the difference in this phase is recorded as the phase shift

Repeat this loop for duration of measurement. The result is a trace of phase-shift data the corresponds to the length of the experiment.

Complete List of References

1. Kammer, M. N. Characterization of aptamer-small molecule interactions with backscattering interferometry. Vanderbilt, Nashville, 2016.
2. Betzig, E.; Chichester, R. J., Single Molecules Observed by near-Field Scanning Optical Microscopy. *Science* **1993,** *262* (5138), 1422-1425.
3. Levene, M. J.; Korlach, J.; Turner, S. W.; Foquet, M.; Craighead, H. G., et al., Zero-mode waveguides for single-molecule analysis at high concentrations. *Science* **2003,** *299* (5607), 682-686.
4. Unsung Heroes. *Science* **2001,** *291* (5507), 1207.
5. Hell, S. W.; Wichmann, J., Breaking the Diffraction Resolution Limit by Stimulated-Emission - Stimulated-Emission-Depletion Fluorescence Microscopy. *Opt Lett* **1994,** *19* (11), 780-782.
6. Liedberg, B.; Nylander, C.; Lundstrom, I., Biosensing with Surface-Plasmon Resonance - How It All Started. *Biosens Bioelectron* **1995,** *10* (8), R1-R9.
7. Yu, Y.; Ramachandran, P. V.; Wang, M. C., Shedding new light on lipid functions with CARS and SRS microscopy. *Bba-Mol Cell Biol L* **2014,** *1841* (8), 1120-1129.
8. Moreira, B. G.; You, Y.; Behlke, M. A.; Owczarzy, R., Effects of fluorescent dyes, quenchers, and dangling ends on DNA duplex stability. *Biochem Bioph Res Co* **2005,** *327* (2), 473-484.
9. Olmsted, I. R.; Kussrow, A.; Bornhop, D. J., Comparison of Free-Solution and Surface-Immobilized Molecular Interactions Using a Single Platform. *Anal Chem* **2012,** *84* (24), 10817-10822.
10. Bornhop, D. J.; Latham, J. C.; Kussrow, A.; Markov, D. A.; Jones, R. D., et al., Free-solution, label-free molecular interactions studied by back-scattering interferometry. *Science* **2007,** *317* (5845), 1732-1736.
11. Cubrilovic, D.; Biela, A.; Sielaff, F.; Steinmetzer, T.; Klebe, G., et al., Quantifying Protein-Ligand Binding Constants Using Electrospray Ionization Mass Spectrometry: A Systematic Binding Affinity Study of a Series of Hydrophobically Modified Trypsin Inhibitors. *J Am Soc Mass Spectr* **2014,** *23* (10), 1768-1777.
12. Kaltashov, I. A.; Bobst, C. E.; Abzalimov, R. R.; Wang, G. B.; Baykal, B., et al., Advances and challenges in analytical characterization of biotechnology products: Mass spectrometry-based approaches to study properties and behavior of protein therapeutics. *Biotechnol Adv* **2012,** *30* (1), 210-222.
13. Hu, H. T.; Sheehan, J. H.; Chazin, W. J., The mode of action of centrin - Binding of Ca2+ and a peptide fragment of Kar1p to the C-terminal domain. *J Biol Chem* **2004,** *279* (49), 50895-50903.
14. Tzeng, S. R.; Kalodimos, C. G., Protein dynamics and allostery: an NMR view. *Curr Opin Struc Biol* **2011,** *21* (1), 62-67.
15. Ababou, A.; Ladbury, J. E., Survey of the year 2005: literature on applications of isothermal titration calorimetry. *Journal of Molecular Recognition* **2007,** *20* (1), 4-14.
16. Liang, Y., Applications of isothermal titration calorimetry in protein folding and molecular recognition. *J Iran Chem Soc* **2006,** *3* (3), 209-219.
17. Wienken, C. J.; Baaske, P.; Rothbauer, U.; Braun, D.; Duhr, S., Protein-binding assays in biological liquids using microscale thermophoresis. *Nat Commun* **2010,** *1*.
18. Zhang, W.; Duhr, S.; Baaske, P.; Laue, E., Microscale thermophoresis for the assessment of nuclear protein-binding affinities. *Methods Mol Biol* **2014,** *1094*, 269-276.

19. Baksh, M. M.; Kussrow, A. K.; Mileni, M.; Finn, M. G.; Bornhop, D. J., Label-free quantification of membrane-ligand interactions using backscattering interferometry. *Nat Biotechnol* **2011,** *29* (4), 357-360.
20. Kussrow, A.; Enders, C. S.; Bornhop, D. J., Interferometric Methods for Label-Free Molecular Interaction Studies. *Anal Chem* **2012,** *84* (2), 779-792.
21. Olmsted, I. R.; Hassanein, M.; Kussrow, A.; Hoeksema, M.; Li, M., et al., Toward Rapid, High-Sensitivity, Volume-Constrained Biomarker Quantification and Validation using Backscattering Interferometry. *Anal Chem* **2014,** *86* (15), 7566-7574.
22. Saetear, P.; Perrin, A. J.; Bartholdson, S. J.; Wanaguru, M.; Kussrow, A., et al., Quantification of Plasmodium-host protein interactions on intact, unmodified erythrocytes by back-scattering interferometry. *Malaria J* **2015,** *14*.
23. Wang, Z. L.; Swinney, K.; Bornhop, D. J., Attomole sensitivity for unlabeled proteins and polypeptides with on-chip capillary electrophoresis and universal detection by interferometric backscatter. *Electrophoresis* **2003,** *24* (5), 865-873.
24. Pesciotta, E. N.; Bornhop, D. J.; Flowers, R. A., Backscattering Interferometry: An Alternative Approach for the Study of Hydrogen Bonding Interactions in Organic Solvents. *Org Lett* **2011,** *13* (10), 2654-2657.
25. Houlne, M. P.; Hubbard, D. S.; Makhatadze, G. I.; Bornhop, D. J., Refractive Index-Based Calorimetric Studies of RNase T1 Unfolding in Small Volumes using Interferometric Backscatter. *Proceedings of the Society of Photo-Optical Instrumentation Engineers* **1996,** *2982*, 159-167.
26. Sota, H.; Hasegawa, Y.; Iwakura, M., Detection of conformational changes in an immobilized protein using surface plasmon resonance. *Analytical chemistry* **1998,** *70* (10), 2019-2024.
27. Craus, C.; Willand, N.; Villemagne, B.; Flipo, M.; Willery, E., et al., Unconventional surface plasmon resonance signals reveal quantitative inhibition of transcriptional repressor EthR by synthetic ligands. *Analytical biochemistry* **2014,** *452*, 54-66.
28. Gestwicki, J. E.; Hsieh, H. V.; Pitner, J. B., Using receptor conformational change to detect low molecular weight analytes by surface plasmon resonance. *Analytical chemistry* **2001,** *73* (23), 5732-5737.
29. Sulmann, S.; Dell'Orco, D.; Marino, V.; Behnen, P.; Koch, K. W., Conformational Changes in Calcium-Sensor Proteins under Molecular Crowding Conditions. *Chem-Eur J* **2014,** *20* (22), 6756-6762.
30. Daniels, P. B.; Deacon, J. K.; Eddowes, M. J.; Pedley, D. G., Surface-Plasmon Resonance Applied to Immunosensing. *Sensor Actuator* **1988,** *15* (1), 11-18.
31. Jung, L. S.; Campbell, C. T.; Chinowsky, T. M.; Mar, M. N.; Yee, S. S., Quantitative Interpretation of the Response of Surface Plasmon Resonance Sensors to Adsorbed Films. *Langmuir* **1998,** *14* (19), 5636-5648.
32. Sjolander, S.; Urbaniczky, C., Integrated Fluid Handling-System for Biomolecular Interaction Analysis. *Anal Chem* **1991,** *63* (20), 2338-2345.
33. Stenberg, E.; Persson, B.; Roos, H.; Urbaniczky, C., Quantitative-Determination of Surface Concentration of Protein with Surface-Plasmon Resonance Using Radiolabeled Proteins. *J Colloid Interf Sci* **1991,** *143* (2), 513-526.
34. Matthews, B. W., In *The Proteins III*, Academic Press: New York, 1977; pp 403-590.
35. Zhao, H.; Brown, P. H.; Schuck, P., On the Distribution of Protein Refractive Index Increments. *Biophys J* **2011,** *100* (9), 2309-2317.

36. Golander, C. G.; Kiss, E., Protein Adsorption on Functionalized and Esca-Characterized Polymer-Films Studied by Ellipsometry. *J Colloid Interf Sci* **1988,** *121* (1), 240-253.
37. Haussling, L.; Ringsdorf, H.; Schmitt, F. J.; Knoll, W., Biotin-Functionalized Self-Assembled Monolayers on Gold - Surface-Plasmon Optical Studies of Specific Recognition Reactions. *Langmuir* **1991,** *7* (9), 1837-1840.
38. Marsh, J. A.; Teichmann, S. A., Relative Solvent Accessible Surface Area Predicts Protein Conformational Changes upon Binding. *Structure* **2011,** *19* (6), 859-867.
39. Davis, T. M.; Wilson, W. D., Determination of the refractive index increments of small molecules for correction of surface plasmon resonance data. *Anal Biochem* **2000,** *284* (2), 348-353.
40. Tumolo, T.; Angnes, L.; Baptista, M. S., Determination of the refractive index increment (dn/dc) of molecule and macromolecule solutions by surface plasmon resonance. *Anal Biochem* **2004,** *333* (2), 273-279.
41. Boussaad, S.; Pean, J.; Tao, N. J., High-resolution multiwavelength surface plasmon resonance spectroscopy for probing conformational and electronic changes in redox proteins. *Anal Chem* **2000,** *72* (1), 222-226.
42. Salamon, Z.; Cowell, S.; Varga, E.; Yamamura, H. I.; Hruby, V. J., et al., Plasmon resonance studies of agonist/antagonist binding to the human delta-opioid receptor: New structural insights into receptor-ligand interactions. *Biophys J* **2000,** *79* (5), 2463-2474.
43. Hsieh, H. V.; Pitner, J. B.; Gestwicki, J. E. Detection of ligands by refractive surface methods. US 6,576,430 B1, June 10th, 2003.
44. Frostell-Karlsson, A.; Remaeus, A.; Roos, H.; Andersson, K.; Borg, P., et al., Biosensor analysis of the interaction between immobilized human serum albumin and drug compounds for prediction of human serum albumin binding levels. *J Med Chem* **2000,** *43* (10), 1986-1992.
45. Karlsson, R., Real-Time Competitive Kinetic-Analysis of Interactions between Low-Molecular-Weight Ligands in Solution and Surface-Immobilized Receptors. *Anal Biochem* **1994,** *221* (1), 142-151.
46. Karlsson, R.; Kullman-Magnusson, M.; Hamalainen, M. D.; Remaeus, A.; Andersson, K., et al., Biosensor analysis of drug-target interactions: Direct and competitive binding assays for investigation of interactions between thrombin and thrombin inhibitors. *Anal Biochem* **2000,** *278* (1), 1-13.
47. Metzger, J.; von Landenberg, P.; Kehrel, M.; Buhl, A.; Lackner, K. J., et al., Biosensor analysis of beta 2-glycoprotein I-reactive autoantibodies: Evidence for isotype-specific binding and differentiation of pathogenic from infection-induced antibodies. *Clin Chem* **2007,** *53* (6), 1137-1143.
48. Rich, R. L.; Myszka, D. G., Survey of the 2001 commercial optical biosensor literature. *Journal of Molecular Recognition* **2002,** *15* (6), 352-376.
49. Chen, H. J.; Kou, X. S.; Yang, Z.; Ni, W. H.; Wang, J. F., Shape- and size-dependent refractive index sensitivity of gold nanoparticles. *Langmuir* **2008,** *24* (10), 5233-5237.
50. Luan, Q. F.; Xue, Y.; Yao, X.; Lu, W., Hairpin DNA probe based surface plasmon resonance biosensor used for the activity assay of E. coli DNA ligase. *Analyst* **2010,** *135* (2), 414-418.
51. Christopeit, T.; Gossas, T.; Danielson, U. H., Characterization of Ca2+ and phosphocholine interactions with C-reactive protein using a surface plasmon resonance biosensor. *Anal Biochem* **2009,** *391* (1), 39-44.

52. Dell'Orco, D.; Muller, M.; Koch, K. W., Quantitative detection of conformational transitions in a calcium sensor protein by surface plasmon resonance. *Chem Commun* **2010,** *46* (39), 7316-7318.
53. Luka, Z.; Moss, F.; Loukachevitch, L. V.; Bornhop, D. J.; Wagner, C., Histone Demethylase LSD1 Is a Folate-Binding Protein. *Biochemistry-Us* **2011,** *50* (21), 4750-4756.
54. Hruby, V. J.; Tollin, G., Plasmon-waveguide resonance (PWR) spectroscopy for directly viewing rates of GPCR/G-protein interactions and quantifying affinities. *Current Opinions in Pharmacology* **2007,** *7*, 507-514.
55. Swann, M. J.; Peel, L. L.; Carrington, S.; Freeman, N. J., Dual-polarization interferometry: an analytical technique to measure changes in protein structure in real time, to determine the stoichiometry of binding events, and to differentiate between specific and nonspecific interactions. *Anal Biochem* **2004,** *329* (2), 190-198.
56. Cross, G. H.; Reeves, A. A.; Brand, S.; Popplewell, J. F.; Peel, L. L., et al., A new quantitative optical biosensor for protein characterisation. *Biosens Bioelectron* **2003,** *19* (4), 383-390.
57. Adams, N. M.; Olmsted, I. R.; Haselton, F. R.; Bornhop, D. J.; Wright, D. W., The effect of hybridization-induced secondary structure alterations on RNA detection using backscattering interferometry. *Nucleic Acids Res* **2013,** *41* (9), e103.
58. Ivanov, V. I.; Minchenk.Le; Minyat, E. E.; Frankkam.Md; Schyolki.Ak, Bbar to Abar Transition of DNA in Solution. *J Mol Biol* **1974,** *87* (4), 817-833.
59. Kypr, J.; Kejnovska, I.; Renciuk, D.; Vorlickova, M., Circular dichroism and conformational polymorphism of DNA. *Nucleic Acids Res* **2009,** *37* (6), 1713-1725.
60. Pesciotta, E. N.; Bornhop, D. J.; Flowers, R. A., Back-Scattering Interferometry: A Versatile Platform for the Study of Free-Solution versus Surface-Immobilized Hybridization. *Chemistry-an Asian Journal* **2011,** *6* (1), 70-73.
61. Markov, D.; Begari, D.; Bornhop, D. J., Breaking the 10(-7) barrier for RI measurements in nanoliter volumes. *Anal Chem* **2002,** *74* (20), 5438-5441.
62. Wang, Z. L.; Bornhop, D. J., Dual-capillary backscatter interferometry for high-sensitivity nanoliter-volume refractive index detection with density gradient compensation. *Analytical chemistry* **2005,** *77* (24), 7872-7877.
63. Swinney, K.; Markov, D.; Bornhop, D. J., Chip-scale universal detection based on backscatter interferometry. *Analytical chemistry* **2000,** *72* (13), 2690-2695.
64. Swinney, K.; Markov, D.; Bornhop, D. J., Ultrasmall volume refractive index detection using microinterferometry. *Rev Sci Instrum* **2000,** *71* (7), 2684-2692.
65. Jepsen, S. T.; Jorgensen, T. M.; Zong, W.; Trydal, T.; Kristensen, S. R., et al., Evaluation of back scatter interferometry, a method for detecting protein binding in solution. *The Analyst* **2015,** *140* (3), 895-901.
66. Project, E.; Friedman, R.; Nachliel, E.; Gutman, M., A molecular dynamics study of the effect of Ca2+ removal on calmodulin structure. *Biophys J* **2006,** *90* (11), 3842-3850.
67. Torok, K., Calmodulin conformational changes in the activation of protein kinases. *Biochem Soc T* **2002,** *30*, 55-61.
68. Vandonselaar, M.; Hickie, R. A.; Quail, J. W.; Delbaere, L. T., Trifluoperazine-induced conformational change in Ca(2+)-calmodulin. *Nat Struct Biol* **1994,** *1* (11), 795-801.
69. Skoog, D. A.; West, D. M.; Holler, F. J.; Crouch, S. R., *Fundamentals of Analytical Chemistry*. 9th ed.; Brooks/Cole: Belmont, CA, 2014.
70. Dickinson, T. A.; White, J.; Kauer, J. S.; Walt, D. R., A chemical-detecting system based on a cross-reactive optical sensor array. *Nature* **1996,** *382* (6593), 697-700.

71. Gharagheizi, F.; Ilani-Kashkouli, P.; Kamari, A.; Mohammadi, A. H.; Ramjugernath, D., Group Contribution Model for the Prediction of Refractive Indices of Organic Compounds. *J Chem Eng Data* **2014,** *59* (6), 1930-1943.
72. Katritzky, A. R.; Sild, S.; Karelson, M., Correlation and prediction of the refractive indices of polymers by QSPR. *J Chem Inf Comp Sci* **1998,** *38* (6), 1171-1176.
73. Koradi, R.; Billeter, M.; Wuthrich, K., MOLMOL: A program for display and analysis of macromolecular structures. *J Mol Graphics* **1996,** *14* (1), 51-55.
74. *CRC Handbook of Chemistry and Physics*. 77th ed.; Chemical Rubber Publishing Company: Boca Raton, 1996-1997.
75. Pettersen, E. F.; Goddard, T. D.; Huang, C. C.; Couch, G. S.; Greenblatt, D. M., et al., UCSF chimera - A visualization system for exploratory research and analysis. *Journal of computational chemistry* **2004,** *25* (13), 1605-1612.
76. Grosberg, A. Y.; Khokhlov, A. R., *Statistical Physics of Macromolecules*. American Institute of Physics: New York, 1994.
77. Fixman, M., Radius of Gyration of Polymer Chains. II. Segment Density and Excluded Volume Effects. *The Journal of Chemical Physics* **1962,** *36* (12), 3123-3129.
78. Sun, S. T.; Nishio, I.; Swislow, G.; Tanaka, T., The Coil-Globule Transition - Radius of Gyration of Polystyrene in Cyclohexane. *J Chem Phys* **1980,** *73* (12), 5971-5975.
79. Permyakov, S. E.; Cherskaya, A.; Senin, I. I.; Zargarov, A. A.; Shulga-Morskoy, S. V., et al., Effects of mutations in the calcium-binding sites of recoverin on its calcium affinity: evidence for successive filling of the calcium binding sites. *Protein Eng* **2000,** *13* (11), 783-790.
80. Nitsche, C.; Otting, G., NMR studies of ligand binding. *Curr Opin Struct Biol* **2017,** *48*, 16-22.
81. Ishii, K.; Noda, M.; Uchiyama, S., Mass spectrometric analysis of protein-ligand interactions. *Biophysics and physicobiology* **2016,** *13*, 87-95.
82. Cubrilovic, D.; Biela, A.; Sielaff, F.; Steinmetzer, T.; Klebe, G., et al., Quantifying Protein-Ligand Binding Constants using Electrospray Ionization Mass Spectrometry: A Systematic Binding Affinity Study of a Series of Hydrophobically Modified Trypsin Inhibitors. *J Am Soc Mass Spectr* **2012,** *23* (10), 1768-1777.
83. Ababou, A.; Ladbury, J. E., Survey of the year 2005: literature on applications of isothermal titration calorimetry. *Journal of molecular recognition : JMR* **2007,** *20* (1), 4-14.
84. Di Trani, J. M.; Moitessier, N.; Mittermaier, A. K., Measuring Rapid Time-Scale Reaction Kinetics Using Isothermal Titration Calorimetry. *Analytical chemistry* **2017,** *89* (13), 7022-7030.
85. Wienken, C. J.; Baaske, P.; Rothbauer, U.; Braun, D.; Duhr, S., Protein-binding assays in biological liquids using microscale thermophoresis. *Nat Commun* **2010,** *1*, 10.1038/ncomms1093.
86. Kussrow, A.; Enders, C. S.; Bornhop, D. J., Interferometric Methods for Label-Free Molecular Interaction Studies. *Analytical chemistry* **2012,** *84* (2), 779-792.
87. Ciesielski, G. L.; Hytonen, V. P.; Kaguni, L. S., Biolayer Interferometry: A Novel Method to Elucidate Protein-Protein and Protein-DNA Interactions in the Mitochondrial DNA Replisome. *Methods in molecular biology* **2016,** *1351*, 223-231.
88. Guerreiro, J. R. L.; Frederiksen, M.; Bochenkov, V. E.; De Freitas, V.; Sales, M. G. F., et al., Multifunctional Biosensor Based on Localized Surface Plasmon Resonance for Monitoring Small Molecule-Protein Interaction. *ACS nano* **2014,** *8* (8), 7958-7967.

89. Vashist, S. K.; Dixit, C. K.; MacCraith, B. D.; O'Kennedy, R., Effect of antibody immobilization strategies on the analytical performance of a surface plasmon resonance-based immunoassay. *The Analyst* **2011,** *136* (21), 4431-4436.
90. Wang, M.; Kussrow, A. K.; Ocana, M. F.; Chabot, J. R.; Lepsy, C. S., et al., Physiologically relevant binding affinity quantification of monoclonal antibody PF-00547659 to mucosal addressin cell adhesion molecule for in vitro in vivo correlation. *British journal of pharmacology* **2017,** *174* (1), 70-81.
91. Bornhop, D. J.; Kammer, M. N.; Kussrow, A.; Flowers, R. A., 2nd; Meiler, J., Origin and prediction of free-solution interaction studies performed label-free. *Proc Natl Acad Sci USA* **2016,** *113* (12), E1595-1604.
92. Olmsted, I. R.; Hassanein, M.; Kussrow, A.; Hoeksema, M.; Li, M., et al., Toward rapid, high-sensitivity, volume-constrained biomarker quantification and validation using backscattering interferometry. *Analytical chemistry* **2014,** *86* (15), 7566-7574.
93. Estevez, M. C.; Alvarez, M.; Lechuga, L. M., Integrated optical devices for lab-on-a-chip biosensing applications. *Laser Photonics Rev* **2012,** *6* (4), 463-487.
94. Lin, V. S.; Motesharei, K.; Dancil, K. P.; Sailor, M. J.; Ghadiri, M. R., A porous silicon-based optical interferometric biosensor. *Science* **1997,** *278* (5339), 840-843.
95. Feng, J.; Siu, V. S.; Roelke, A.; Mehta, V.; Rhieu, S. Y., et al., Nanoscale Plasmonic Interferometers for Multispectral, High-Throughput Biochemical Sensing. *Nano Lett* **2012,** *12* (2), 602-609.
96. Mariani, S.; Strambini, L. M.; Barillaro, G., Femtomole Detection of Proteins Using a Label-Free Nanostructured Porous Silicon Interferometer for Perspective Ultrasensitive Biosensing. *Analytical chemistry* **2016,** *88* (17), 8502-8509.
97. Mariani, S.; Strambini, L. M.; Barillaro, G., Electrical Double Layer-Induced Ion Surface Accumulation for Ultrasensitive Refractive Index Sensing with Nanostructured Porous Silicon Interferometers. *ACS sensors* **2018,** *3* (3), 595-605.
98. Li, D. F.; Feng, J.; Pacifici, D., Nanoscale optical interferometry with incoherent light. *Scientific reports* **2016,** *6*.
99. Born, M.; Wolf, E., *Principles of optics: electromagnetic theory of propagation, interference and diffraction of light*. 7th expanded ed.; Cambridge University Press: Cambridge ; New York, 1999; p xxxiii, 952 p.
100. Guha, B.; Gondarenko, A.; Lipson, M., Minimizing temperature sensitivity of silicon Mach-Zehnder interferometers. *Optics express* **2010,** *18* (3), 1879-1887.
101. Schneider, B. H.; Edwards, J. G.; Hartman, N. F., Hartman interferometer: versatile integrated optic sensor for label-free, real-time quantification of nucleic acids, proteins, and pathogens. *Clin Chem* **1997,** *43* (9), 1757-1763.
102. Baksh, M. M.; Kussrow, A. K.; Mileni, M.; Finn, M. G.; Bornhop, D. J., Label-free quantification of membrane-ligand interactions using backscattering interferometry. *Nature biotechnology* **2011,** *29* (4), 357-U173.
103. Wang, Z.; Bornhop, D. J., Dual-capillary backscatter interferometry for high-sensitivity nanoliter-volume refractive index detection with density gradient compensation. *Analytical chemistry* **2005,** *77* (24), 7872-7877.
104. Morcos, E. F.; Kussrow, A.; Enders, C.; Bornhop, D., Free-solution interaction assay of carbonic anhydrase to its inhibitors using back-scattering interferometry. *Electrophoresis* **2010,** *31* (22), 3691-3695.

105. Stjernstrom, M.; Roeraade, J., Method for fabrication of microfluidic systems in glass. *J Micromech Microeng* **1998,** *8* (1), 33-38.
106. Markov, D.; Begari, D.; Bornhop, D. J., Breaking the $10^{(-7)}$ barrier for RI measurements in nanoliter volumes. *Analytical chemistry* **2002,** *74* (20), 5438-5441.
107. Glière, A.; Delattre, C., Modeling and fabrication of capillary stop valves for planar microfluidic systems. *Sens Actuators, A* **2006,** *130-131*, 601-608.
108. Schwarz, F. P.; Puri, K. D.; Bhat, R. G.; Surolia, A., Thermodynamics of monosaccharide binding to concanavalin A, pea (Pisum sativum) lectin, and lentil (Lens culinaris) lectin. *The Journal of biological chemistry* **1993,** *268* (11), 7668-7677.
109. Sharon, N.; Lis, H., History of lectins: from hemagglutinins to biological recognition molecules. *Glycobiology* **2004,** *14* (11), 53R-62R.
110. Swanson, M. D.; Winter, H. C.; Goldstein, I. J.; Markovitz, D. M., A lectin isolated from bananas is a potent inhibitor of HIV replication. *The Journal of biological chemistry* **2010,** *285* (12), 8646-8655.
111. Olmsted, I. R.; Kussrow, A.; Bornhop, D. J., Comparison of Free-Solution and Surface-Immobilized Molecular Interactions Using a Single Platform. *Analytical chemistry* **2012,** *84* (24), 10817-10822.
112. Sulmann, S.; Kussrow, A.; Bornhop, D. J.; Koch, K. W., Label-free quantification of calcium-sensor targeting to photoreceptor guanylate cyclase and rhodopsin kinase by backscattering interferometry. *Scientific reports* **2017,** *7*, 45515.
113. Sulmann, S.; Dell'Orco, D.; Marino, V.; Behnen, P.; Koch, K. W., Conformational changes in calcium-sensor proteins under molecular crowding conditions. *Chemistry* **2014,** *20* (22), 6756-6762.
114. Polans, A. S.; Witkowska, D.; Haley, T. L.; Amundson, D.; Baizer, L., et al., Recoverin, a photoreceptor-specific calcium-binding protein, is expressed by the tumor of a patient with cancer-associated retinopathy. *Proceedings of the National Academy of Sciences of the United States of America* **1995,** *92* (20), 9176-9180.
115. Permyakov, S. E.; Cherskaya, A. M.; Senin, II; Zargarov, A. A.; Shulga-Morskoy, S. V., et al., Effects of mutations in the calcium-binding sites of recoverin on its calcium affinity: evidence for successive filling of the calcium binding sites. *Protein engineering* **2000,** *13* (11), 783-790.
116. Monnier, J. D., Optical interferometry in astronomy. *Rep Prog Phys* **2003,** *66* (5), 789-857.
117. Ligo Scientific Collaboration, GW151226: Observation of Gravitational Waves from a 22-Solar-Mass Binary Black Hole Coalescence. *Physical review letters* **2016,** *116* (24), 241103.
118. Dancil, K. P. S.; Greiner, D. P.; Sailor, M. J., A porous silicon optical biosensor: Detection of reversible binding of IgG to a protein A-modified surface. *J Am Chem Soc* **1999,** *121* (34), 7925-7930.
119. Hradetzky, D.; Claas, M.; Holger, R., Interferometric label-free biomolecular detection system. *Journal of Optics A: Pure and Applied Optics* **2006,** *8* (7), S360.
120. Schmitt, K.; Schirmer, B.; Hoffmann, C.; Brandenburg, A.; Meyrueis, P., Interferometric biosensor based on planar optical waveguide sensor chips for label-free detection of surface bound bioreactions. *Biosens Bioelectron* **2007,** *22* (11), 2591-2597.
121. Durbin, B. M. Development of a compensated interferometric detector. Vanderbilt, Nashville, TN, 2015.
122. Bornop, D. J.; Kammer, M. N. Robust Interferometer and Methods of Using Same. 2016.

123. Mayor, A., *Greek fire, poison arrows, and scorpion bombs : biological and chemical warfare in the ancient world*. 1st ed.; Overlook Duckworth: Woodstock, 2003; p 319 p.
124. Vucinic, S.; Antonijevic, B.; Tsatsakis, A. M.; Vassilopoulou, L.; Docea, A. O., et al., Environmental exposure to organophosphorus nerve agents. *Environmental Toxicology and Pharmacology* **2017,** *56*, 163-171.
125. Wiener, S. W.; Hoffman, R. S., Nerve Agents: A Comprehensive Review. *Journal of Intensive Care Medicine* **2004,** *19* (1), 22-37.
126. Holstege, C. P.; Kirk, M.; Sidell, F. R., CHEMICAL WARFARE: Nerve Agent Poisoning. *Critical Care Clinics* **1997,** *13* (4), 923-942.
127. Kyle, B. O., Aum Shinrikyo: Once and Future Threat? *Emerging Infectious Disease journal* **1999,** *5* (4), 413.
128. Rosman, Y.; Eisenkraft, A.; Milk, N.; et al., Lessons learned from the syrian sarin attack: Evaluation of a clinical syndrome through social media. *Annals of Internal Medicine* **2014,** *160* (9), 644-648.
129. Stone, R., U.K. attack puts nerve agent in the spotlight. *Science* **2018,** *359* (6382), 1314-1315.
130. A., B. M.; A., B. K., Review of health consequences from high-, intermediate- and low-level exposure to organophosphorus nerve agents. *Journal of Applied Toxicology* **1998,** *18* (6), 393-408.
131. Mangas, I.; Estevez, J.; Vilanova, E.; França, T. C. C., New insights on molecular interactions of organophosphorus pesticides with esterases. *Toxicology* **2017,** *376*, 30-43.
132. Talabani, J. M.; Ali, A. I.; Kadir, A. M.; Rashid, R.; Samin, F., et al., Long-term health effects of chemical warfare agents on children following a single heavy exposure. *Human & Experimental Toxicology* **2017,** *37* (8), 836-847.
133. Salvi, R. M.; Lara, D. R.; Ghisolfi, E. S.; Portela, L. V.; Dias, R. D., et al., Neuropsychiatric Evaluation in Subjects Chronically Exposed to Organophosphate Pesticides. *Toxicological Sciences* **2003,** *72* (2), 267-271.
134. Ray, D. E.; Richards, P. G., The potential for toxic effects of chronic, low-dose exposure to organophosphates. *Toxicology Letters* **2001,** *120* (1), 343-351.
135. Bowman, P. D.; Schuschereba, S. T.; Johnson, T. W.; Woo, F. J.; McKinney, L., et al., Myopathic changes in diaphragm of rats fed pyridostigmine bromide subchronically. *Fundamental and Applied Toxicology* **1989,** *13* (1), 110-117.
136. Baker, D. J.; Sedgwick, E. M., Single fibre electromyographic changes in man after organophosphate exposure. *Human & Experimental Toxicology* **1996,** *15* (5), 369-375.
137. Dési, I.; Nagymajtényi, L., Electrophysiological biomarkers of an organophosphorous pesticide, dichlorvos. *Toxicology Letters* **1999,** *107* (1), 55-64.
138. Hulse, E. J.; Davies, J. O. J.; Simpson, A. J.; Sciuto, A. M.; Eddleston, M., Respiratory Complications of Organophosphorus Nerve Agent and Insecticide Poisoning. Implications for Respiratory and Critical Care. *American Journal of Respiratory and Critical Care Medicine* **2014,** *190* (12), 1342-1354.
139. Phillips, K. F.; Deshpande, L. S., Repeated low-dose organophosphate DFP exposure leads to the development of depression and cognitive impairment in a rat model of Gulf War Illness. *NeuroToxicology* **2016,** *52*, 127-133.
140. Gunnell, D.; Eddleston, M.; Phillips, M. R.; Konradsen, F., The global distribution of fatal pesticide self-poisoning: Systematic review. *BMC Public Health* **2007,** *7* (1), 357.
141. Ellison, D. H., *Handbook of chemical and biological warfare agents*. 2nd ed.; CRC Press: Boca Raton, 2008; p xxxv, 762 p.

142. Bloch-Shilderman, E.; Rabinovitz, I.; Egoz, I.; Yacov, G.; Allon, N., et al., Determining a threshold sub-acute dose leading to minimal physiological alterations following prolonged exposure to the nerve agent VX in rats. *Archives of toxicology.* **2018,** *92* (2), 873,892.
143. Viveros, L.; Paliwal, S.; McCrae, D.; Wild, J.; Simonian, A., A fluorescence-based biosensor for the detection of organophosphate pesticides and chemical warfare agents. *Sensors and Actuators B: Chemical* **2006,** *115* (1), 150-157.
144. Walton, I.; Davis, M.; Munro, L.; Catalano, V. J.; Cragg, P. J., et al., A Fluorescent Dipyrrinone Oxime for the Detection of Pesticides and Other Organophosphates. *Organic Letters* **2012,** *14* (11), 2686-2689.
145. Du, D.; Wang, J.; Wang, L.; Lu, D.; Smith, J. N., et al., Magnetic Electrochemical Sensing Platform for Biomonitoring of Exposure to Organophosphorus Pesticides and Nerve Agents Based on Simultaneous Measurement of Total Enzyme Amount and Enzyme Activity. *Analytical chemistry* **2011,** *83* (10), 3770-3777.
146. Wang, D.; Zhao, Q.; Zoysa, R. S. S. d.; Guan, X., Detection of nerve agent hydrolytes in an engineered nanopore. *Sensors and Actuators B: Chemical* **2009,** *139* (2), 440-446.
147. Funari, R.; Della Ventura, B.; Schiavo, L.; Esposito, R.; Altucci, C., et al., Detection of Parathion Pesticide by Quartz Crystal Microbalance Functionalized with UV-Activated Antibodies. *Analytical chemistry* **2013,** *85* (13), 6392-6397.
148. Zourob, M.; Simonian, A.; Wild, J.; Mohr, S.; Fan, X., et al., Optical leaky waveguide biosensors for the detection of organophosphorus pesticides. *The Analyst* **2007,** *132* (2), 114-120.
149. Knaack, J. S.; Zhou, Y.; Abney, C. W.; Jacob, J. T.; Prezioso, S. M., et al., A High-Throughput Diagnostic Method for Measuring Human Exposure to Organophosphorus Nerve Agents. *Analytical chemistry* **2012,** *84* (21), 9470-9477.
150. No, H.-Y.; Kim, Y. A.; Lee, Y. T.; Lee, H.-S., Cholinesterase-based dipstick assay for the detection of organophosphate and carbamate pesticides. *Anal Chim Acta* **2007,** *594* (1), 37-43.
151. Apilux, A.; Isarankura-Na-Ayudhya, C.; Tantimongcolwat, T.; Prachayasittikul, V., Paper-based acetylcholinesterase inhibition assay combining a wet system for organophosphate and carbamate pesticides detection. *EXCLI Journal* **2015,** *14*, 307-319.
152. Rajapakse, B. N.; Thiermann, H.; Eyer, P.; Worek, F.; Bowe, S. J., et al., Evaluation of the Test-mate ChE (Cholinesterase) Field Kit in Acute Organophosphorus Poisoning. *Annals of Emergency Medicine* **2011,** *58* (6), 559-564.e556.
153. Ellman, G. L.; Courtney, K. D.; Andres, V.; Featherstone, R. M., A new and rapid colorimetric determination of acetylcholinesterase activity. *Biochemical Pharmacology* **1961,** *7* (2), 88-95.
154. Mishra, R. K.; Hubble, L. J.; Martin, A.; Kumar, R.; Barfidokht, A., et al., Wearable Flexible and Stretchable Glove Biosensor for On-Site Detection of Organophosphorus Chemical Threats. *ACS sensors* **2017,** *2* (4), 553-561.
155. Kammer, M. N.; Kussrow, A. K.; Olmsted, I. R.; Bornhop, D. J., A Highly Compensated Interferometer for Biochemical Analysis. *ACS sensors* **2018**.
156. Tiefenbrunn, T.; Forli, S.; Baksh, M. M.; Chang, M. W.; Happer, M., et al., Small Molecule Regulation of Protein Conformation by Binding in the Flap of HIV Protease. *ACS chemical biology* **2013,** *8* (6), 1223-1231.
157. Wang, M. M.; Kussrow, A. K.; Ocana, M. F.; Chabot, J. R.; Lepsy, C. S., et al., Physiologically relevant binding affinity quantification of monoclonal antibody PF-00547659

to mucosal addressin cell adhesion molecule for in vitro in vivo correlation. *British Journal of Pharmacology* **2017,** *174* (1), 70-81.
158. Olmsted, I. R.; Hassanein, M.; Kussrow, A.; Hoeksema, M.; Li, M., et al., Toward Rapid, High Sensitivity, Volume-Constrained Biomarker Quantification and Validation using Backscattering Interferometry. *Analytical chemistry* **2014,** *in press*.
159. Kammer, M. N.; Olmsted, I. R.; Kussrow, A. K.; Morris, M. J.; Jackson, G. W., et al., Characterizing aptamer small molecule interactions with backscattering interferometry. *The Analyst* **2014,** *139* (22), 5879-5884.
160. Cho, E. J.; Lee, J. W.; Ellington, A. D., Applications of Aptamers as Sensors. *Annu Rev Anal Chem* **2009,** *2*, 241-264.
161. Kaur, G.; Roy, I., Therapeutic applications of aptamers. *Expert Opin Inv Drug* **2008,** *17* (1), 43-60.
162. Toulme, J. J.; Di Primo, C.; Boucard, D., Regulating eukaryotic gene expression with aptamers. *Febs Lett* **2004,** *567* (1), 55-62.
163. Chu, T. C.; Twu, K. Y.; Ellington, A. D.; Levy, M., Aptamer mediated siRNA delivery. *Nucleic Acids Res* **2006,** *34* (10).
164. Chu, T. C.; Marks, J. W.; Lavery, L. A.; Faulkner, S.; Rosenblum, M. G., et al., Aptamer : toxin conjugates that specifically target prostate tumor cells. *Cancer Res* **2006,** *66* (12), 5989-5992.
165. Chu, T. C.; Shieh, F.; Lavery, L. A.; Levy, M.; Richards-Kortum, R., et al., Labeling tumor cells with fluorescent nanocrystal-aptamer bioconjugates. *Biosens Bioelectron* **2006,** *21* (10), 1859-1866.
166. Cao, Z.; Tong, R.; Mishra, A.; Xu, W.; Wong, G. C., et al., Reversible cell-specific drug delivery with aptamer-functionalized liposomes. *Angewandte Chemie* **2009,** *48* (35), 6494-6498.
167. Kussrow, A.; Kaltgrad, E.; Wolfenden, M. L.; Cloninger, M. J.; Finn, M. G., et al., Measurement of monovalent and polyvalent carbohydrate-lectin binding by back-scattering interferometry. *Analytical chemistry* **2009,** *81* (12), 4889-4897.
168. Schulze, N. D.; Hamelin, E. I.; Winkeljohn, W. R.; Shaner, R. L.; Basden, B. J., et al., Evaluation of Multiple Blood Matrices for Assessment of Human Exposure to Nerve Agents. *J Anal Toxicol* **2016,** *40* (3), 229-235.
169. Hamelin, E. I.; Schulze, N. D.; Shaner, R. L.; Coleman, R. M.; Lawrence, R. J., et al., Quantitation of five organophosphorus nerve agent metabolites in serum using hydrophilic interaction liquid chromatography and tandem mass spectrometry. *Analytical and bioanalytical chemistry* **2014,** *406* (21), 5195-5202.
170. Crow, B. S.; Pantazides, B. G.; Quinones-Gonzalez, J.; Garton, J. W.; Carter, M. D., et al., Simultaneous Measurement of Tabun, Sarin, Soman, Cyclosarin, VR, VX, and VM Adducts to Tyrosine in Blood Products by Isotope Dilution UHPLC-MS/MS. *Analytical chemistry* **2014,** *86* (20), 10397-10405.
171. Carter, M. D.; Crow, B. S.; Pantazides, B. G.; Watson, C. M.; Thomas, J. D., et al., Direct Quantitation of Methyl Phosphonate Adducts to Human Serum Butyrylcholinesterase by Immunomagnetic-UHPLC-MS/MS. *Analytical chemistry* **2013,** *85* (22), 11106-11111.
172. Mathews, T. P.; Carter, M. D.; Johnson, D.; Isenberg, S. L.; Graham, L. A., et al., High-Confidence Qualitative Identification of Organophosphorus Nerve Agent Adducts to Human Butyrylcholinesterase. *Analytical chemistry* **2017,** *89* (3), 1955-1964.

173. Florence, C. S.; Zhou, C.; Luo, F.; Xu, L., The Economic Burden of Prescription Opioid Overdose, Abuse, and Dependence in the United States, 2013. *Medical care* **2016,** *54* (10), 901-906.
174. Pryor, J. R.; Maalouf, F. I.; Krans, E. E.; Schumacher, R. E.; Cooper, W. O., et al., The opioid epidemic and neonatal abstinence syndrome in the USA: a review of the continuum of care. *Archives of disease in childhood. Fetal and neonatal edition* **2017,** *102* (2), F183-F187.
175. Tolia, V. N.; Patrick, S. W.; Bennett, M. M.; Murthy, K.; Sousa, J., et al., Increasing incidence of the neonatal abstinence syndrome in U.S. neonatal ICUs. *The New England journal of medicine* **2015,** *372* (22), 2118-2126.
176. Wachman, E. M.; Schiff, D. M.; Silverstein, M., Neonatal Abstinence Syndrome: Advances in Diagnosis and Treatment. *Jama* **2018,** *319* (13), 1362-1374.
177. Wexelblatt, S. L.; Ward, L. P.; Torok, K.; Tisdale, E.; Meinzen-Derr, J. K., et al., Universal maternal drug testing in a high-prevalence region of prescription opiate abuse. *The Journal of pediatrics* **2015,** *166* (3), 582-586.
178. Eckart, K.; Rohrich, J.; Breitmeier, D.; Ferner, M.; Laufenberg-Feldmann, R., et al., Development of a new multi-analyte assay for the simultaneous detection of opioids in serum and other body fluids using liquid chromatography-tandem mass spectrometry. *J Chromatogr B* **2015,** *1001*, 1-8.
179. Aukes, D. I.; Roofthooft, D. W. E.; Simons, S. H. P.; Tibboel, D.; van Dijk, M., Pain Management in Neonatal Intensive Care: Evaluation of the Compliance With Guidelines. *The Clinical journal of pain* **2015,** *31* (9), 830-835.
180. Mundt, L. A.; Graff, L.; Shanahan, K., *Graff's textbook of routine urinalysis and body fluids*. 2nd ed.; Wolters Kluwer/Lippincott Williams & Wilkins Health: Philadelphia, 2011; p xxii, 330 p.
181. Luzzi, V. I.; Saunders, A. N.; Koenig, J. W.; Turk, J.; Lo, S. F., et al., Analytic performance of immunoassays for drugs of abuse below established cutoff values. *Clin Chem* **2004,** *50* (4), 717-722.
182. Kohler, K. M.; Hammer, R.; Riedy, K.; Auwarter, V.; Neukamm, M. A., Evaluation of CEDIA and DRI Drugs of Abuse Immunoassays for Urine Screening on a Thermo Indiko Plus Analyzer. *Journal of clinical laboratory analysis* **2017,** *31* (1).
183. Kammer, M. N.; Kussrow, A. K.; Bornhop, D. J., Longitudinal pixel averaging for improved compensation in backscattering interferometry. *Optics letters* **2018,** *43* (3), 482-485.
184. Nutiu, R.; Li, Y., In vitro selection of structure-switching signaling aptamers. *Angewandte Chemie* **2005,** *44* (7), 1061-1065.
185. Bornhop, D. J.; Kammer, M. N.; Kussrow, A.; Flowers, R. A., 2nd; Meiler, J., Origin and prediction of free-solution interaction studies performed label-free. *Proc Natl Acad Sci U S A* **2016,** *113* (12), E1595-1604.
186. Houston, J. B.; Taylor, G., Drug Metabolite Concentration-Time Profiles - Influence of Route of Drug Administration. *British journal of clinical pharmacology* **1984,** *17* (4), 385-394.
187. Valitalo, P.; Kokki, M.; Ranta, V. P.; Olkkola, K. T.; Hooker, A. C., et al., Maturation of Oxycodone Pharmacokinetics in Neonates and Infants: a Population Pharmacokinetic Model of Three Clinical Trials. *Pharm Res* **2017,** *34* (5), 1125-1133.
188. Pacifici, G. M., Metabolism and pharmacokinetics of morphine in neonates: A review. *Clinics* **2016,** *71* (8), 474-480.
189. Yazdy, M. M.; Desai, R. J.; Brogly, S. B., Prescription Opioids in Pregnancy and Birth Outcomes: A Review of the Literature. *Journal of pediatric genetics* **2015,** *4* (2), 56-70.

190. Poyhia, R.; Seppala, T.; Olkkola, K. T.; Kalso, E., The pharmacokinetics and metabolism of oxycodone after intramuscular and oral administration to healthy subjects. *British journal of clinical pharmacology* **1992,** *33* (6), 617-621.
191. Pokela, M. L.; Anttila, E.; Seppala, T.; Olkkola, K. T., Marked variation in oxycodone pharmacokinetics in infants. *Paediatric anaesthesia* **2005,** *15* (7), 560-565.
192. Kokki, M.; Heikkinen, M.; Valitalo, P.; Hautajarvi, H.; Hokkanen, J., et al., Maturation of oxycodone pharmacokinetics in neonates and infants: Oxycodone and its metabolites in plasma and urine. *British journal of clinical pharmacology* **2017,** *83* (4), 791-800.
193. Kart, T.; Christrup, L. L.; Rasmussen, M., Recommended use of morphine in neonates, infants and children based on a literature review .1. Pharmacokinetics. *Paediatric anaesthesia* **1997,** *7* (1), 5-11.
194. Encinas, E.; Calvo, R.; Lukas, J. C.; Vozmediano, V.; Rodriguez, M., et al., A predictive pharmacokinetic/pharmacodynamic model of fentanyl for analgesia/sedation in neonates based on a semi-physiologic approach. *Paediatric drugs* **2013,** *15* (3), 247-257.
195. Ku, L. C.; Smith, P. B., Dosing in neonates: special considerations in physiology and trial design. *Pediatric research* **2015,** *77* (1-1), 2-9.
196. Davis, P. J.; Stiller, R. L.; Cook, D. R.; Brandom, B. W.; Davin-Robinson, K. A., Pharmacokinetics of sufentanil in adolescent patients with chronic renal failure. *Anesthesia and analgesia* **1988,** *67* (3), 268-271.
197. Kokki, H.; Rasanen, I.; Reinikainen, M.; Suhonen, P.; Vanamo, K., et al., Pharmacokinetics of oxycodone after intravenous, buccal, intramuscular and gastric administration in children. *Clinical pharmacokinetics* **2004,** *43* (9), 613-622.
198. Pomerance, H. H., Nelson Textbook of Pediatrics. *Archives of pediatrics & adolescent medicine* **1997,** *151* (3), 324.
199. Jones, M. D., Jr.; Gresham, E. L.; Battaglia, F. C., Urinary flow rates and urea excretion rates in newborn infants. *Biology of the neonate* **1972,** *21* (5), 321-329.
200. Kokki, H.; Rasanen, I.; Lasalmi, M.; Lehtola, S.; Ranta, V. P., et al., Comparison of oxycodone pharmacokinetics after buccal and sublingual administration in children. *Clinical pharmacokinetics* **2006,** *45* (7), 745-754.
201. Kussrow, A.; Baksh, M. M.; Bornhop, D. J.; Finn, M. G., Universal sensing by transduction of antibody binding with backscattering interferometry. *Chembiochem : a European journal of chemical biology* **2011,** *12* (3), 367-370.
202. Cheng, S.; Shi, F.; Jiang, X.; Wang, L.; Chen, W., et al., Sensitive detection of small molecules by competitive immunomagnetic-proximity ligation assay. *Analytical chemistry* **2012,** *84* (5), 2129-2132.
203. Nutiu, R.; Li, Y., Structure-switching signaling aptamers. *J Am Chem Soc* **2003,** *125* (16), 4771-4778.
204. Jackson, G. W. Methods for simultaneous generation of functional ligands. 2012.
205. Backmund, M.; Meyer, K.; Von Zielonka, M.; Eichenlaub, D., Ofloxacin causes false-positive immunoassay results for urine opiates. *Addict Biol* **2000,** *5* (3), 319-320.
206. Baden, L. R.; Horowitz, G.; Jacoby, H.; Eliopoulos, G. M., Quinolones and false-positive urine screening for opiates by immunoassay technology. *Jama-J Am Med Assoc* **2001,** *286* (24), 3115-3119.
207. French, D.; Wu, A.; Lynch, K., Hydrophilic interaction LC-MS/MS analysis of opioids in urine: significance of glucuronide metabolites. *Bioanalysis* **2011,** *3* (23), 2603-2612.

208. Jacobson, S. W.; Bihun, J. T.; Chiodo, L. M., Effects of prenatal alcohol and cocaine exposure on infant cortisol levels. *Development and psychopathology* **1999,** *11* (2), 195-208.
209. Milone, M. C., Laboratory testing for prescription opioids. *Journal of medical toxicology : official journal of the American College of Medical Toxicology* **2012,** *8* (4), 408-416.
210. Administration, S. A. a. M. H. S. Drug-Free Workplace Guidelines and Resources. https://www.samhsa.gov/workplace/resources.
211. French, D., The challenges of LC-MS/MS analysis of opiates and opioids in urine. *Bioanalysis* **2013,** *5* (22), 2803-2820.
212. Anand, K. J.; Hall, R. W.; Desai, N.; Shephard, B.; Bergqvist, L. L., et al., Effects of morphine analgesia in ventilated preterm neonates: primary outcomes from the NEOPAIN randomised trial. *Lancet* **2004,** *363* (9422), 1673-1682.
213. Siegel, R. L.; Miller, K. D.; Jemal, A., Cancer Statistics, 2015. *Ca-Cancer J Clin* **2015,** *65* (1), 5-29.
214. Aberle, D. R.; Adams, A. M.; Berg, C. D.; Black, W. C.; Clapp, J. D., et al., Reduced Lung-Cancer Mortality with Low-Dose Computed Tomographic Screening. *New Engl J Med* **2011,** *365* (5), 395-409.
215. Moyer, V. A.; Force, U. S. P. S. T., Screening for lung cancer: U.S. Preventive Services Task Force recommendation statement. *Ann Intern Med* **2014,** *160* (5), 330-338.
216. Wiener, R. S.; Gould, M. K.; Arenberg, D. A.; Au, D. H.; Fennig, K., et al., An Official American Thoracic Society/American College of Chest Physicians Policy Statement: Implementation of Low-Dose Computed Tomography Lung Cancer Screening Programs in Clinical Practice. *American Journal of Respiratory and Critical Care Medicine* **2015,** *192* (7), 881-891.
217. Hori, S. S.; Gambhir, S. S., Mathematical model identifies blood biomarker-based early cancer detection strategies and limitations. *Sci Transl Med* **2011,** *3* (109), 109ra116.
218. Rifai, N.; Ridker, P. M., High-sensitivity C-reactive protein: a novel and promising marker of coronary heart disease. *Clin Chem* **2001,** *47* (3), 403-411.
219. Ridker, P. M.; Rifai, N.; Clearfield, M.; Downs, J. R.; Weis, S. E., et al., Measurement of C-reactive protein for the targeting of statin therapy in the primary prevention of acute coronary events. *The New England journal of medicine* **2001,** *344* (26), 1959-1965.
220. Chaturvedi, A. K.; Caporaso, N. E.; Katki, H. A.; Wong, H. L.; Chatterjee, N., et al., C-reactive protein and risk of lung cancer. *Journal of clinical oncology : official journal of the American Society of Clinical Oncology* **2010,** *28* (16), 2719-2726.
221. Chen, Z. H.; Liang, R. L.; Guo, X. X.; Liang, J. Y.; Deng, Q. T., et al., Simultaneous quantitation of cytokeratin-19 fragment and carcinoembryonic antigen in human serum via quantum dot-doped nanoparticles. *Biosens Bioelectron* **2017,** *91*, 60-65.
222. Li, J.; Skeete, Z.; Shan, S. Y.; Yan, S.; Kurzatkowska, K., et al., Surface Enhanced Raman Scattering Detection of Cancer Biomarkers with Bifunctional Nanocomposite Probes. *Analytical chemistry* **2015,** *87* (21), 10698-10702.
223. Pastor, A.; Menendez, R.; Cremades, M.; Pastor, V.; Llopis, R., et al., Diagnostic value of SCC, CEA and CYFRA 21.1 in lung cancer: a Bayesian analysis. *European Respiratory Journal* **1997,** *10* (3), 603-609.
224. Wang, J.; Ahmad, H.; Ma, C.; Shi, Q. H.; Vermesh, O., et al., A self-powered, one-step chip for rapid, quantitative and multiplexed detection of proteins from pinpricks of whole blood. *Lab Chip* **2010,** *10* (22), 3157-3162.

225. Fan, R.; Vermesh, O.; Srivastava, A.; Yen, B. K. H.; Qin, L. D., et al., Integrated barcode chips for rapid, multiplexed analysis of proteins in microliter quantities of blood. *Nature biotechnology* **2008,** *26* (12), 1373-1378.
226. Garcia-Cordero, J. L.; Maerkl, S. J., A 1024-sample serum analyzer chip for cancer diagnostics. *Lab Chip* **2014**, DOI: 10.1039/c1033lc51153g.
227. Lee, H. J.; Kim, Y. T.; Park, P. J.; Shin, Y. S.; Kang, K. N., et al., A novel detection method of non–small cell lung cancer using multiplexed bead-based serum biomarker profiling. *The Journal of Thoracic and Cardiovascular Surgery* **2012,** *143* (2), 421-427.e423.
228. Lee, H. J.; Nedelkov, D.; Corn, R. M., Surface plasmon resonance imaging measurements of antibody arrays for the multiplexed detection of low molecular weight protein biomarkers. *Analytical chemistry* **2006,** *78* (18), 6504-6510.
229. Teramura, Y.; Iwata, H., Label-free immunosensing for alpha-fetoprotein in human plasma using surface plasmon resonance. *Analytical biochemistry* **2007,** *365* (2), 201-207.
230. Huang, C. S.; Chaudhery, V.; Pokhriyal, A.; George, S.; Polans, J., et al., Multiplexed Cancer Biomarker Detection Using Quartz-Based Photonic Crystal Surfaces. *Analytical chemistry* **2012,** *84* (2), 1126-1133.
231. Cunningham, B.; Li, P.; Lin, B.; Pepper, J., Colorimetric resonant reflection as a direct biochemical assay technique. *Sensor Actuat B-Chem* **2002,** *81* (2-3), 316-328.
232. Cunningham, B. T.; Laing, L., Microplate-based, label-free detection of biomolecular interactions: applications in proteomics. *Expert Rev Proteomics* **2006,** *3* (3), 271-281.
233. Guerra, E. N. S.; Rêgo, D. F.; Elias, S. T.; Coletta, R. D.; Mezzomo, L. A. M., et al., Diagnostic accuracy of serum biomarkers for head and neck cancer: A systematic review and meta-analysis. *Critical Reviews in Oncology / Hematology* **2016,** *101*, 93-118.
234. Biosystems, A. Protein Biomarker Discovery, Verification and Validation.
235. Mischak, H.; Schanstra, J. P., CE-MS in biomarker discovery, validation, and clinical application. *Proteom Clin Appl* **2011,** *5* (1-2), 9-23.
236. Diamandis, E. P., Biomarker validation is still the bottleneck in biomarker research. *Journal of internal medicine* **2012,** *272* (6), 620-620.
237. Gillette, M. A.; Carr, S. A., Quantitative analysis of peptides and proteins in biomedicine by targeted mass spectrometry. *Nat Methods* **2013,** *10* (1), 28-34.
238. Gilbert, M.; Livingston, R.; Felberg, J.; Bishop, J. J., Multiplex single molecule counting technology used to generate interleukin 4, interleukin 6, and interleukin 10 reference limits. *Analytical biochemistry* **2016,** *503*, 11-20.
239. Rissin, D. M.; Kan, C. W.; Campbell, T. G.; Howes, S. C.; Fournier, D. R., et al., Single-molecule enzyme-linked immunosorbent assay detects serum proteins at subfemtomolar concentrations. *Nature biotechnology* **2010,** *28* (6), 595-599.
240. Rissin, D. M.; Kan, C. W.; Song, L. N.; Rivnak, A. J.; Fishburn, M. W., et al., Multiplexed single molecule immunoassays. *Lab Chip* **2013,** *13* (15), 2902-2911.
241. Gold, L.; Ayers, D.; Bertino, J.; Bock, C.; Bock, A., et al., Aptamer-Based Multiplexed Proteomic Technology for Biomarker Discovery. *PloS one* **2010,** *5* (12).
242. Russell, T. M.; Green, L. S.; Rice, T.; Kruh-Garcia, N. A.; Dobos, K., et al., Potential of High-Affinity, Slow Off-Rate Modified Aptamer Reagents for Mycobacterium tuberculosis Proteins as Tools for Infection Models and Diagnostic Applications. *J Clin Microbiol* **2017,** *55* (10), 3072-3088.

243. Chen, C.; Zhou, S.; Cai, Y.; Tang, F., Nucleic acid aptamer application in diagnosis and therapy of colorectal cancer based on cell-SELEX technology. *npj Precision Oncology* **2017,** *1* (1), 37.
244. Barak, V.; Goike, H.; Panaretakis, K. W.; Einarsson, R., Clinical utility of cytokeratins as tumor markers. *Clin Biochem* **2004,** *37* (7), 529-540.
245. Takada, M.; Masuda, N.; Matsuura, E.; Kusunoki, Y.; Matui, K., et al., Measurement of cytokeratin 19 fragments as a marker of lung cancer by CYFRA 21-1 enzyme immunoassay. *British Journal Of Cancer* **1995,** *71*, 160.
246. Molina, R.; Filella, X.; Augé, J. M.; Fuentes, R.; Bover, I., et al., Tumor Markers (CEA, CA 125, CYFRA 21-1, SCC and NSE) in Patients with Non-Small Cell Lung Cancer as an Aid in Histological Diagnosis and Prognosis. *Tumor Biology* **2003,** *24* (4), 209-218.
247. Molina, R.; Marrades, R. M.; Augé, J. M.; Escudero, J. M.; Viñolas, N., et al., Assessment of a Combined Panel of Six Serum Tumor Markers for Lung Cancer. *American Journal of Respiratory and Critical Care Medicine* **2016,** *193* (4), 427-437.
248. Integrative Analysis of Lung Cancer, E.; Risk Consortium for Early Detection of Lung, C., Assessment of lung cancer risk on the basis of a biomarker panel of circulating proteins. *JAMA Oncology* **2018**, e182078.
249. Pujol, J. L.; Molinier, O.; Ebert, W.; Daurès, J. P.; Barlesi, F., et al., CYFRA 21-1 is a prognostic determinant in non-small-cell lung cancer: results of a meta-analysis in 2063 patients. *British Journal Of Cancer* **2004,** *90*, 2097.
250. Roeraade, J., Cutting of Glass and Fused-Silica Capillaries. *J High Res Chromatog* **1983,** *6* (3), 140-144.
251. Tarigan, H. J.; Neill, P.; Kenmore, C. K.; Bornhop, D. J., Capillary-scale refractive index detection by interferometric backscatter. *Analytical chemistry* **1996,** *68* (10), 1762-1770.
252. He, A.; Liu, T. C.; Dong, Z. N.; Ren, Z. Q.; Hou, J. Y., et al., A novel immunoassay for the quantization of CYFRA 21-1 in human serum. *Journal of clinical laboratory analysis* **2013,** *27* (4), 277-283.
253. Muzyka, K., Current trends in the development of the electrochemiluminescent immunosensors. *Biosens Bioelectron* **2014,** *54*, 393-407.
254. Atwater, T.; Cook, C. M.; Massion, P. P., The Pursuit of Noninvasive Diagnosis of Lung Cancer. *Semin Resp Crit Care* **2016,** *37* (5), 670-680.
255. Gould, M. K.; Ananth, L.; Barnett, P. G.; Cooperative, V. A. S., A clinical model to estimate the pretest probability of lung cancer in patients with solitary pulmonary nodules. *Chest* **2007,** *131* (2), 383-388.
256. Saetear, P.; Perrin, A. J.; Bartholdson, S. J.; Wanaguru, M.; Kussrow, A., et al., Quantification of Plasmodium-host protein interactions on intact, unmodified erythrocytes by back-scattering interferometry. *Malaria journal* **2015,** *14*, 88.
257. Kussrow, A.; Enders, C. S.; Castro, A. R.; Cox, D. L.; Ballard, R. C., et al., The potential of backscattering interferometry as an in vitro clinical diagnostic tool for the serological diagnosis of infectious disease. *The Analyst* **2010,** *135* (7), 1535-1537.
258. Adams, N. M.; Olmsted, I. R.; Haselton, F. R.; Bornhop, D. J.; Wright, D. W., The effect of hybridization-induced secondary structure alterations on RNA detection using backscattering interferometry. *Nucleic Acids Res* **2013,** *41* (9), e103.
259. Darnell, J. E.; Lodish, H.; Baltimore, D., *Molecular Cell Biology*. Scientific American Books: New York, 1990.

260. Leslie, T. E.; Lilley, T. H., Aqueous-Solutions Containing Amino-Acids and Peptides .20. Volumetric Behavior of Some Terminally Substituted Amino-Acids and Peptides at 298.15 K. *Biopolymers* **1985,** *24* (4), 695-710.
261. Fasman, G. D.; Schaffha.B; Goldsmit.L; Adler, A., Conformational Changes Associated with F-1 Histone-Deoxyribonucleic Acid Complexes - Circular Dichroism Studies. *Biochemistry-Us* **1970,** *9* (14), 2814-&.
262. Qian, R. L.; Mhatre, R.; Krull, I. S., Characterization of antigen-antibody complexes by size-exclusion chromatography coupled with low-angle light-scattering photometry and viscometry. *J Chromatogr A* **1997,** *787* (1-2), 101-109.
263. Velazquez-Campoy, A.; Freire, E., Isothermal titration calorimetry to determine association constants for high-affinity ligands. *Nat Protoc* **2006,** *1* (1), 186-191.
264. Latham, J. C.; Markov, D. A.; Sorensen, H. S.; Bornhop, D. J., Photobiotin surface chemistry improves label-free interferometric sensing of biochemical interactions. *Angew Chem Int Edit* **2006,** *45* (6), 955-958.
265. Markov, D. A.; Swinney, K.; Bornhop, D. J., Label-free molecular interaction determinations with nanoscale interferometry. *J Am Chem Soc* **2004,** *126* (50), 16659-16664.
266. Sorensen, H. S.; Larsen, N. B.; Latham, J. C.; Bornhop, D. J.; Andersen, P. E., Highly sensitive biosensing based on interference from light scattering in capillary tubes. *Appl Phys Lett* **2006,** *89* (15).
267. Kussrow, A.; Kaltgrad, E.; Wolfenden, M. L.; Cloninger, M. J.; Finn, M. G., et al., Measurement of Monovalent and Polyvalent Carbohydrate-Lectin Binding by Back-Scattering Interferometry. *Anal Chem* **2009,** *81* (12), 4889-4897.
268. Bornhop, D. J., Microvolume Index of Refraction Determinations by Interferometric Backscatter. *Appl Optics* **1995,** *34* (18), 3234-3239.
269. Sorensen, H. S. Self Calibrating Interferometric Sensing. PhD, Technical University of Denmark, Roskilde, 2006.
270. Bornhop, D. J.; Latham, J. C.; Kussrow, A.; Markov, D. A.; Jones, R. D., et al., Materials and Methods are available as supporting material on *Science* online. *Science* **2007**.